Contents

1 Introduction **5**

2 Physics Framework **8**
2.1 Electron Scattering. . . . 8
2.1.1 The Born Approximation. . . . 8
2.1.2 Kinematics. . . . 8
2.1.3 Reaction Cross Section. . . . 10
2.2 Nuclear Excitation Spectrum. . . . 12
2.2.1 Elastic Scattering. . . . 12
2.2.2 Inclusive Quasi-Elastic Scattering. . . . 15
2.2.3 The Resonance Region. . . . 18
2.2.4 Deep Inelastic Scattering. . . . 20
2.2.5 The Parton Model. . . . 23
2.2.6 Operator Product Expansion. . . . 25
2.2.7 A Link between the DIS and the Resonances Region: The Bloom-Gilman (Parton-Hadron) Duality. . . . 26
2.3 Conclusion. . . . 26

3 Sum Rules **27**
3.1 Introduction. . . . 27
3.2 The Bjorken and Gerasimov-Drell-Hearn Sum Rules. . . . 28
3.2.1 The Bjorken Sum Rule. . . . 28
3.2.2 The Gerasimov-Drell-Hearn Sum Rule. . . . 28
3.3 The GDH Integral Extension at Finite Q^2. . . . 33
3.3.1 Anselmino et al. Extension. . . . 34
3.3.2 The Extended GDH *Sum Rule*, a Link Between the Bjorken and the GDH Sum Rules. . . . 37
3.4 Summary and Conclusion. . . . 38

4 The Experiment and its Instrumentation **40**
4.1 Kinematic Coverage. . . . 40
4.2 Polarized Electrons. . . . 42
4.2.1 The Electron Source. . . . 42
4.2.2 Acceleration. . . . 43
4.3 Hall A 43
4.3.1 Beam Characterization. . . . 43
4.3.2 High Resolution Spectrometers. . . . 47

4.3.3 Detector Package. 48
4.3.4 Triggers, Data Acquisition and Beam Helicity Information Management. 54
4.3.5 The Helium-3 Polarized Target. 57
4.4 Typical Data Taking. 67

5 Data Analysis **69**
5.1 Introduction. 69
5.1.1 Cross Section and Asymmetry Extraction. 69
5.2 Principle of the Magnetic Analysis. 71
5.3 Spectrometer Database. 71
5.3.1 Optics. 71
5.3.2 Acceptance. 73
5.3.3 Experimental Simulation. 73
5.3.4 Comparison of the Different Acceptance Functions and the Experimental Data. 76
5.4 Detector Analysis. 80
5.4.1 Trigger inefficiency 80
5.4.2 Shower Detector. 80
5.4.3 Čerenkov. 82
5.4.4 Vertical Drift Chambers (VDC). 82
5.5 Luminosity and Charge Asymmetry. 84
5.5.1 Charge. 84
5.5.2 Charge Asymmetry. 85
5.5.3 Target Density. 85
5.5.4 Contamination and Dilution. 86
5.6 Data Acquisition Deadtime. 87
5.6.1 Correction to the Cross Section. 87
5.6.2 Correction to the Asymmetry. 87
5.7 Radiative Corrections. 87
5.8 Analysis of the Elastic Data. 88
5.8.1 Elastic Asymmetries. 88
5.8.2 Elastic Cross Sections. 92
5.9 Analysis of the Inelastic Data. 93
5.9.1 Error Estimate. 94

6 Results **95**
6.1 Inelastic Asymmetries and Cross Sections for ^3He. 95
6.2 Extraction of the Physics Results for ^3He. 98
6.2.1 The g_1 and g_2 Spin Structure Functions. 98
6.2.2 The GDH* Integral. 101
6.3 Extraction of the Neutron Data from the ^{3}He Data. 105
6.3.1 Extraction of the neutron Spin Structure Functions and Asymmetries from ^3He. 105
6.3.2 Extraction of integrated quantities. 106
6.3.3 Conclusion. 106
6.4 The GDH Integral on Neutron. 107

6.4.1 Behavior of the Extended GDH Integral with Q^2. 107
6.4.2 Extrapolation to the Real Photon Point. 107
6.4.3 Higher Twist Estimate. 108

7 Summary and Perspectives 111

A More on Sum Rules 114
A.1 Anselmino et al. Extraction of the Higher Twist Terms. 114
A.2 Corrected Anselmino et al. Extension 115
A.3 Burkert and Li Model. 115
A.3.1 The A.O. Model. 115
A.4 Scholten and Korchin GDH Integral Extension. 116
A.5 The Unitary Isobar Model. 116
A.6 The GDH Sum Rule and Integral in a Constituent Quark Model Framework.117
A.6.1 Constituent Quarks Models. 117
A.6.2 Z. Li GDH Sum Rule Derivation and Extension in a CQM framework.118
A.7 GDH and the Chiral Perturbation Theory. 119
A.7.1 Chiral Perturbation Theory. 119
A.7.2 GDH Extension Using the Heavy Baryon Ch.P.T 119
A.8 The GDH integral and the Burkhardt-Cottingham Sum Rule. 120
A.8.1 The Burkhardt-Cottingham (BC) Sum Rule. 120
A.8.2 Evolution of the extended GDH integral using the BC Sum Rule. . 120
A.9 Ji Higher Twist Extraction Method. 121
A.9.1 Extraction Method for the twist four matrix elements. 121

B Etude expérimentale de la structure en spin du neutron et de l'Helium 3 à petit Q^2. 122
B.1 Introduction. 122
B.2 Définitions. 123
B.3 Règles de somme. 123
B.3.1 La règle de somme de Bjorken 124
B.3.2 La règle de somme de GDH. 124
B.4 L'expérience. 127
B.4.1 Couverture cinématique. 127
B.4.2 L'appareillage expérimental. 128
B.4.3 Le faisceau d'électrons. 128
B.4.4 La cible polarisée. 130
B.4.5 Les spectromètres à haute résolution. 132
B.4.6 Mesure de l'erreur systématique. 132
B.5 Résultats. 133
B.5.1 Résultats bruts. 133
B.5.2 Les fonctions de structure en spin. 134
B.5.3 La dualité. 134
B.5.4 L'intégrale GDH généralisée. 135
B.6 Conclusion. 137

C Kinematics. 147

D Integration Limits. 150

Chapter 1

Introduction

The nucleon is the most common form of hadronic matter in the universe. Tremendous efforts have been spent over the last half century to understand its structure. This thesis reports on the contribution to this quest by experiment E94010 performed at the electron accelerator Thomas Jefferson National Accelerator Facility (Jefferson Lab). The research tool that we use here is the oldest known by mankind: To cast light on the unknown object. In our case the light is highly energetic (a few GeV), highly virtual and polarized. This electromagnetic probe is created *via* an electron beam. The virtual photon probes the target object. By analysing the scattered electron (inclusive experiments) or more particles from the reaction (semi-inclusive and exclusive experiments), we study the target structure and dynamics. The photon generation is described by Quantum ElectroDynamics (QED), the well known quantum theory of electromagnetic interactions. The relatively weak strength of this interaction brings three advantages and one drawback. First, the electromagnetic interaction is calculable using perturbative methods. The second advantage is that the target is not too disturbed by the measurement. The last interest is that the photon probes the entire target volume. The drawback is the low counting rates but it is now overcome by the new high current and high duty cycle machines such as CEBAF at Jefferson Lab.

We have known since the Hofstadter experiments [86] in 1960 that the nucleon is an extended object. The experimental study of the nucleon composition began at SLAC in 1969 when Taylor, Friedman and Kendal saw the first evidence of a nucleon substructure [168]. This discovery had been anticipated by Bjorken's prediction [19] that the response of a composite nucleon under a highly energetic and highly virtual light must depend only on the ratio of the light virtuality over its energy. This is the celebrated "Bjorken scaling" and the SLAC experiment confirmed this behavior. The experimental result was also in accordance with the Feynman parton model [74]. The partons were soon identified to the quarks and gluons introduced by Gell-Mann [79] and Zweig [181] to explain hadron mass spectroscopy. In this description a hadron is made of quarks interacting *via* eight kind of gluons. This new theory describing the Strong Interaction was called Quantum ChromoDynamics (QCD). A particular feature of QCD is that the coupling constant increases with the distance between the quarks. Consequently, QCD is calculable perturbatively only in the domain where the distances probed are small, i.e where the electron-hadron interaction is mediated by highly energetic and highly virtual light. This region is called the Deep Inelastic Scattering (DIS) domain. When one leaves this domain the strong interaction increases and the hadron begins to react coherently, that is, all the charged partons react together to the probe. As a consequence the target is no longer describable in term of partons but rather in term of “glued” partons, the nucleon. The transition between these two descriptions of the strong interaction occurs in the resonance region, the domain of the excited nucleonic states. Here science has only a phenomenological understanding of Nature.

The nucleon structure in the DIS region has been widely studied with unpolarized beams. We have learned that the quarks carry about half of the nucleon momentum. The remaining part should be carried by the gluons. As soon as polarised beams were available, one was able to study the spin content of the nucleon. Experiments at SLAC in 1976 [64] and 1980 [65] measured the contribution of the quark spins to the total nucleon spin. A parton model predicted that the quarks carried about 60% of the nucleon spin. These first results were in agreement with the parton model, but the EMC experiment [71] performed at CERN on a larger kinematic domain found that the quark spins carried only 12±17 % of the nucleon spin. This result gave birth to a great experimental and theoretical excitement known as the “spin crisis”.

The experimental response to the spin crisis was the experiments E142 and E143 at SLAC and SMC at CERN, followed by the experiments E154 and E155 at SLAC and HERMES at DESY. Collectively they measured the spin structure functions of both nucleons in the DIS domain. These experiments, and the associated theoretical efforts, clarified our picture of the nucleon spin structure: The quark spins contribute about 30% of the nucleon spin while the gluon spins and the partons orbital momenta share the remainder. Experiments are under way to measure the gluon spin contribution (HERMES, RHIC/Spin and COMPASS at CERN).

During the spin crisis, Anselmino, Ioffe and Leader published a paper [8] arguing that some QCD corrections called Higher Twists were underestimated. They used the extension of a sum rule to estimate them. This sum rule, which hold for real photons, was derived by Gerasimov in 1965 [80] and independently by Drell and Hearn in 1966 [63]. The Gerasimov-Drell-Hearn sum rule (GDH) states that the integral of the difference of the photo-production cross sections for the two photon helicity states divided by the photon energy is proportional to the target's anomalous magnetic moment:

$$\int_{\nu_{thr}}^{\infty} \frac{\sigma^{1/2} - \sigma^{3/2}}{\nu} d\nu \propto -\kappa^2 \tag{1.1}$$

Anselmino et al. extended the integral (the left hand side of eq. 1.1) to the virtual photon case and found that the Higher Twist correction must be significant for the EMC results. Although this result was controversial, their paper triggered interest in the GDH sum rule, and several experiments were proposed to measure its behaviour when it is extended beyond the real photon point [112]. The important point here is that Anselmino et al. pointed out the intimate connection between the GDH integral extended to the DIS domain and another sum rule of eminent importance in the DIS domain, the celebrated Bjorken sum rule.

Many authors extended the GDH “sum rule” beyond the real photon point. However the extensions cannot be called a sum rule anymore: We know several ways to extend the integral side of eq. 1.1, for example by considering cross sections for electroproduction instead of for photoproduction, but we do not know what this extended integral should equal. Recently Ji and Osborn [107] extended the sum *rule* by linking the integral to the spin dependent virtual Compton amplitude. The two sides of the sum rule are independently calculable, and must be equal. Their work unified the two fundamental QCD sum rules: The Bjorken sum rule in the DIS regime and the GDH sum rule at the real photon point. This unification provides a theoretical tool for exploring the transition between the DIS realm of perturbative QCD, and the non perturbative QCD region.

Our experiment studied the neutron. It is the first experiment to provide an absolute polarized cross section measurement in this region. As such, it provides crucial new information on the transition region, where polarized measurements are non-existent and unpolarized measurements scarce. I should emphasize here the fact that we detect only the scattered electrons (inclusive experiment), that is we take a global sum over all the possible reactions at a fixed kinematics. In the same spirit, the quantity we are interested in is an integral over a broad kinematical range. These two points make the experiment and the theory easier to handle because the effects of the individual resonances are averaged.

To study the neutron spin structure we used a polarized ^{3}He target as an effective polarized neutron target. The products of the beam-target interaction were detected by the High Resolution Spectrometer of Hall A.

In this thesis, I present in chapter 2 the formalism of nucleon structure and spin physics. Then, the nuclear excitation spectrum covered by the experiment -from the elastic scattering to the DIS regime passing through the quasi-elastic and the resonance region-will be described. the underlying mechanisms will be explained. Chapter 3 presents the sum rules and their extensions. Chapter 4 describes the experiment and its instrumentation. Chapter 5 explains the data analysis, and chapter 6 presents the results. Chapter 7 summarizes our conclusions. A short version of this thesis, written in French, is given in appendix B.

Chapter 2

Physics Framework

This chapter is divided in two sections. The first presents the theoretical framework of the experiment. The second presents the excitation spectrum of a nucleus from elastic to DIS regions. The general mechanisms and features of the spectrum will be explained. The experiment aims to study the neutron spin structure. However, dense free neutron targets do not exist, so we use the polarized ^{3}He nucleus as an effective polarized neutron target. Hence, we will focus our description of the nuclear excitation spectrum on the ^{3}He nucleus. In the following, the spin of the scattering center is $1/2$ and the weak interaction part of the lepton-hadron interaction is neglected.

As usual in particle physics we take $\hbar = c = 1$.

2.1 Electron Scattering.

We recall here the formalism used for the inclusive electron scattering off a nucleus. The forces involved in this reaction are the electromagnetic interaction (for the scattering) and the strong interaction (ruling both the nuclear and nucleon structures).

2.1.1 The Born Approximation.

The electromagnetic interaction of an electron with the target nucleus is described by the exchange of virtual photons. Often, only the first order term is used. This is the “first Born approximation”, also called the ”one photon exchange”.

If one photon exchange is not a sufficient description then higher order terms, called radiative corrections, need to be taken into account. Part of these corrections depends on the experimental hardware and the radiative correction calculations are customarily left to the experimentalists.

2.1.2 Kinematics.

The Feynman diagram of the $^3\overrightarrow{He}(\overrightarrow{e}, e')X$ reaction is drawn, in the one photon exchange approximation, in the figure 2.1.

The circle represents the unknown processes at the virtual photon-nucleus vertex due to the ^{3}He structure. The reaction is inclusive: X is not detected and can be :

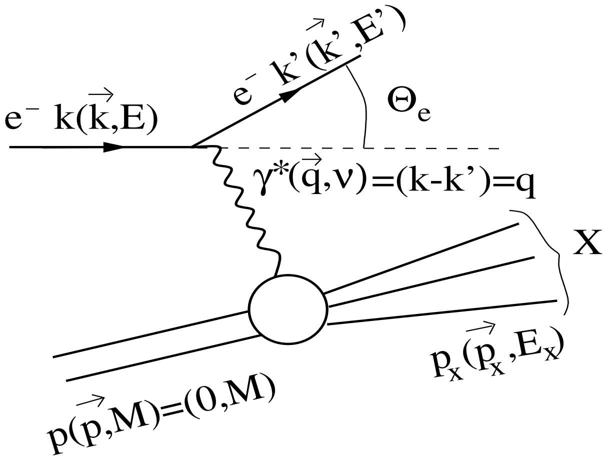

Figure 2.1: First order Feynman graph for electron scattering off a nucleus.

- The bound nucleus (elastic scattering for ^{3}He. For more complex nuclei it can be the elastic scattering from the ground state or the scattering from excited nuclear states).
- Fragments of the nucleus (inelastic scattering).

The virtual photon energy $\nu = E - E'$ is also called the "energy loss".

We define a laboratory frame (Fig. 2.2) such as its origin is at the photon-nucleus vertex, $\overrightarrow{z}$ follows the virtual photon direction $\overrightarrow{q} \equiv \overrightarrow{k} - \overrightarrow{k'}$, $\overrightarrow{x}$ is in the plane $(\overrightarrow{k}, \overrightarrow{k'})$. $\overrightarrow{P}$ is the target spin, θ^* is the target spin polar angle and φ^* is the azimuthal one.

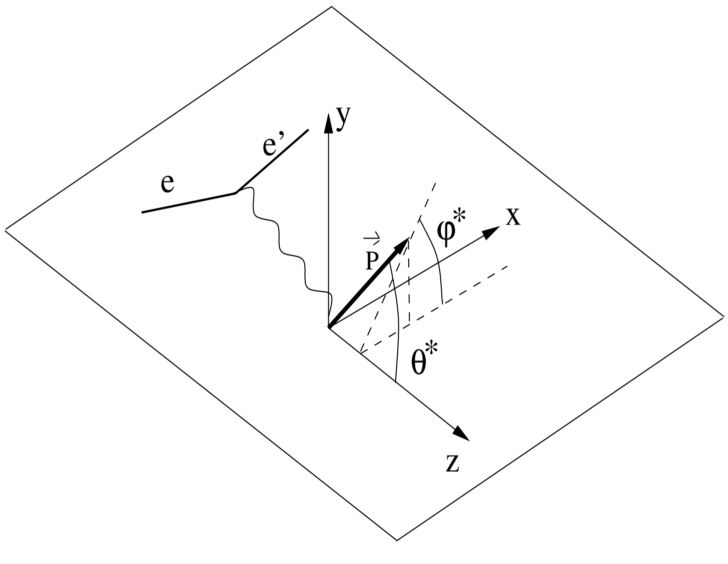

Figure 2.2: The polar and azimuthal target spin angles. The thick arrow is the target spin.

Let us define some relativistic invariants characterizing the reaction:

- The virtuality of the exchanged photon $Q^2 \equiv -(k-k')^2 = -q^2$. $Q^2 = 4EE' sin^2\frac{\theta_e}{2}$ for ultrarelativistic electrons. For real photons $Q^2 = 0$.

- The invariant mass is defined as $W^2 \equiv (p+q)^2 = M_t^2 + 2pq - Q^2$ where M_t is the mass of the scattering center.
- The "scaling variable" (or Bjorken variable) $x \equiv \frac{Q^2}{2p.q} = \frac{Q^2}{2M\nu}$. This invariant is introduced in the DIS framework. DIS scaling will be explained in section 2.2.4.

As Q^2 and ν vary, the target goes through different excitation states. It is more convenient to study the excitation spectrum with W rather than ν. As seen in fig. 2.3, the excitation states are not at fixed ν when Q^2 varies while they stay at a fixed W.

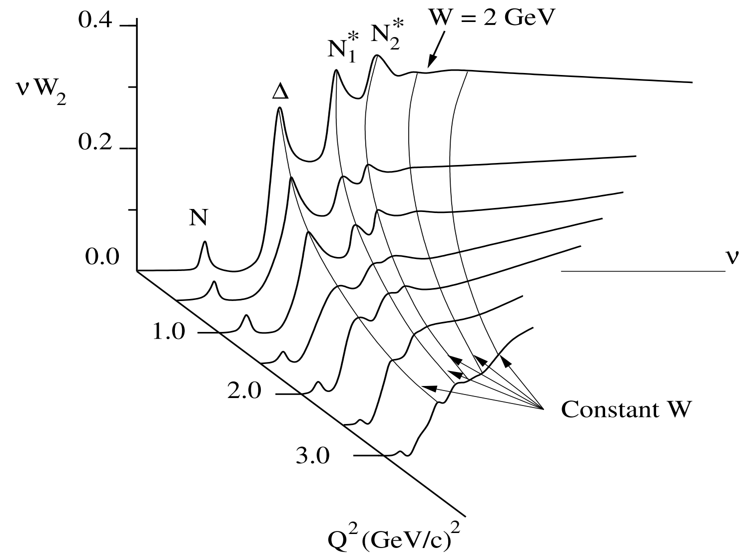

Figure 2.3: Response function W_2 of a nucleon versus Q^2 and ν. The cross section is proportional to the target response functions. The excitation peak positions (N, Δ, ...) change with ν as Q^2 varies. The plot is from the lectures of F. Gross [82].

2.1.3 Reaction Cross Section.

General Expression of the Cross Section.

In the following, the word hadron will refer to both the nucleon or the nucleus.

The transition amplitude of the reaction is constructed using the hadronic current J^μ and leptonic current j^ν. They are conserved at both vertices of fig. 2.1 because of gauge invariance. Applying the Feynman rules, the scattering amplitude is:

$$T_{fi} = \langle k'| j^\mu(0) |k\rangle \frac{1}{q^2} \langle P_x| J_\mu(0) |P\rangle \tag{2.1}$$

with the leptonic current:

$$j^\mu = e\overline{\psi}\gamma^\mu\psi$$

where ψ is the electron spinor and γ^μ the Dirac matrices.

The hadronic current is unknown due to our ignorance of the hadronic structure. This ignorance is parameterized by functions that are measured experimentally. These functions are either called "form factors" (for elastic scattering, described in section 2.2.1), "response functions" (for quasi-elastic scattering, see section 2.2.2) or "structure functions" (for DIS, see section 2.2.4). Models can express these functions in terms of more fundamental QCD quantities as we will see in the second part of this chapter. It is a goal of nuclear and hadronic experiments to provide enough information on these quantities such that they can be derived from the fundamental QCD theory.

The differential cross section is expressed as $|T_{fi}|^2$ times the incident electron flux and a space phase factor. We write ([77]):

$$d\sigma = (2\pi)^4 \left[\frac{1}{4\sqrt{(Pk)^2 - m_e^2 M^2}} \right] \left[\delta^4(k + p - k' - p_x) \frac{d^3k'}{n(k')} \prod_{j=1}^{n} \frac{d^3p_j}{n(p_j)} \right] |T_{fi}|^2 \qquad (2.2)$$

With p_j the target fragment momenta: $\sum_{j=1}^{n} p_j = p_x$ and where the n are the normalization of the states. In the laboratory frame $n(k') = (2\pi)^3 k'_0$

Leptonic and Hadronic Tensors.

$|T_{fi}|^2$ can be expressed in terms of the leptonic and hadronic tensors: The leptonic tensor is defined as $\eta^{\mu\nu} \equiv \frac{1}{2} \sum j^{\mu^*} j^{\nu}$ where the sum runs over the indiscernible lepton states (for example spin states for unpolarized experiments). The hadronic tensor is $W^{\mu\nu} \equiv \frac{1}{2} \sum J^{\mu^*} J^{\nu}$. From eq. 2.1 and 2.2 we see that $d\sigma \propto |T_{ij}|^2 = \eta^{\mu\nu} \frac{1}{Q^4} W_{\mu\nu}$.

In the unpolarized case, i.e. with summation over the spin states, the cross section can be decomposed into six photoabsorption terms. Three originate from the three allowed polarization states of the virtual photon[1]. The last three are the cross terms coming from the multiplication of the two tensors. In particular, the three latter depend on the azimuthal angle. For inclusive experiments there is no azimuthal dependence of the cross section so the cross terms disappear. We have [77]:

$$|T_{fi}|^2 = \frac{e^2}{Q^2(1-\epsilon)} \left[(w_{RR} + w_{LL}) + 2\epsilon w_{ll} \right]$$

where:

- w_{ll} is the longitudinal term (only for virtual photons).
- w_{RR} is the right helicity term.
- w_{LL} is the left helicity term.

$\epsilon \equiv 1/(1 + 2(\overrightarrow{q}^2/Q^2) tan^2(\theta_e/2)$ is the degree of polarization of the virtual photon for ultrarelativistic electrons ($m_e = 0$). The longitudinal term can be separated by varying ϵ ("Rosenbluth separation") but the right helicity term cannot be separated from the left helicity term. Thus we write the cross section as:

$$d\sigma \propto |T_{fi}|^2 = \frac{e^2}{Q^2(1-\epsilon)} \left[w_T + 2\epsilon w_L \right] \qquad (2.3)$$

[1] Let us note that the virtual photon spin is a four-vector but with only three independent components because of gauge invariance.

Hence the total unpolarized inclusive cross section is expressed in terms of two photoabsorption cross sections, σ_L and σ_T, times a virtual photon flux[2]. We understand this parametrization choice in terms of virtual photon quantities if we recall that the electron role is only to create the virtual photon probe.

In the case of polarized inclusive inelastic reactions we need two other parameters to take into account the hadron spin structure. We use for example the four structure functions $W_1(Q^2,\nu)$, $W_2(Q^2,\nu)$, $G_1(Q^2,\nu)$, $G_2(Q^2,\nu)$ to express the inclusive inelastic cross section:

$$\frac{d\sigma}{d\Omega dE'} = \sigma_{mott}(W_2(Q^2,\nu) + 2W_1(Q^2,\nu)tan^2\frac{\theta_e}{2} \pm 2tan^2\frac{\theta_e}{2}(E + E'cos\theta_e)MG_1(Q^2,\nu)$$
$$\mp 2Q^2tan^2\frac{\theta_e}{2}G_2(Q^2,\nu))$$

In this particular example the target spin is parallel or antiparallel to the beam direction. $\pm$ refers to the beam polarization direction (parallel/antiparallel). The factor σ_{mott} will be explained in section 2.2.1.

2.2 Nuclear Excitation Spectrum.

I will describe now the nuclear excitation spectrum for a typical inclusive experiment and express the cross section for each part of the spectrum. A typical inclusive electron-nucleus cross section is drawn in Fig. 2.4.

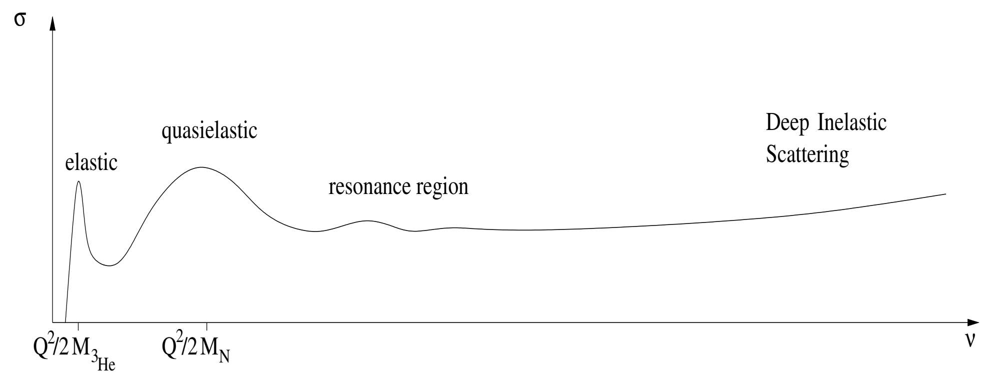

Figure 2.4: A typical ^{3}He excitation spectrum. The elastic peak should be a delta function. Its finite width comes from the detection apparatus resolution, the beam energy spread, straggling and radiative processes.

2.2.1 Elastic Scattering.

Mechanism.

At low Q^2 and ν the distances probed are not small enough to see the nucleus' composition and it appears as an extended coherent object: All the components of the nucleus

[2]For virtual photon the flux is arbitrary. We use here either the Hand convention or the Gilman convention [147].

participate in the scattering. The momentum transfer is shared between all the nucleons and the target remains intact with its structure undisturbed. The virtual photon energy, i.e. the recoil energy of the target (in the elastic case), is computed applying the four-momenta conservation for the four incoming and outgoing lines of fig. 2.1:

$$\nu_{el} = \frac{Q^2}{2M} \tag{2.4}$$

So the scattered electron energy is:

$$E' = \frac{E}{1 + 2(E/M)sin^2(\theta_e/2)} \tag{2.5}$$

Unpolarized Cross Sections.

We assume first a point-like and infinitely heavy target of charge Z. Then $W^{\mu\nu}$ is similar to $\eta^{\mu\nu}$. The eq. 2.2 yields [172]:

$$\frac{d\sigma}{d\Omega} = \frac{Z^2\alpha^2 cos^2(\theta_e/2)}{4E^2 sin^4(\theta_e/2)} \equiv \sigma_{Mott} \tag{2.6}$$

where α is the fine structure constant. Taking into account the finite mass (recoil) of the target gives:

$$\frac{d\sigma}{d\Omega} = \sigma_{Mott}\frac{1}{1 + 2(E/M)sin^2(\theta_e/2)} = \sigma_{Mott}\frac{E'}{E}$$

where we recognize the recoil term in eq. 2.5. Any deviation from this formula reveals a spatial extension of the target.

We consider now an extended nucleus. The nuclear tensor must be constructed using the independent four-vectors p and q and the scalar Q^2. In the first Born approximation we have seen that only two functions are needed to parametrize the tensor:

$$W^{\mu\nu} \equiv W_1(Q^2)(g^{\mu\nu} + \frac{q^\mu q^\nu}{Q^2}) + W_2(Q^2)(p^\mu - \frac{pq}{Q^2}q^\mu)(p^\nu - \frac{pq}{Q^2}q^\nu)$$

with $g^{\mu\nu}$ the metric tensor.

The contraction of this tensor with the leptonic tensor and the eq. 2.2 leads to ([172]):

$$\frac{d\sigma}{d\Omega dE'} = \sigma_{Mott}\left[\left(\frac{Q^2}{\vec{q}^{\,2}}\right)^2 R_L(Q^2,\nu) + \left(tan^2(\theta_e/2) - \frac{1}{2}\frac{Q^2}{\vec{q}^{\,2}}\right) R_T(Q^2,\nu)\right] \tag{2.7}$$

Where $R_L \equiv W^{00}$ is the longitudinal response function of the nucleus and $R_T \equiv W^{11}+W^{22}$ is the transverse response function (see eq. 2.3). R_L comes from the virtual photon longitudinal polarization while R_T comes from the transverse one.

Note : Elastic Scattering from a Nucleon. It is useful to treat quickly the inclusive electron-nucleon elastic scattering since, as we will see, it is the underlying process of the quasi-elastic scattering. The leptonic and hadronic tensor contraction yields:

$$\frac{d^3\sigma}{d\Omega dE'} = \sigma_{Mott}\left(W_2(Q^2) + 2W_1(Q^2)tan^2(\theta_e/2)\right) \tag{2.8}$$

the celebrated Rosenbluth formula. The hadronic current is more often parametrized with the Sachs form factors $G_E(Q^2)$ and $G_M(Q^2)$. The relations are:

$$W_1(Q^2) = \tau G_M(Q^2)^2$$

$$W_2(Q^2) = \frac{G_E(Q^2) + \tau G_M(Q^2)}{1+\tau}$$

where the recoil term $\tau \equiv Q^2/(4M_N)$. We will also use the Dirac and Pauli form factors $F_1(Q^2)$ and $F_2(Q^2)$. The relation with the Sachs form factors is:

$$G_E(Q^2) = F_1(Q^2) - \tau\kappa F_2(Q^2)$$

$$G_M(Q^2) = F_1(Q^2) + \kappa F_2(Q^2)$$

Form factors are related to the Fourier transform of the charge and current distributions.

Polarized Case.

We have dealt so far with the unpolarized case. By using electrons and targets in defined spin states (polarized target and beam) we do not average on the final spin states and we gain information on the target spin structure.

The polarized cross section is written as :

$$\frac{d\sigma}{d\Omega dE'} = \Sigma(E, \theta_e, Q^2) \pm \Delta(\theta^*, \phi^*, E, \theta_e, Q^2) \tag{2.9}$$

where Σ is the unpolarized cross section (eq. 2.7). $\pm$ is the beam helicity sign and Δ is the spin dependent part of the cross section.

We need to add two new response functions to take into account the nuclear spin structure. We have [52]:

$$\Delta = -\sigma_{mott}\left(V_{T'}R_{T'}(Q^2)cos\theta^* + V_{TL'}R_{TL'}(Q^2)sin\theta^* cos\phi^*\right) \tag{2.10}$$

where the kinematic factors are:

- $V_{T'} \equiv tan\frac{\theta}{2}\sqrt{\frac{Q^2}{\overrightarrow{q}^2} + tan^2\frac{\theta}{2}}$
- $V_{TL'} \equiv -\frac{Q^2}{\sqrt{2}\,\overrightarrow{q}^2}tan\frac{\theta}{2}$

Similarly we denote the kinematic factors of eq. 2.7:

- $V_L \equiv \left(\frac{Q^2}{\overrightarrow{q}^2}\right)^2$
- $V_T \equiv \frac{Q^2}{2\overrightarrow{q}^2} + tan^2\frac{\theta}{2}$

We use also the ^{3}He magnetic and Coulomb form factors F_m and F_c to parametrize the ^{3}He elastic cross section and asymmetry. They are related to the structure functions of a nucleus (A,Z) by [169]:

$$R_{T'}(Q^2) = \frac{2\tau E'}{E}(\mu_A F_m)^2$$

$$R_{TL'}(Q^2) = -\frac{2\sqrt{2\tau(1+\tau)}E'}{E}(ZF_c)(\mu_A F_m)$$

where $\tau \equiv \frac{Q^2}{4M_A}$ and μ_A is the magnetic moment of the nucleus. Let us note that in the particular case of the polarized elastic scattering one does not need to use two new form factors: The unpolarized and polarized parts of the cross section are both parametrized by the magnetic and charge form factors.

In polarized experiments cross section asymmetries normalized to the unpolarized cross section are useful quantities. To simplify the writing we will simply call them "asymmetries". In a general manner:

$$A = \frac{\Delta(\theta^*, \phi^*, E, \theta_e, Q^2)}{\Sigma(E, \theta_e, Q^2)} \tag{2.11}$$

The longitudinal asymmetry is defined as:

$$A_\parallel \equiv \frac{\sigma^{\downarrow\Uparrow} - \sigma^{\uparrow\Uparrow}}{\sigma^{\downarrow\Uparrow} + \sigma^{\uparrow\Uparrow}} \tag{2.12}$$

The transverse asymmetry is defined as:

$$A_\perp \equiv \frac{\sigma^{\downarrow\Rightarrow} - \sigma^{\uparrow\Rightarrow}}{\sigma^{\downarrow\Rightarrow} + \sigma^{\uparrow\Rightarrow}} \tag{2.13}$$

where $\uparrow$ is the beam helicity direction and $\Uparrow$ the target spin direction. If the electron flux is the same for both helicities, then (see eq. 5.1 page 69):

$$A_\parallel = \frac{N^{\downarrow\Uparrow} - N^{\uparrow\Uparrow}}{N^{\downarrow\Uparrow} + N^{\uparrow\Uparrow}}$$

where N is a raw counting rate. All the normalization factors of the cross sections disappear. Hence asymmetries are relative measurements, and are easier to carry out than absolute measurements. Most of previous spin structure experiments only measured asymmetries. However the GDH measurement requires that we measure either cross sections and asymmetries or polarized cross section differences.

2.2.2 Inclusive Quasi-Elastic Scattering.

Mechanism.

As the distances probed get smaller the photon becomes sensitive to the nucleus' components. Let us picture the nucleus as a set of quasi-free nucleons bound in a mean potential (Fermi gas model). When the energy loss ν is larger than the nuclear binding energy, the nucleons are no longer reacting coherently. Thus the electron scatters elastically from a nucleon and the target breaks. This is called quasi-elastic scattering. Its threshold is, with respect to the elastic peak, equal to the nuclear binding energy (5.49 MeV for the ^{3}He two body breakup and 7.72 MeV for the three body breakup). We have an inelastic inclusive reaction since some energy is lost in the breakup process and the target debris is not detected. Unlike the elastic case, the scattering centers are not at rest in the laboratory frame: The nucleons have typical momenta of 100 MeV/c because they are bound in a small region ($\Delta P \Delta x \sim \hbar$). This "Fermi motion" causes a Doppler-like broadening of the quasi-elastic line around $Q^2/2M_N$, the energy loss from elastic scattering off a free nucleon.

Experiments have shown that this picture describes qualitatively the features of quasi-elastic scattering, but it fails to predict the individual transverse and longitudinal components or the edges of the peak. A better agreement is obtained by abandoning the quasi-free hypothesis and taking into account the nucleon-nucleon interaction.

Let us take the picture of incoherent scattering, neglect the Fermi motion and nuclear effects. Then using eq. 2.8 expressed with the Sachs form factors we can write the ^{3}He quasi-elastic response functions as the sum of the nucleon form factors:

$$R_T(Q^2) = 2\tau\left((G_M^n)^2 + 2(G_M^p)^2\right)$$

$$R_L(Q^2) = (1+\tau)\left((G_E^n)^2 + 2(G_E^n)^2\right)$$

$$R'_T(Q^2) = 2\tau\left(p_n(G_M^n)^2 + 2p_p(G_M^p)^2\right)$$

$$R'_{LT}(Q^2) = -2\sqrt{2\tau(1+\tau)}\,(p_n G_M^n G_E^n + 2p_p G_M^p G_E^p)$$

where τ is now the recoil term for the nucleon and p_p (p_n) is the proton (neutron) effective polarization within the nucleus.

These response functions and the equations 2.11, 2.10 and 2.7 give the ^{3}He quasi-elastic cross section and asymmetry in this rough view.

Quasi-Elastic Cross Section and Asymmetries in Plane Wave Impulse Approximation.

A simple description of the quasi-elastic reaction is given in Plane Wave Impulse Approximation (PWIA), see fig. 2.5:

- PW: The incoming and outgoing particles are described by Plane Waves.
- IA: The nucleons lie in the nuclear mean field. The momentum (impulse) of the struck nucleon is not modified by this mean field: The nucleons are quasi-free. A consequence is that we neglect the interaction of the struck nucleon with the target debris (in the ^{3}He case, a deuteron for the two body breakup or two nucleons for the three body breakup [176]). Two nucleons are spectators while the third is kicked out of the nuclei.

One takes into account the energy and momentum distribution of the nucleons. The distribution function is called the "spectral function" $P(k,E)$. In the PWIA hypothesis the nuclear tensor is related to the hadronic tensor by [143]:

$$W^A_{\mu\nu}(\overrightarrow{q}) = \int d^3k dE P(k,E)\frac{m_N}{E_k}W_{\mu\nu}(\widetilde{k},q)$$

where E_k is the energy of the struck nucleon after the interaction and m_N the on-shell nucleon mass.

The next steps beyond PWIA take into account:

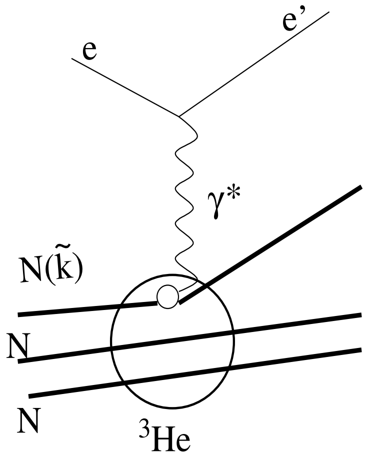

Figure 2.5: The quasi-elastic scattering (pictured as an incoherent sum of elastic scatterings off individual nucleons of momentum $\widetilde{k}$) in the PWIA approximation.

- On the electron side: The Coulomb correction (distortion of the electron plane wave due to the electromagnetic interaction with the nucleus).
- On the hadron side: The interaction between the struck nucleon and the debris (Final State Interaction "FSI", which are small for light nuclei such as the ^{3}He) and the meson exchange (Meson Exchange Currents)

The ^{3}He Nucleus

I briefly describe the ^{3}He nucleus structure to understand how we can extract the neutron information from the ^{3}He data. In the simplest picture the ^{3}He nucleons are in S wave. As a consequence and because of the Pauli principle, the two proton spins point in opposite direction and their spin contribution to the nucleus cancels. This is why ^{3}He polarized targets are used as effective - first order - polarized neutron targets. Three-body Fadeev calculations show that the wave function is composed of $\sim$90% of S state, 8% of D state and $\sim$1.5% of S' state [159]. See Fig. 2.6. Hence the protons also contribute to the ^{3}He spin and we need proton data or a model to extract the neutron information. Let us note that the use of a model here is not a limitation since the corrections due to the protons are small.

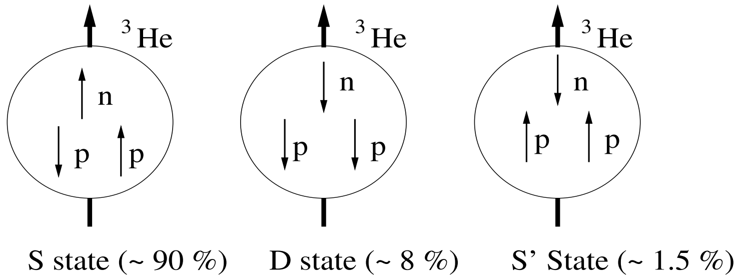

Figure 2.6: The wave components of the ^{3}He nucleus.

2.2.3 The Resonance Region.

As the energy and virtuality of the photon increase we leave the quasi-elastic domain and enter the resonance region. These resonances are spin or momentum excited states of the nucleon. They decay mainly by emitting mesons. Thus there is significant pion electroproduction in the resonance region. Beyond $W \sim 1.4$ GeV the resonances and their tails overlap. As noted in the introduction, no exact calculation can yet be carried out in the resonance domain. We are relying on qualitative models (see section A.6.1 in the Appendix A). Thus it is important to have experimental data in this not well-known region. In addition the resonance region is the transition domain between pQCD (partonic degrees of freedom) and the nuclear/hadronic theory (hadronic degrees of freedom). This transition is still not understood and experimental data on the extended GDH sum rule in this domain are important as we will see in the next chapter.

The Δ Resonance.

The first resonance is the $\Delta(1232)$ (M_Δ=1232 MeV). In the Constituent Quark Model the nucleon ground state has two spins anti-aligned, see Fig. 2.7.

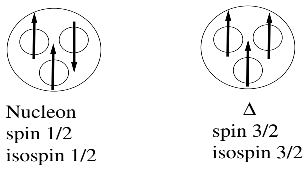

Figure 2.7: The nucleon and Δ quark spin structure in a constituent quark picture.

Hence the nucleon to Δ transition is, in the simplest way (SU(6)=SU(3)$_{flavor}\otimes$SU(2)$_{spin}$ mass symmetry), described as a simple spin flip (and isospin flip), that is a pure M_{1+} magnetic dipole transition[3]. Given that the nucleon to Δ transition is mainly a transverse process (spin flip), the cross section can be written as [24]:

$$\sigma_\Delta = \frac{4\pi}{\Gamma} \frac{|\overrightarrow{q_L}|^2}{w(w^2 - M_N^2)} \left(\left| G_m^\Delta \right|^2 + 3 \left| G_e^\Delta \right|^2 \right) \tag{2.14}$$

where Γ is the resonance width, $\overrightarrow{q_L}$ the photon 3-momentum in the laboratory frame and the G^Δ are the transverse transition form factors.

Other Resonances

Resonances lying at higher W are separated in two classes: The isospin 1/2 class (N*) and the isospin 3/2 class (Δ^*). The resonance nomenclature is: L$_{2I\,2J}$.

- L=S (for l=0), P (l=1), D (l=2), F (l=3) is the angular momentum.
- I=1/2 or 3/2 is the isospin.

[3] Experiments show that there is also a small E_{1+} electric quadrupole transition ($E_{1+}/M_{1+}< 0.01$ at Q^2=0. [22]) revealing a SU(6) violation. Constituent Quark Model hyperfine magnetic structure (see A.6.1 in Appendix A) violates SU(6) and allows small E_{1+} and S_{1+} scalar transitions)

- $J=|l \pm 1/2|$ is the total angular momentum.

In this notation the Δ is written P_{33}. Figure 2.8 from [21] identifies the proton states of strangeness 0 and mass below 2 GeV and the inclusive p(e,e')X cross section for Q^2=0.6 GeV^2.

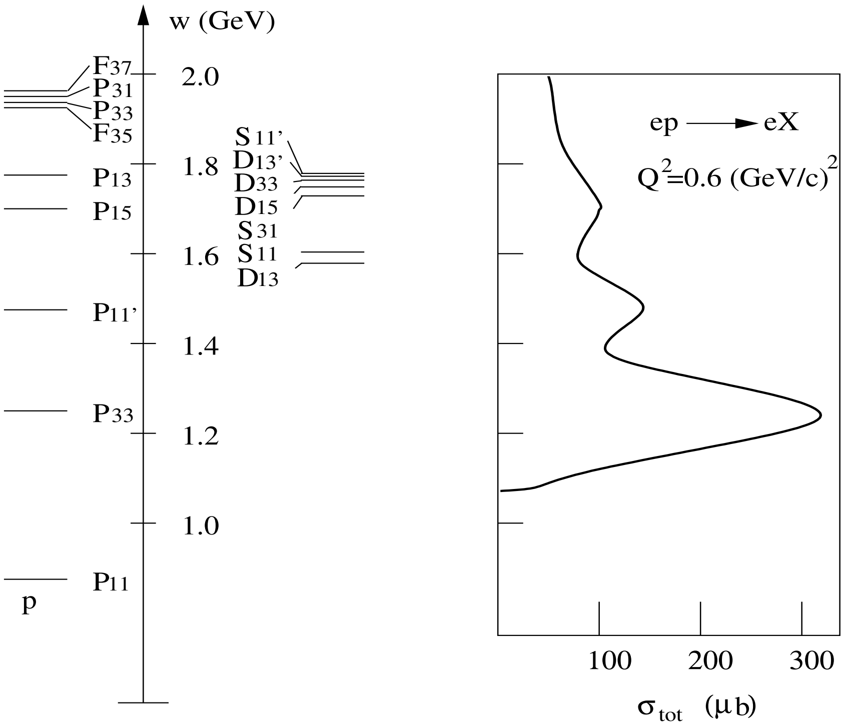

Figure 2.8: Proton states of strangeness 0 and mass below 2 GeV (left) and the inclusive p(e,e')X cross section (right) for Q^2=0.6 GeV^2. There is no quasi-elastic scattering on the cross section plot because the scattering is off a free nucleon. The elastic scattering is not shown.

We see that only the Δ is unambiguously visible in our inclusive experiment. The next peak is a pack of resonances that unpolarized cross section measurements cannot disentangle (the $P_{11'}$ also called "Roper resonance", the D_{13} and the S_{11} which dominates). This peak does not stay at fixed W since the relative amplitude of the different resonances change with Q^2.

Since no rigorous calculations are available, the cross section of a resonance R is often parametrized with a Breit Wigner form. For example [24]:

$$\sigma_{res}(W) = A_R \frac{\left|\overrightarrow{q_R^*}\right|^2}{\left|\overrightarrow{q^*}\right|^2} \frac{w_R^2 \Gamma \Gamma_\gamma}{(w_R^2 - w^2)^2 + \Gamma^2 w_R^2}$$

where Γ is the total resonance width, Γ_γ the radiative width and $\overrightarrow{q^*}$ the photon 3-momentum in the hadron rest frame. A_R is a scale parameter obtained by a fit to the experimental data.

Non-Resonant Background

Resonances do not explain the entire excitation spectrum. A non resonant background needs to be added to satisfy the unitarity of the S matrix (on the theoretical side) and to fit the data (on the experimental side).

Note. Double polarized pion data give information on the nucleon and resonances spin structure. Our π^- data are not yet analysed so I will not discuss this topic. Pion production is reviewed by V. Burkert [23], [24] and by D. Drechsel [57] in terms of multipole analysis.

2.2.4 Deep Inelastic Scattering.

Mechanism.

The last domain of fig. 2.4 is the DIS region. DIS traditionally begins at W =2 GeV although resonances of masses higher than 2 GeV have been seen ([26]). The DIS is interpreted as scattering off partons: The photon virtuality and energy are now large enough to probe the nucleon's constituents. One of the particular features of QCD is asymptotic freedom, i.e. the quark-quark interaction strength decreases with decreasing distance. Consequently, the interaction can be treated perturbatively and calculations are possible. If the photon energy and virtuality are high enough the DIS is described as elastic scattering off free quarks and antiquarks (it is the Bjorken domain: $\nu \to \infty$, $Q^2 \to \infty$, x stays finite). This region displays no peak because it is smeared (as in quasi-elastic scattering but more dramatically) by the quark momenta.

Scaling.

The DIS is basically interpreted in the Bjorken domain as an elastic scattering off free, pointlike scattering centers. Bjorken has pointed out that in hadronic processes the response functions can be expressed as functions of x and Q^2/M^2. In particular, elastic scattering off a nucleon has a strong Q^2/M^2 dependence. M is the typical scale of a hadronic (non perturbative) process. However M is not relevant for incoherent scattering off free pointlike objects within the hadron and the structure functions should depend only on x. Therefore we expect a scaling behaviour (i.e. the independence of the structure function with Q^2) in the DIS domain. This was experimentally checked by Taylor et al. The scaling of the structure functions with x was the first experimental signature of the nucleon's composition.

Formalism.

In DIS we introduce $\gamma^2 \equiv \frac{Q^2}{\nu^2}$. We have seen that in the inclusive polarized case four structure functions are needed to describe the nucleon structure and dynamics. We customarily name the two unpolarized scaling structure functions $F_1(Q^2,\nu)$ and $F_2(Q^2,\nu)$ (beware to not confuse them with the Pauli and Dirac form factors). The relations with $W_1(Q^2,\nu)$ and $W_2(Q^2,\nu)$ are:

$$W_1(Q^2,\nu) \equiv \frac{F_1(Q^2,\nu)}{M_N}$$

$$W_2(Q^2,\nu) \equiv \frac{F_2(Q^2,\nu)}{\nu}$$

We name $g_1(Q^2,\nu)$ and $g_2(Q^2,\nu)$ the polarized structure functions. We also use $G_1(Q^2,\nu)$ and $G_2(Q^2,\nu)$ defined as:

$$G_1(Q^2,\nu) \equiv \frac{M_N g_1(Q^2,\nu)}{\nu}$$

$$G_2(Q^2,\nu) \equiv \frac{M_N^2 g_2(Q^2,\nu)}{\nu^2}$$

The contraction of the tensors yields, in the case of a target polarization along the beam direction [153]:

$$\frac{d^2\sigma}{d\Omega dE'} = \sigma_{mott}\left[\frac{2}{M_N}F_1(Q^2,\nu)tan^2\frac{\theta_e}{2} + \frac{F_2(Q^2,\nu)}{\nu} \pm 2tan^2\frac{\theta_e}{2}[(E+E'cos\theta_e)\frac{M_N^2}{\nu}g_1(Q^2,\nu) - \gamma^2 M_N^2 g_2(Q^2,\nu)]\right] \tag{2.15}$$

where +/- correspond to the electron helicity being parallel/antiparallel to the beam direction. In the case of a target polarization perpendicular to the beam direction (the unpolarized structure function coefficients are obviously unchanged since it is spin independent) we have:

$$\frac{d^2\sigma}{d\Omega dE'} = \sigma_{mott}\left[\frac{2}{M_N}F_1(Q^2,\nu)tan^2\frac{\theta_e}{2} + \frac{F_2(Q^2,\nu)}{\nu} \pm 2tan^2\frac{\theta_e}{2}E'sin\theta_e(\frac{M_N^2}{\nu}g_1(Q^2,\nu) + \frac{2M_N^2 E}{\nu^2}g_2(Q^2,\nu))\right] \tag{2.16}$$

From these formula we deduce the two asymmetries:

$$A_{\parallel} \equiv \frac{\sigma^{\downarrow\Uparrow} - \sigma^{\uparrow\Uparrow}}{\sigma^{\downarrow\Uparrow} + \sigma^{\uparrow\Uparrow}} = \frac{2tan^2\frac{\theta_e}{2}\left[(E+E'cos\theta_e)\frac{M_N^2}{\nu}g_1(Q^2,\nu) - \gamma^2 M_N^2 g_2(Q^2,\nu)\right]}{\frac{2}{M_N}F_1(Q^2,\nu)tan^2\frac{\theta_e}{2} + \frac{F_2(Q^2,\nu)}{\nu}}$$

$$A_{\perp} \equiv \frac{\sigma^{\downarrow\Rightarrow} - \sigma^{\uparrow\Rightarrow}}{\sigma^{\downarrow\Rightarrow} + \sigma^{\uparrow\Rightarrow}} = \frac{2tan^2\frac{\theta_e}{2}E'sin\theta_e(\frac{M_N^2}{\nu}g_1(Q^2,\nu) + \frac{2M_N^2 E}{\nu^2}g_2(Q^2,\nu))}{\frac{2}{M_N}F_1(Q^2,\nu)tan^2\frac{\theta_e}{2} + \frac{F_2(Q^2,\nu)}{\nu}}$$

These are the two asymmetries directly measured.

Photo-absorption Asymmetries.

As was already mentioned at the end of section 2.1.3, the probe is the virtual photon so we prefer to express the asymmetries in terms of photo-absorption cross sections.

The photo-absorption cross section is linked by the "optical theorem" to the imaginary part of the forward Compton scattering amplitude.

The theorem states that the dispersive part of the process (the cross section) is proportional to the imaginary part of the transition amplitude as in classical optics (Fig.2.9). Its demonstration relies on the unitarity of the scattering amplitude.

Of the ten Compton amplitudes conserving the angular momentum, only four are independent because of parity and time reversal invariance. The corresponding cross sections customarily used are (from Roberts [153] using the Gilman convention for the virtual photon flux):

$$\sigma^T_{3/2} = \frac{4\pi^2\alpha}{M_N\sqrt{\nu^2+Q^2}}(F_1(Q^2,\nu) - g_1(Q^2,\nu) + \gamma^2 g_2(Q^2,\nu)) \tag{2.17}$$

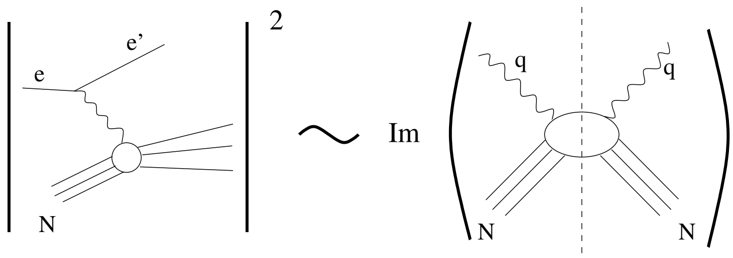

Figure 2.9: Illustration of the optical theorem.

$$\sigma^T_{1/2} = \frac{4\pi^2\alpha}{M_N\sqrt{\nu^2+Q^2}}(F_1(Q^2,\nu) + g_1(Q^2,\nu) - \gamma^2 g_2(Q^2,\nu)) \tag{2.18}$$

$$\sigma^L_{1/2} = \frac{4\pi^2\alpha}{M_N\sqrt{\nu^2+Q^2}}(-F_1(Q^2,\nu) + \frac{M_N}{\nu}(1+\frac{1}{\gamma^2})F_2(Q^2,\nu)) \tag{2.19}$$

$$\sigma^{TL}_{3/2} = \frac{4\pi^2\alpha}{M_N\sqrt{\nu^2+Q^2}}\frac{\gamma M_N}{\nu}(g_1(Q^2,\nu) + g_2(Q^2,\nu)) \tag{2.20}$$

(As already noted the choice of the virtual photon flux is arbitrary. For the virtual cross sections expressed in the Hand convention, replace the factor $\sqrt{\nu^2+Q^2}$ by $\nu - Q^2/(2M_N)$.

We define the combinations:

- $\sigma^T \equiv (\sigma^T_{1/2} + \sigma^T_{3/2})/2$
- $\sigma^{TT} \equiv (\sigma^T_{1/2} - \sigma^T_{3/2})/2$
- $\sigma^L \equiv \sigma^L_{1/2}$
- $\sigma^{TL} \equiv \sigma^{TL}_{3/2}$
- $R \equiv \frac{\sigma^L}{\sigma^T} = \frac{1+\gamma^2}{2x}\frac{F_2}{F_1} - 1$

and the two photon-nucleon asymmetries:

- $A_1 \equiv \frac{\sigma^{TT}}{\sigma^T}$ hence $|A_1| \leq 1$
- $A_2 \equiv \frac{\sigma^{TL}}{\sqrt{2}\sigma^T}$ and $|A_2| \leq R$ since $\left|\sigma^{TL}\right| < \sqrt{\sigma^T\sigma^L}$

The last step is to link these asymmetries to the measured ones:

$$A_\parallel = D(A_1 + \eta A_2) \tag{2.21}$$

$$A_\perp = d(A_2 - \zeta A_1)$$

where:

- $D \equiv \frac{1-\epsilon E'/E}{1+\epsilon R}$

- $d \equiv D\sqrt{\frac{2\epsilon}{1+\epsilon}}$
- $\eta \equiv \frac{\epsilon\sqrt{Q^2}}{E-\epsilon E'}$
- $\zeta \equiv \eta\frac{1+\epsilon}{2\epsilon}$

with the virtual photon degree of polarization ϵ already introduced in eq. 2.3.

2.2.5 The Parton Model.

DIS in the Bjorken Limit.

In the Bjorken limit the nucleon is described as a sum of free partons (quarks, antiquarks and gluons). The electron scatters incoherently on pointlike free quarks and antiquarks (gluons have no electric charge). With this description the partonic tensor is calculable and similar to the leptonic tensor. This is the parton model. The parton masses and transverse momenta and spins are neglected. We integrate over the charged parton momenta and sum over their flavour. A comparison of the tensor obtained in this model with the hadronic tensor parametrized by the structure functions yields [134]:

$$
\begin{aligned}
F_1(x) &= \sum_i \frac{Q_i^2}{2}(q_{i+}(x) + q_{i-}(x) + \overline{q}_{i+}(x) + \overline{q}_{i-}(x)) \\
F_2(x) &= 2xF_1(x) \\
g_1(x) &= \sum_i \frac{Q_i^2}{2}(q_{i+}(x) - q_{i-}(x) + \overline{q}_{i+}(x) - \overline{q}_{i-}(x)) \qquad (2.22) \\
g_2(x) &= 0
\end{aligned}
$$

where i is the quark flavour, Q_i is the parton charge, $q_{i+}(x)$ ($q_{i-}(x)$) is the probability that a quark of flavour i with its spin aligned (anti-aligned) with the nucleon spin has a momentum xP (in a frame where the nucleon has an infinite momentum P).

The model yields naturally:

- Bjorken scaling: The structure functions depend only on the scaling variable.
- The Callan-Gross relation: $F_2 = 2xF_1$.
- An interpretation of x: It is the fraction of nucleon momentum carried by the struck quark in the infinite momentum frame.

The parton model shows that only two structure functions are needed to describe the nucleon in the Bjorken limit. g_2 arises from parton interactions involving the transverse momenta and transverse spins which are not taken into account in the parton model. Hence the relation $g_2 = 0$ in the Bjorken limit.

We define the unpolarized parton distributions $q_i(x) \equiv q_{i+}(x) + q_{i-}(x)$ and the polarized ones $\delta q_i(x) \equiv q_{i+}(x) - q_{i-}(x)$. Our experiment, occurring at Jefferson Lab energies, is only sensitive to the three lightest quarks so the neutron structure functions are:

$$F_1^n(x) = \frac{1}{2}\left(\frac{1}{9}(u(x)+\overline{u}(x)) + \frac{4}{9}(d(x)+\overline{d}(x)) + \frac{1}{9}(s(x)+\overline{s}(x))\right)$$

$$g_1^n(x) = \frac{1}{2}\left(\frac{1}{9}(\delta u(x)+\delta\overline{u}(x)) + \frac{4}{9}(\delta d(x)+\delta\overline{d}(x)) + \frac{1}{9}(\delta s(x)+\delta\overline{s}(x))\right)$$

pQCD at Finite Q^2

The experiments run at finite Q^2 and ν. Hence the quarks are not free and Bjorken scaling is violated. The lowest order Feynman graphs involving gluons are drawn in Fig. 2.10.

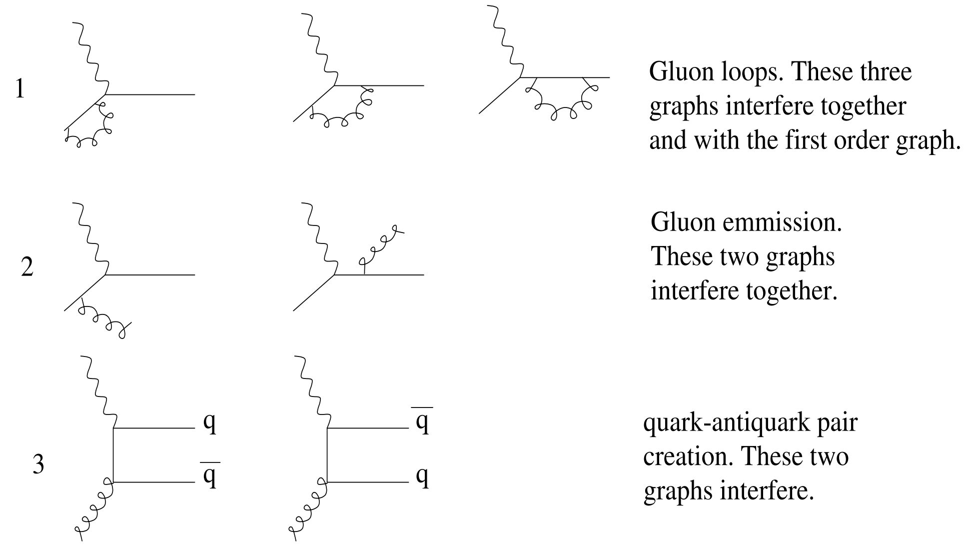

Figure 2.10: QCD radiative corrections (Leading Order).

The drawings correspond to the leading order beyond the first order. Now calculations are carried out up to the "next to next to leading order" (NNLO). These gluon radiations are very similar to the photon emissions (radiative corrections). In figure 2.10 the graphs 1 are equivalent to the vertex corrections and the photon loops. The graphs 2 are equivalent to the bremsstrahlung and the graphs 3 to the vacuum polarization. Infrared and ultraviolet divergences appear as in QED radiative corrections. They need to be renormalized. The dimensional regularization, see for example [127], can be used as well in QCD (it is the minimal subtraction scheme $\overline{MS}$).

We write the quark distribution as a first order term and use the graphs 1, 2 and 3 to compute the perturbative leading order term [147]:

$$q_i(x,Q^2) = q_{iFO}(x) + \frac{\alpha_s}{2\pi} ln(Q^2/\mu^2) \int_x^1 \frac{dy}{y}(q_i(x,Q^2)P_{qq}(x/y) + g(x,Q^2)P_{qg}(x/y)) \qquad (2.23)$$

where α_s is the strong coupling constant and μ a mass scale. $q_{iFO}(x)$ corresponds to the first order (free quarks). Now the quark distributions depend on two variables (scaling violation). We have introduced the "partition functions" p_{qq} and p_{qf}. Their expressions can be found in

[147]. $p_{qq}(z)$ is the probability that a quark of momentum fraction $z \equiv \frac{x}{y}$ of the initial quark momentum has emitted a gluon. $p_{qg}(z)$ is the probability that a gluon materializes in a quark antiquark pair, with the quark having a momentum fraction z of the gluon momentum. We recognize in the equation 2.23 the $ln(Q^2)$ factor characteristic of radiative corrections. Defining $t \equiv ln(Q^2/\mu^2)$ and taking the derivative of eq. 2.23 we get the Altarelli-Parisi (or DGLAP) Q^2 evolution equation:

$$\frac{dq_i(x,Q^2)}{dt} = \frac{\alpha_s}{2\pi}\int_x^1 \frac{dy}{y}(q_i(y,t)P_{qq}(x/y) + g(y,t)P_{qg}(x/y)) \tag{2.24}$$

Similarly, the Q^2 evolution equations for the unpolarized gluon, the polarized quark and the polarized gluon distributions are:

$$\frac{dg(x,Q^2)}{dt} = \frac{\alpha_s}{2\pi}\int_x^1 \frac{dy}{y}\sum_{i=1}^{2f}(q_i(y,t)P_{gq}(x/y) + g(y,t)P_{gg}(x/y)) \tag{2.25}$$

$$\frac{d\delta q_i(x,Q^2)}{dt} = \frac{\alpha_s}{2\pi}\int_x^1 \frac{dy}{y}(\delta q_i(y,t)\delta P_{qq}(x/y) + \delta g(y,t)\delta P_{qg}(x/y)) \tag{2.26}$$

$$\frac{d\delta g(x,Q^2)}{dt} = \frac{\alpha_s}{2\pi}\int_x^1 \frac{dy}{y}\sum_{i=1}^{2f}(\delta q_i(y,t)\delta P_{gq}(x/y) + \delta g(y,t)\delta P_{gg}(x/y)) \tag{2.27}$$

This formalism predicts the behaviour of the DIS structure functions at finite Q^2 and ν in the parton model framework. It is well verified experimentally and it is used to evolve the data to a desired Q^2.

2.2.6 Operator Product Expansion.

This technique is used to derive DIS sum rules such as the Bjorken sum rule. It also permits their extension to finite Q^2. Another important application is to compute the perturbative part of the corrections (other than gluon radiative corrections) to DIS that arise when we leave the Bjorken domain.

The Operator Product Expansion (OPE[4]) was introduced in 1969 by Wilson in an attempt to introduce a substitute to Quantum Field Theory, in order to carry out the Quantum Field Theory non-perturbative calculations. OPE separates the perturbative part of a product of local (i.e. short distances d) operators from the non-perturbative part. In the limit of small distance the product of two operators can be written as:

$$lim_{d\to 0}\sigma_a(d)\sigma_b(0) = \sum_k C_{abk}(d)\sigma_k(0)$$

The C_{abk} are the Wilson coefficients and contain the perturbative part. Consequently they are calculable. The operators σ_k contain the non-calculable, non-perturbative information. In DIS this formalism is used to develop a product of currents on a local operator basis. Ref. [134] shows that any operator σ_k contributes to the cross section by a factor $x^{-n}(M/Q)^{D-2-n}$. Here n is the spin and D the dimension of the operator. One defines the "twist" $t = D - n$. We see that at large Q^2 the leading twist $t = 2$ dominates. At this order, we find the parton model and the DIS sum rules valid in the Bjorken

[4]The abbreviation OPE is also valid for "One Pion Exchange" in conventional nuclear theory. One does not mistake the two abbreviations.

limit. As Q^2 gets smaller higher-twist operators have to be taken into account. The Wilson coefficients are computed perturbatively. Due to their non-perturbative nature, the higher-twist operators have to be calculated using sum rule techniques or experimental data.

2.2.7 A Link between the DIS and the Resonances Region: The Bloom-Gilman (Parton-Hadron) Duality.

It is observed that the structure function $F_2(x)$ measured in the DIS region (parton description) overlaps $F_2(x, Q^2)$ measured from the results of experiments in the resonance region (hadron description) if one smears the resonance peaks. This is known as the Bloom-Gilman duality. This means that the Bjorken scaling, corrected by the DGLAP equation, holds also in the resonance region if one averages over the resonance structure. The higher twist terms are small in the resonance region. Ji [101] gives an enlightening interpretation of duality: it is a region where the higher twists are neither large nor negligible and where the low-lying resonances dominate. This overlap means that the transition region can be described in two dual ways: the hadron or the parton description.

2.3 Conclusion.

We have presented the ^{3}He excitation spectrum and its associated reaction mechanisms from the region of low photon virtuality and low energy loss (described with the nucleon and meson degrees of freedom) to the high energy loss domain (described with the quark and gluon degrees of freedom). The spectrum can be understood in terms of the different excitations of the scattering center depending on the spatial scale ν and the strength Q^2 of the probe. Looking at the spectrum another way, from high to low energy loss, help us to understand the transition between the two domains. In the Bjorken limit the quarks are free because of QCD asymptotic freedom. As Q^2 and ν decrease, soft gluons are emitted, and the evolution is described with the DGLAP equations (logarithm corrections). When Q^2 and ν are low enough ($W \sim 2$ GeV) the quarks begin to be linked by hard gluons (power corrections). These "Higher Twist terms" are Initial and Final State Interactions. Their amplitudes are proportional to $(Q/M_N)^{2-t}$ where t is the twist order. We are leaving the perturbative domain for the non-perturbative one. Meanwhile the hard gluons linking the quarks make them to begin to react coherently to the electron, and we must consider all the quarks with their interactions rather than a quasi-free quark: we are leaving the quark-gluon description for the nucleon-meson one. We understand now why the pQCD to QCD transition comes with a change of the kind of degrees of freedom. At low Q^2 the higher twists dominate: the process is fully non-perturbative, the FSI due to the hard gluon exchanges keep the nucleon unbroken and we are in the nuclear domain.

Chapter 3

Sum Rules

3.1 Introduction.

This chapter presents the Bjorken, the GDH and the extended GDH sum rules. From these three sum rules only the extended GDH sum rule is extracted from our data so it might seem unnecessary to talk about the other sum rules. However, we will see that they are intimately connected to the GDH sum rule.

The interest of the sum rules is that their verification provide a powerful check of the theory: Historically the Bjorken sum rule is the most celebrated in hadronic physics. Its verification by DIS experiments was a fundamental check of QCD that increased our confidence in QCD being the right theory to describe the Strong Interaction. We understand also why sum rules are convenient tools to study the transition region: The summation of inclusive cross sections over the resonance region is less sensitive to the complicated structure of each point of the region.

The GDH sum rule holds at $Q^2 = 0$ while the Bjorken holds in the DIS domain at $Q^2 = \infty$. They belong to a domain where calculations are achievable but use different degrees of freedom (hadronic degrees of freedom versus partonic degrees of freedom). As we have seen in the previous chapter the domain at intermediate Q^2 is the transition region. We will see that a sum rule stands in this domain. It is the GDH sum rule generalized to any Q^2. The GDH sum rule is the limit of this extended GDH sum rule at $Q^2 = 0$. This latter can be connected to the Bjorken sum rule in the DIS domain. Therefore, it links these three domains and it is a unique tool to study the transition from the non-perturbative regime to the perturbative regime of QCD.

After the presentation of the three sum rules, we discuss the validity of the GDH sum rule, which is still not verified. Even if our experiment is not going to $Q^2 = 0$ it constrains the GDH sum rule validity *via* Q^2 evolution models. In addition it is critical for the interpretation of our data to know if the sum rule is valid. In that context we give the principal steps of the GDH sum rule derivation in order to present the assumptions upon which it is based.

Next we summarize the principal theoretical extensions of the integral part of the sum rule beyond the real photon point ($Q^2 \neq 0$) and their purposes. Other extensions are described in the Appendix A. Many extensions differ, so their evolution predictions will be different too. Here we have to emphasize an important point: we have lost the sum rule power since we don't know to what the extended integral is equal to. However we will see that the study of the generalized GDH integral has its own interest. Then we present the extension of both sides of the GDH sum rule. This complete extension unifies the GDH and Bjorken sum rules and provides a sum rule constraining the full QCD range.

We conclude the chapter by a summary of the motivations and the interest of the GDH extension for our understanding of QCD.

3.2 The Bjorken and Gerasimov-Drell-Hearn Sum Rules.

3.2.1 The Bjorken Sum Rule.

This sum rule was derived by Bjorken in 1966 using current algebra and isospin symmetry [19]. It is a fundamental check of QCD because there is no assumption beyond QCD made for its derivation. A violation forces us to reconsider QCD. The sum rule is:

$$\int_0^1 (g_1^p(x,Q^2) - g_1^n(x,Q^2))dx = \frac{1}{6}g_a \tag{3.1}$$

where g_a is the axial coupling constant measured in the neutron β decay. g_1^p and g_1^n are the proton and neutron first polarized structure functions. This sum rule holds in the Bjorken limit. At finite Q^2 the sum rule is generalized using the DGLAP equations and the twist expansion:

$$\int_0^1 (g_1^p(x,Q^2) - g_1^n(x,Q^2))dx = \frac{1}{6}g_a f(Q^2) + HT(Q^2) \tag{3.2}$$

We limit the eq. 3.2 to the twist four. The QCD radiative corrections and the twist four correction can be written as [93], [102]:

- $f(Q^2) = 1 - \frac{\alpha_s(Q^2)}{\pi} - 3.58\left(\frac{\alpha_s(Q^2)}{\pi}\right)^2 - 20.2\left(\frac{\alpha_s(Q^2)}{\pi}\right)^3 + ...$
- $HT(Q^2) = \frac{b_{p-n}}{Q^2}$

The sum rule is now verified at about the 10% level [67].

3.2.2 The Gerasimov-Drell-Hearn Sum Rule.

The GDH sum rule was first derived by Gerasimov in 1965 [80] then independently by Drell and Hearn [63] and Hosoda and Yamamoto in 1966 [87]. The Gerasimov and Drell-Hearn derivations, detailed in next section, make use of:

- The analicity of the forward Compton scattering amplitude (dispersion relations).
- Unitarity (the optical theorem).
- Relativity and Gauge invariance (A Low Energy Theorem).

The sum rule stands at the real photon point (Q^2= 0). It is written as:

$$\int_{\nu_{thr}}^{\infty} \frac{\sigma^{1/2} - \sigma^{3/2}}{\nu} d\nu = -2\pi^2\alpha\frac{\kappa^2}{m_t^2} \tag{3.3}$$

where:

- σ are the inclusive photoproduction cross sections when the photon helicity is aligned (3/2) or anti-aligned (1/2) with the target polarization.
- m_t is the target mass.
- ν is the photon energy. The threshold on the integral is the first (the lightest) photo-produced particle: the pion. In the laboratory frame $\nu_{thr} = m_\pi + (m_\pi^2 + Q^2)/2m_t$ with $Q^2 = 0$.
- κ is the target anomalous moment in Bohr nuclear magnetons.

The GDH sum rule is valid for any kind of target: Its value for the ^{3}He, neutron and proton are:

$$\begin{aligned}
-2\pi^2\alpha\frac{\kappa^2}{m_t^2} &= -496\,\mu b\,(^3He) = -1.268\,GeV^{-2} \\
&= -233.5\,\mu b\,(neutron) = -0.597\,GeV^{-2} \\
&= -204\,\mu b\,(proton) = -0.526\,GeV^{-2}
\end{aligned}$$

Our experiment measures an extended GDH integral on the ^{3}He nucleus and extracts from it the (model dependent) extended GDH integral on the neutron.

Note: If the target is a structureless particle, i.e. $\kappa = 0$, the sum rule holds diagram per diagram [107]. That is if we compute $\sigma^{1/2} - \sigma^{3/2}$ at any order in perturbation theory, then eq. 3.3 should be verified (if the sum rule is true).

We present now the important steps of the derivation to be aware of the assumptions and to discuss its validity.

Derivation.

Let us define S_1 as the spin dependent part of the forward Compton amplitude. Causality implies the analyticity of the amplitude in the complex plane, so we have the Cauchy relation:

$$S_1(z) = \frac{1}{2i\pi}\oint \frac{S_1(\nu')}{\nu' - z}d\nu' = \frac{1}{2i\pi}\int_{-\infty}^{+\infty} \frac{S_1(\nu')}{\nu' - z}d\nu' \tag{3.4}$$

The last equality stands if the Jordan lemmas are valid for $S_1(\nu')$ (i.e. if $S_1(\nu')$ goes to 0 quicker than $1/\nu'$ when $\nu' \to \infty$). Then:

$$\Re e(S_1(\nu)) = \frac{1}{\pi}P\int_{-\infty}^{+\infty} \frac{\Im m(S_1(\nu'))}{\nu' - \nu}d\nu' \tag{3.5}$$

which is the classical Kramer-Kroenig dispersion relation used in all fields of Physics.

From crossing symmetry we have $S_1(\nu) = -S_1(-\nu)^*$. Applying it to eq. 3.5 yields:

$$\Re e(S_1(\nu)) = \frac{2\nu}{\pi}P\int_{0}^{+\infty} \frac{\Im m(S_1(\nu'))}{\nu'^2 - \nu^2}d\nu'$$

The optical theorem gives:

$$\Im m(S_1(\nu)) = \frac{\nu}{8\pi}(\sigma^{1/2} - \sigma^{3/2})$$

A Low Energy Theorem states that the Compton amplitude can be expanded in ν:

$$S_1(\nu) = -\frac{\alpha\kappa^2}{2m_t^2}\nu + \gamma\nu^3 + \sigma(\nu^5) \tag{3.6}$$

After we take the derivative of the eq. 3.6 and use the two previous equations, we find the GDH sum rule:

$$\frac{dS_1(\nu)}{d\nu}\Big|_{\nu=0} = -\frac{\alpha\kappa^2}{2m_t^2} = \frac{1}{4\pi^2}\int_0^{\infty}(\sigma^{1/2} - \sigma^{3/2})\frac{d\nu'}{\nu'}$$

Note: The Non-Subtraction Hypothesis. To be sure to fulfil the Jordan lemmas we can consider $S_1(\nu)/(\nu' - \nu_0)$ that has a better convergence than $S_1(\nu)$. Then the Kramer-Kroenig relation becomes:

$$\Re e(S_1(\nu)) = \Re e(S_1(\nu_0)) + \frac{\nu - \nu_0}{\pi}P\int_{-\infty}^{+\infty}\frac{\Im m(S_1(\nu'))}{(\nu' - \nu_0)(\nu' - \nu)}d\nu'$$

where we have a "subtracted term" $\Re e(S_1(\nu_0))$. We assume $S_1(\nu)$ obeys Jordan lemmas (the "non subtraction hypothesis").

The derivation uses three assumptions:

- The optical theorem
- A Low Energy Theorem
- The hypothesis of a non subtracted dispersion relation.

The two first are well tested and based on solid grounds. The latter is the only input beyond QCD.

As stated previously, the GDH sum rule has not been verified but measurements are under way and preliminary data begin to be published. In addition, data on single pion production give an indirect verification.

GDH Sum Rule Validity: The Theoretical Side.

Consistency of the Unsubtracted Sum Rule in Perturbative models. The consistency of the sum rule can be checked in the framework of perturbation theories. The scattering center has to be structureless ($\kappa = 0$). One can explicitly compute the integral side of eq. 3.3 and check that it is zero. This can be done since,as already said,the GDH sum rule holds diagram per diagram if the target is a fundamental particle of the theoretical framework. Three frameworks are presented:

- The nuclear theory framework (pions and nucleons as fundamental particles i.e without anomalous magnetic moment). The two graphs of pion photo-production off the neutron in fig. 3.1 interfere. The calculation, carried through by Gerasimov and Moulin [81], shows that the GDH integral equals zero and the GDH sum rule is consistent.

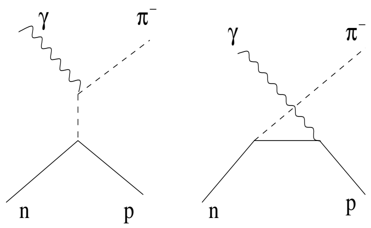

Figure 3.1: Pion photoproduction off neutron.

- The QED framework (photon exchanges and electron target). Pantförder [144] calculated the integral and found that the GDH sum rule is consistent.
- The Weinberg-Salam model framework (photon, $w^{\pm}$, z^0 and Higgs exchanges for an electron target). Pantförder also verified the consistency of the GDH sum rule validity within this model.

Convergence of the Integral. Bass argues that the unitarity bound of QCD supports the convergence of the integral without need of the non subtraction hypothesis [12]. The same author used Regge theory and soft pomeron exchange to check that the integral was convergent [13], [14].

Invalidation of the Sum Rule Due to a Pole. One has postulated the existence of a pole at J=1 in the angular-momentum plane [2]. If so the eq. 3.4 is not valid anymore and we have to add the residue of the pole (name it $S_1(\infty)$) to eq. 3.4. This will add a constant term to the sum rule: $\mathrm{GDH}_{pole}=\mathrm{GDH}_{no\,pole}+4\pi^2 S_1(\infty)$. Nevertheless, Pantförder [144] has shown that the unitarity of the forward Compton amplitude forbids the pole. The absence of the pole is supported by the computations within perturbative models described above. In addition Bass argues that the Bjorken sum rule would be violated as well in the case of the existence of a pole at J=1 [13]. As stated above the Bjorken sum rule has been verified experimentally..

Summary. The unsubtracted sum rule consistency was checked in several descriptions and found valid. Its convergence - without pole trouble - is supported by unitarity and Regge theory. Hence all the theoretical arguments favour the unsubtracted GDH sum rule validity.

GDH Sum Rule Validity: The Experimental Side.

Several analyses using experimental data or fit to experimental data have been conducted in order to check the sum rule validity. The first analysis presented use unpolarized data on pion production as an indirect way to estimate the GDH integral:

Pion Photoproduction Multipole Analysis. Under isospin symmetry the nucleon anomalous moment can be written as $\kappa_p = \kappa_s/2 + \kappa_v/2$ and $\kappa_n = \kappa_s/2 - \kappa_v/2$. The sum rule on the nucleon is then decomposed into isoscalar, isovector and "interference" sum rules : GDH=GDH^V+GDH^S+GDH^{VS} where the "interference" comes from the cross term in $(\kappa_v \pm \kappa_s)^2$. The three sum rules can be checked independently.

In 1973 Karliner estimated the three integral GDH^V, GDH^S, GDH^{VS} with a multipole analysis of single pion photoproduction [115]. Her analysis shows that one pion production nearly saturates the sum rule (see the Nπ columns in the table below). Karliner also estimated the double pion production (the N$\pi\pi$ column). The Nπ contribution was recalculated by Workman and Arndt [173] who confirm Karliner analysis. In the table below we give the integral estimate of the GDH integral from Karliner and Workman and Arndt. The last column is the right hand side of the sum rule.

	Nπ [115]	Nπ [173]	N$\pi\pi$ [115]	Tot [115]	Tot [173]	$-2\pi^2\alpha\kappa^2/m_t^2$
V	-170	-178	-49	-219	-227	-218.5
S	-2	+3	-1	-3	+2	-0.3
VS	-24	-50	-15	-39	-65	+14.7
Neutron				-183	-160	-233.5
Proton				-261	-289	-204

From the analyses they conclude that:

- The isovector sum rule is verified and saturated by the Δ.
- Data are too scarce to check significantly the validity of the isoscalar sum rule.
- The interference sum rule is violated.

The discrepancies between the sum rule prediction and the estimates from photoproduction data could be explained by:

- the limit on the GDH integral used to estimate the one and two pion contribution (at ν =1.2 GeV [115] or 1.7 GeV [173]).
- The use of a multipole E_{0+} with limited accuracy [54].
- Uncertainty on the multipole analysis method [14].
- The strangeness contribution to the anomalous moment [14].

More recent estimates [29], [158] are more or less in accordance with the previous results. See for example the review in [61]. I conclude this part on the estimate of the GDH integral using multipole analysis with the recent results from the Mainz theory group [61]: Their estimate of the GDH integral on the proton verifies the sum rule at the 10 % level. However they found the sum rule on the neutron to be violated by almost 50 % (Let us note that their results on the Burkhardt-Cottingham integral (BC integral, see Appendix A) on the neutron are also in disagreement while the proton BC integral verifies the sum rule).

Validity of the Sum Rule from the DIS data. We will see in section 3.3 how the GDH integral can be extended to $Q^2 > 0$. A wealth of DIS data are available so one can calculate the extended GDH integral and extrapolate the results back to $Q^2 = 0$.

N. Bianchi and E. Thomas use a Regge type empirical fit to the data to estimate the extended GDH integral at $Q^2 \geq 0$ [18]. The photo-production and electroproduction cross sections are separated in their isoscalar and isovector parts:

- $\Delta\sigma_V \sim S^{\alpha^0_{a_1}-1}$
- $\Delta\sigma_I \sim S^{\alpha^0_{f_1}-1}$

with the two Regge trajectories given by the $a_1(1260)$ and the $f_1(1260)$ mesons: $\alpha^0_{a_1} \sim -0.3 \pm 0.02$ and $\alpha^0_{f_1} \sim -0.4 \pm 0.1$. These forms are used to fit the DIS experimental results and to deduce the GDH integral at the photon point. They found $-207 \pm 23\ \mu B$ (proton) and $-226 \pm 22\ \mu B$ (neutron), that is the sum rule is not violated.

The Mainz Data. Preliminary results from the experiment done at MAMI with a real photon beam ([1]) of energy up to 800 MeV seems to indicate that the sum rule is not violated. The analysis is under way and part of the results published ([6]). They are in agreement with the multipole analysis carried out by the Mainz theory group.

Conclusion. The results of Karliner and Workman and Arndt question the sum rule validity. However these analyses have weaknesses and the more recent multipole analyses verify the sum rule as far as the proton is concerned. Experimental studies tend to confirm the validity GDH sum rule on the proton. For the neutron sum rule none of the multipole analyses validate the sum rule, including the recent one of Drechsel et al. [62], although it does validate the proton GDH sum rule. However the extrapolation of DIS data from Bianchi et al. [18] verifies both the neutron and proton GDH sum rules. Our experimental data on the neutron, via GDH Q^2 evolution models, will help to clarify this point. The discrepancy of the “interference” sum rule is even worse since the integral calculation has the wrong sign.

3.3 The GDH Integral Extension at Finite Q^2.

If one assumes a smooth transition between the photo-production and electroproduction cross sections it seems natural to extend the GDH integral beyond the photon point by replacing the photoproduction cross sections by the transverse electroproduction cross sections. The total electroproduction cross section can be found in [56] in term of transverse, longitudinal and interference cross sections as well as in terms of multipole expansion.

The first GDH integral extension was proposed in 1989 by Anselmino et al. [8] as an attempt to solve the spin crisis: GDH was used to estimate the higher twist corrections to the DIS experiments. This work was refined by Burkert, Li and Ioffé [27], [28], [29] in adding the resonances to the model. Other authors have attempted to extend GDH using Chiral Perturbation Theory (Ch.P.T) [16], [107], the Burkhardt-Cottingham sum rule (cf. Appendix A) [164], [165], a multipole analysis [60] or the Constituent Quark Model framework [180].

I will review the first extension of the integral by Anselmino et al. for historical purpose. Then in the next section I will emphasize the important work done by Ji et al. on the sum **rule** extension [107]. Here not only the integral side is extended but the right hand side is also generalized to any Q^2.

This chapter aims to be concise. For completeness the other GDH integral extensions are given in the Appendix A. Another method of higher twist extraction, different from the method of Anselmino, is proposed by Ji et al. [105], [106]. It is also summarized in the Appendix A. For a complete and recent review of the GDH and extended GDH studies, in particular on the various definitions of the extended GDH integrals and their available estimations, see the reference [62] of Drechsel et al.

Different predictions on the generalized integral behavior with Q^2 are given in fig. 3.2. Let us note that definition of the extended GDH integral differs from various authors. Therefore they are plotted separately.

- The slope of the extended GDH integral at the photon point is calculated at the leading order by Bernard et al. (section A.7 in Appendix A) and X. Ji et al. at the leading and next to leading orders (section 3.3.2) using the Ch.P.T.
- The different predictions of Burkert and Li use a phenomenological model (the A.O model), see section A.3.1 in Appendix A. The differences come from the way the Roper resonance is modelled (as a quark-gluon hybrid or a Non Relativistic Quark Model prediction).
- The extended GDH integral calculation from Z. Li (section A.6.2 in Appendix A) is based on an electromagnetic Hamiltonian describing a few quark system. The nucleon wave function is estimated in a Constituent Quark Model framework.
- The calculation of Drechsel et al. (section A.5 in Appendix A) relies on the Unitary Isobar Model from the Mainz theory group.
- Soffer and Teryaev use the Burkhardt-Cottingham sum rule to generalize the GDH integral, see section A.8 in Appendix A.

From now we will call the extended GDH integral "GDH*".

3.3.1 Anselmino et al. Extension.

Generalization and Connection to the Bjorken Integral.

The first GDH extension was prompted by the spin crisis when the EMC experiment gave a quark spin contribution to the nucleon spin compatible with zero. Let us call $I_N(Q^2)$ the GDH integral on the nucleon extended at finite Q^2.

We write the first moment of g_1 as:

$$\Gamma_N(Q^2) \equiv \int_0^{x_0} g_1^N(x, Q^2)dx$$

where $x_0 < 1$, i.e. x_0 is not including the elastic reaction (see the note after the section on the motivation to extend the GDH integral). It links the DIS data to GDH* as we

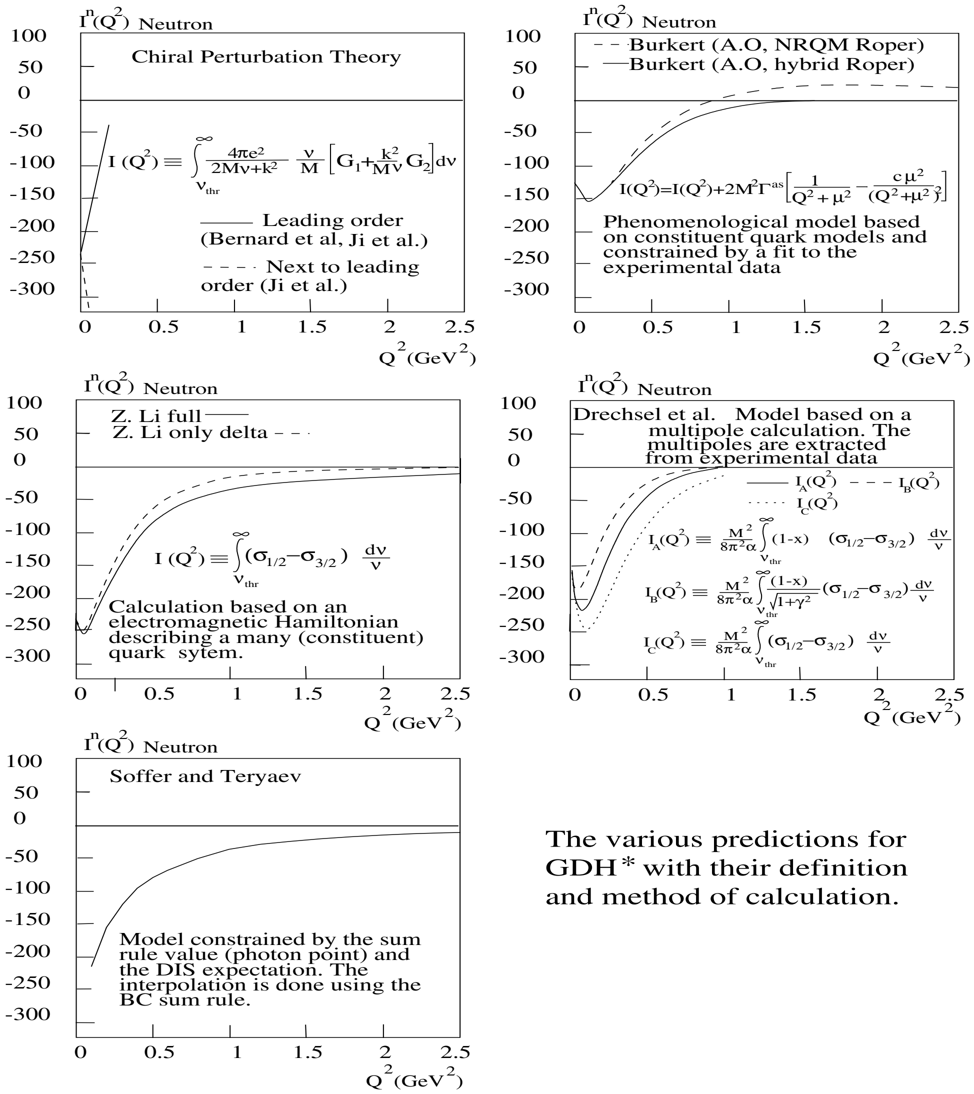

Figure 3.2: Predictions for the GDH sum rule and extended GDH integral in function of Q^2. The last plot gather all the predictions.

see immediately by subtracting eq. 2.17 from eq. 2.18, neglecting g_2 and replacing ν by $Q^2/(2M_n x)$ in the GDH integral:

$$I_N(Q^2) \equiv \int_{\nu_{thr}}^{\infty} \frac{\sigma^{1/2}(Q^2,\nu) - \sigma^{3/2}(Q^2,\nu)}{\nu} d\nu = \frac{2M_N^2}{Q^2}\Gamma_N(Q^2) \qquad (3.7)$$

Connection with the Bjorken Integral. If we subtract Γ_p from Γ_n we have:

$$\frac{Q^2}{2M_N^2}(I_p(Q^2) - I_n(Q^2)) = \Gamma_p(Q^2) - \Gamma_n(Q^2) = \int_0^{x_0} g_1^p(x,Q^2) - g_1^n(x,Q^2)dx \qquad (3.8)$$

which is the Bjorken integral.

Motivation.

The EMC experiment measured a positive $I_p(Q^2)$. A fit of these data, assuming a scaling behaviour down to a few GeV^2, gives $I_p(Q^2) = (0.222 \pm 0.018 \pm 0.026)/Q^2$. At $Q^2 = 0$ the GDH sum rule predicts a negative value. That is, there is a strong Q^2 dependence of the extended integral at low Q^2 that flips the GDH* sign (see Fig. 3.3). We have encountered

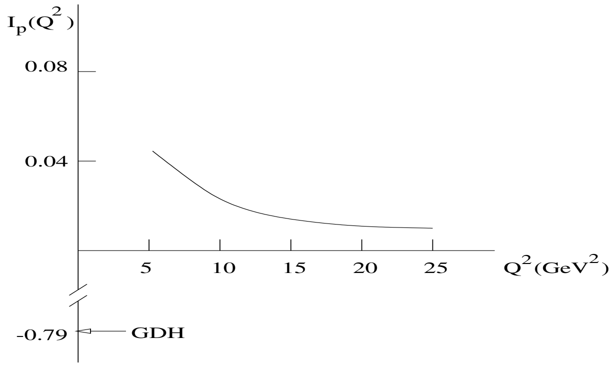

Figure 3.3: $I_P(Q^2)$, fit from the EMC results (from [8]). $I_P(Q^2)$ must have a strong Q^2 dependence at moderate values (0-5 GeV^2).

such terms rising as $(Q/M_N)^{2-t}$ in section 2.2.6: the higher twist terms. Hence GDH* in the transition region is sensitive to these terms and can be used to extract them. If these terms are large then the DIS results have to be reinterpreted and that may solve the spin crisis. It turned out the "spin crisis" was solved by more precise data and using a less naive view of the nucleon spin structure taking into account the gluon spin, the Dirac sea and the parton orbital momenta. In addition the extraction of higher twists, even after its refinement by Burkert, Ioffé and Li (cf Appendix A) is controversial because of the disagreement with the other extraction methods. Nevertheless the most important points are:

- The rapid evolution of the nucleon helicity structure at moderate Q^2 which characterizes the transition from coherent to incoherent reactions.
- The intimate relation between the GDH* integral and the Bjorken integral (eq. 3.8). This relation connects the low Q^2 domain to the DIS domain which will help in unifying the hadronic description of the strong interaction to the quark-gluon description.

Note about the elastic reaction: In the DIS domain, the inclusion of the elastic contribution is not relevant because of the rapid fall off of the form factors. Hence quantities such as the moments of the spin structure functions are defined up to $x = 1$ (the elastic reaction on the nucleon). It is customary to define GDH* without including the elastic contribution because the GDH sum rule at the photon point does not include it (it is below the pion production threshold). However, as pointed out by Ji [101] the elastic, if included, is the dominant contribution at low Q^2. Indeed the strong dependence and the sign flip of GDH* on the proton disappear when the elastic reaction is added. To include the elastic or not is then a matter of choice but, as argued by Ji [101], [106] and Musatov [140] the elastic must be included for a meaningful higher twist study. Evidently if one chooses to include the elastic in defining GDH*, the data must also include it in order to allow for meaningful comparison. In this thesis, all the discussions and results will exclude the elastic reaction.

3.3.2 The Extended GDH *Sum Rule*, a Link Between the Bjorken and the GDH Sum Rules.

Small Q^2 extension.

A rigorous GDH sum rule extension has been derived by Ji and Osborn [107]: Let us write the dispersion relation between the spin-dependent forward Compton scattering $S_1(\nu, Q^2)$ and the structure function $G_1(\nu, Q^2)$ at $Q^2 \neq 0$:

$$S_1(\nu, Q^2) = 4\int_{Q^2/2M_n}^{\infty} \frac{\nu' d\nu'}{\nu'^2 - \nu^2} G_1(\nu', Q^2) \tag{3.9}$$

and expand in Q^2 the forward Compton amplitude. Since the GDH integral does not include the elastic contribution we have to expand $\overline{S_1} \equiv S_1 - S_1^{el}$ with S_1 given by:

$$\overline{S_1}(Q^2, \nu = 0) = -\frac{\kappa^2}{M_N^2} + \overline{S_1}'(0,0)Q^2 + \frac{1}{2}\overline{S_1}''(0,0)Q^4 + ...$$

where the differential terms $\overline{S_1^i}$ are themselves expanded in Chiral Perturbation Theory (Ch.P.T) in power series of m_π:

$$\overline{S_1}'(0,0) = \frac{a}{m_\pi^2} + \frac{b}{m_\pi}(log(m_\pi) + \beta) + ...$$

The coefficients a, b, ... are calculated in Heavy Baryon Ch.P.T:

We have to leading order $a = 0$ [107]. As pointed out by Ji et al., this result is not surprising because the spin dependent effects of a non relativistic particle go as the inverse of its mass (see for ex. [147]). Since in Heavy Baryon Ch.P.T the nucleon mass is taken infinite and since $S_1(\nu, Q^2)$ is the spin-dependent forward Compton scattering amplitude, then the leading contribution is expected to be zero. The extension is presently available up to the next to leading order [108]:

$$\overline{S_1}'(0,0) = \frac{4}{M_N^2} 5.54\, GeV^{-4} \text{ (for the neutron)}$$

Note: This extension has a common point with the first Ch.P.T integral extension done by V. Bernard, N. Kaiser and U. Meissner (see the Appendix A) since both use Heavy Baryon Ch.P.T to extend the integral to small Q^2. The differences between the two predictions are that the integrand differs as well as the photon flux. However the two extensions agree when using the same conventions. In fig. 3.2 the definition of Ji et al. is modified in order to be consistent with the one of Bernard et al., see [107], [108] and [62]

DIS Domain.

The OPE is used to extend the sum rules from the Bjorken domain to finite Q^2:

$$\Gamma_N(Q^2) = \sum_{t=2,4...} \frac{\mu_t(Q^2)}{(Q^2)^{(t-2)/2}} \tag{3.10}$$

where the coefficients μ_t depend on the twist t and also higher twists because of the finite mass of the nucleon. They are calculated in perturbations [102] up to μ_4 (in neglecting the QCD radiative corrections). $\Gamma_N(Q^2)$ changes very little from $Q^2 = \infty$ to $Q^2 = 0.5$ GeV^2 [103]. The twist 4 is not negligible in the range $0.5 < Q^2 < 3$ GeV^2: It contributes by ~8 % to the Bjorken sum rule at $Q^2 = 2$ GeV^2. The correction mostly applies to the proton part of the sum rule and is negligible on the neutron part.

Note: One does not need proton and neutron data to link the Bjorken and the GDH sum rules: As pointed out by Ji [107], Bjorken actually derives two sum rules holding for each nucleon:

$$\Gamma^{p(n)}(Q^2) \equiv \int_0^1 g_1^{p(n)} dx \rightarrow_{Q^2\rightarrow\infty} \pm\frac{1}{12}g_1 + \frac{1}{36}g_8 + \frac{1}{9}g_0$$

where the g_i are weak interaction constants. $\Gamma^p - \Gamma^n$ gives the usual Bjorken sum rule. The right hand side can be expressed in terms of parton distributions, assuming the SU(3) symmetry and $\Delta s = 0$. The sum rule is then known as the Ellis-Jaffe sum rule. The DIS experiments show that this sum rule is violated at more than two standard deviations, invalidating the assumption $\Delta s = 0$.

Intermediate Domain

Ji et al. interpolate in order to link the two predictions made in the calculable domains. Several interpolations are given in [102], [103] according to whether the elastic reaction is included or not.

Ji and Osborn [107] argue that Ch.P.T is valid from $Q^2 = 0$ to ~ 0.2 GeV^2. The twist expansion is valid from ∞ to ~ 0.5 GeV^2. Between them, in the domain covered by our experiment, only experimental data can give an insight of the GDH* behaviour. Other Ch.P.T techniques valid up to 0.4 GeV^2 [135] may bridge the gap. Let us note that the difference between the integral on the neutron and proton is less Q^2 dependent since, as discussed in section A.3 of the Appendix A, the Δ contribution that causes the strong Q^2 dependence, cancels. As pointed out by Burkert [30], the calculation of Bernard et al. and Ji et al. may be valid to a Q^2 higher than 0.2 GeV^2 in this particular case.

3.4 Summary and Conclusion.

There are large theoretical efforts going on with regard to the GDH*, even if there is some disagreement with the methods or the extensions. Nevertheless, most of the studies (see the Appendix A) are in accord on the major role played by the Δ in the Q^2 behaviour of the generalized GDH integral. However some authors disagree on the mechanisms ruling the GDH* evolution: Ioffé and Burkert explain it in terms of chiral symmetry restoration, Ji et al. point out the dominant role of the elastic contribution while Soffer and Teryaev emphasize the role of the Burkhardt-Cottingham sum rule. Another point of disagreement is the higher twist extraction method. Anselmino et al. had raised the interest on the extended GDH as a tool to extract higher twists. Then Burkert and Ioffé corrected the method by taking into account the role of the resonances. Li confirmed their result that the Higher Twists corrections to DIS data are significant. On the other hand, the QCD Sum Rule method of higher twist estimate gives much smaller corrections. Ji et al. disagree with the method of Anselmino et al. arguing again that the major role of the elastic reaction is not taken into account by the first authors. They propose another extraction method based on duality and experimental data in the resonance region. This last method agrees in magnitude with the QCD sum rule extraction method.

Several models or calculations of the GDH integral are available (Bernard et al, Burkert et al., Cardarelli, Drechsel et al., Ji et al., Li, Scholten and Korchin). All agree in the limit ($Q^2 = 0$ and $Q^2 \to \infty$). The agreement in the DIS domain is related to the fact that g_2 is negligible here. However the models disagree at intermediate Q^2. This disagreement comes from the different definitions used for the virtual photon flux and also from the way the authors include g_2 in the generalization of the integral. Our experimental data will test these models. The experimental data can fix some of the free parameters of the models such as the anomalous magnetic moment of the constituent quarks in the extension of Cardarelli based on Constituent Quark Models or can cast light on the nature of the Roper resonance in the Burkert and Li model. Also, Li pointed out how the experimental data on the GDH extended integral for the neutron will measure the importance of the $SU(6) \times O(3)$ symmetry breaking and help to improve Constituent Quarks Models.

A most important theoretical result is the Ji et al. GDH sum rule extension and its link to the Bjorken sum rules. It is:

$$\overline{S_1}(0, Q^2) = 4 \int_{Q^2/2M_n}^{\infty} \frac{d\nu'}{\nu} G_1(\nu', Q^2)$$

where the $\overline{S_1}$ means the elastic contribution has been subtracted. $\overline{S_1}$ is extended in Ch.P.T or higher twists. It provides a rigorous tool to explore the complete hadronic spectrum. It will help to understand the transition mechanism between the hadron description and the parton description. This point represents fundamental progress in our understanding of QCD: *For the first time we can compare an experimental quantity (the extended GDH integral) to a rigorously calculable quantity (the forward Compton amplitude*[1]*) over the full strong interaction domain.* It will also tell where the Ch.P.T and Twist development break down. Perhaps the Twists expansion and Ch.P.T validity domains overlap and then we will be able to carry out calculations on the full QCD domain for the first time. This would be a tremendous advance for the Strong Interaction study. If not, we will need to rely on models and experimental data until lattice QCD calculations are available.

[1] The forward Compton amplitude is not measurable since it needs forward (θ_e=0) detection.

Chapter 4

The Experiment and its Instrumentation

The major aim of experiment E94010 was to measure the Q^2 evolution of the extended GDH sum rule on the neutron and ^{3}He. This task requires either absolute polarized cross section measurements or asymmetry and absolute cross section measurements of the $^3\overrightarrow{He}(\overrightarrow{e},e')X$ reaction. Absolute cross section measurements require a precise knowledge of the incoming electron beam, the target and the detector system. The experimental devices used to produce and to analyse the $^3\overrightarrow{He}(\overrightarrow{e},e')X$ reaction will be presented in this chapter. The constraints on the data taking imposed by both the characteristics of the experimental apparatus and the limited running time will be described, as well as the solutions to these constraints.

4.1 Kinematic Coverage.

In Fig. 4.1 we present the kinematic coverage of the experiment in the Q^2 vs W plane (details can be found in Appendix C). Ideally we have to integrate the measured cross-sections from the pion threshold to infinite energy loss ν (see eq. 3.3). An infinite ν is not achievable experimentally. However, at our low and moderate Q^2 values, the electroproduction cross sections at large ν are expected to make only a small contribution to the GDH* integral. The kinematics of fig. 4.1 cover the quasi-elastic region, the resonance region and the Deep Inelastic Scattering. Elastic scattering was also included for the three lowest energies. The elastic reaction is measured as a cross check: Its agreement with previous data tells us that the following quantities are collectively well understood:

- The spectrometer acceptances.
- The detectors efficiencies.
- The target density.
- The incoming electron flux and energy.
- The thickness of matter crossed by the scattered electrons.

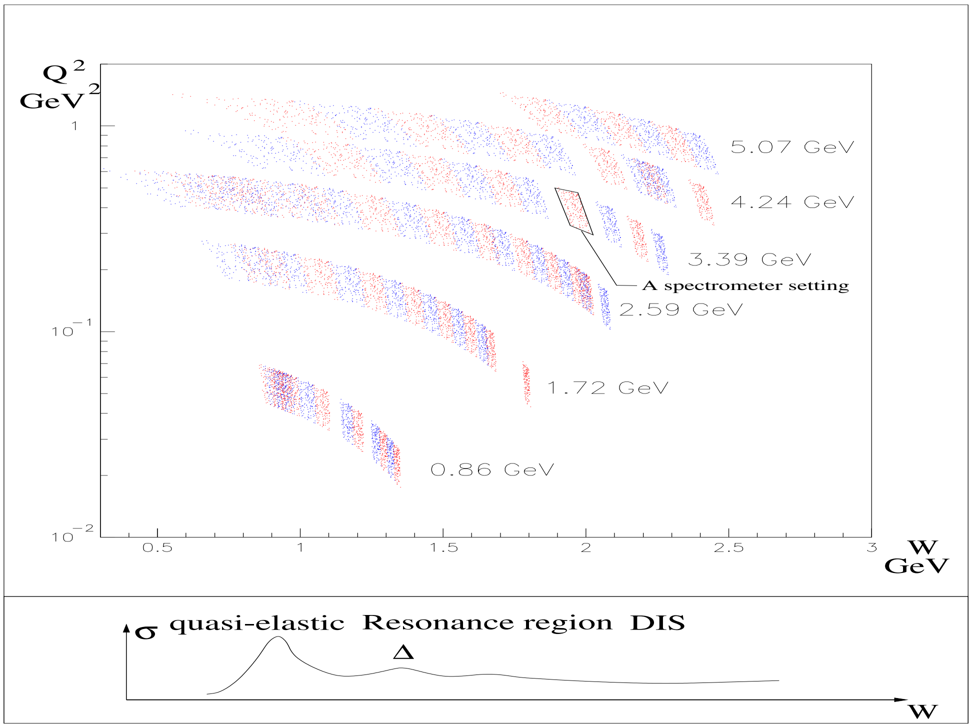

Figure 4.1: Kinematic coverage of the experiment. Two consecutive spectrometer settings are in different colours (let us note the overlap of two consecutive settings). Each strip corresponds to one of the six beam energies used. The bottom plot symbolizes the corresponding hadronic spectrum.

- The data acquisition.
- The beam and target polarization.

The six different strips seen in fig. 4.1 correspond to the six beam energies used for the experiment. The substructures are the spectrometer acceptances at different central momentum settings. These settings were chosen to have some overlap to check that the edges of the acceptance connect smoothly. Not all the settings do overlap in order to save beam time: We chose to do so when the cross section evolution was expected to be smooth so the interpolation between the two consecutive settings is easy.

We need to integrate over W at fixed Q^2 to form the GDH* integral. To see its evolution we need points at different Q^2. Ideally the strips in fig. 4.1 would be horizontal. This can be done by playing with the incoming beam energy or the scattered electron angle. However it is not practical to change the beam energy frequently because it takes beam time and the other halls are running too. It is also not convenient to change the scattering angle often because we need to have several sets of data at different energies for each angle in order to carry out radiative corrections.

The strategy is to go to forward angles (15.5^o, the most forward angle achievable with both spectrometers) in order to have the largest counting rate to cover as completely as possible the kinematic domain and interpolate between the strips to integrate at a fixed Q^2. This choice gives a reasonable counting rate and covers the largest kinematics domain.

The drawback is that an energy change takes much longer (it can take a few hours or longer) than a angle change (half a hour) but the gain in the counting rate is enough to overcome this drawback (see [42] on the experiment simulation and [43] on the run plan of the experiment).

For all the covered domains, data are taken with both the target spin antiparallel and perpendicular to the beam direction in order to measure $A_\parallel$ and $A_\perp$. Our asymmetries of interest are A_1 and A_2. They are linear combination of $A_\parallel$ and $A_\perp$ (see eq. 2.21). The time spent in each target configuration was optimized by minimizing the uncertainty ΔA_1 ($\partial\Delta A_1^2$=0). The running time management depends only on the asymmetry uncertainty since the relative statistical uncertainty on an asymmetry A is about $\sqrt{2}/A$ larger than relative statistical uncertainty on a cross section.

We use the Jefferson Lab polarized electron beam to cover this kinematics domain. A polarized beam (and a polarized target) is required to measure asymmetries.

4.2 Polarized Electrons.

Polarized electrons are extracted from GaAs sources. The beam is then accelerated by two identical linacs linked by two recirculation arcs.

4.2.1 The Electron Source.

The electrons are extracted from a photocathode by illuminating it with a polarized laser light and are accelerated to about 45 MeV by an injector. Two kinds of polarized sources are available at Jefferson Lab:

- A bulk GaAs photocathode source giving a maximum theoretical beam polarization of 50%. It delivers a maximum current over 100 μA and an actual polarization of P$\sim$ 40%.
- A strained GaAs crystal photocathode source with 100% maximum polarization achievable. The maximal current was 50 μA and the polarization was $\sim$ 70%.

We use the strained GaAs source because it provides the higher polarization. We cannot take advantage of the high current capabilities of the bulk GaAs source because the radiation damage, increasing with the current, shortens the lifetime of the target cell. The best compromise between the target depolarization due to the beam (c.f. section 4.3.5), the radiation damage and the current was 10 μA.

Random 1 or 30 Hz flips of the beam helicity cancel most of the systematic errors in asymmetry measurements that arise, for example, from beam current drifts, beam position drifts (inducing acceptance variations),... One could also flip the target polarization but it is much more convenient and feasible to flip the beam helicity. It is done by the Pockel cell that controls the helicity of the laser light *via* the Kerr effect (the Kerr effect is the birefringence apparition in dielectrics under an electric field). That way, the laser helicity can be quickly controlled. The Pockel cell information is coded in a logical signal sent to the data acquisition system. We explain in section 4.3.4 how this information is decoded and used for the data analysis. In addition, a half wave plate can be inserted in the laser path to reverse the helicity of the electron beam. This is used to check systematic errors arising from helicity correlated electronic noise. The data taken with the half wave plate in and out must be consistent.

4.2.2 Acceleration.

The electrons extracted from the source were accelerated to about 45 MeV by the injector linac. They are then injected in the first linac, bent by 180^o in a recirculation arc, accelerated by the second linac and re-injected in the first linac by a second arc or sent to the halls. This cycle is named a pass and CEBAF can go up to 5 passes, each pass increasing the energy by the same amount. Each linac is made of superconducting RF cavities and accelerates the beam by 400 to 500 MeV.

Ideally the electron spin should be aligned with the beam. During the experiment it was most of the time oriented at an angle between 5^o to 10^o (at worst 30^o) relative to the beam. This is due to the spin precession during the acceleration in the arcs and the constraint that the other halls also needed a longitudinally polarized beam. However the transverse component (in the Hall) shrinks by a factor γ_p due to the Lorentz boost. The small transverse spin component modifies the relation between (A_1,A_2) and ($A_\parallel$,$A_\perp$) but the effect stays negligible. E. Lakuriqi in [90] has computed the new relations that we use in [42] to optimise the data taking.

4.3 Hall A

To study the $^3\overrightarrow{He}(\overrightarrow{e}, e')X$ reaction one has to:

- know the beam and target characteristics.
- detect the electron scattered off the ^{3}He nucleus and to identify the reaction.

For such an inclusive double polarized experiment we know the initial target and electron spin states as well as their momenta. The electron final momentum and scattering angle were measured but not their helicity. The recoiling target debris were not detected. In this section we will specify the information we need on the beam and how this information was collected along the beam line. This beam interacts with a polarized target. A large part of this section will be devoted to a description of the target. Then we will discuss the two spectrometers used to detect the electrons. They are nearly identical and set symmetrically to the beam line to double the statistics and to cross check our data analysis. Fig. 4.2 shows the experimental Hall A

4.3.1 Beam Characterization.

The cross sections and asymmetries depend on the following beam characteristics:

- Beam position: the spectrometer acceptances depend on the beam position on the target. We used continuously the Beam Position Monitors (BPM) that provide a non-destructive online position monitoring. They are calibrated with a second device, the Superharp.

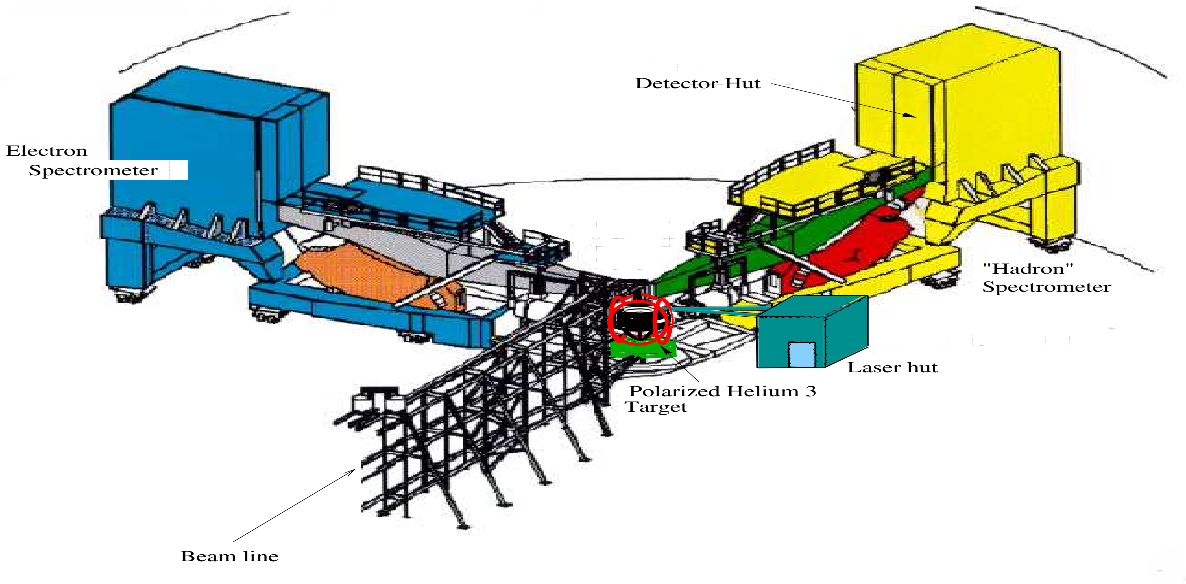

Figure 4.2: The Hall A.

- Particle energies: Two devices of 5 $\times 10^{-4}$ accuracy level measure the beam energy. If the spectrometer momentum is calibrated to a comparable level and if the spectrometer angle is precisely known (at the mr level), we can also measure the beam energy using the elastic reaction.

- The beam current: We aim to measures absolute cross sections at 5% level, The beam current uncertainty goes directly into the cross section uncertainty. In addition asymmetries are measured. Since they are a cross section ratio it could seem unnecessary to measure the incoming flux of electrons. However asymmetries must be corrected from the charge asymmetry (c.f. 4.3.4) so a beam current measurement is also needed. Integrated charge and charge asymmetries are both measured by the Beam Current Monitor (BCM). Taking advantage of the online BCM capacity, the charge asymmetry was kept as low as possible but can reach 20 % of the raw physics asymmetry. This effect is corrected by computing the asymmetry with the charge normalized counting rate

- The beam polarization: The fact that the beam (and the target) are not fully polarized dilutes the $^3\overrightarrow{He}(\overrightarrow{e},e')X$ asymmetry. The Møller polarimeter provides the beam polarization needed for the correction.

Beam Position.

Beam Position Monitors. A BPM consists of four pick-up antennas surrounding the beam. The beam induces a signal in an antenna proportional to the inverse of the beam-antenna distance. The four antennas provide the beam's horizontal and vertical position. Two sets of BPM measure the beam position and angle. One is at 7.5 meters upstream from the target and the second at 1.3 meters upstream the target.

Superharp. A Superharp set is made of three wires bent by 45^o, -45^o and vertical. During a measurement the wires scan the beam path and each beam-wire encounter is detected by an ion chamber. The three different wire orientations are needed to determine the beam profile. Details can be found in D. Marchand's thesis [51]. The Superharp measurements are used to calibrate the BPM which provided the online and offline beam position.

Absolute Energy Measurement.

The eP Measurement. The eP method, detailed in O. Ravel's Thesis [150], uses the elastic p(e,e'p) reaction. The angles of the recoiling proton (θ_p) and the scattered electron (θ_e) are linked to the energy E by:

$$E = M_p \left(cos\theta_e + sin\theta_e / \left[tan\theta_p - 1\right]\right) / \left(1 - cos\theta_e\right) + \sigma\left(m_e^2/k_e'^2\right)$$

with m_e and M_p the electron and proton masses and k_e' the scattered electron momentum. Protons and electrons are detected in coincidence. The target is a solid polyethylene $(CH_2)^n$ film of 13 μm thickness.

Two measurements symmetric to the beam line are done simultaneously and their results added to cancel first order errors arising from beam misalignment. Microstrips measure the angles, the trigger is done by scintillators and a Čerenkov while the reaction coplanarity requirement selects the elastic reaction.

The ARC Measurement. The ARC [51] measures the deflection of a charged particle under a magnetic field; the bend angle is inversely proportional to its momentum. During an ARC operation the field bending the beam to direct it to the hall is mapped and the beam position, *via* the Superharp, is measured.

During our experiment both energy measurement devices were commissioned. Only four of the six energies were measured reliably. Fortunately elastic scattering data were taken at the two other energies and, could be used to extract the beam energy.

A 5^{-4} level of accuracy in the beam energy is enough as we can see in the elastic cross section analysis (section 5.8). For example at 1.7185 GeV and 15.5^o a 1.2^{-3} error brings a 2.6 % error on the elastic cross section to compare with the 5% total uncertainty goal.

Note. The beam energy spread is a few 10^{-5}, an order of magnitude below the beam energy measurement accuracy.

In the table below we list the six beam energies (in MeV). The error on the ARC measurement is 5^{-4} and the error on the elastic determination is 10^{-3} (see [50] for details). Arc results are from [156] and eP results from [17].

Linacs Pass	ARC	Elastic	eP
1	-	862.0	-
2 (first period)	-	1717.9	-
2 (second period)	-	1716.9	1717.9±0.39 (stat)±0.2 (syst)
3	2581.1	-	-
4	3385	-	3381.8±0.6 (syst)
5	4238.2	-	4236.2±0.36 (stat)±0.7 (syst)
5	5058.2	-	-

Beam Current Monitor.

Two passive cavities allow a non-invasive online measurement of the beam current. They are tuned on the CEBAF beam frequency. Antennas inside the cavities collect a signal proportional to the beam current. An Unser monitor, sandwiched between the two cavities and providing an absolute measurement, is used to calibrate the cavities. The cavity measurements depend on the temperature. The calibration is repeated periodically because of this instability and because of the readout electronic drift. The Unser is a Direct Current Transformer made of two toroids centered on the beam. They are driven by a sinusoidal signal at 250 Hz and mounted in opposite way. Consequently, no signal comes out of the Unser in the absence of external field. The beam induces a signal proportional to the beam current. The Unser is calibrated with a wire simulating the beam and powered by a high precision current source. The external conditions make the measurements fluctuate with a 200 nA variance (see G. Laveissiere report [124]). Consequently it is not usable at few μA which correspond to the running conditions of our experiment. Since the RF cavities have a good linearity on the achievable current range, a standard procedure was to calibrate the Unser at highest current possible (50 μA with the strained GaAs source, 100 μA otherwise), then to calibrate the cavities with it and to use them for monitoring. During part of the experiment the calibration of the cavities was provided by a different method using a Faraday cup (it is a copper plug inserted on the beam line that collects the beam charge). The BCM voltage output is converted to a frequency by a VtoF to be read by a scaler. The precision reached by the BCM is better than 1% [156].

Møller Polarimeter.

The beam polarimeter is based on the $\overrightarrow{e^-}(\overrightarrow{e^-}, e^-e^-)$ reaction (Møller scattering) whose cross section asymmetry depends on both beam and target polarizations. The beam is scattered on a target made of two supermendur foils. They are polarized by a 300 Gauss external magnetic field yielding a 7.60±0.23% electron polarization, (see E. Chudakov report in [167]). Scattered electrons are directed to a lead-glass detector by three quadrupoles and a dipole[1]. Final electrons are detected in coincidence. The following table summarizes the average beam polarization for each energy. The (relative) systematic error on these results is 3 %. The statistical error is negligible.

Energy (GeV)	Average beam polarization
1.718 (first period)	66.2 %
3.382	69.8 %
1.718 (second period)	70.9%
4.239	70.5%
0.862	70.9%
2.581	68.9%
5.059	70.1%

Note: A Mott polarimeter is located after the injector (Mott Polarimeters work at low energy) and measures the beam polarization before the linac acceleration. This mea-

[1]The three quadrupoles are also used for the beam transport in the Hall A as well as the fourth quadrupole of Hall A beam line. This latter is not used by the Møller. Each Møller measurement requires a magnetic setting change of the beam line.

surement with spin precession calculations allows to deduce the beam polarization in any hall. During the experiment one or more Mott measurements were done for each beam energy.

4.3.2 High Resolution Spectrometers.

The hall is built around two spectrometers of about 6 msr acceptance called high resolution Spectrometers. These arms measure the momentum, the vertex and angle and identify the beam-target reaction products. They are nearly identical in design and rotate around the target. In coincidence experiments one arm is used to detect the recoiling hadron while the other detects the scattered electron. Thus one arm is referred as the "hadron arm" and the second as the "electron arm". Our experiment detects only electrons. The dipoles are both set to electron detection polarity, the only purpose of having two arms is to double our statistics (and to provide two simultaneous independent measurements, increasing our confidence in the results. However, by convention I will still refer to the right spectrometer (looking downstream from the beam) as the "hadron" arm. The spectrometer focal plane is at the vertical drift chambers (VDC) location and bent by about 17^o with respect to the VDC plane. The VDC set measures the scattered particle angles and positions in its local frame. They are then transformed in the focal plane frame. The vertex and scattering angles are reconstructed using the focal quantities and the spectrometer optical tensor (stored in the "optics database"). The VDC precision allows a high $\delta p/p$ resolution (10^{-4} by design) of the particle momentum.

Spectrometer Magnets

Magnets bend and focus the scattered particles. Each spectrometer is composed of one dipole and three $\cos 2\theta$ quadrupoles in a QQDQ configuration, see Fig. 4.3. As previously

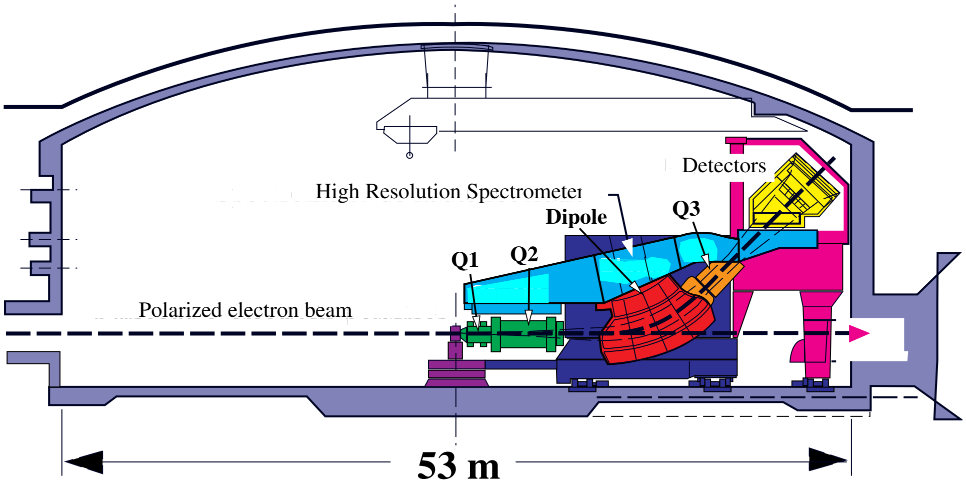

Figure 4.3: The spectrometer magnetic configuration.

mentioned, the magnetic optics combined with the VDC allow a precise momentum measurement. It also sweeps away oppositely-charged particles and neutral particles. The two first quadrupoles focus the beam on the dipole entrance to increase the spectrometer acceptance. Q1 is focusing in the vertical plane while Q2 provides horizontal focusing. Q3 focuses the beam horizontally in the focal plane. The spectrometer acceptance is mainly driven by the Tungsten 6 msr entrance collimator. Nominal characteristics of the spectrometers are listed in the table below.

Characteristic	value
Momentum range:	0.3-4.0 GeV
Optical length:	23.4 m
Momentum acceptance:	$\pm 4.5\%$
Horizontal angular acceptance:	± 28 mr
Vertical angular acceptance:	± 60 mr
Solid angle :	6 msr
Horizontal angular resolution (FWHM):	0.6 mr
Vertical angular resolution (FWHM):	2.0 mr
Relative momentum resolution	10^{-4}

Spectrometer nominal characteristics.

Spectrometer Optics Studies.

A precise spectrometer knowledge is necessary for the analysis (acceptance simulation, accurate vertex and angle reconstruction). In this perspective "optics" measurements were taken for a complete understanding of the apparatus.

No satisfying database for extended targets existed at the time of the experiment. Some running time was dedicated to a complete spectrometer optics study with a seven-foil ^{12}C target. Foils (of thickness 51.46$\pm$0.03 mg/cm^2) were spaced by about 7 cm along the beam direction. Data were taken with a beam of 0.862 GeV. The spectrometer relative momentum varies from $\Delta P/P = \pm 4.5\%$ for a complete scan of the momentum acceptance. The spectrometer entrance collimator is either in, as standard running condition, or out for a better understanding of the acceptance. The spectrometer acceptance model used for our data analysis and simulation is extracted from these data. Runs are also taken with a sieve slit (a plate pierced with holes at known positions). The reconstructed hole positions allow us to optimise the optics database. Elastic ^{12}C data were analysed and compared to the world's data as a check on our understanding of the acceptance. The agreement is at least within 4 % for each foil and each arm. This is more difficult to do with the elastic runs taken on ^{3}He since discrepancies can be also attributed to the target density, temperature, length or spectrometer acceptance. The solid targets have a well known density and thickness and one can directly check the acceptance model.

4.3.3 Detector Package.

The spectrometer detector package is composed of a VDC pair for trajectory reconstruction, two scintillator planes to trigger the data acquisition, a Čerenkov and a shower counter[2] for particle identification. The electron arm has a preshower counter in addition

[2] The "Hadron" arm shower counter was specific to our experiment.

to the shower counter. Figure 4.4 shows the detector package configuration for electron arm (the hadron arm is similar).

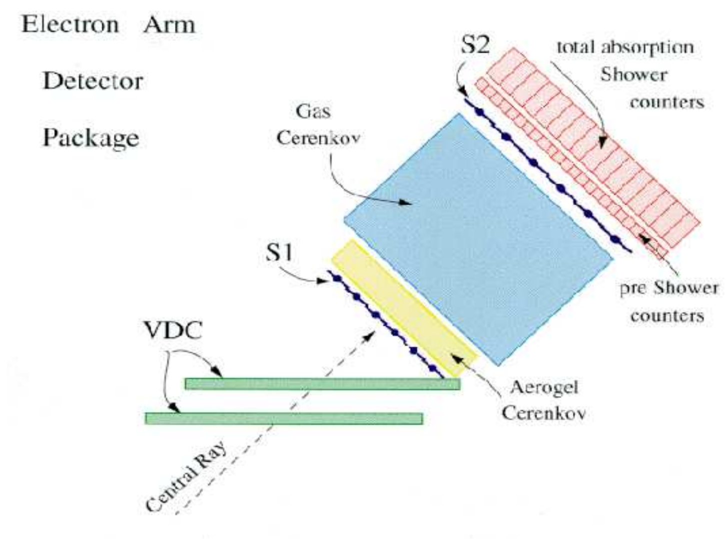

Figure 4.4: The detector package configuration for the electron arm. The aerogel Čerenkov was removed in our case.

Vertical Drift Chambers.

Two Vertical Drift Chambers (VDC), made of 2 wires planes (U,V) each, measure the particle position and angles near the spectrometer focal plane. Wire chambers are composed of several wire planes enclosed in a gaseous medium. Each plane is closed by a window of aluminized mylar at negative high voltage while the wires are either grounded or at positive high voltage. As a result the electric field lines between the window and the wires will be parallel near the window, while the extend radially near the wires, as illustrated on Fig. 4.5. Often "shaping wires" placed between the detection wires are used to optimize the field line pattern ([157] p 75). This is not the case for the Hall A VDC because in order to minimize multiple scatterings, which degrades the high resolution of the spectrometer.

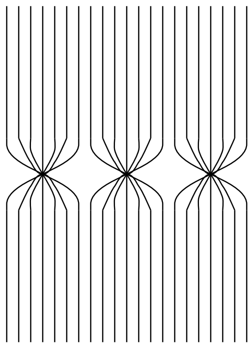

Figure 4.5: Electric field lines between the frame and the wires.

A charged particle coming through a chamber will ionize the gas. In the parallel field line region, the electrons resulting from the gas ionization will drift toward the wires. In the radial region, accelerated by the stronger electric field, they will gain enough energy in their mean free path to ionize other atoms, inducing an *avalanche* process [157]. Ions drift toward the negatively-charged frame. The electrons drift toward the detection wires, inducing a negative signal. By knowing when this signal is induced, when the particle is crossing the wire plane, and the avalanche drift velocity we can compute the particle crossing point.

A Wire Chamber consists of different wire planes. This provides an trajectory angle determination. Since a particle crosses the wire planes with an angle and since the wires are close to each other (a few mm. to a few cm.) several wires will get a signal. The requirement to have several firing wires avoids noisy wire problems (it also provides a crude angle determination). Another source of noise comes from the low energy photons resulting for example from ion-electron recombination [157]. As they can induce ionization far from the crossing point, which makes its determination more difficult, a small quantity of quencher gas is added. This gas has the property of absorbing these photons.

Both the drift velocity in the gas and the timing of the processes must be well known in order to compute the crossing point. Time information is given by a Time to Digital Converter (TDC) which is basically a clock delivering a signal suitable for the acquisition. The TDC begins to count when the first wire signal arrives and is stopped by a signal coming from the scintillator trigger. Consequently a high TDC channel represents a short drift time and *vice versa*.

Jefferson Lab Hall A Vertical Drift Chambers

This section describes the particular features of the Hall A VDC package. It consists of two identical pairs of VDCs spaced by 50 cm (Fig. 4.6). Each VDC contains two wire planes spaced by 2.6 cm. Each plane consists of 400 gold plated wires of 20 μm diameter. The windows are at negative high voltage (-4 kV) and the wires are grounded. Wires are separated by 4.243 mm and the frame width is 2.6 cm. This makes a particle crossing with the nominal 45^o trajectory to fire five wires (Fig. 4.7). A minimum of 3 firing wires is required to validate a good cluster in order to limit noise and to avoid the left-right ambiguity[3]. The crossing point between the particle and the wire plane is known at 225 μm (FWHM) [76] and [130]. With the VDC spaced by 50 cm we reach an angular precision of approximately 0.3 mr (FWHM). A 65% argon gas (ionization gas) and 35% ethane gas (quencher) mixture is used to operate the VDC.

Scintillator Planes.

Two scintillator planes S1 and S2 are separated by 2 m. We use them to trigger the data acquisition. They are made of Bicron BC-408 plastic and are 1.27 cm thick. They are perpendicular to the average particle track, as seen in fig 4.4. Each plane consists of six scintillator paddles with a 5 mm overlap (See Fig. 4.8). When a charged particle passes through a scintillator, it generates a light, which is collected by two phototubes at the

[3]When a particle fires a wire, the only information is the TDC and one is unable to know if it crossed on the left or the right of the wire.

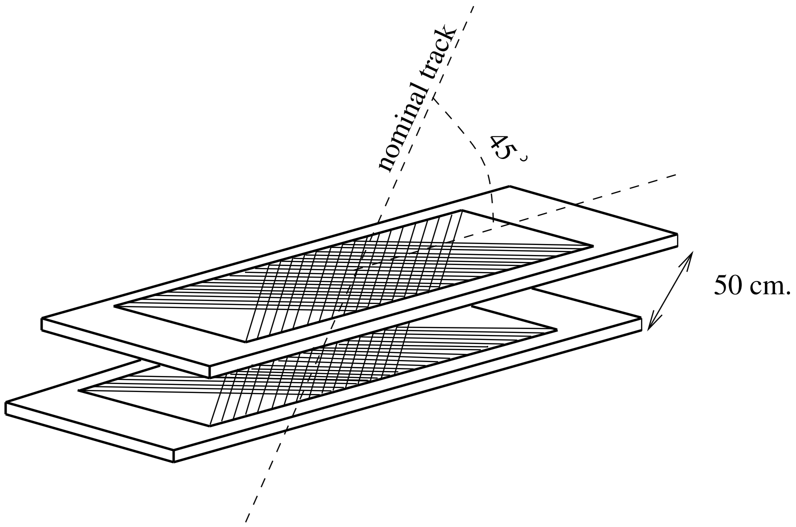

Figure 4.6: A VDC detector package.

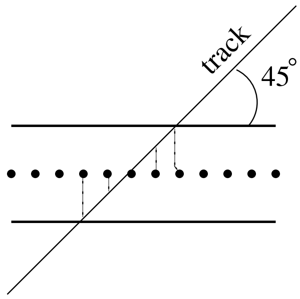

Figure 4.7: A particle going through a wire plane with the nominal 45^o track fires five wires.

end of the scintillator paddle. For each paddle the two phototube signals are required for a good trigger since they are needed to compute the particle-paddle crossing point. The phototube output signal is sent to:

- A discriminator that shapes it into a logical signal used by the data acquisition and by a Time to Digital Converter (TDC) for timing. We chose the TDC of the S2 right phototube to define a time basis for the event.
- An Analog to Digital Converter (ADC). It converts the phototube analog output to the digital signal used in the data analysis.

During the experimental runs the deterioration of the phototubes, due to ^{4}He present in the Hall, degraded the efficiency of these detectors significantly (see section 5.4.1).

Particle Identification.

The electron data can be contaminated by π^- electroproduction. The data analysis shows that we have a π^-/e^- ratio of 5 at worst. The spectrometers are each equipped with two independent detectors of 10^{-2} rejection inefficiency. Consequently we reach 10^{-4} rejection inefficiency. Particle identification performances are given in the section 5.4.2.

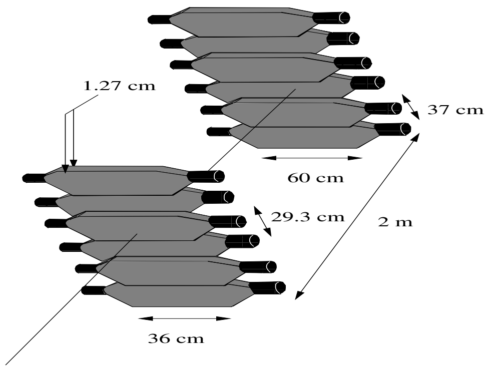

Figure 4.8: Scintillator plane.

Threshold Gas Čerenkov Counter. The Čerenkov counter is a detector dedicated to particle identification. The principle of this detector relies on the fact that if a charged particle travels in a medium (called a "radiator") of optical index n with a speed greater than the light speed in the medium, then this particle radiates (Čerenkov light). The light is emitted at an angle $\theta = arcos(1/\beta n)$ from the particle direction. The condition $cos(\theta) \leq 1$ imposes a threshold for the Čerenkov light emission: if $\beta < n^{-1}$, no light is emitted. This is used to discriminate the electrons from heavier particles such as the π^-. In our case the radiator is CO_2 at one atmosphere (1.5 meters length for the electron arm and 1.0 meter for "Hadron" arm). Its index of 1.00041 provides a threshold of 17 MeV for electrons and 4.87 GeV for pions. The Čerenkov light is focused toward phototubes by 10 mirrors covering the spectrometer acceptance. The Čerenkov detector has an electron detection efficiency greater than 99 %. Rejection inefficiency for pions can come from electron knock-on: Pions knock atomic electrons from matter before the Čerenkov detector. These are called δ-electrons, and may trigger the Čerenkov. Thus, pions can be associated with a good Čerenkov signal and mistaken for electrons. Particle discrimination redundancy with the shower counter allows us to correct for this effect. To minimize it, a high density of matter before a Čerenkov should be avoided. We show in fig. 4.9 from the note [39] a simulation of δ-electrons production in a Hall A spectrometer. We concluded from this study that the δ-electron contamination is tolerable for our experiment. The Čerenkov rejection inefficiency needs to be analysed using the shower and, *vice versa*, the shower efficiency will be estimated using the Čerenkov.

Preshower and Shower Counters. The shower counter is an independent detector for particle identification.

Principle. Shower counters are segmented lead glass blocks coupled to a phototube. Two different dominant processes happen following the mass of the particle crossing the block.

- When an electron interacts with the lead glass, bremsstrahlung is released and the photons will create e^-/e^+ pairs. These will also radiate and create new particles (showers). The photons emitted by the particles (Čerenkov emission, bremsstrahlung,...) are collected and their number is proportional to the particle energy.

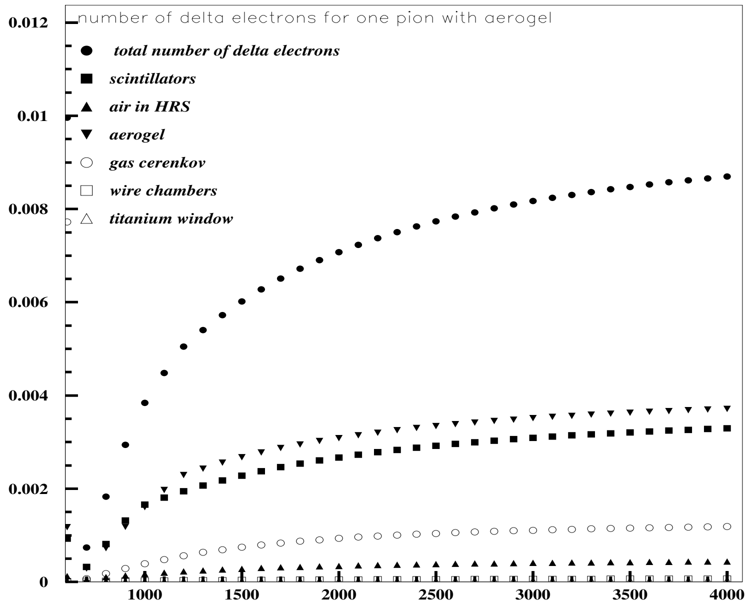

Figure 4.9: The δ-ray production. The horizontal is the pion energy in MeV while the vertical is the number of δ-ray produced for one pion. The dominant production comes from the aerogel Čerenkov.

- For heavier particles the bremsstrahlung is small as it decreases as $1/\mathrm{m}^2{}_{particle}$ and the dominant energy loss is due to ionization (given by the Bethe-Bloch equation [146]). Since no shower is produced, the photon emission is much smaller than for electrons.

Consequently The phototube's ADC spectrum shows two peaks corresponding to the electrons and the heavier particles. A cut on this spectrum allows us to select the desired particles.

Electron Arm Shower and Preshower Counters. The electron arm preshower counters consists of 48 TF-1 lead glass blocks placed in 2 columns. One block represents 3.65 radiation lengths. The electron shower is made of 96 SF- 5 blocks in 6 columns. Each block presents 15.22 radiation lengths. The shower-preshower configuration is drawn in fig. 4.10. The combination of a preshower and shower allows a better particle discrimination as we shall see in section 5.4.2.

Hadron Arm Shower Counter. The "hadron" arm shower counter was built for our experiment since a lone Čerenkov detector was not sufficient for the desired electron-pion separation. It consists of 32 lead glass blocks in 2 columns. The thickness is 6 radiation lengths (15 cm).

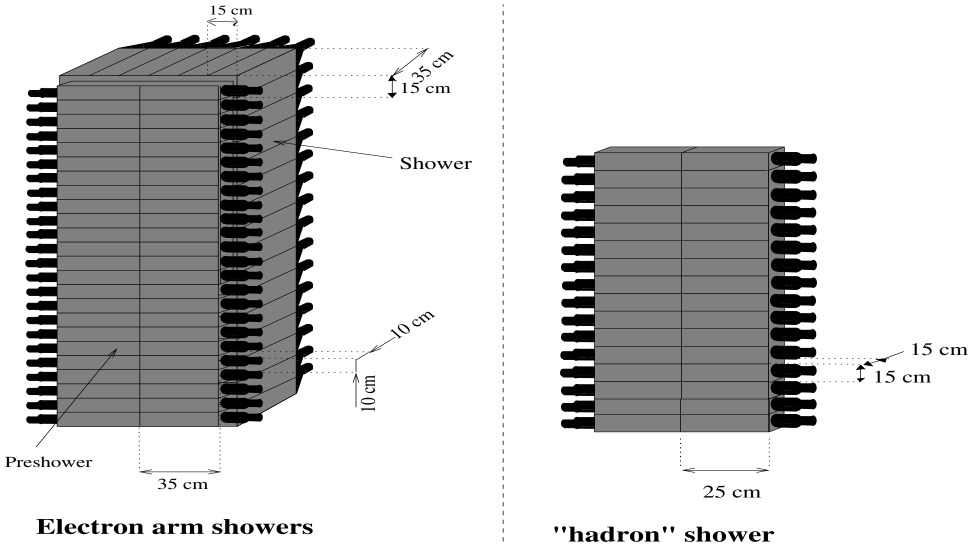

Figure 4.10: The electron arm shower and preshower configuration (left) and the "hadron" arm shower (right).

4.3.4 Triggers, Data Acquisition and Beam Helicity Information Management.

The data acquisition (DAQ) records all the signals making an event. The trigger system decreases the amount of data recorded in selecting only reasonable events by requiring the coincidence of selected detector signals.

Triggers and Deadtime.

Triggers. The two scintillator planes S1 and S2 form the main trigger for each arm. A secondary trigger for each arm is necessary for trigger inefficiency correction. In the following trigger definitions we say that a particle has a "good track" if it fires, say, paddle n in the plane S1 and paddle n-1,n or n+1 in plane S2 (i.e. the particle had a trajectory with the rough 45^o angle expected from the spectrometer geometry). A "bad track" is a track that is not meeting this criteria. Events are classified as one of the following trigger types:

- T1: Electron arm main trigger (S1 & S2 & good track).
- T2: Electron arm secondary trigger ((S1 & Čerenkov or S2 & Čerenkov) & not T1).
- T3: "Hadron" arm main trigger (S1 & S2 & good track).
- T4: "Hadron" arm secondary trigger ((S1 & Čerenkov or S2 & Čerenkov) & not T3).

S1 and S2 scintillator planes should detect an event in coincidence to generate a T1 or a T3 trigger. In addition the two phototubes of each firing paddle must deliver a signal and the paddles location must be consistent with an approximate 45^o track. T2 and T4 triggers are T1 and T3 exclusive. They require either a Čerenkov signal and only a S1 or S2 phototube signals. A simplified trigger layout is presented in Fig. 4.11.

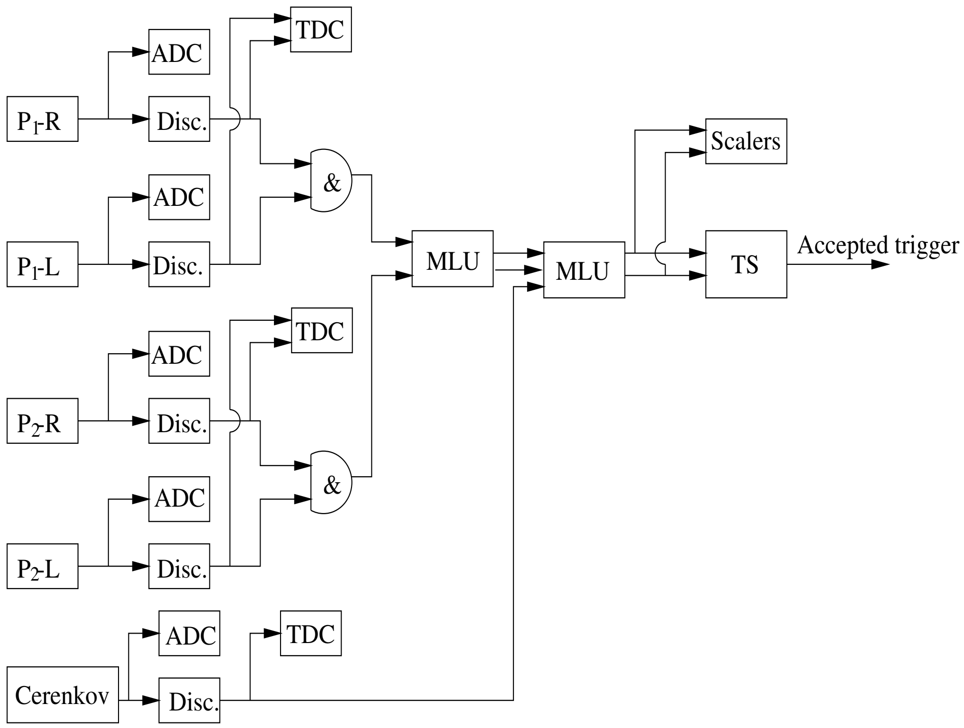

Figure 4.11: Simplified single arm trigger layout.

The left and right phototube signals from a scintillator paddle are shaped into a logical signal by the discriminators. The TDC of the right phototube on each S2 paddle defines a time fiducial for each event. The left TDC allows us to compute the position of the crossing in the paddle. The AND gates selects left and right signals in coincidence. The Memory Lookup Unit (MLU) manages the S1-S2 coincidence requirement. The next MLU manages the Čerenkov coincidence. Combined S1 and S2 TDC data can be used for β optimisation (the electron must have the speed of light) and particle identification (time of flight).

In addition to being sent to the Trigger Supervisor (TS), each trigger increments a scaler for raw event counting. Other quantities such as the beam charge are counted by scalers. Three scalers are associated to each of these quantities. A first one counts without regarding the beam helicity while the two others count only for a given helicity. Scalers allow raw data checks, integrated charge estimates, and charge asymmetry and deadtime corrections.

Deadtime. The livetime L_t is defined as the fraction of the total time when the DAQ is able to record an event. The deadtime is 1-L_t. Cross sections have to be corrected for it. The electronics and the acquisition are the main sources of deadtime: The MLU dominates the electronic deadtime. It is busy a few hundreds of nanoseconds after each event is registered. The DAQ will be busy for 300 μs after an event to register and build it. This is the software deadtime. The TS checks if the data acquisition is busy. If so the event is not recorded. Other processes can contribute to the deadtime: event size variations, busy network or DAQ computers busy with other tasks. These other processes caused deadtime random fluctuations that affect the asymmetry as we will see in the chapter 5.

The TS has prescale functions that allow to stay at a reasonable deadtime level (30 %). It will arbitrarily ignore a fraction of the total event number of a given trigger. The fraction is adjusted accordingly to the DAQ rate. If a prescaler of a T_i trigger is set to n, the TS will register the first trigger T_i and wait n-1 future events before to record the next T_i.

Data Acquisition.

Jefferson Lab DAQ software is CODA [36]. We ran first with a DAQ common to both arms then with two independent DAQ for each arm. This feature multiplied by three the DAQ limit rate (instead of the expected factor two because the added DAQ computer was more efficient than the old one). The recorded data are:

- CODA events from the detectors and the beam helicity signal. The maximal acceptable DAQ frequency before we reached a $\sim 30\%$ deadtime was 2 or 6 kHz, depending on whether we used one or two DAQ systems.
- Data from EPICS [72], the Slow Control Software used at Jefferson Lab, such as spectrometer magnet fields or currents, target temperature, Fast Raster coil currents...
- CODA scalers: every 2 or 10 second the DAQ reads the scaler values and stores them. The DAQ reads them before the TS so the scalers are not affected by the deadtime and allow us to correct the other data from it.

Beam Helicity Information Management.

The helicity information is critical for a polarized experiment. The signal coding the beam helicity is a logical signal: A high value identifies a helicity state while a low value identifies the other[4]. When the beam helicity flips, a 200 μs gate is set during the flip where the helicity is uncertain. Events coming in the gate have an undefined helicity. The helicity signal coming from the accelerator is split and sent to two ADCs.[5] An inverter before one of the ADC reverses the value of the signal. A 2D plot of the two ADCs values then allows to select the good helicity events (see fig. 4.12). A high value of one ADC with a low value of the other identifies one helicity type. The contrary identifies the other helicity. Two low ADC values means the beam helicity was flipping. A cut will be applied in this region (the 200 μs gate). Two high values of the ADCs should never happen. The table sums up the helicity assignment.

ADC15	up	down	down	up
ADC16	down	down	up	up
helicity code	0	1	2	3
meaning	helicity+	undefined	helicity-	undefined

[4]The coding inverts depending on whether the accelerator half wave plate is in or out.

[5]In the case of "hadron" arm DAQ we have two other ADCs for redundant information.

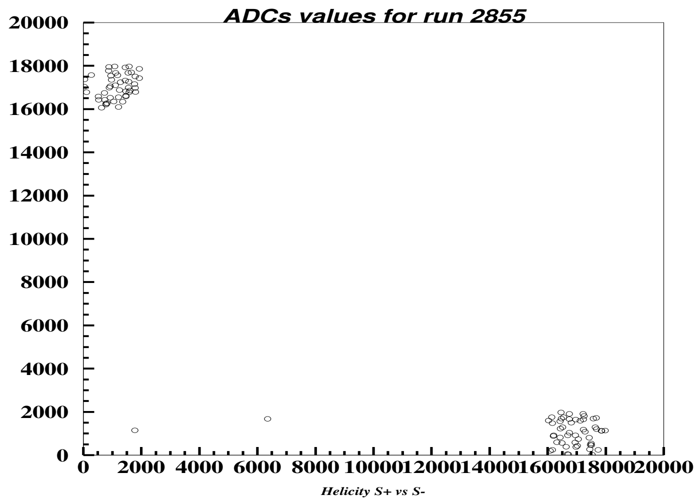

Figure 4.12: Helicity ADC values.

4.3.5 The Helium-3 Polarized Target.

Why a ^{3}He Polarized Target.

There are no free neutron targets because of the neutron's short lifetime (about 15 min.). Polarized deuterium and ^{3}He can be used for experiments on neutrons. The first has to be corrected for its proton part that shares the polarization while the second is, to first order, a polarized neutron target. ^{3}He is made of a neutron and two protons. If the nucleus is in its ground state (S state), the Pauli Principle forces the protons to have anti-parallel spins so their contribution to the ^{3}He spin is cancelled. As a result, polarized ^{3}He targets can be viewed as polarized free neutron targets diluted by two unpolarized protons. Protons will contribute to the nucleus' spin at second order due to the D-wave and S'-wave components (see fig. 2.6). As for Deuterium, proton data are needed to extract the neutron data. These corrections will be detailed in chapter 5. Some questions exist about the possibility of gathering the neutron GDH integral by using a nuclear target. Let us note the recent article of Arenhövel questioning the possibility of extracting the GDH sum rule on the neutron from the deuteron [10] due to the model dependence. Therefore, when we present the results on the neutron extracted from the ^{3}He data we have to keep in mind that this neutron information is model dependent.

We use a 40 cm target at approximately 10 atm to achieve a high density of about 2.5 10^{20} cm^{-3}. The luminosity reached can be as high as 10^{36} s^{-1}cm^{-2}. An average of 35% target polarization was achieved with a 3-15 μA beam current. This polarization represents an equilibrium between the polarization efficiency and depolarization processes. The target can be polarized and kept polarized either parallel or transverse to the beam direction. This new feature allows us to take data on both g_1 and g_2 with a negligible statistical error in a reasonable time.

Polarization.

To achieve the ^{3}He nuclear polarization we polarize first some Rubidium atoms and then exchange the polarization by collision with the ^{3}He. The Rb is an alkali element so its lone valence electron determines its atomic polarization. The depletion of one of its two spin ground states S creates the polarization:

1. A laser light optically pumps the Rb atoms from the ground states $5S_{1/2}$ to one of the excited states $5P_{1/2}$.

2. Angular momentum conservation implies either $\triangle m_z = +1$ or $\triangle m_z = -1$ transitions, depending respectively on the right or left circular polarization of the laser beam.

3. The possible transitions for the excited electrons are $\triangle m_z = \pm 1, 0$: They can come back to the two $5S_{1/2}$ levels (and the emitted light is consequently unpolarized).

4. In the case of Fig. 4.13 the electrons return to the $5S_{1/2}$ levels following the $\triangle m_z = -1$ and $\triangle m_z = 0$ transitions. However, as the m=-1/2 is still pumped out, it depopulates in favour of the other.

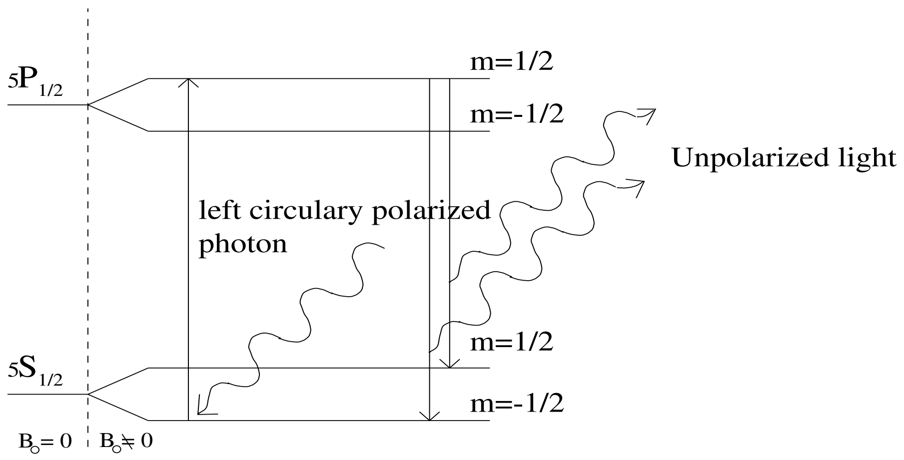

Figure 4.13: Optical pumping of the Rb atoms by depletion of the $5S_{1/2}$ m=-1/2 state.

The energy gap between the levels 5S and 5P is 1.56 eV (794.8 nm). The lasers are thus set to this wavelength.

The right circularly polarized component of the unpolarized emitted light can be re-absorbed by the Rb and remove an electron from the m=1/2 state. This inverse process decreases the polarization efficiency. About 1% of N_2 is added to the ^{3}He to quench the phenomenon. The Rb will transfer its energy to the N_2 molecule vibrational or rotational states by collision, allowing a non radiative decay.

Spin Exchange Collisions.

In the ^{3}He nucleus rest frame we define r as the position of the Rb valence electron. During a ^{3}He-Rb collision, the part of the Hamiltonian describing the interaction between the ^{3}He nucleus and the Rb valence electron is :

$$H = \frac{16\pi}{3} g_n \mu_n \mu_b \overrightarrow{K}.\overrightarrow{S} \psi_e(r=0)$$

where the electron wave function ψ_e is taken at r=0 since the ^{3}He nucleus is point-like in regard with the ψ_e extension. g_n is the neutron Landé factor, μ_b the Bohr magneton, μ_B the Bohr nuclear magneton, $\overrightarrow{K}$ and $\overrightarrow{S}$ are respectively the ^{3}He nucleus and the Rb valence electron spins. The coupling $\overrightarrow{K}.\overrightarrow{S}$ allows a spin exchange between the two systems. The cross section is of order 10^{-24}cm^2. This process, together with the depolarization processes, determines the polarization evolution. A study of these processes can be found in M. Washgull's thesis [174].

The cell Geometry.

The cell is composed of two chambers (see Fig. 4.14). The important point is the creation of a strong temperature gradient between the upper cell, which is enclosed in an oven at 170 ^{o}C [6], and the lower cell, which is at room temperature. Polarization happens in the

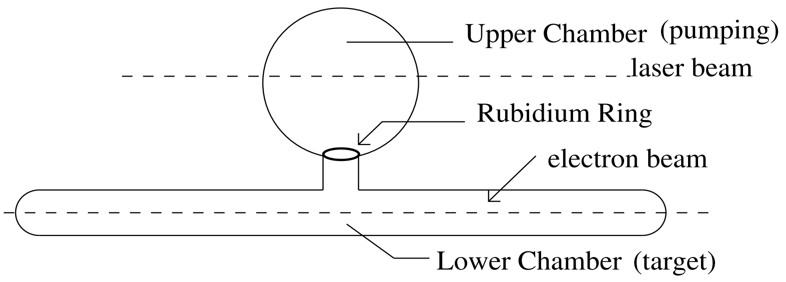

Figure 4.14: The two chambers cell.

upper chamber containing a mixture of ^{3}He and Rb gas. The latter comes from solid Rb vaporized thanks to the oven. In addition the high temperature increases the collision rate between the two species. The thermal gradient prevents the Rb vapor for going into the lower chamber (where the beam is scattered) by condensating on the target neck. The Rb concentration is given by [117]:

$$log_{10}(k_b T[Rb]) = (10.55 - \frac{4132}{T})$$

where [Rb] is the Rb saturated vapour concentration expressed in cm^{-3}, the Boltzmann constant k_b is in CGS units and T in K. The average temperature in the lower chamber where Rb is unwanted is 60 ^{o}C. The temperature gradient acts as a thermal barrier and the Rb density is about 10^{-4} time smaller in the scattering chamber than in the upper chamber.

[6] The operating temperature was hotter (230 ^{o}C) because the chamber is also warmed up by the lasers.

Depolarization.

When the target is not pumped the polarization loss can be written, using the evolution equation of [174]:

$$P(t) = P_0 e^{-\Gamma_D t}$$

where P_0 is the initial polarization and Γ_D^{-1} is the depolarization time constant. The depolarization has four causes:

- ^{3}He-^{3}He collisions.
- ^{3}He interaction with the cell wall.
- Field inhomogeneity.
- Beam depolarization.

So Γ_D can be written as $\Gamma_D = \Gamma_{He-He} + \Gamma_{wall} + \Gamma_{\Delta B} + \Gamma_{beam}$.

- The depolarization coming from ^{3}He-^{3}He collisions is inherent to the target and is an intrinsic limitation. It occurs during a collision when the nuclear spin couples with the orbital ^{3}He-^{3}He momentum and flips. The depolarization constant has been calculated by Newbury et al. [141]: Γ^{-1}_{He-He}=744/[^{3}He] hours with the ^{3}He density in amagats[7].
- the depolarization constant due to the ^{3}He interaction with the cell wall depends on the cell fabrication. It drives the quality of the polarization lifetime. Typically $\Gamma^{-1}_{wall} = 90$ hours.
- A field inhomogeneity is viewed by a moving particle as a time dependent field that can induce nuclear transitions. The associated depolarization factor is: $\Gamma_{\Delta B} \propto \frac{|\nabla B_x|^2 + |\nabla B_y|^2}{B_z^2}$ [174]. Mappings and a field model were done ([41]) to adjust the Helmholtz coils to minimise $\Gamma_{\Delta B}$. $\Gamma^{-1}_{\Delta B}$ was computed to be 1719 hours, which is negligible. Magnet models were used to compute the field gradient at the target due to the spectrometers' magnets. It was found negligible too [148].
- The beam depolarizes the target by ionising the ^{3}He atoms. The hyperfine interaction couples the nuclear spin to the remaining atomic electron spin and nuclear spin flip can occur. H. Middleton thesis [137] details this process.

The total depolarization factor (without beam current) was measured for each cell. Typically $\Gamma_D^{-1} = 40$ hours.

The NMR Polarimetry.

An online polarization measurement is required because of the polarization evolution. Elastic asymmetry data are taken, in part, for beam depolarization studies [40].

The polarimetry is performed by NMR (Nuclear Magnetic Resonance). The NMR apparatus is calibrated by two methods: The water and the EPR (Electron Paramagnetic Resonance) calibrations. Let us note that the EPR is an independent polarimetry. However our setup did not allow us to make online measurements and the few EPR measurements done are used for the NMR calibration.

[7] 1 amagat corresponds to 1 atmosphere at O ^{o}C . 1 amg=2.6868 10^{19} atoms/cm^3

NMR principle. Consider a $\frac{1}{2}$ spin system with two states : $|\uparrow>$ and $|\downarrow>$ degenerate in absence of magnetic field. The degeneracy is removed when an external magnetic field B_0 is applied and an energy gap $\triangle E = \gamma\hbar B_0$ separates the two states. γ is the gyromagnetic ratio of the system. A sinusoidal radio-frequency field $B_1(\omega)$ will induce

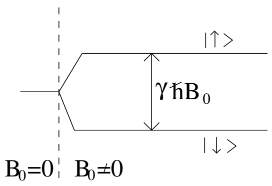

transitions between the sates $|\uparrow>$ and $|\downarrow>$. The transition probability has the following shape:

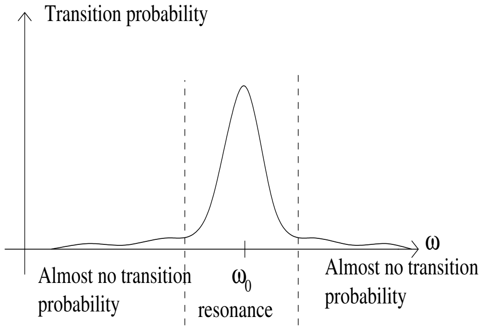

where $\omega_0 = \gamma B_0 = \frac{E(\downarrow)-E(\uparrow)}{\hbar}$.

This simply expresses the fact that the system has discrete energy levels, so it can only absorb the ω_0 frequency (and nearby frequencies because of the Heisenberg uncertainty and Doppler effect). In other words the spin-flip induces an energy absorption at a well determined frequency characteristic of the system. This is the Magnetic Resonance. When the spin system is a nucleus the phenomenon is called Nuclear Magnetic Resonance.

A NMR application is the magnetic field measurement knowing the gyromagnetic ratio γ of a system (the system being a NMR probe). One deduces the magnetic field amplitude $B_0 = \frac{\omega_0}{\gamma}$ by sweeping the RF field and finding the system resonance frequency. The NMR probes of the Hall A spectrometer dipoles use this principle.

Our application of interest is the polarimetry. Contrary to the first application, the resonance frequency ω_0 is known and fixed and it is the magnetic field amplitude that is swept. Radio Frequency (RF) coils generate the RF signal to induce a NMR signal. If we are not in the NMR condition there is no absorption by the system. The pick up coils that are perpendicular to the RF coil detect nothing since the pick up coil area seen by RF field is zero. As soon as we meet the resonance condition the RF photons are absorbed and re-emitted in every direction, and are detected by the pick up coils. As shown in the next section the amplitude of the collected signal is proportional to the target polarization.

Polarimetry Measurement. Consider n_0 systems, each of spin μ. The definition of the system polarization is:

$$P = \frac{n^+ - n^-}{n_0}$$

where n^+ is the number of states $|\uparrow>$ and n^- the number of states $|\downarrow>$.

The magnitude of the system's magnetic moment is the result of all the spins of the systems :

$$< \mu >= \frac{n^+ - n^-}{n_0}\mu = P\mu \tag{4.1}$$

The RF field makes $< \vec{\mu} >$ precess around an axis determined by $\overrightarrow{B_{eff}}$, the effective field seen from a frame rotating around $\overrightarrow{B_0}$ with the angular frequency ω_0. If $\overrightarrow{B_0}$ is swept slowly enough to allow $< \vec{\mu} >$ to follow the direction of $\overrightarrow{B_{eff}}$, but quickly enough with respect to the spin thermic relaxation characteristic time, we perform an "Adiabatic Fast Passage", described by A. Abragam in [3], and the magnetic moment of the system always remains aligned with $\overrightarrow{B_{eff}}$:

$$< \vec{\mu} >= \frac{< \mu >}{| \overrightarrow{B_{eff}} |}\overrightarrow{B_{eff}}$$

The magnetisation of the system is proportional to the magnetic moment of the system :

$$\vec{M} = \alpha < \vec{\mu} > \tag{4.2}$$

One has only to consider $\overrightarrow{M_T}$ the transverse part of $\vec{M}$ since the NMR signal is detected by the pick up Coils which axis is perpendicular to the RF coils.

Equations 4.1 and 4.2 show that the polarization is proportional to the magnetisation:

$$P(t) = \frac{M_T(t)}{\alpha\mu}$$

The transverse magnetisation gives rise to a transverse oscillating magnetic field proportional to the magnetisation: $\overrightarrow{B_T(t)} = \alpha' M_T(t)\overrightarrow{u_T}$. It induces a signal in the pick up coils. The Lenz law gives the induced voltage :

$$\epsilon = -\frac{d\phi}{dt} = -\frac{d}{dt}\int_{S_{pu}} \overrightarrow{B_T(t)}d\vec{s}$$

where S_{pu} is the pick up coils surface. Under the Adiabatic Fast Passage condition, we have $\frac{dM_T(t)}{dt} \simeq 0$ thus :

$$\epsilon = -M_T\frac{d}{dt}\int \alpha'\overrightarrow{u_T}d\vec{s} = -P(t)\mu\alpha\alpha'\frac{d}{dt}\int \overrightarrow{u_T}d\vec{s}$$

The signal induced in the pick up coils is proportional to the polarization of the target and provides a polarization measurement .

The factor $\alpha\alpha'\mu\frac{d}{dt}\int \overrightarrow{u_T}d\vec{s}$ is difficult to calculate. We avoid it by calibrating the system.

The NMR setup is described in [88] and S. Jensen Thesis [99]. The NMR has online capabilities and the target polarization was measured every few hours.

NMR Water Calibration. We use a cell filled with water and identical to the target cell in order to calibrate the NMR system. At a temperature T, the protons of the water cell have a known thermic polarization: $P = tanh\frac{\overrightarrow{\mu_p}\overrightarrow{B}}{k_bT}$ where $\overrightarrow{B}$ is the magnetic field, $\overrightarrow{\mu_p}$ the proton magnetic moment and k_b the Boltzmann constant. Measurements of the proton NMR signal calibrates the system. The analysis is complicated by several facts:

- The smallness of the water signal.
- The actual differences of geometry and position of the water cell and the ^{3}He cell.
- The NMR relaxation times T_1 and T_2 that distorts the Lorentzian shape of the water signal.
- The fact that the water is not isotopically pure.

De-oxygenated pure water was used in order to have T_1 close to the world value [49]. The water calibration analysis can be found in S. Incerti's note on the water calibration [88] or in [99].

EPR Calibration. The EPR is an independent polarimetry method. However, because of the lack of online capabilities of our EPR setup, this measurement was performed less frequently and used as an independent NMR calibration. See [122] for details.

Fig. 4.15 shows the evolution of the target polarization during the experiment. The pump up and the beam depolarization are clearly visible.

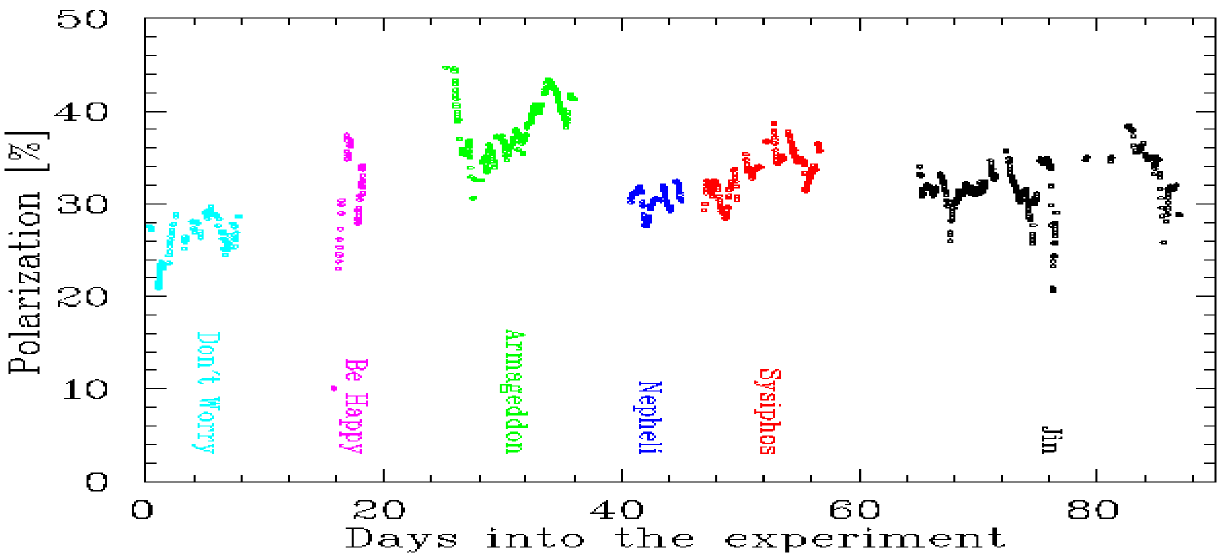

Figure 4.15: The target polarization during the experimental run. The nicknames refer to the different cells used.

Cell characteristics

The cell construction, filling and dimensional measurements are described in I. Kominis' note on the cell characteristics [118]. The cross section measurement and the polarimetry accuracy depends linearly on the target density. The cell density was measured by 3 independent methods. The first relies on the cell dimension and filling measurements. The second uses the broadening of the D1 and D2 absorption lines of the Rb due to the ^{3}He pressure (the lifetime of the excited levels is decreased by the collisions between the Rb and ^{3}He atoms and the energy-time Heisenberg inequality explains the broadening [142]). The table[8] below gives the density for the cells [118]. Numbers are given in amagat for cells at uniform temperature. A third method will be described at the end of the section.

Cell	D1	D2	Average	Fill	Total average
A	10.03±0.17	9.94±0.15	9.99±0.22	9.71±0.03	9.90±0.23
B	9.28±0.15	9.39±0.14	9.34±0.20	9.23±0.02	9.30±0.21
C	10.09±0.17	10.25±0.15	10.17±0.22	10.09±0.03	10.14±0.23
D	11.47±0.19	11.32±0.17	11.40±0.25	10.95±0.02	11.25±0.25
E	8.31±0.14	8.14±0.12	8.23±0.18	8.00±0.02	8.15±0.19
F	8.46±0.14	8.42±0.13	8.44±0.19	8.25±0.02	8.39±0.19

The N_2 density is given in the next table (in amagat) [119].

Cell	$[N_2]$
A	0.092±0.03
B	0.077±0.03
C	0.125±0.03
D	0.112±0.03
E	0.081±0.03
F	0.089±0.03

The upper chamber is at about 230 ^{o}C. The lower chamber is at about 60 ^{o}C. The pressure gradient increases the density in the lower chamber as:

$$n_t = n_0 \left(1 + \frac{V_p}{V_0}\left(\frac{T_s}{T_p} - 1\right)\right)^{-1} \tag{4.3}$$

where n_t is the corrected density, n_0 is the density at uniform temperature, V_p the pumping chamber volume, V_0 the cell total volume, T_s the temperature in the scattering chamber and T_p the temperature in the pumping chamber. The volumes are given in the following table (from [118]).

[8] The cell are often referred by their nickname. I give here the correspondence. A=Don't Worry, B=Be Happy, C=Armageddon, D=Nepheli, E=Sysiphos, F=Jin

Cell	Pumping chamber (cm^3)	transfer tube (cm^3)	target chamber (cm^3)	Total
A	107.2	8.59	103.0	244.39
B	139.85	6.03	104.73	250.61
C	118.85	6.45	107.27	232.57
D	123.46	7.93	109.35	240.74
E	132.8	7.12	117.72	257.64
F	123.58	10.37	110.2	244.15

Target entrance window and exit side wall thicknesses are needed for radiative corrections. Measurements of the entrance windows was done *via* thin film interferometry and mechanical measurement. The exit side wall thickness is known only on average and is estimated from the type of glass used for the cell. The table below, from [118], gives the thickness of the cells.

Cell	entrances	mechanical. μm.	optical. μm.	exit side mm.
A	2 / 21	137.2±1.3 / 143.5±1.3	135.9±0.6 / 140.1±0.5	0.86
B	4 / 5	129.5±1.3 / 132.1±1.3	- / 135.3±1.6	0.87
C	VII / XVIII	125.7±1.3 / 142.2±1.3	121.9±0.6 / 139.1±0.7	1.35
D	-	-	-	0.84
E	9 / 18	152.4±1.3 / 132.1±1.3	134.2±1.0 / 121.0±1.0	0.80
F	14 / 15	142.2±1.3 / 137.2±1.3	136.1±1.2 / 134.8±0.8	0.84

Error on the side exit can reach 20 %. The thin film method was applied on surviving cells after the data taking. The next table gives the measurements ([100], the error bars correspond to the dispersion on the measurements).

Cell	exit (“hadron” arm side)	exit (electron arm side)
A	1.02±0.04 mm	0.98±0.04 mm
E	1.00±0.04 mm	0.98±0.04 mm
F	0.90 ±0.04mm	0.85 ±0.04mm
Ref. Cell.	-	1.16 ±0.07mm
Water Cell	1.1 ±0.1mm	-

A 10% error on the entrance window brings a 1% error on the elastic cross section while 2% error (typically the uncertainty of the thin film method) on the exit side wall yields 0.6% errors. This gives a feeling of the precision needed on these thicknesses knowing that our goal is to measure cross sections at the 5% level.

The asymmetry can be diluted by some unpolarized material: The target cell windows and unpolarized N_2 mixed with the ^{3}He gas. A cell called “reference cell”, nearly identical to the one containing the polarized ^{3}He, was filled with unpolarized N_2 to study this dilution. In our kinematics the structure of the hadronic spectrum (cf fig.2.4) is different for the Nitrogen and the Helium. N_2 experimental data at the same kinematics as the ^{3}He data are needed. N_2 data are missing for some kinematics because of reference cell failures. In this case a model of the nitrogen spectra was used for the correction. Empty reference cell runs were also taken to study the cell window contamination. A last correction on the asymmetries is the target polarization local losses due to beam-target interaction. This overall depolarization as a function of time is well seen by the data (see Fig. 4.15) but local depolarization on the beam path is harder to see. It depends on the depolarization rate, the convection and the diffusion inside the target. In the case of our experiment, a model shows that this effect decreases the depolarization by less than 1% [119]. As we will see in the next chapter the measured elastic asymmetries are in agreement with the world data [40]. We conclude that there is no significant effect of this local depolarization.

Target Description.

The heart of the target is the two chamber cell. The target can be polarized parallel or transverse to the beam direction thanks to two sets of laser. Three to four 30 Watt lasers pump longitudinally and three others are for transverse. The oven surrounding the upper chamber is constructed with a perfect optic window to let the laser light in. A concrete laser hut protects the laser setup from radiation. The laser beam is led to the cell trough a beam pipe. The cell is surrounded by two Helmholtz coil pairs. Their axis defines the quantization axis of the Helium-3 nucleus spins. Superposition of the two fields allows us to align the spins in any direction. Between the Helmholtz coils sit the radio frequency (RF) coils, and the pick up coils. The polarization control rack and the control computer sit in the counting house. A gas system feeds the reference cell with either Helium-3 or Nitrogen. Eleven temperature sensors (RTDs) measure the temperature of the oven, of the reference cell and of the cell chambers. The RTD hardware and control setup is described in Ref [152]. The target is enclosed in a hard plastic cylinder with aluminium windows. The lower chamber is cooled by two ^{4}He jets to avoid beam heat damage (the next section describes how the beam is rastered at 20 kHz to avoid a large heat load in a small volume). The cooling jets fill the cylinder with ^{4}He, which minimizes the energy loss of the scattered particles. The cylinder also assures the safety in case of a cell explosion. Fig. 4.16 shows the hardware setup.

Raster.

The unrastered beam radius is of the order of 50 μm. The volume dissipating the beam power is extended by rastering the beam. Another method would be to simply defocus the beam but then the beam halo would extend too far. In addition beam rastering allows a more accurate vertex reconstruction (hundredth of mm instead of a few mm). The Raster apparatus is composed by two coils for horizontal and vertical rastering. Each coil is powered by a function generator delivering a $\sim$20 kHz sinusoidal signal. The coils are 23 meters upstream from the target. During the experiment the raster had a homogeneous elliptical pattern. The phase between the two sinusoidal frequencies is $\frac{\pi}{2}$ and the amplitudes are modulated as a 49 Hz square root function of time. The square root function modulation allows a homogeneous heat load on the target. Two Pearson probes measure the coil currents. Each are read by two ADCs (LeCroy 1182 and VMIC 3123) and sent to the EPICS data stream. The acquisition is triggered by the spectrometer main triggers T1 (electron arm) or T3 ("Hadron arm"). Details on the hardware can be found in the report on the Hall A cryogenic target [38]. Details on the extraction of the beam position from the raster and BPM data can be found in [48].

Slow Control.

The target slow control was done either through EPICS (see the notes from Y. Roblin and O. Hansen [151] [83] for the laser control and the temperature readout) or through

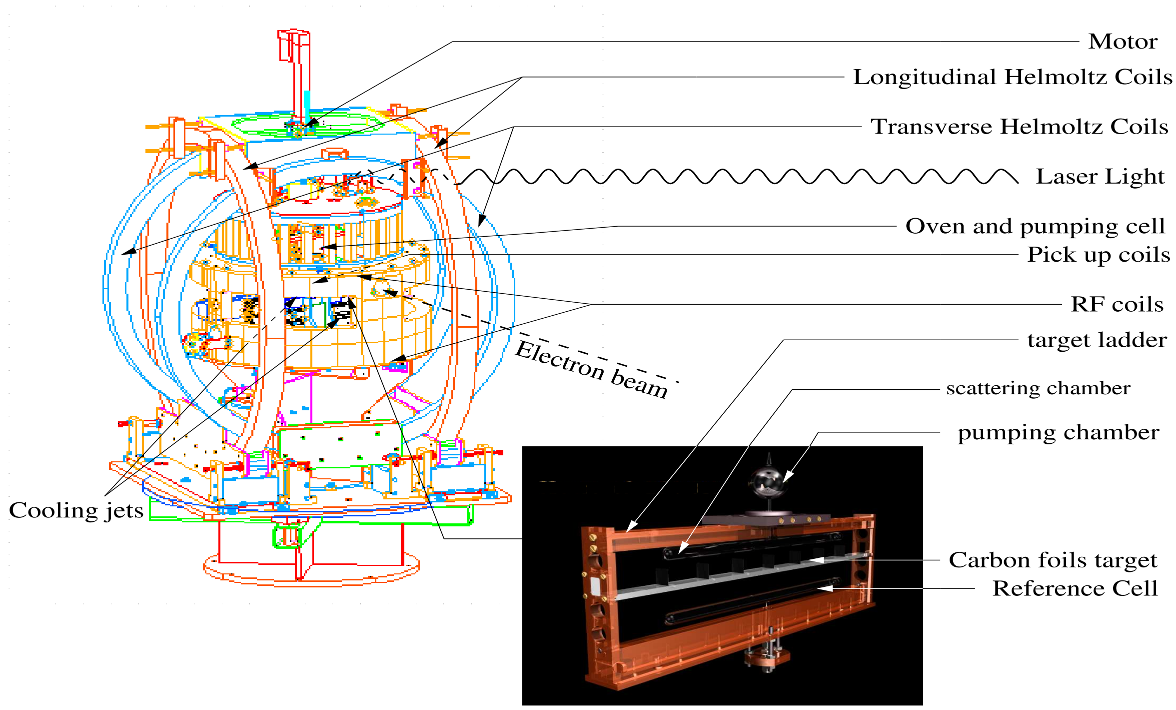

Figure 4.16: Target setup.

Labview for the polarimetry (see S. Incerti description in [88]). A target ladder holds the cell and the reference cell. During measurements, the cell or the reference cell has to be moved in the beam path. For polarimetry the scattering chamber has to be lowered between the pick up coils. This is done by a motor controlled remotely from the counting house.

4.4 Typical Data Taking.

To conclude this chapter I present typical data taking procedure.

1. Energy measurement (Arc and/or eP). Only after a beam energy change.
2. Beam Polarimetry (Møller). Only after a beam energy change or any change at the polarized source.
3. Beam Current Monitor calibration. Typically after an energy change.
4. Change spectrometer magnetic settings.
    - Check that the spectrometer dipole fields are set at the right values (at better than the 10^{-4} level).
    - Check the raster size.
    - Take data in both longitudinal and transverse configurations. Each four hours an NMR polarimetry is performed.

- At the same time:
  - The online analysis checks the data quality and the detector performances.
  - Online monitoring of the spectrometer magnets, deadtime, beam position and current are performed.

Chapter 5

Data Analysis

5.1 Introduction.

In this chapter I will describe the analysis of the data, that is what we do to transform the information from our experimental apparatus into physics quantities usable by the scientific community. First I will enumerate the steps needed to obtain a cross section. The details of these steps will be the core of the chapter. Then I will summarize the elastic cross section and asymmetry analyses, which provide an overall check of our understanding of the apparatus.

5.1.1 Cross Section and Asymmetry Extraction.

The fundamental quantity obtained in our experiment is a cross section. Experimentally it is the proportionality constant between the number of detected electrons N on one hand and the target density N_t, the number of incoming electrons Q/e (Q being the time integrated current of the beam and e the electron charge) and the spectrometer acceptance $d\Omega dE'$ in the other hand:

$$\left\langle \frac{d^3\sigma^\pm}{dE'd\Omega} \right\rangle_{bin} \equiv \frac{N^\pm(E',\varphi,\theta)}{N_t \Delta E' \Delta\Omega Q^\pm/e} \tag{5.1}$$

where the cross section is averaged on a $\Delta E'\Delta\Omega$ bin. φ and θ are the usual polar scattering angles. The $\pm$ means the incident electron helicity. The asymmetry is determined by:

$$A = \frac{N^+ - N^-}{N^+ + N^-}\frac{1}{fP_bP_t} \tag{5.2}$$

Where P_b is the beam polarization, P_t the target polarization and f the dilution due to the unpolarized material within the target (protons and nitrogen). $N^\pm$ are corrected for charge asymmetries. We see from the formula 5.1 that to obtain the cross section we must determine:

- The spectrometer optics to be able to bin in E', φ and θ (magnetic analysis).
- The spectrometer acceptance $\Delta\Omega$. This will be done by a simulation code.

- The number of scattered electrons $N^{\pm}$. It differs from the number of events detected by:

  - The correction for the detector efficiencies.

  - The subtraction of the π^- that can reach our detectors.

  - The deadtime correction due to the data acquisition system.

- The luminosity which is the product of the number of scattering centers in the target times the integrated charge. We must correct for the dilution stemming from parasitic elements in the cell.

Then to extract the physical quantities we must:

- Correct for the radiative processes. (Radiative corrections).
- Calculate the spin structure functions g_1 and g_2 and the sum rules.
- Extract the neutron information from the ^{3}He data.

The analysis is done through the Hall A analyser code ESPACE (Event Scanning Program for the hall A Collaboration Experiments, [73]). The Fig. 5.1 summarizes the cross section extraction.

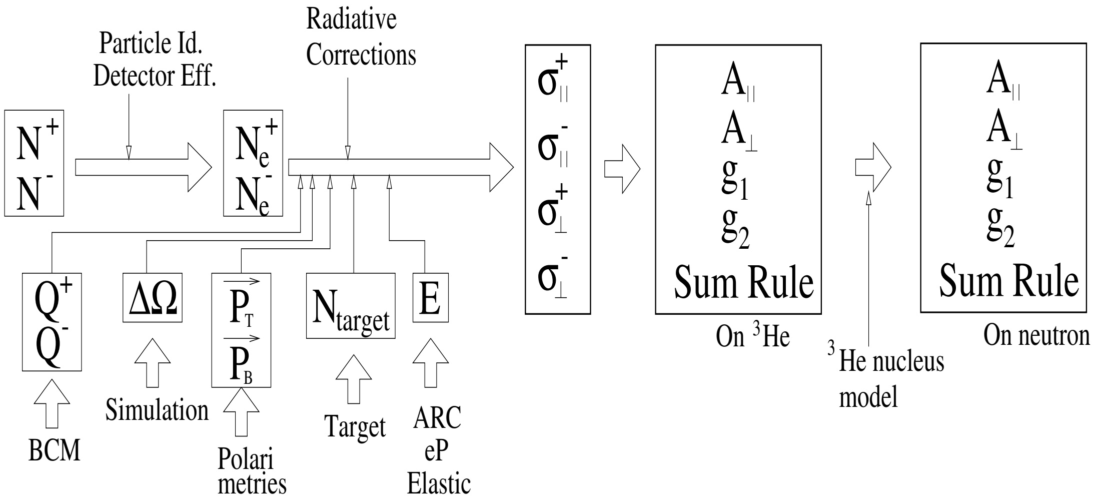

Figure 5.1: Flow digram of the cross section and physics results extraction.

Note. Although they are similar in design the two spectrometers present small differences. In addition they have slightly different central angles and pointing. Independent analyses must be done for each of them. The agreement of the results from the two arms increases our confidence in our control of the systematic errors.

5.2 Principle of the Magnetic Analysis.

In this section we describe how the information collected in the detectors is used to characterize the particle at the target interaction point.

At the target, a scattered particle is defined by six variables:

- Three spatial coordinates (vertex) x_t, y_t, z_t.
- Two angles θ_t, φ_t.
- A momentum p.

Here θ_t, φ_t are not the polar angles but the Cartesian ones in the spectrometer reconstructed coordinate system: θ_t is the scattering angle in the dispersive (i.e. vertical, see figure 4.3) plane and φ_t is the angle in the transverse (horizontal) plane. The origin of these angles is the spectrometer central axis. x_t is the coordinate in the dispersive plane and y_t is the one in the transverse plane [73].

Let us notice that during the particle transport the momentum magnitude is conserved. Once the particle has travelled in the spectrometer it crosses the drift chambers. The drift chamber information allows us to determine where the particle crosses the spectrometer focal plane and its direction. We index with $_f$ the variables in this plane: (x_f, y_f, θ_f, φ_f). Here also x_f and θ_f are the dispersive variables. The variables in the focal plane are connected by a tensor to the variables, or product of the variables, at the target. The spectrometer transport is symbolized in Fig. 5.2.

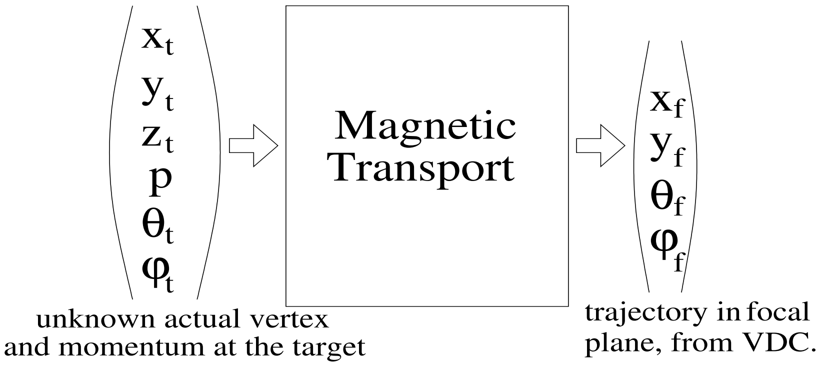

Figure 5.2: Event characterization before and after the spectrometer.

The reconstruction from the focal plane to the target is done assuming a thin target (z_t=0) and a centered beam (x_t = y_t=0). Then raster and Beam Position Monitor information allows us to complete the 6 dimensional vector (Fig. 5.3). One iteration is done to apply extended target corrections.

5.3 Spectrometer Database.

5.3.1 Optics.

The knowledge of the inverse transport of the spectrometer is critical for our experiment. We have spent part of our beam time to determine it. This section describes how we reconstruct the target quantities and how the inverse transport matrix is optimized.

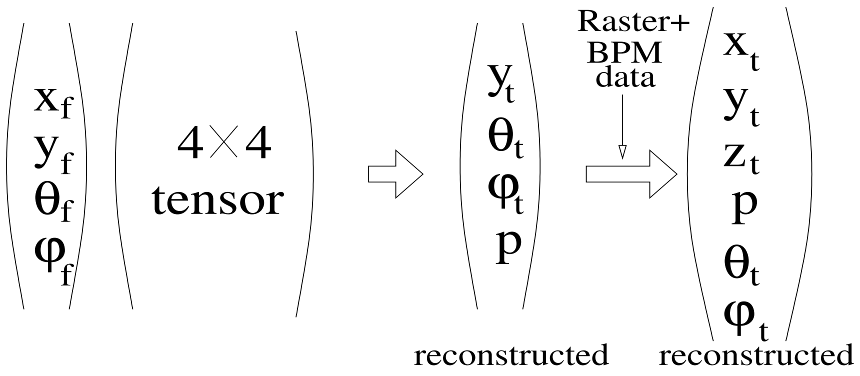

Figure 5.3: Reconstruction of the reaction informations at the target. The tensor transports the focal plane variables back to the target location

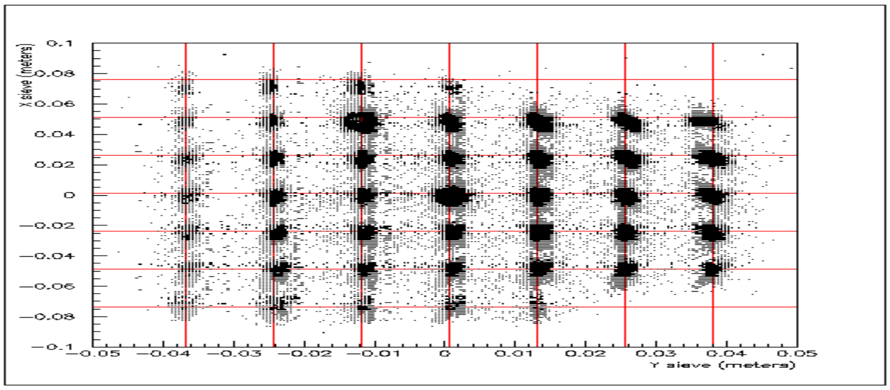

Figure 5.4: Sieve slit reconstruction.

As previously stated, the target variables are computed from the focal plane variables using a set of tensors. The tensor elements are expanded in power of x_f [73]. All the polynomial coefficients are stored in an “optics database” along with the different spectrometer and target offsets measured by the survey team. This database describes completely the spectrometer transport (up to fourth order in x_f). Knowledge of the magnetic field gives a first approximated database. It is then optimized (using the ^{12}C data with or without collimator and with or without sieve slit, see section 4.3.2) in order to reconstruct more accurately the scattering angles and the vertex position.

The reconstruction of the trajectory at the sieve slit location (angular φ_t and θ_t constraints), the knowledge of the ^{12}C foil positions and the beam position on each foil (y_t constraint) allows us to optimize the optic database by minimizing the difference between the surveyed quantities and the reconstructed quantities. Fig. 5.4 is a sieve slit reconstruction. Fig. 5.5 shows the $z_{lab} \equiv y_t/sin(\theta_{spectro})$ spectrum (i.e. the reconstruction of the foils along the beam line: $\theta_{spectro} = 15.5^o$).

The spectrometer performances with the optimized database ([131]) are:

- transverse angle determination accuracy: 0.2 mr

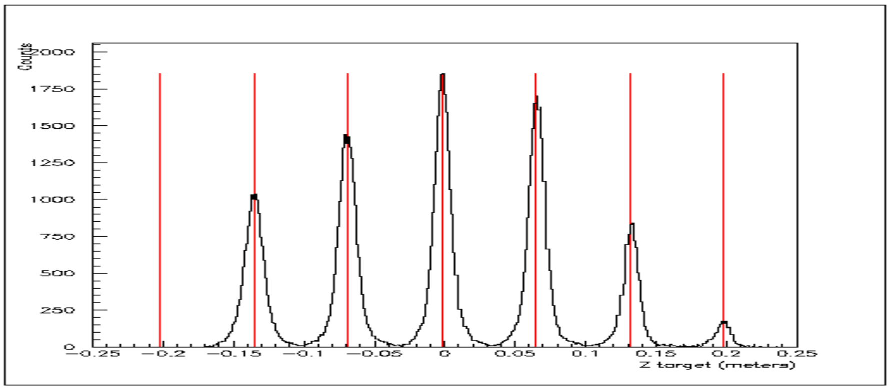

Figure 5.5: z_{lab} spectrum. Each peak corresponds to the scattering off a carbon foil. All the foils have the same density so the difference of the peak heights is due to the spectrometer acceptance. The straight lines give the expected position of each peak. The deviation of the peak center from the expected value gives the accuracy of the determination. The peak FWHM gives the resolution.

- dispersive angle determination accuracy: 0.8 mr
- transverse angular resolution (FWHM): 2.0 mr
- Dispersive angular resolution (FWHM): 6.5 mr
- momentum resolution (FWHM): 4.0^{-4}
- position determination (along z_{lab}): ± 0.5 mm
- position resolution (along z_{lab}): ± 3.7 mm

5.3.2 Acceptance.

Although the spectrometer acceptance was simulated before the experiment by J. LeRose [126] and independently by H. Fonvieille and S. Jaminion [98], no reliable acceptance model was available for our experiment. An acceptance simulation dedicated to our experiment was performed by X. Jiang [111]. The three different acceptances are detailed in section 5.3.3. We present in Fig. 5.6 an absolute comparison of the measured and the simulated acceptance. Data were taken at the elastic peak on ^{12}C for five different spectrometer central momentum settings dp/p. The experimental cross sections agree to better than 4 % [111] with the cross sections computed using the form factor fits known at 1% [32].

5.3.3 Experimental Simulation.

The study of the acceptance was done with the ^{12}C target. However the target used is thin and of well known density. An independent and complementary study was done using

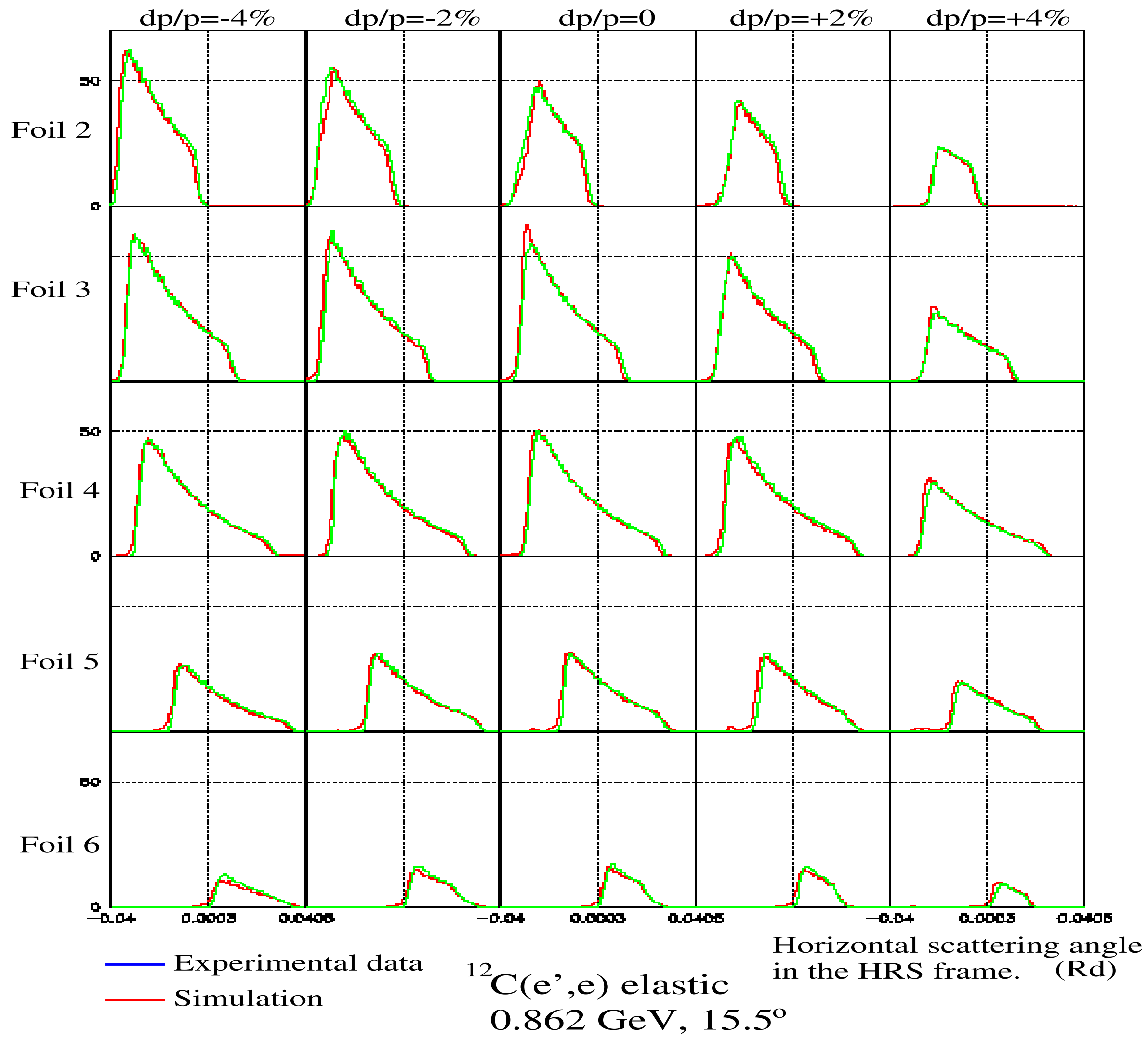

Figure 5.6: Absolute comparison of the experimental ^{12}C target and the simulated data for the seven foils ^{12}C target at different spectrometer central momentum settings dp/p.

the ^{3}He experimental data and a simulation reproducing the experimental setup. [44]. This comparison is a more global check of the experiment: In addition to the acceptance it checks the target density and purity, beam and target polarization, straggling in the target, beam position, energy offset or radiative effects, detectors or acquisition efficiency, ect. This simulation also allowed us to compare the different acceptances available, to choose the one that is best suited for our experiment and to define the analysis cuts.

Simulation Procedure.

The simulations work the following way: Ranges for the variables $(z_{lab}, x_{lab}, y_{lab}, \varphi_t, \theta_t, dp/p)$ are set in an input file. These ranges define a domain. Events are drawn in this domain with an uniform random distribution. The small spectrometer acceptance, about 30×60 mr^2, allows us to sample uniformly in the two Cartesian angles φ_t and θ_t of the spectrometer. For a meaningful estimate of the solid angle the illuminated domain must be larger than the spectrometer acceptance. The six dimensional vector $(z_{lab}, x_{lab}, y_{lab}, \varphi_t, \theta_t, dp/p)$ defines an event. Then we check if the event is within the spectrometer acceptance (the way the check is done depends on the simulation version, see next section for details). If so the event is stored in the output file. Meanwhile multiple scattering and radiative energy losses are applied each time the electron crosses some material. The cross section and asymmetry corresponding to the event kinematics are computed and stored in the output ntuple along with the other quantities characterizing the event.

Simulation versions.

Four versions of the simulation exist. The main difference is the acceptance used and how it is implemented.

- In the version 1 we use J.J. LeRose transport functions [126] based on magnetic field models. It allows to compute focal and target quantities. All these functions are fits of the results given by the ray tracing code SNAKE ([149]) that simulates a particle trajectory within the spectrometers. A function transports the particle to a critical place constraining the acceptance, typically a magnet entrance or exit, where we test if the particle passes the aperture. After having reached the aperture the event is reconstructed at the target using the inverse of the function. Then it is transported to the next critical place with a new function until reaching the focal plane. The event is then reconstructed back to the target.

- In the version 2 we use the acceptance function from H. Fonvieille and S. Jaminion [98] based on the fields mapping [149]. The acceptance function is a logical function of the vector (θ_t, φ_t, $\delta p/p$, y_t). It indicates whether or not the particle reaches the spectrometer focal plane according to the vector value. As a consequence only target variables are available but no focal plane variables. The function used here is a polynomial fit of the acceptance tested with SNAKE.

- In the version 3 we use J.J LeRose functions to provide the focal quantities and the experimental optic database optimized using the ^{12}C data to reconstruct the target quantities as ESPACE does. The advantage is that it follows the same procedure as ESPACE and includes the imperfections of the experimental database. This method works if the transport functions and the true transport of the spectrometer are similar.

- In the version 4 we use X. Jiang acceptance simulation. SNAKE was used to reproduce the focal plane experimental data taken during our optics runs. The acceptance is simulated by different virtual collimators or magnet sections cutting some of the particle trajectories (in 27 locations). A comparison of the experimental focal plane and reconstructed target quantities with the simulated data allows to adjust the collimator or section cuts until a good acceptance reproduction. The simulated reconstructed quantities spectra are stored in a ntuple and used as an acceptance weight.

Physics in the Simulation.

Physics can be added into the simulation results as a weighting factor (cross section) or an asymmetry.

Elastic cross sections and asymmetries. The ^{3}He elastic cross section and asymmetry calculations rely on a world data fit of the ^{3}He elastic form factors [7].

The way the code treats the elastic scattering is different from the other physics choices because of the correlation between the scattering angle and the outgoing electron momentum. In our case the scattering angle is drawn.

Elastic radiative corrections can be set on or off. Vertex correction, vacuum polarization, ionization, external and internal bremsstrahlung are treated

Quasi-elastic cross sections and asymmetries. The ^{3}He quasi-elastic computation is based on a PWIA model [159]. Unlike the elastic scattering, where the asymmetry and the cross section can be computed quickly, the PWIA code is rather slow. To avoid running it for each event, different sets of data covering the kinematic domain of the experiment were stored in tables available each 0.1 GeV . Each table corresponds to a particular energy from 0.700 GeV to 5.07 GeV. After one has set the incoming beam energy, the simulation picks the closest energy available in these tables. The table contains a set of energy losses covering the quasi-elastic region. The asymmetry and cross section at the energy loss drawn (say ν) are computed by interpolating linearly between the two energy loss values surrounding ν.

5.3.4 Comparison of the Different Acceptance Functions and the Experimental Data.

This section summarizes the studies done on the acceptance. Details can be found in [45]. A comparison between the different acceptance functions is presented as well as a comparison with experimental data collected at E=4.225 GeV, 15.5^o (Deep Inelastic Scattering domain). The data are taken with three overlapping momenta: $p_1 = 1.70$ GeV/c, $p_2 = 1.77$ GeV/c and $p_3 = 1.84$ GeV/c. This kinematic is chosen because the dependency of $\delta p/p$ with the virtual photon energy is small. Hence the acceptance effect is clearly visible on a $\delta p/p$ spectrum. The experimental data are corrected for trigger efficiency.

Comparison of the Target Variables.

We used three values of cuts on the target length along the beam line: 1 cm, 15 cm and 40 cm. Let us note that the cuts are applied on a reconstructed variable obtained from the data and inverse transport matrix. The uncertainty on this length is ± 3.7 mm. All the simulation versions gives reasonable results except the version 3 which fails to give a good y_t and φ_t spectrum. We will see why in the following discussion.

- **1 cm and 15 cm targets**: Results for 1cm are not shown here (see [45]). All the versions and data agree well for 1 cm and 15 cm targets (except version 3). However φ_t is overestimated for values larger than 10 mr for both versions 1 and 2.
- **40 cm target**: The version 2 is not reproducing the relative momentum dp/p for the 40 cm target. version 1 and 2 are still overestimating φ_t for value higher than 10 mr. As a consequence y_t data are not fitted well for negative values. The version 4 is matching well the data.

Overlapping Momenta.

The three spectrometer momentum settings were chosen close enough to have large overlaps. After acceptance correction the yield of each setting must overlap the next momentum setting if the functions simulate the acceptance well. We deduce from the study that the spectra overlap over the range -3.5%$<\delta p/p<$2.7%. This range defines our momentum cut used in the analysis.

Discussion

General Conclusions

- It appears that the simulation 3 using J. LeRose transport functions and the optic database fails for y_t and φ_t. The problem comes from the fact that the simulated transport functions (let us call them JJL and JJL^{-1} the inverse functions) are not reproducing the true spectrometer transport function (let us call it HRS and let us call DB the database). With a good database we have HRS.DB$\simeq$1. Also we must have JJL.JJL^{-1}=1. But the study shows that we do not have JJL.DB $\simeq$ 1.
- X. Jiang's acceptance function is the best suited for our data.
- None of the acceptances give a good simulation at large φ_t.

φ_t and y_t Acceptance. The analysis done on the ^{3}He elastic data shows that the discrepancy on the left side of y_t acceptance for a 40 cm target is due to a bad φ_t simulation. A cut on the positive values of φ_t (φ_t<10 mr) makes the simulated y_t shape to fit better the experimental data. This was studied with J. LeRose's acceptance simulation.

Summary: The comparison between the different simulations showed the necessity for our experiment to use the acceptance from X. Jiang. However there is still a discrepancy in φ_t that induces a discrepancy in y_t. The study determines the $\delta p/p$ cut. This analysis, completed by the elastic data study, determines the cuts on the other variables, see section 5.8.

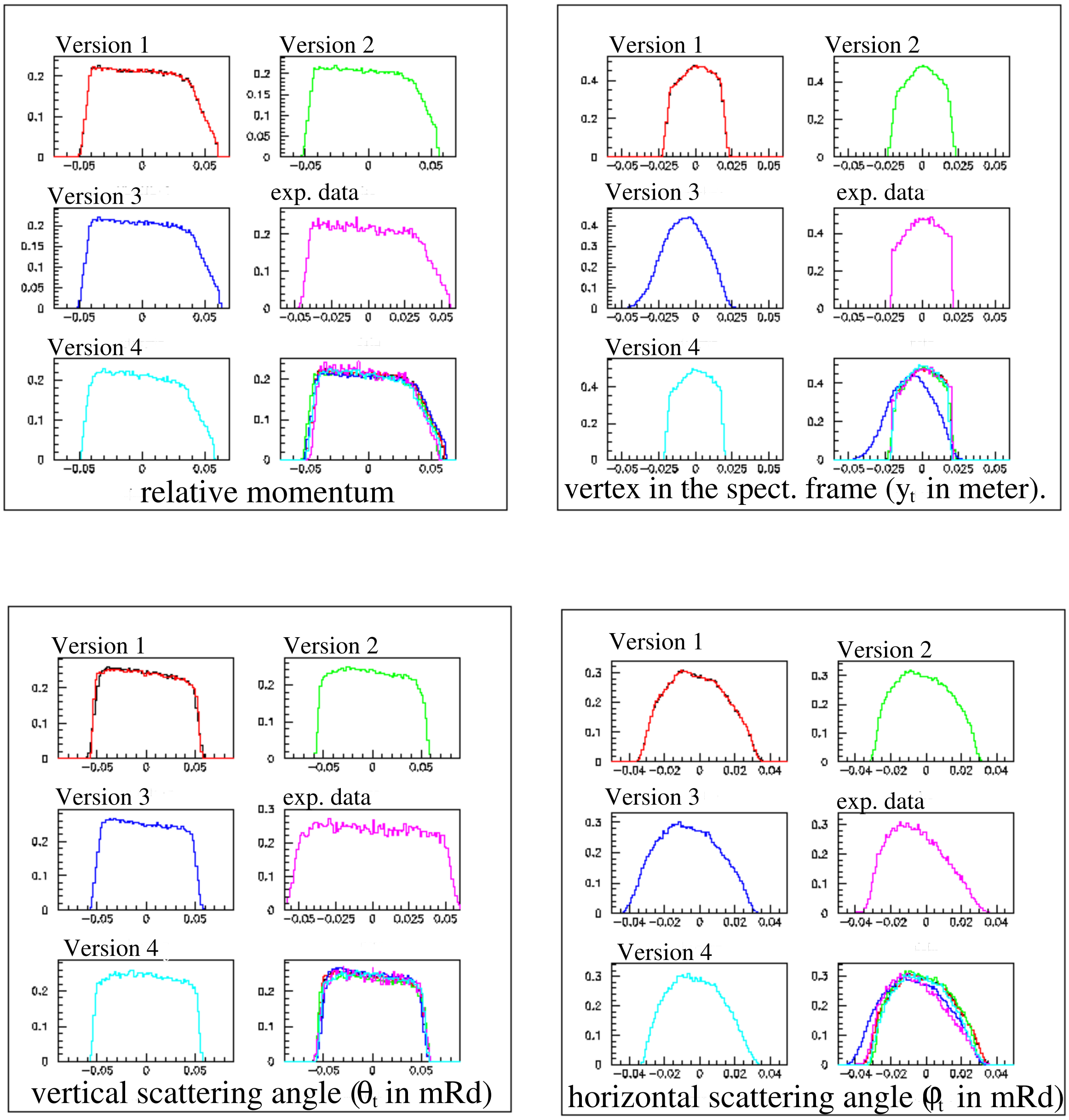

15 cm target

Figure 5.7: Comparison of the different simulations with the data for a 15 cm target. The sixth plot is the superposition of the five first ones. We see that the version 3 fails for the non-dispersive variables (φ_t and y_t). The asymmetrical shapes in φ_t and y_t are due to the Mott cross section dependency. The comparison between simulations is absolute while the simulations comparison with the data is relative.

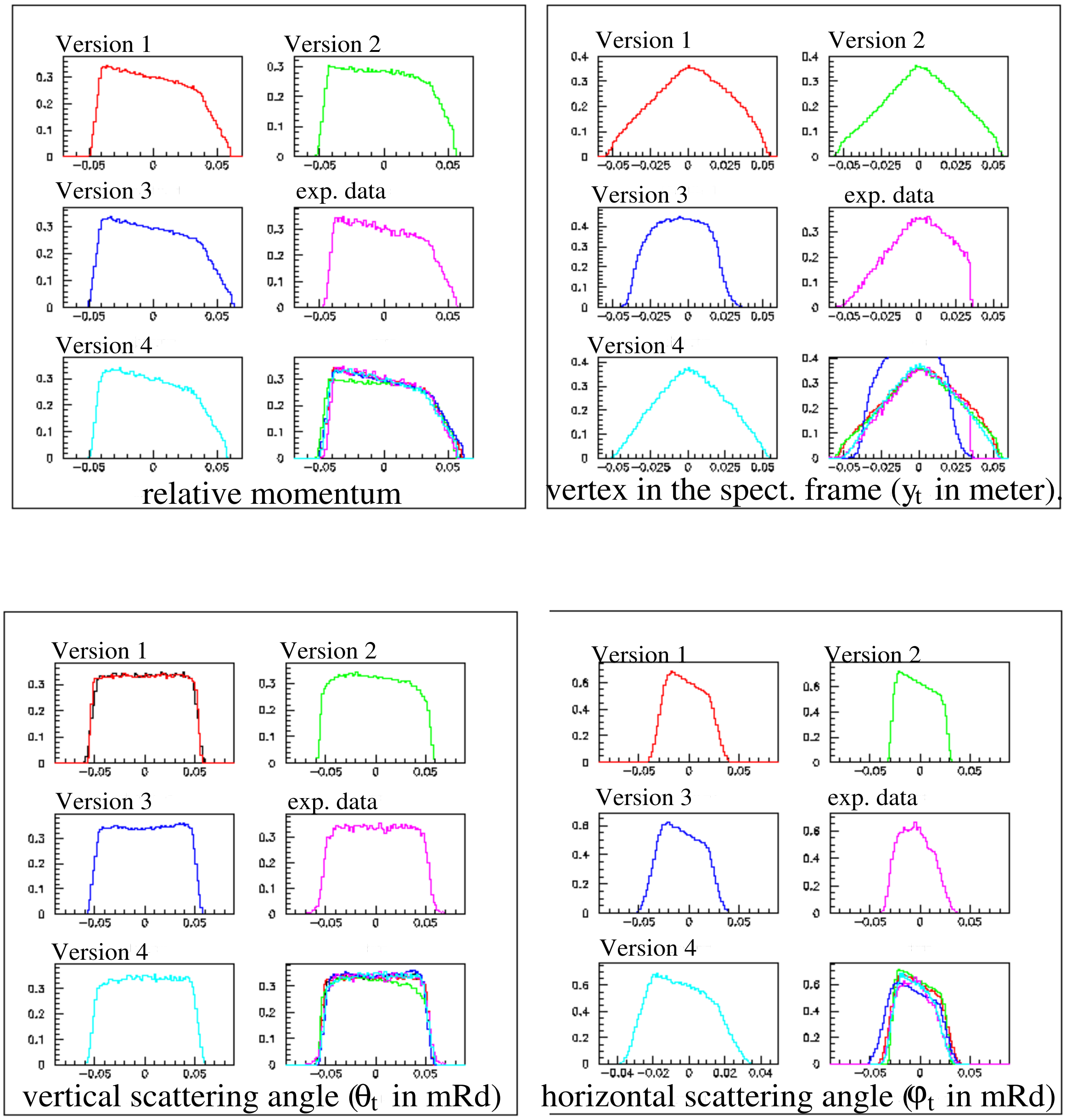

40 cm target

Figure 5.8: Same as fig. 5.7 with a 40 cm target.

5.4 Detector Analysis.

We summarize here the detector analysis focusing on the efficiency determinations.

5.4.1 Trigger inefficiency

During the experimental run the vacuum in the scintillator phototubes was compromised because of the presence of ^{4}He presents in the Hall. This deteriorated the phototube performance. Consequently, the global trigger inefficiency reached values as high as about 10 %. It is a significant correction to the cross sections (It is small to negligible for the averaged asymmetry. We explain here how the trigger inefficiency can affect the averaged asymmetry: If the inefficiency vary significantly in the focal plane, then it is correlated with the kinematics. Since the asymmetries varies within the spectrometer acceptance the trigger inefficiency must be corrected even if the inefficiency is helicity independent. However the elastic asymmetry analysis shows that the trigger inefficiency correction is not important).

The time evolution of the trigger inefficiency makes it necessary for us to correct them run by run. We apply particle identification criteria on the shower and the Čerenkov to select electrons because the inefficiency is related to the nature of the particles. The correction is done using the secondary trigger (T2 or T4, call it T_{second}). Let us remember that, after having required an electron identification, only events with one scintillator signal S1 and S2 go in the secondary trigger. The main trigger (call it T_{main}) is T_{second} exclusive. The trigger efficiency can be written as:

$$E_{trigger}(y_f) = \frac{ps_{main}T_{main}}{ps_{main}T_{main} + ps_{second}T_{second}}$$

where ps_{main} and ps_{second} are the prescaler factors of the main and second triggers. The correction is performed for each paddle pair that is consistent with a possible track. The y_f (i.e horizontal) dependence of the inefficiency is taken into account. Typically, the overall trigger inefficiency was 5 %.

5.4.2 Shower Detector.

The calibration of the electronics associated to the shower detectors was studied by I. Kominis [120] and K. Slifer [163]. The calibration is done such that each blocks' phototube is gain-matched to the other and the total energy deposited in the preshower and shower is proportional to the electron momentum (for the electron arm total shower). The electron-pion separation efficiency is studied run by run. Assuming the Čerenkov efficiency to be 100 % we can estimate the pion contamination since the two detectors are independent. The pion peak has a tail going below the electron peak (see left plots of fig.5.9) so a simple cut on the shower spectrum is not enough to separate the pions from the electrons. A two dimensional preshower-shower spectrum, see fig. 5.9, allows a better separation. The cuts are chosen to provide the best compromise between the pion rejection and the electron identification. We have a rejection factor of about 1/3000 and an electron detection efficiency better than 98%. The table below gives the shower cuts and efficiency for E=5.06 GeV. E'_0 is the spectrometer central momentum setting. For the other energies, see [120].

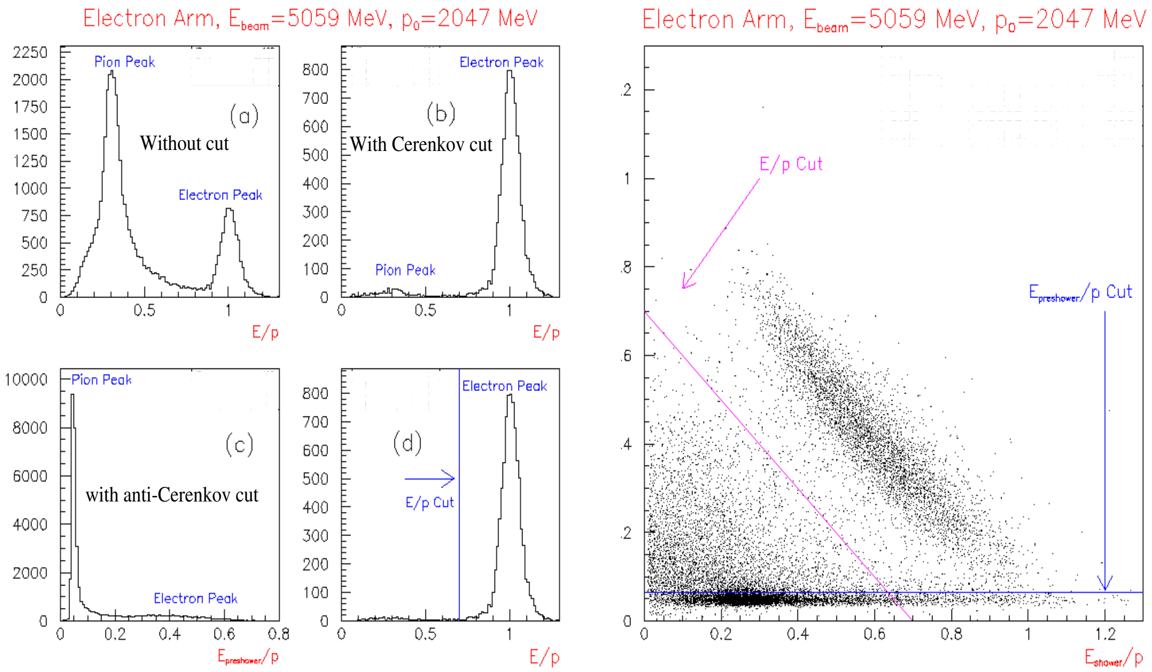

Figure 5.9: On the left figure is shown the pion peak for one of the worst contamination cases. We see the effect of a Čerenkov, anti Čerenkov and Čerenkov-shower cut. In the right figure is shown the cut applied on a preshower-shower plot. The vertical axis is the preshower channels while the horizontal is the shower channels. The events are distributed along a strait line since it is a total shower: $E_{loss_{prsh}} + E_{loss_{sh}} = E'$. The line is wide because of the detector resolutions and spectrometer momentum acceptance.

Electron arm

E'$_0$ (GeV)	π/e ratio	E$_{psh}$/E' cut	E/E' cut	Tot Eff.	Tot rej.	π contam. %
3.086	0.31	0.06	0.82	0.988	652.8	0.047
2.846	0.58	0.07	0.81	0.990	1036.0	0.056
2.625	1.02	0.06	0.81	0.987	1443.0	0.071
2.423	1.65	0.09	0.81	0.988	1976.0	0.083
2.233	2.68	0.09	0.81	0.992	2644.0	0.101
2.059	3.87	0.06	0.80	0.986	2327.0	0.166

"Hadron" arm

E'$_0$ (GeV)	π/e ratio	Čerenkov rejection	π dilution. %
3.086	0.33	93.3	0.35
2.846	0.59	91.1	0.65
2.625	1.05	170.1	0.62
2.423	1.67	147.4	1.13
2.233	2.67	134.6	1.98
2.059	4.07	170.7	2.39

Note: "Hadron" arm shower efficiency. The "hadron" arm shower acceptance is smaller than the spectrometer acceptance. In addition a gap between the two rows of blocks creates an inefficiency area (see fig. 4.10). Typically a few percent of good events do not develop a shower. The analysis takes care of this assuming the pion-electron ratio for the events coming in the gap or outside the shower acceptance is the same as for the events developing the shower.

5.4.3 Čerenkov.

Let us remember that the cerenkov signal is the sum of the ten mirrors' phototube signals. They are gain-matched by software by alignment of the one photo-electron peak. The Čerenkov efficiency is estimated using the shower (and preshower for hadron arm) and is found to be better than 99%. This analysis was carried out by K. Slifer [162]. A sample of results for the six energies is given below.

E (GeV)	E'$_0$ (GeV)	Eff. e-arm (%)	Cut eff. e-arm (%)	Eff. h-arm (%)	Cut eff. h-arm (%)
0.862	0.461	99.8559	99.9241	99.4576	99.8465
1.718	1.167	99.9272	99.8715	99.4137	99.7754
2.581	1.346	99.9244	99.7218	99.0632	99.5817
3.382	2.030	99.9466	99.7413	99.2908	99.6265
4.239	2.433	99.9428	99.7065	99.2553	99.5784
5.059	3.086	99.9579	99.7869	——	——

5.4.4 Vertical Drift Chambers (VDC).

The VDC analysis is detailed in [46]. We summarize the results here.

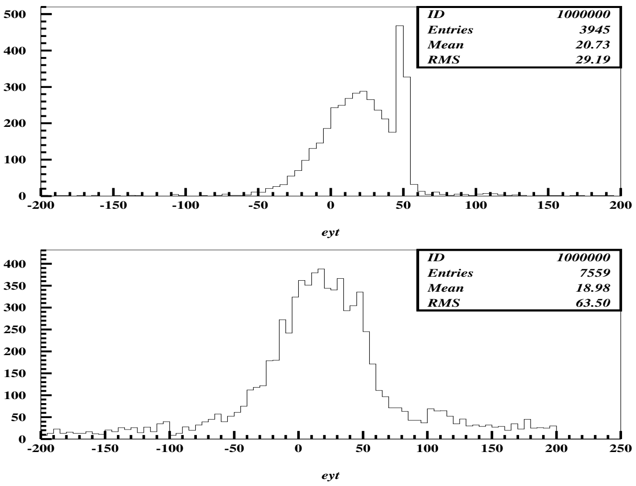

Figure 5.10: Comparison of the vertex reconstruction for one track events (top) and two tracks events. The loss of resolution is clear. The peak on the top plot corresponds to a target end cap. It is smeared out in the bottom plot due to the worsened resolution.

Vertical Drift Chambers Inefficiency.

We call "hardware inefficiency" the absence of response from wires. It was checked online during the experiment. Three contiguous firing wires are required to define a cluster. Five wires are supposed to fire for a 45^o track (see fig.4.7). Since the efficiency of a wire is above 90 % the hardware inefficiency is negligible.

The track reconstruction algorithm that chooses the right track in the case an event with two or more possible tracks is not perfect and can bias the cross section or asymmetry measurements (see fig.5.10). We chose to keep only the one track events, the two track events being taken as a software VDC inefficiency. This should not introduce any error if the two tracks events have the same distributions (the actual distributions, not the ones reconstructed by ESPACE) as the one track events. The software inefficiency, that is the removal of good multitrack events, is of the order of a percent.

Zero Track Events.

The first VDC analysis pass yields a large ratio of zero track events (above 10%) with half of them identified as electron events. This was due to a bad time fiducial T_0 (see [46]). After the detector database optimization the number of zero track events is about 5%. After a Čerenkov cut and a shower cut these 5% go down to less than 0.1%.

"Low Energy Events".

Some events deposit more energy in the shower than a pion but less than an electron (hence I name them "Low Energy Events"). The amount "Low Energy Events" is relatively more important for the zero, two and three tracks events than for the one track events. These events fire the cerenkov. They are interpreted as electrons at the edge of the acceptance: They lose energy by scattering inside the spectrometer and can miss the VDC because of their unusual trajectories. This contamination, which can reach 20%, depends on the

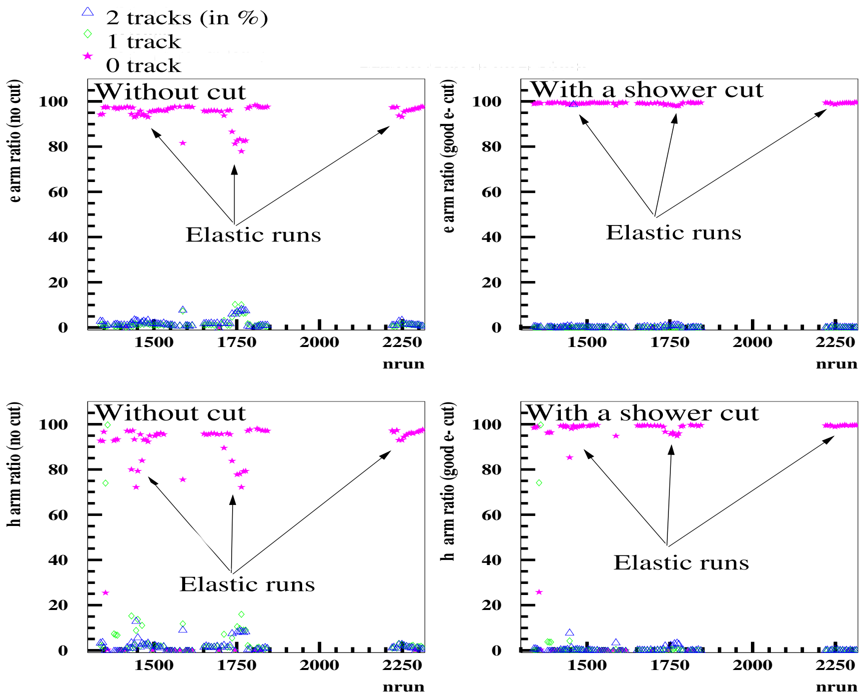

Figure 5.11: Percentage of 0,1 and 2 track events versus the run number for the 1.72 GeV data. The plots on the left are before the shower cuts and the plots on the right are after the shower cuts (the φ_t and y_t cuts are not applied yet).

kinematics and is especially large for the 1.72 GeV elastic kinematics. The number of events according to the number of possible tracks for 1.72 GeV is shown on Fig. 5.11. Although this contamination is large, it is efficiently cut away by shower-preshower, φ_t and y_t cuts (since the particles have unusual trajectories).

Procedure to Estimate the VDC Efficiency.

The VDC efficiency is estimated by taking the ratio of one track events to the total number of events. The events must pass shower and preshower two dimensional cut to remove the "Low Energy Event" contamination. In the case of the "hadron" arm where no preshower is available we do a cut at high shower channel since the number of "low energy events" drops with the shower channel. No cuts on target reconstructed quantities should be applied since it may remove good 2 track events with wrong reconstruction and thus overestimate the VDC efficiency.

5.5 Luminosity and Charge Asymmetry.

5.5.1 Charge.

The charge calibration was provided by A. Saha [155]. The Beam Current Monitor output loses its linearity at low current (a few μA). Hence the charge calibration "constant" depends on the beam current used in each run. The charge integrated over a run period is given by the scaler time the calibration constant. **It is accurate to better than 1%.**

5.5.2 Charge Asymmetry.

As mentioned, independent scalers record each beam helicity. They allow us to compute and correct the false asymmetry arising from the fact that the beam pulses of helicity plus may contain a different number of electrons than beam pulses of helicity minus. The expression of the corrected asymmetry is:

$$A = \frac{N^+/Q^+ - N^-/Q^-}{N^+/Q^+ + N^-/Q^-}$$

where N^i is the number of count of helicity i and Q^i is the integrated charge of helicity i. In this case the calibration used for Q^+ and Q^- is the same. Hence the systematic 1% errors cancel.

Runs using unpolarized N_2 reference cells and the ^{12}C target are analysed to check whether we control the false asymmetries. If we neglect the weak interaction which gives an asymmetry of the order of one ppm, the asymmetry must be zero. Both N_2 and ^{12}C runs give an asymmetry compatible with zero after charge and deadtime corrections [47]. The asymmetries computed with the scalers (scaler) and the number of triggers (coda) are given below. The error quoted is the statistical error.

Nitrogen runs average asymmetry:

"Hadron" arm coda	4.19349E-03 ± 1.75600E-02 %
Hadron" arm scaler	-6.80454E-03 ± 1.05050E-02 %
electron arm coda	8.94332E-04 ± 1.64959E-02 %
electron arm scaler	1.10352E-03 ± 1.02050E-02 %
charge asymmetry	0.243738 %

Carbon runs average asymmetry:

"Hadron" arm coda	1.25112E-02 ± 1.60046E-02 %
"Hadron" arm scaler	1.21744E-02 ± 8.76910E-03 %
"Hadron" arm charge asymmetry	3.15154E-02 %
electron arm coda	-1.35775E-02 ± 1.84897E-02 %
electron arm scaler	2.08384E-03 ± 1.25235E-02 %
electron arm charge asymmetry	5.71982E-02 %

5.5.3 Target Density.

Target density is known from the cell construction (see page 63). However the density depends on the temperatures of both the scattering and the pumping chambers. The pumping cell temperature is known with an accuracy of $\pm 30^o$ because the laser heat load is difficult to evaluate and because the temperature sensors (RTD) measure the outside temperature of the glass, not the inside temperature. In addition the beam heats the target locally, which decreases the density. "Pressure curve runs" using the ^3He reference cell check the density in the running conditions: The pressure on the ^3He reference cell is read on a pressure gauge. The counting rate normalized to the charge (yield) is proportional to this pressure. The slope of the pressure curve gives the proportionality constant. We deduce then the density of the ^3He target cell from its yield.

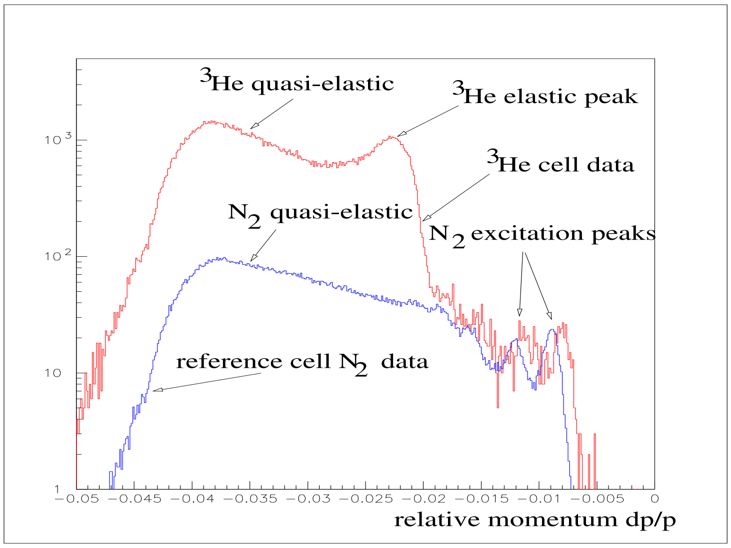

Figure 5.12: The N_2 content of a ^{3}He cell (for target B, data taken at 1.72 GeV). The N_2 excitation peaks of the reference cell data are shifted because the reference cell wall is thicker and more energy loss by ionization occurs. No radiative corrections are done in this plot.

This analysis was carried out by I. Kominis [121]. Radiative corrections have to be applied because the wall thickness of the reference cell and the ^{3}He cell are different. Hence the radiative effects for both cells do not compensate each other.

The densities deduced from this study are (within 4%) in agreement with the numbers given on p. 64 (after the temperature correction).

5.5.4 Contamination and Dilution.

As mentioned, approximately 1% of N_2 is mixed with the ^{3}He as a quencher. This unpolarized matter dilutes the asymmetry and increases the counting rate.

Nitrogen Contamination Part of our data are in the quasi-elastic and resonance regions where the N_2 and ^{3}He cross sections vary differently with the energy loss. Consequently we need experimental data to subtract the N_2 background. The matching to the N_2 elastic peaks from the ^{3}He cell and N_2 reference cell allows us to normalize the N_2 experimental data and to subtract them from the ^{3}He (see fig. 5.12). For the same reasons stated in section 5.5.3, radiative corrections have to be carried out. We did not estimate the uncertainty on this correction because the correction itself is small.

Glass Contamination. One of the target end caps is within the spectrometer acceptance (see for ex. Fig. 5.10). As for N_2, the unpolarized glass contamination has to be removed. This is done by software cut on y_t.

5.6 Data Acquisition Deadtime.

5.6.1 Correction to the Cross Section.

Data acquisition deadtime is an important correction to the cross section: It can make a 30% correction with our acquisition rate of 2 to 6 kHz (depending of whether we use one or two independent data acquisition systems). Since the scalers are not deadtime sensitive we use them to correct the number of counts:

$$N_{count_{cor}} = \frac{N_{count_{cut}}}{N_{count_{nocut}}} N_{scaler} \tag{5.3}$$

where N_{count} is the number of main triggers with or without the software cuts and N_{scaler} is the number of count of the scaler corresponding to the trigger. **The deadtime correction does not create sizeable systematic or statistic errors on the cross section.**

5.6.2 Correction to the Asymmetry.

If the asymmetry is different from zero then the rate is helicity dependent. Hence the deadtime is also helicity dependent. We have demonstrated [40] that in addition to this effect:

- Deadtime fluctuations, which can cause the deadtime to approach 80 %, affect the measured asymmetry. The induced false asymmetries can reach 4 % (absolute).
- We can correct for this effect by applying the formula 5.3.
- The correction is under control: We checked with unpolarized target data that the distribution of the asymmetry affected by the deadtime fluctuations and corrected with the formula 5.3 is a Gaussian centered on zero. The Gaussian width is the same as for uncorrected asymmetries not affected by the deadtime fluctuation. This means that the deadtime fluctuation problem and its correction add no significant systematic error to the asymmetry uncertainty.

In addition the data compression is not helicity dependent, increasing the event size for one helicity. This induces an helicity correlated deadtime. It creates a false asymmetry that can reach up to 0.7% (relative) [136].

5.7 Radiative Corrections.

Radiation arises as soon as the electron interacts with the scattering center or with the matter surrounding it. A consequence is that, for a given (E, E') bin, the events from reactions at lower incident energies or higher scattered particle energies can both go into that bin. The cross section and asymmetry must be corrected for this effect. In addition, some events leave the bin because of the energy radiation. Here too the cross sections must be corrected for the loss. If the photon radiation is helicity dependent, the asymmetries have to be corrected as well. This is the case for the inelastic data. In the elastic case the radiative corrections are almost helicity independent: The correction to the asymmetry is below 0.1 % (relative) [128]. The radiation affects the elastic asymmetry averaged over the spectrometer acceptance by changing the kinematics of the events that have radiated. This effect is negligible too: The correction to the asymmetry is below 0.3 % (relative) [40]). For the inelastic data we use our lowest 0.862 GeV data as a starting point of an iterative radiative correction procedure (unfolding). In the elastic case we fold the radiative effects in our simulation and compare it to the experimental data uncorrected for the radiations.

5.8 Analysis of the Elastic Data.

The results on the elastic asymmetry and cross sections are presented here. Details of the analysis can be found in [40] and [50].

5.8.1 Elastic Asymmetries.

Finite Acceptance Effect.

The cross section and asymmetry vary within the spectrometer finite acceptance. These variations decrease the elastic asymmetry by 12% relative to the asymmetry we would measure with a pointlike acceptance spectrometer.

Quasi-elastic threshold and Nitrogen Correction.

Invariant mass spectra (W) for E=0.862 GeV and E=1.72 GeV are shown in fig. 5.13. The closeness of the elastic threshold (about 5 MeV) forces us to have a tight W cut. This prohibits us from using the standard (*à la Mo and Tsai*) radiative correction method [139] to the elastic peak. It is one of the reasons why we study the elastic reaction through a complete simulation, including the radiative processes, of the experiment. The dilution from the 1% nitrogen depends on the W cut chosen. With the cut $-1 < W - M_{He3} < 4\,MeV$ used in this analysis, we have 0.7 % dilution for the 0.862 GeV elastic and 8.5 % for the 1.72 GeV elastic.

Systematic Error Estimate.

We list the systematic errors on the asymmetry. They are in percent and relative:

- Error on the target polarimetry: $\pm$**4%**. [99]
- Error on the beam polarimetry: $\pm$**3%**. [35]
- The error on the asymmetry due to a $\pm$2 MeV uncertainty on the beam energy is at worst $\pm$ **0.6**%.
- The Nitrogen contamination is 0.7% for the 0.862 GeV elastic data (It is modelled because of our lack of nitrogen data at this energy. The contamination is mainly due to the radiative tail of the nitrogen elastic peak). The uncertainty on the asymmetry is less than **0.3**%; The contamination for the 1.72 GeV elastic data is 8.5 %. Since we used our experimental nitrogen data to compute it, we expect an uncertainty below **0.5**%.

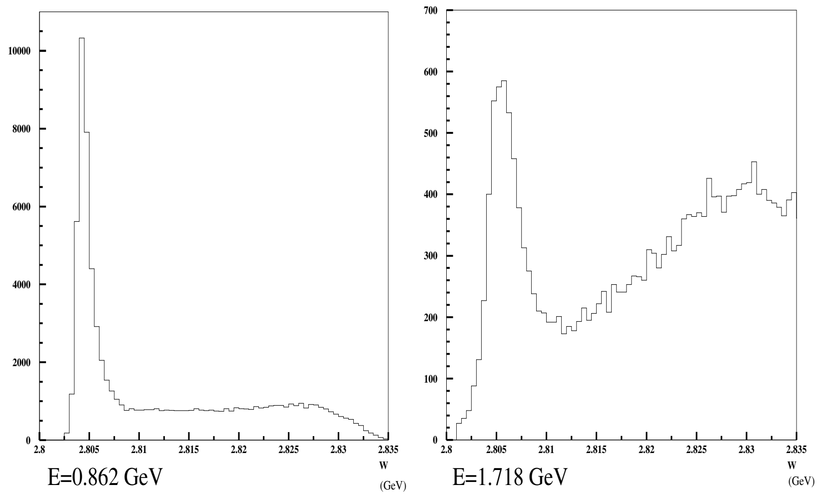

Figure 5.13: W spectrum for E=0.862 GeV and E=1.72

- The errors on the deadtime correction and detector efficiency are neglected according to the conclusion of the study presented in section 5.6.
- We take 0.3% as an upper value of the uncertainty due to the acceptance (it is the difference between the asymmetry computed with the version 3 of the simulation, well suited for our experiment, and version 1. See section 5.3.3).
- The effect of the radiative corrections on the elastic asymmetry is typically 0.3% (relative). The uncertainty on this number is at the percent level. Hence the uncertainty due to the radiative corrections is of the order of a few tenths of ppm.
- The error from the elastic form factor fit is **±2%**. [7]. In our case the scattering is essentially from the charge form factor. The uncertainty propagates to the asymmetry to be 4%.
- The error on the asymmetry due to a ±0.7 mr uncertainty [133] on the spectrometer angle is at worst **±1%**.
- The error on the asymmetry due to a $\pm 0.5^o$ uncertainty on the target spin angle [91] is **±0.3%** for the longitudinal asymmetry and **±2.8%** for the transverse one for the 0.862 GeV data. It is **±0.5%** for the longitudinal asymmetry at 1.718 GeV.

The uncertainties are added in quadrature because they are numerous and assumed to be independent. We have a systematic error of **6.5%** for the longitudinal asymmetry and **7%** for the transverse asymmetry. The experimental and simulated data are consistent showing that part of the systematic errors compensate each other. This measurement of the systematics justifies *a posteriori* the addition in quadrature.

Results.

The corrected experimental and expected raw asymmetries are compared in Fig 5.14, 5.15 and 5.16 for respectively 1.72 GeV first period, 1.72 GeV second period and 0.862 GeV.

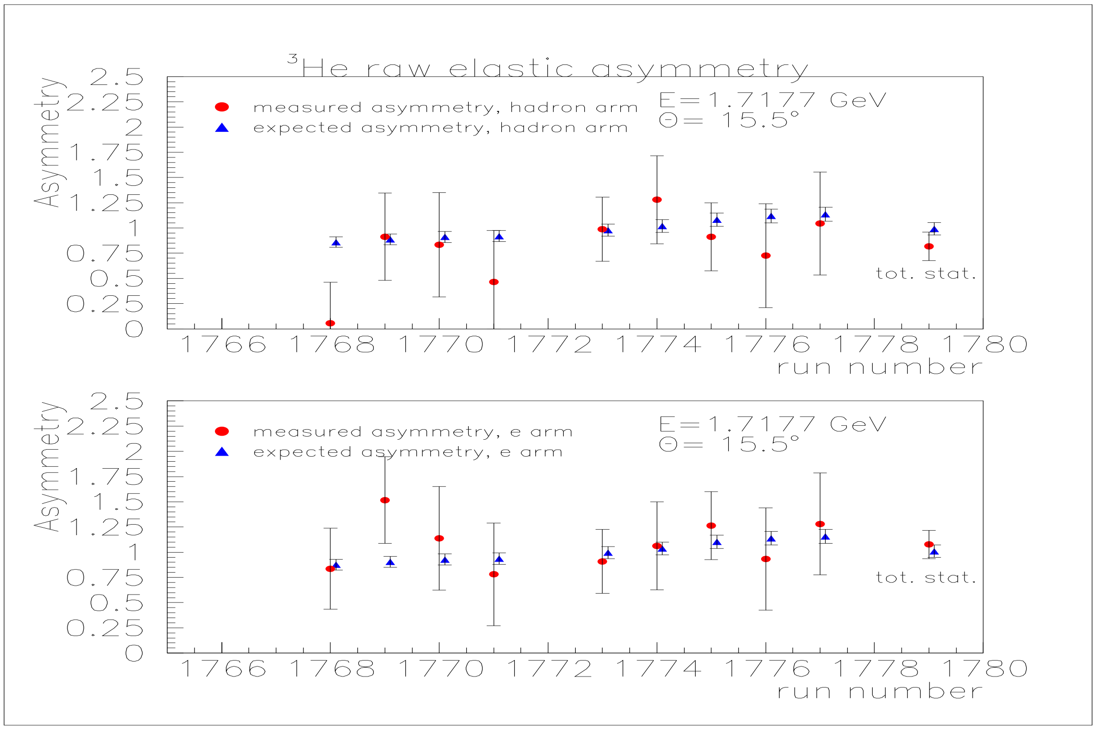

Figure 5.14: Experimental and expected raw asymmetries for 1.72 GeV first period. The last points are all the runs summed together.

The fact that the target and the beam are not fully polarized dilutes the expected asymmetry according to:

$A_{expected} = A_{theo}.P_{beam}.P_{target}.f$

A_{theo} is the asymmetry computed according to the world data with the spectrometer acceptance effect (and other minor corrections) folded in. f is the dilution from the unpolarized material. The value of P_{beam}, from the Møller polarimeter measurements, is given on page 46. P_{target} is computed using the averaged water+EPR calibration, see fig. 4.15. The error bars on the experimental asymmetries are statistical (the systematics are negligible). The error bars on the expected asymmetries are systematic. The last points on the plots are all the runs added together for the different data taking. We summarize the results in the following tables. The first table gives the results for the "hadron" arm and the second table gives the electron arm results:

Energy	$A^{exp}{}_{\parallel}$ (%)	$A^{simu}{}_{\parallel}$ (%)	$A_{\perp}{}^{exp}$ (%)	$A_{\perp}{}^{simu}$ (%)
1.72 (period 1)	0.82±0.14	1.01±0.07	-	-
1.72 (period 2)	1.80±0.22	1.69±0.11	-	-
1.72 (1+2)	1.10±0.12	1.22±0.08	-	-
0.86	0.72±0.03	0.78±0.05	-0.20±0.05	-0.25±0.02

Energy	$A^{exp}{}_{\parallel}$ (%)	$A^{simu}{}_{\parallel}$ (%)
1.72 (period 1)	1.08±0.14	1.02±0.07
1.72 (period 2)	1.51±0.23	1.73±0.11
1.72 (1+2)	1.19±0.12	1.24±0.08

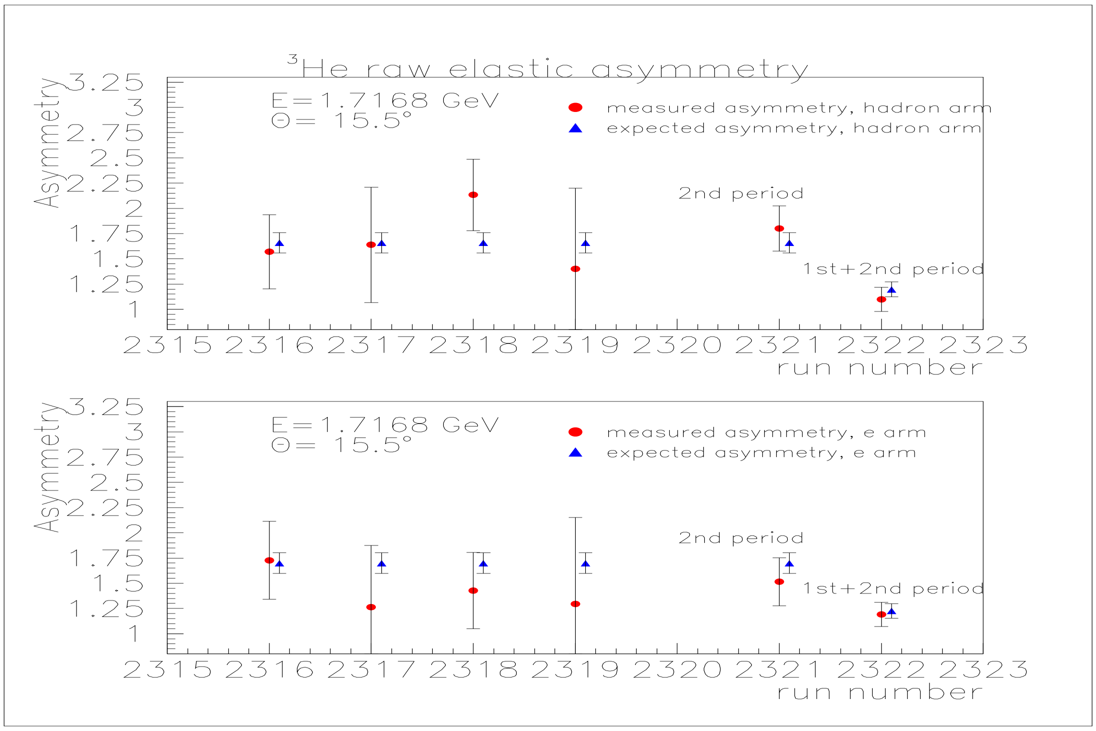

Figure 5.15: Experimental and expected raw asymmetries for 1.72 GeV second period. The last points contains the full first and second period statistics. For the second period of data taking the beam and target polarizations are higher. This explains why the raw asymmetry is larger.

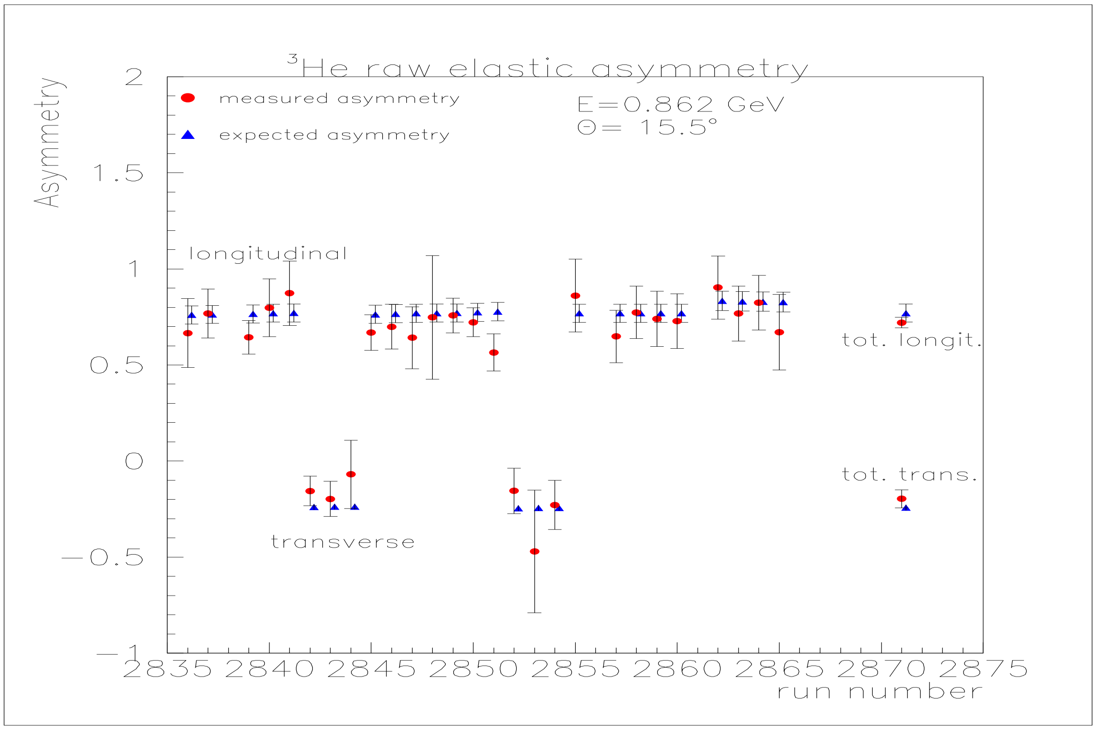

Figure 5.16: Experimental and expected raw asymmetries for 0.862 GeV.

Conclusion.

There is agreement between the experimental and simulated data within the systematic errors added in quadrature. The level of agreement is an estimate of our systematic uncertainty for the whole experiment. However the special features of the elastic reaction (scattering angle correlated with the momentum, quick variations of the asymmetry within the spectrometer acceptance, high counting rate,...) make us believe that this estimate gives an upper bound for the systematic uncertainty on our inelastic data.

5.8.2 Elastic Cross Sections.

The elastic cross sections are computed using eq. 5.1 with the proper detector efficiencies, luminosity and deadtime corrections. The acceptance and radiation effects are folded in the simulated results. I give here only the uncertainty estimate and the final results.

Uncertainty Estimate

Uncertainty on data

- Beam current uncertainty is $\pm$**1%**.
- Statistical uncertainty is negligible.
- Trigger inefficiency can reach 20% at worst for some paddle combinations for 0.86 GeV. The uncertainty on this number is about 0.5 % for a typical 5 million events run. Therefore the uncertainty on the cross section is below 1%.
- Target density uncertainty, including the temperature uncertainty, is $\pm$**3.4 %** (target E used for the 0.86 GeV data) and $\pm$**3.2 %** (target B used for the 1.72 GeV data) [119].
- Target length uncertainty: $\pm$3.7 mm [131], i.e. $\pm$**1.4%** uncertainty with our chosen target length cut.
- N_2 contamination uncertainty was taken to be $\pm$**1%** for 0.86 GeV data and $\pm$**2%** for 1.72 GeV data.
- The uncertainty on the deadtime is neglected.
- The error on the energy is taken as $\pm$2 MeV. This yields a $\pm$**2.2 %** error on the cross sections for the 0.86 GeV data and a $\pm$**2.6 %** error for the 1.72 GeV data.
- The spectrometer angle accuracy is taken as $\pm$ 0.7 mr. This yields a $\pm$**1.8%** error on the 0.86 GeV data and a $\pm$**4%** error on the 1.72 GeV data.

The uncertainties are assumed to be independent. Added in quadrature (see the argument of section) they yield a $\pm$**5.0 %** error for the 0.86 GeV data and $\pm$**6.3 %** for the 1.72 GeV data.

Uncertainties on simulation

- The statistical error is negligible.
- The $\pm$**2%** uncertainty in the form factors propagates to a $\pm$**4%** error on the cross sections.
- The acceptance uncertainty is estimated to be $\pm$**5%.**
- We have $\pm$**.6 %** uncertainty due to the radiative correction inputs (i.e. uncertainty of 2 % in the length of matter crossed by the outgoing electron).

Adding these estimates in quadrature yields a $\pm$**6.4%** uncertainty on the simulation.

Results

The table below gives the analysis results.

E (GeV)	Sim. cross section	Exp. cross section
1.718 (1st period) e-arm	48.58±3.11 pb	44.84±2.82 pb
1.718 (1st period) h-arm	43.90±2.81 pb	44.33±2.79 pb
0.862 e-arm	7.32±0.47 μb	7.59±0.47 μb
0.862 h-arm	7.28±0.38 μb	7.31±0.37 μb

Conclusion.

The elastic study allows us to determine our analysis cut in order to minimize our uncertainty on the acceptance. The chosen cuts are:

cut	experiment
y_{target} h-arm	-4,+3 cm
y_{target} e-arm	-4,+3 cm
φ_{target}	-20,+15 mr
θ_{target}	-30,+40 mr
$\delta p/p$	-3.5,+2.7 %
w-m_{He}	-1,+5 MeV

The same conclusions regarding the measurement of the upper value of the systematic uncertainty and the quadratic addition of the systematics stand for the elastic cross section as well as for the elastic asymmetries.

5.9 Analysis of the Inelastic Data.

For the elastic data we have compared the simulated results with the experimental ones where the acceptance and radiative effects were still folded in. The analysis of the inelastic data follows a different philosophy. The radiative and acceptance effects have to be unfolded from the experimental data. The results will then be independent of the experimental apparatus and usable by the physics community. The other parts of the analysis: detector efficiencies, deadtime, luminosity and error estimate are similar to the elastic analysis.

5.9.1 Error Estimate.

The systematic errors estimate is still to be done. A preliminary estimate gives a 10% systematic uncertainty.

Note: The e^+e^- ***pair production.*** A photon can materialize as a positron-electron pair. A neutral pion can decay as well into such a pair and a photon (Dalitz decay). The electron from the pair can be identified incorrectly as coming from the $^3\overrightarrow{He}(\overrightarrow{e},e')X$ reaction. The photon contribution was simulated and found to be negligible (0.05% contamination in the worst case [42]). At the end of the experiment, the polarity of the spectrometers was reversed to detect the positrons as an experimental check of the simulation (the positron rate being equal to the electron rate but not overwhelmed by the beam-target reaction rate). The analysis shows that the contamination is below the percent level.

The inelastic asymmetries and cross section will be presented in the next chapter along with the extracted spin structure functions, the GDH integrand (σ^{TT}) and the GDH integrals.

Chapter 6

Results

In this chapter we first present our results on the inelastic asymmetries, $A_{\parallel}$ and $A_{\perp}$, and on the ^{3}He(e,e')X inelastic cross sections. Then we will extract the spin structure functions g_1 and g_2 for ^{3}He and interpret their features. We will discuss the method used to extract the neutron information from the ^{3}He data. We will see, in particular, that, although the method seems to be reasonably under control for the extraction of the neutron GDH integral, the method cannot yet be used to reliably extract non-integrated quantities such as the neutron spin structure functions, the neutron asymmetries or the virtual photon-neutron cross sections. The integrand of the extended ^{3}He GDH integral, σ^{TT}, will be presented as well as the ^{3}He and neutron GDH integrals and the first moment Γ_1 for the neutron. We conclude the chapter by discussing these results.

6.1 Inelastic Asymmetries and Cross Sections for ^{3}He.

The inelastic asymmetries on ^{3}He, $A_{\parallel}$ and $A_{\perp}$, are presented in figure 6.1, while, the inelastic cross sections are shown in figure 6.2.

In fig. 6.2 one can follow the transition from the nuclear domain to the parton domain: The overwhelming elastic peaks (not shown in the figure) at 0.86 GeV and 1.72 GeV disappear at the higher energies. The quasi-elastic and Δ peaks also decrease while the smooth Deep Inelastic contribution becomes dominant for the three highest energies. The overall cross sections drop with the beam energy (as expected from the Mott cross section). Also let us note in particular:

- The relatively large negative value of $A_{\parallel}$ at the Δ resonance. It is about 2% and seems to be insensitive to Q^2.
- The fact that in the resonance region $A_{\parallel}$ and $A_{\perp}$ are almost mirror images. This will be understood when we will discuss the spin structure function results in section 6.2.1.
- In the DIS region $A_{\parallel}$ is large while $A_{\perp}$ is dying out, consistent with the previous DIS experiment results.
- The cross section resonance peaks are hardly visible, apart from the Δ. This arises from the fact that we have inclusive results. Also in their work on the ^{3}He nucleus,

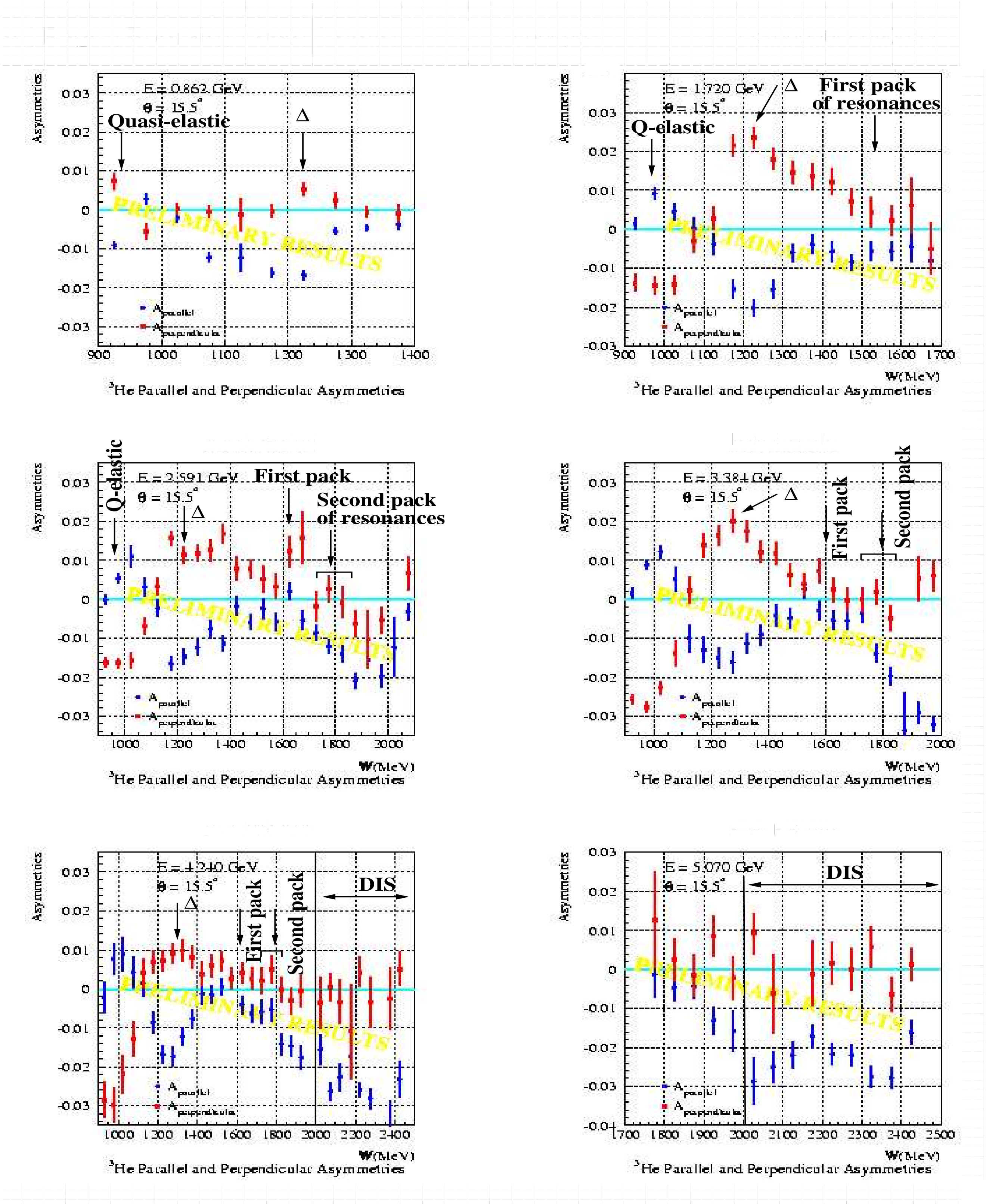

Figure 6.1: $A_\parallel$ and $A_\perp$. Only the statistical errors are shown. The first resonance region contains the P'_{11}, D_{13} and S_{11}. The second resonance region contains the P_{15}, D_{15}, D_{33}, P_{13} $D_{13'}$ and $S_{11'}$.

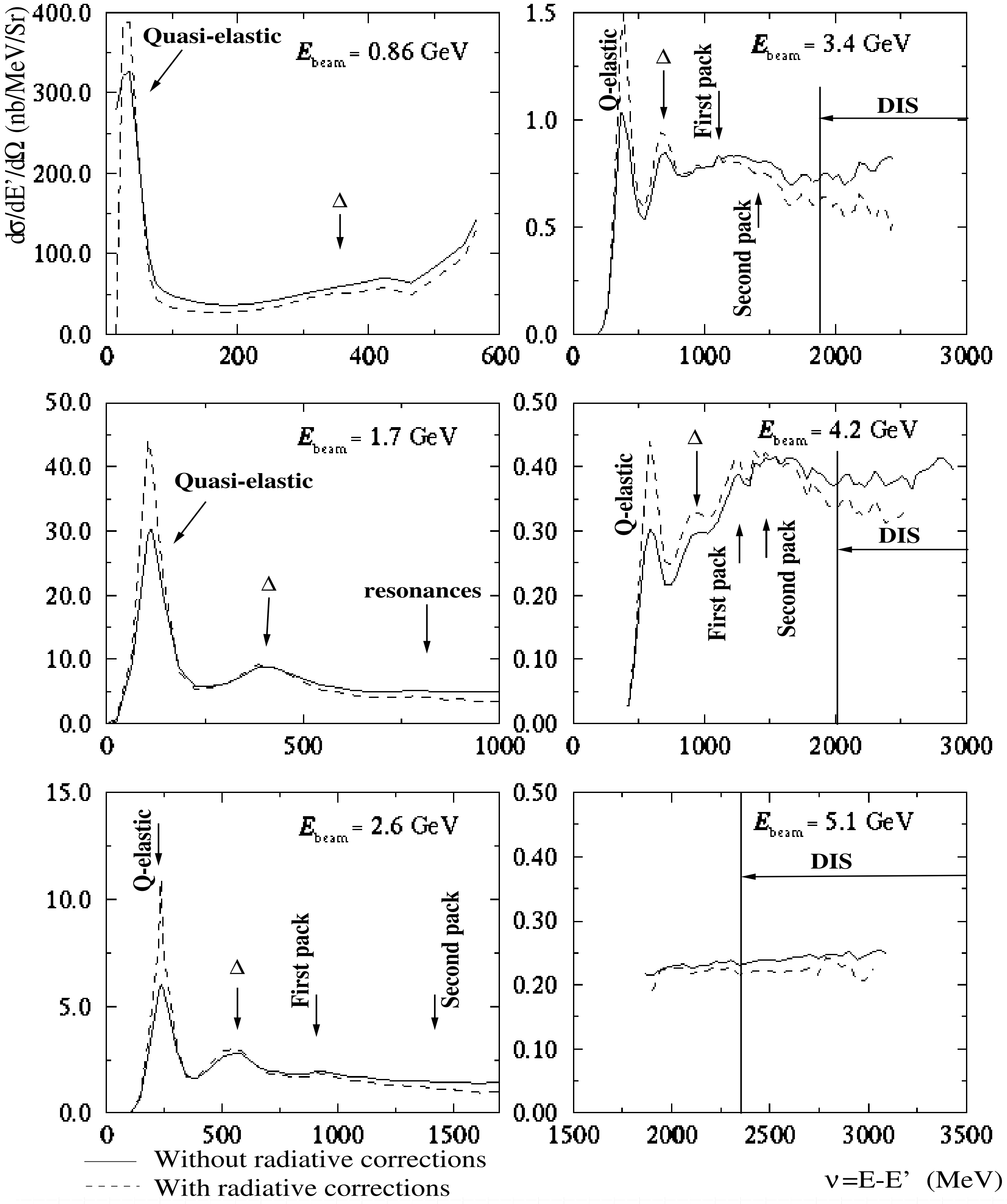

Figure 6.2: Inelastic cross sections. The first resonance region contains the P'_{11}, D_{13} and S_{11}. The second resonance region contains the P_{15}, D_{15}, D_{33}, P_{13} $D_{13'}$ and $S_{11'}$.

Ciofi degli Atti and S. Scopetta [34] have shown that the nuclear effects such as Fermi motion significantly damp the resonance peaks.

6.2 Extraction of the Physics Results for ^{3}He.

6.2.1 The g_1 and g_2 Spin Structure Functions.

Extraction.

g_1 and g_2 are extracted using the longitudinal and transverse cross section expressions on page 21. The helicity plus and helicity minus cross section difference yields for the two equations:

$$\frac{d^2\sigma^{\downarrow\Uparrow}}{dE'd\Omega}-\frac{d^2\sigma^{\uparrow\Uparrow}}{dE'd\Omega}=\frac{4\alpha^2}{M_N^3Q^2}\frac{E'}{E}[\frac{g_1(Q^2,\nu)}{\nu}M_N^2(E+E'cos\theta)-Q^2M_N^2\frac{g_2(Q^2,\nu)}{\nu^2}] \tag{6.1}$$

$$\frac{d^2\sigma^{\uparrow\Rightarrow}}{dE'd\Omega}-\frac{d^2\sigma^{\uparrow\Leftarrow}}{dE'd\Omega}=\frac{4\alpha^2}{M_N^3Q^2}\frac{E'^2}{E}sin\theta[M_N^2\frac{g_1(Q^2,\nu)}{\nu}+2EM_2^N\frac{g_2(Q^2,\nu)}{\nu^2}] \tag{6.2}$$

from which we extract the spin structure functions g_1 and g_2. These are plotted versus the energy loss ν in fig. 6.3.

Duality.

A comparison of g_1^{He3} at $E = 4.2\ GeV$ (average $Q^2 = 0.7\ GeV^2$) with a result of the experiment E154 evolved at $Q^2 = 5.0\ GeV^2$ is given in fig. 6.4. g_1^{He3} is plotted in function of x. We notice in fig. 6.4 that if we smooth our data, i.e. we average the resonance structure, then the two sets of data mostly overlap. This shows that the Bloom-Gilman duality seen on the unpolarized structure functions (see section 2.2.7) seems to hold as well for the polarized structure function g_1 (with the possible exception of the Δ region).

Interpretation.

In fig. 6.3 the resonance structure is clearly visible. As for fig. 6.1, g_1 and g_2 are almost mirror images in the resonance region and behave as expected in the DIS region (g_1 large in comparison with g_2). The similarity between (g_1, g_2) and ($A_\parallel$, $A_\perp$) can be understood by looking at the formula B.7: The factor $(E + E'cos\theta)$ in front of g_1 is larger than the term $Q^2/\nu = 2xM_N$ factorizing g_2 as soon as we leave the quasi-elastic region. As a consequence $A_\parallel$ is mainly driven by g_1 and conversely $A_\perp$ by g_2. In the DIS where g_2 is small in comparison with g_1 and where E/ν may be close to unity, $A_\perp$ is driven by both spin structure functions.

The behavior of g_1 and g_2 in the DIS region is expected from the previous experiments and from the parton model prediction. In this model g_2=0 because the transverse momenta and spin components are neglected. To understand the symmetrical behavior of g_1 and g_2 we have to go beyond the naive parton model: One can express g_2 in terms of transverse quantities (see for example [58]):

$$g_2(x,Q^2)=\sum_i\frac{Q_i^2}{2}(q_i^{\rightarrow}(x,Q^2)-q_i^{\leftarrow}(x,Q^2)+\overline{q}_i^{\rightarrow}(x,Q^2)-\overline{q}_i^{\leftarrow}(x,Q^2))-g_1(x,Q^2) \tag{6.3}$$

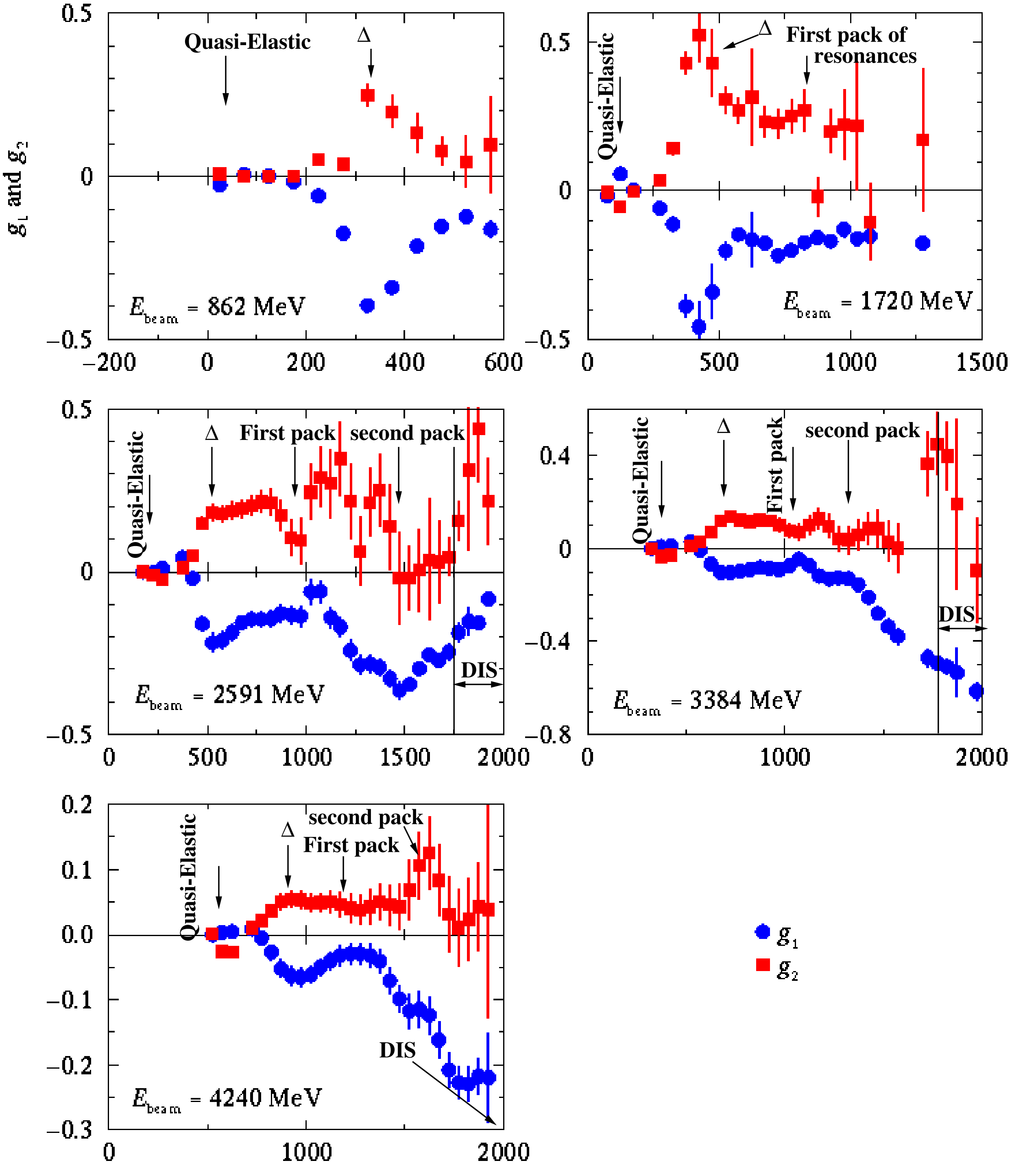

Figure 6.3: g_1 and g_2 on ^{3}He. Only the statistical errors are shown. The first pack of resonances contains the P'_{11}, D_{13} and S_{11}. The second pack of resonances contains the P_{15}, D_{15}, D_{33}, P_{13} $D_{13'}$ and $S_{11'}$

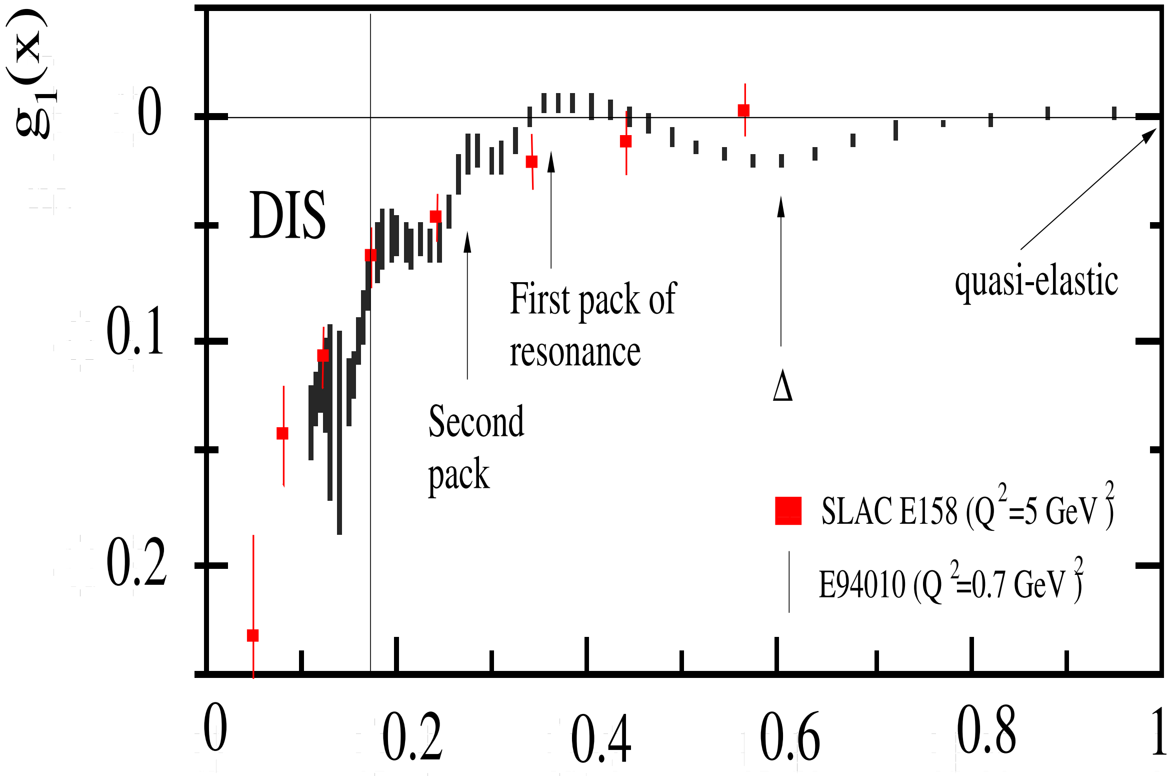

Figure 6.4: Comparison of g_1^{He3} from our experiment and the SLAC E154 experiment. For our data, only the statistical errors are shown. The resonances positions are relevant only for our experiment. The E154 data are in the DIS.

The sum can be expressed in terms of g_1, if we limit ourself to the twist 2 level. It is the Wilczek-Wandzura relation [177]:

$$g_2^{ww}(x,Q^2) = \int_x^1 g_1(x',Q^2)\frac{dx'}{x'} - g_1(x,Q^2) \tag{6.4}$$

which means that at the twist 2 level g_2 does not carry any more information than g_1 and the non-trivial structure of g_2 comes with twist 3 and higher. We say that g_2^{ww} is the trivial part of g_2.

In the resonance region, i.e. at large x, the integral disappears because of its integration limits and we have $g_2^{ww} \simeq -g_1$. From fig. 6.3 we see that indeed $g_2 \simeq -g_1$ which means that the trivial part g_2^{ww} of g_2 dominates, i.e higher twist contributions are small. This might seem surprising because our data are taken at low Q^2. Let us note that these results are similar to the recent preliminary results obtained in the DIS domain by the experiment E155x at SLAC [69]. These results are consistent with the results of fig 6.4 showing that duality stands also for g_1 (in our kinematic domain) i.e that the higher twists are small in this domain (see section 2.2.7).

This explanation uses DIS domain concepts that are extended to the resonance region. At lower Q^2, in the Δ region, the symmetry of the two structure functions can be explained by the fact that the nucleon to Δ transition is mainly a spin flip transition. i.e. mainly transverse photons are involved so the longitudinal and interference cross sections, eq. 2.20, are close to zero. Since σ^{TL} is proportional to $g_1 + g_2$, we expect $g_2 \simeq -g_1$ in the Δ region. Qualitatively our results verify the fact that the Δ is a dominant M_{1+} magnetic dipole transition. The fact that we measure $g_2 \simeq -g_1$ as expected adds to our confidence that our data are consistent. Quantitatively it is a way to study the E_{1+}/M_{1+} ratio (see footnote page 18 and [58]). Finally being at very small Q^2 (comparable to the electron mass squared) the spin of the (quasi-real) photon is essentially transverse. Therefore both the longitudinal and interference cross sections are small. If there is a smooth transition between the real photon and the virtual photon worlds then $g_2 \simeq -g_1$. However our Q^2 is too high to make use of this argument.

Note. The previous discussions were qualitative since I have discussed the ^{3}He data as if they were neutron data, taking advantage of the fact that the polarized ^{3}He nucleus is a good effective polarized neutron.

6.2.2 The GDH* Integral.

The GDH integral is formed by integrating σ^{TT} (see section A.4 in the Appendix A):

$$I(Q^2) = \frac{M_N^2}{4\pi^2\alpha}\int_{thr}^{\infty}\frac{\sigma^{TT}d\nu}{\nu}$$

where the integraton begins at the pion threshold for the neutron (so we can extract the neutron information out of the ^{3} data). The integral is computed at fixed Q^2 by interpolating between the different energies (see fig. 4.1). The integrand σ^{TT} for ^{3}He is given in Fig. 6.5 at fixed beam energy. It is given at fixed Q^2 (i.e. after interpolation) in Fig.6.6 The GDH integral for ^{3}He is given in the Fig. 6.7. To understand what the data of Fig. 6.7 mean we have to know that:

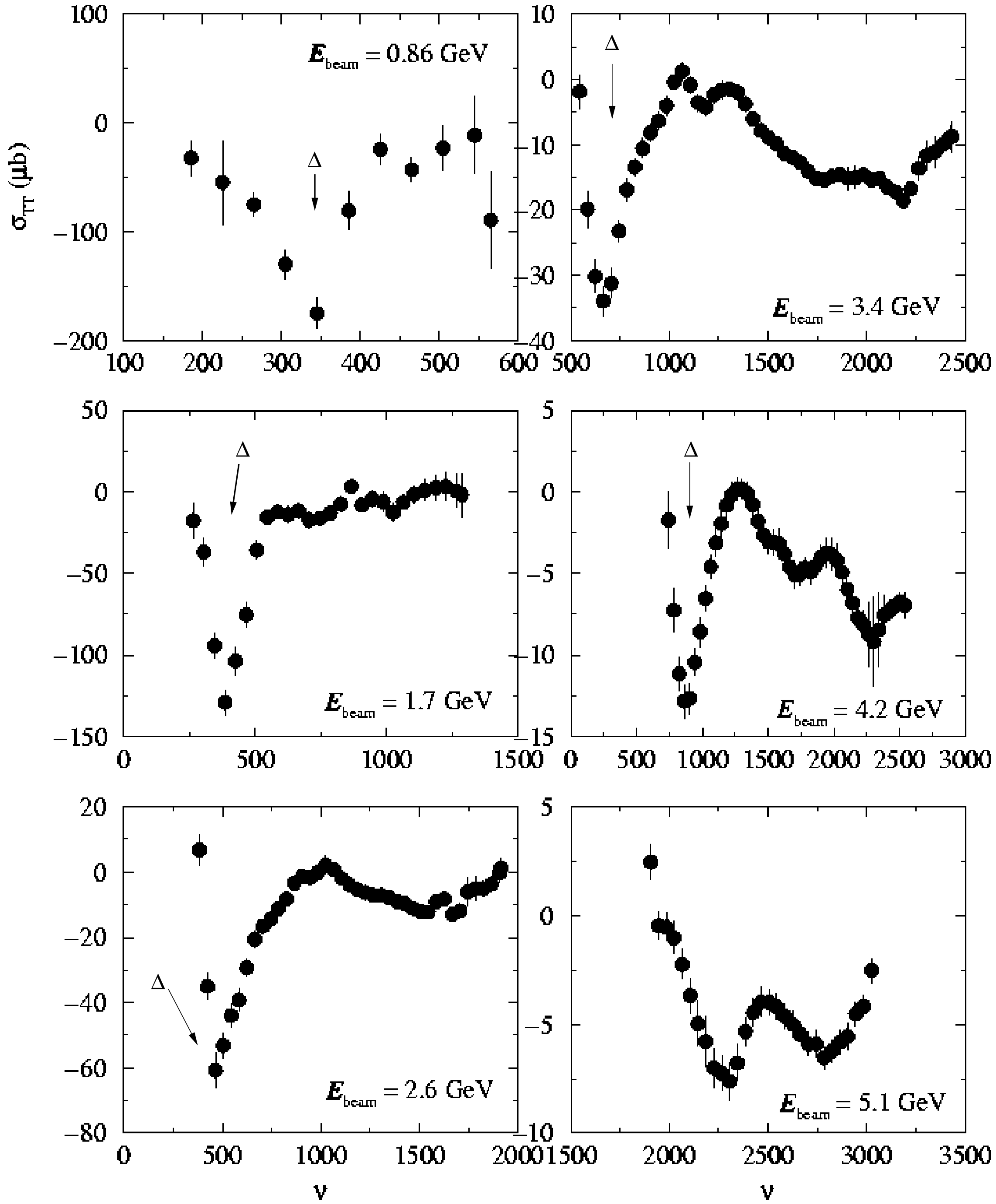

Figure 6.5: σ^{TT}, the GDH* integrand, on ^{3}He. The Gilman convention for the virtual photon flux is used. Only the statistical errors are shown.

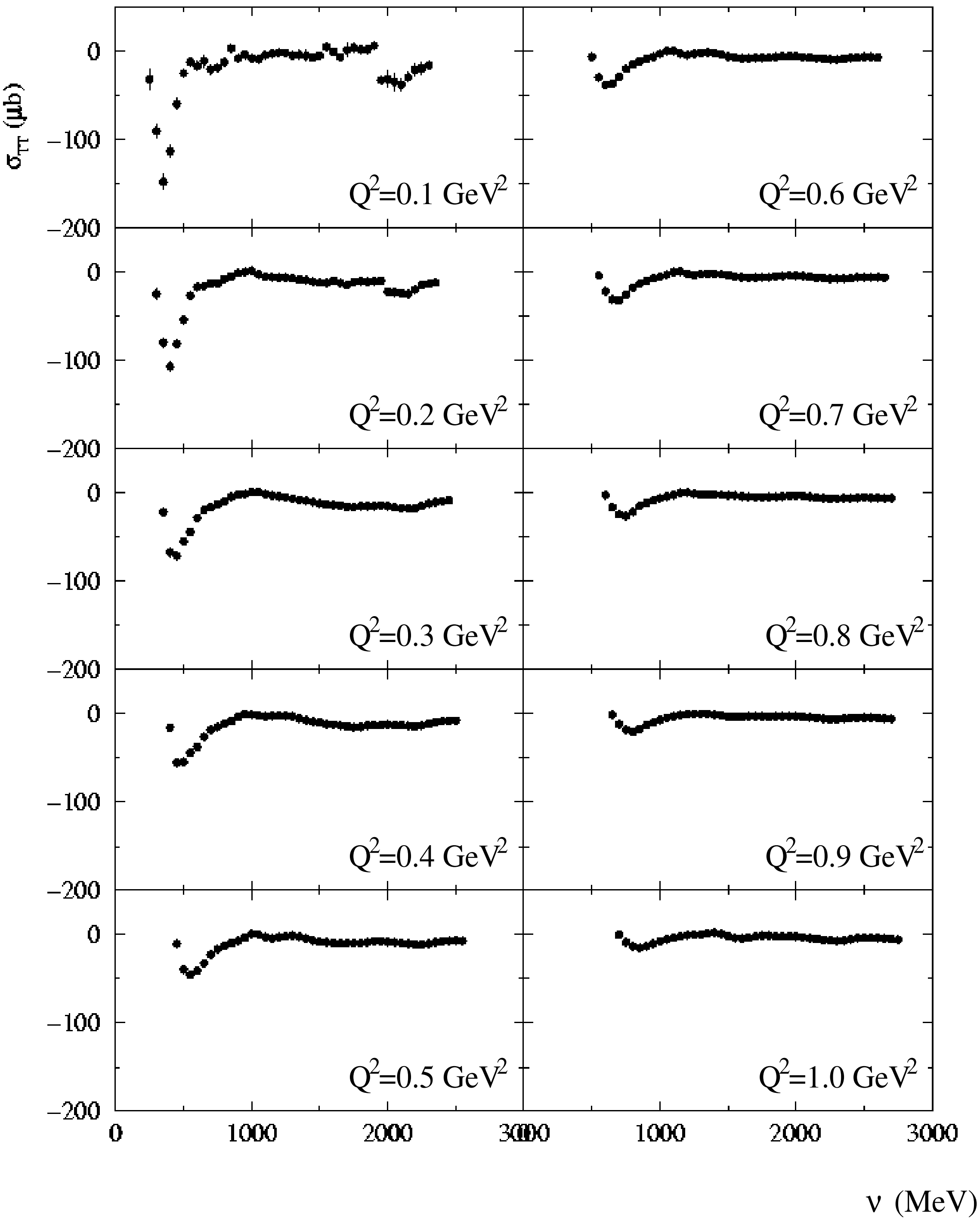

Figure 6.6: σ^{TT}, the GDH* integrand, on ^{3}He, at fixed Q^2. Only the statistical errors are shown.

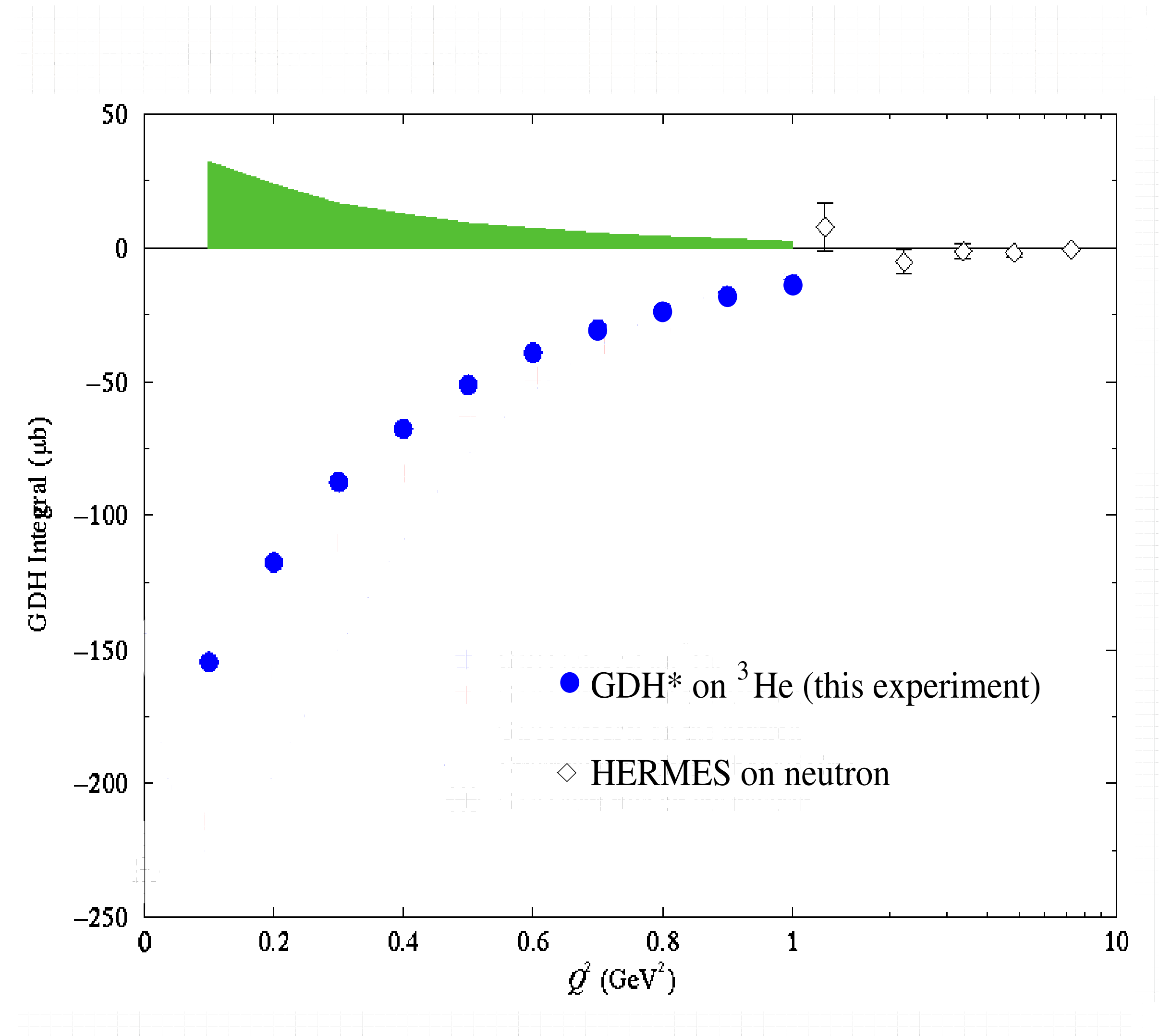

Figure 6.7: The GDH* integral on ^{3}He. The quasi-elastic is not included. Our estimated systematic uncertainty is 10%. The integration range over the energy loss is limited to our kinematical domain. For the lowest Q^2 points, the integration covers only the Δ region. The larger systematic error due to the radiative corrections on the 0.86 GeV data is not shown here. Let us notice that the horizontal scale is linear up to 1 GeV^2 (for our data) and then logarithmic (for the HERMES data).

- The integration is done over our accessible energy loss ν, see fig. 4.1. The range is shorter for the low beam energy data than for the large energy ones. The lower energy just covers the Δ. Hence we have to be careful in extrapolating our data to Q^2=0 in order to see if the sum rule on the ^{3}He is verified.

- The quasi-elastic contribution has to be removed in order to extract GDH* on the neutron. There is an overlap of both contributions especially at large incoming beam energies. A clean separation of the quasi-elastic and the Δ contributions asks for a model of σ^{TT} for both the quasi-elastic and the Δ reactions. This is not done here. Since σ^{TT} is always negative, except for the quasi-elastic reaction (and maybe near the pion threshold according to the Mainz results on the proton [6]), we are missing some strength in the integral. Two effects contribute to reduce the strength:

  - The missing part of the Δ reaction.
  - The contamination of the quasi-elastic reaction that comes with the opposite sign.

  Models will be needed to disentangle the quasi-elastic from the Δ reaction.

- The data at the lowest beam energy (0.86 GeV) are used as the starting point of the radiative corrections by unfolding. These data themselves need a model or an extrapolation of our higher energies data to be corrected. Consequently the lowest energy point has a larger systematic uncertainty.

6.3 Extraction of the Neutron Data from the ^{3}He Data.

We have to extract the neutron information from our ^{3}He data. As said on page 17 the ^{3}He nucleus is not in a pure S state. The admixture of S' and D states can reach about 10%. This makes the protons of the ^{3}He nucleus to come into play (proton effective polarization $p_p \neq 0$). For the same reason part of the neutron spin is pointing in the opposite direction than the ^{3}He spin (neutron effective polarization $p_n \neq 1$). Other nuclear corrections come from the Fermi motion and the binding. The correction method was first worked out for ^{3}He deep inelastic data by Friar et al. [78] and then by C. Ciofi degli Atti et al. [33]. The method was then adapted to the GDH sum rule by C. Ciofi degli Atti and S. Scopetta [34].

6.3.1 Extraction of the neutron Spin Structure Functions and Asymmetries from ^{3}He.

The proton and neutron effective polarisations within the ^{3}He nucleus are computed using three-body Fadeev calculations. Without any nuclear effects than the admixture of the S' and D states, the different spin structure functions would obey the equation:

$$g^{^3He} = 2p_p g^p + p_n g^n \tag{6.5}$$

with $p_p = -0.028 \pm 0.004$ and $p_n = -0.86 \pm 0.02$ [33].

We assume that the spin structure functions have the same form for a bound nucleon and a free nucleon. Then we can take into account the Fermi motion and binding effect by integrating the structure functions over a shifted energy transfer. i.e. these effects are accounted for by convoluting g_1 and g_2 with a quantity related to the ^{3}He spectral function [33]. $g^{^3He}$ is the addition over the three nucleons of the convolutions. This method holds in principle for the quasi-elastic, resonances and DIS domains. $A_\parallel$ and $A_\perp$ on the neutron can then be estimated using the same method. Ciofi degli Atti et al. demonstrate that in the DIS region the formula 6.5 is already a good approximation and the refinement by the convolution method modifies the result by at most 4% (for x<0.8) [33]. However it turns out that in the resonance region the formula 6.5 is not sufficient for a reliable extraction of the neutron data [34]. That is the Fermi motion and binding effect are significant. Furthermore the convolution method does not give satisfactory results up to now. The problem may come mainly from the Final State Interactions that are not taken into account in the model and could be large in the quasi-elastic and resonance regions. Meson Exchange Currents are also neglected by the method. Theoretical efforts are underway to provide a reliable extraction method in the resonance region.

6.3.2 Extraction of integrated quantities.

The generalized GDH integral can be expressed using the spin structure functions. Consequently, the method used to extract the spin structure functions on the neutron can also be applied to the generalized GDH integral. From our data and a model of g_1^p one can deduce the GDH integral on the neutron. The MAID model (see section A.5 in the Appendix A) is used for g_1^p. A comparison of the neutron extraction results using, on the one hand, only the effective polarization (cf formula 6.5) and, on the other hand, taking into account the binding effect and Fermi momentum, shows that in both cases the GDH integral are similar. This is true in the DIS region as well as in the resonance region. The difference is at most 5% [34], so these two latter nuclear effects are not critical for the GDH extraction. Recall that the sum rule is an integration of inclusive quantities so it is less sensitive to the details of the resonance region. However Ciofi degli Atti et al. show that there are appreciable differences between their ^{3}He and neutron GDH integrals. This demonstrates that the nuclear effects giving birth to the S' and D state are not negligible. The 5% difference between the most simple model (eq. 6.5) and the convolution method gives an estimate of the size of the systematics that we can expect from the extraction method (providing that the Final State Interactions are not accounted for and may lead to a larger uncertainty).

6.3.3 Conclusion.

The neutron extraction is performed with a PWIA model. The difference between this model and a simple accounting of only the effective polarization of the nucleons within the nucleus is small. This is not the case for non-integrated quantities such as g_1, g_2, A_1 and A_2 as far as the resonance region is concerned. Consequently, the main goal of the experiment, the extended GDH integral, will be presented both for ^{3}He and far the neutron. However, we can present in this thesis only the spin structure functions and electroproduction cross sections for ^{3}He.

6.4 The GDH Integral on Neutron.

The GDH integral on the neutron is presented in Fig. 6.8. The same caution as for the GDH integral on ^{3}He holds (integration only over our experimental energy loss range, missing strength in the integral, model dependent lowest energy point because of the radiative corrections). In addition the extraction is simply done using the ratio of the neutron GDH integral to the ^{3}He GDH integral modelled in [34]. A preliminary estimate of the systematics, taking into account the uncertainty on the extraction method, is 15%. Our results are compared with different models in Fig. 6.9. One can see again by looking at Z. Li's results that the Δ contribution is largely dominant in our low Q^2 range. According to these results the first point of caution (the limited integration range) is not relevant.

6.4.1 Behavior of the Extended GDH Integral with Q^2.

As far as our principal result is concerned (the Q^2 evolution of the extended GDH integral on the neutron) the overall shape follows the prediction of the models but in general with a smaller amplitude. The missing strength in our integral computation due to the quasi-elastic contamination and the omission of part of the Δ contribution may be accounted for part of this difference. Also, our limited integration range may reduce the amplitude of our GDH* measurement. This will happen if σ^{TT} keeps the same sign as it is the case in our kinematic range as soon as we pass the quasi-elastic reaction. It would be interesting that the different authors could reduce their integration range in order to make the better comparison possible.

We notice that our data extrapoled to larger Q^2 are fairly consistent with the HERMES data.

We have no indication of a turn over for our lowest Q^2 points. The existence and position of the turn over will be a strong constraint for the different theories and models.

6.4.2 Extrapolation to the Real Photon Point.

Our data do not allow to check the validity of the GDH sum rule: If we extrapolate to the real photon point using Z. Li's model, the sum rule seems to hold. However if we use the most recent model (Drechsel et al, which is reproducing well the neutron data) the sum rule is violated. Before to discuss this result I should point out that the verification of the sum rule is not the goal of our experiment. Because our results are not final and because of the restrictions mentioned the discussion below may be too daring.

The Mainz preliminary data on the proton [1] indicate that the sum rule on the proton is not grossly violated. These data, completed with the model of Drechsel et al. [59], validate the sum rule within the error bars. If this result is confirmed it rules out some hypothesis that could imply the violation of the GDH sum rule on the neutron such as:

- The quarks are extended objects (existence of an anomalous magnetic moment) and we are sensitive to their extension.
- The convergence of the integral or the non-subtraction hypothesis.

- Spontaneous breakdown of the electromagnetic gauge invariance [178].

It is not ruling out some hypothesis such as the violation of the causality for processes involving space-like virtual photons [9]: Contrary to the Mainz experiment in which real photons are used, in our case wherein space-like virtual photons are involved, it is not impossible that the causality is violated. Also the above statements are not taking into account the possibility of an "accidental verification" of the proton GDH sum rule. For example the quarks could have an anomalous magnetic moment but their contributions cancel in the case of the proton and not in the case of the neutron. It is interesting here to remind that the "interference" sum rule (see page 31), estimated with the single pion production data is largely violated and the Unitary Isobar Model of Drechsel et al. [59] confirms the sum rules on proton but not on the neutron.

6.4.3 Higher Twist Estimate.

Our resonance and the DIS data can be used for high twist calculations as pointed out in the section A.9.1. Let us recall some features of our data indicating that these higher twist terms are small:

- Our smooth transition from the DIS data to the resonance and quasi-elastic regions.
- Our result on the duality.
- The fact that g_1 is almost the mirror image of g_2

This is in accordance with the claims of Ji et al. and Balitsky but in disagreement with the analyses of Anselmino et al. and Burkert et al.

To conclude, let us remember a last interest of having performed an experiment in this kinematic domain: Our data, when compared with the Ch. P. T. calculations and twist developments, will show where the validity of these theories breaks down and if the validity domains overlap.

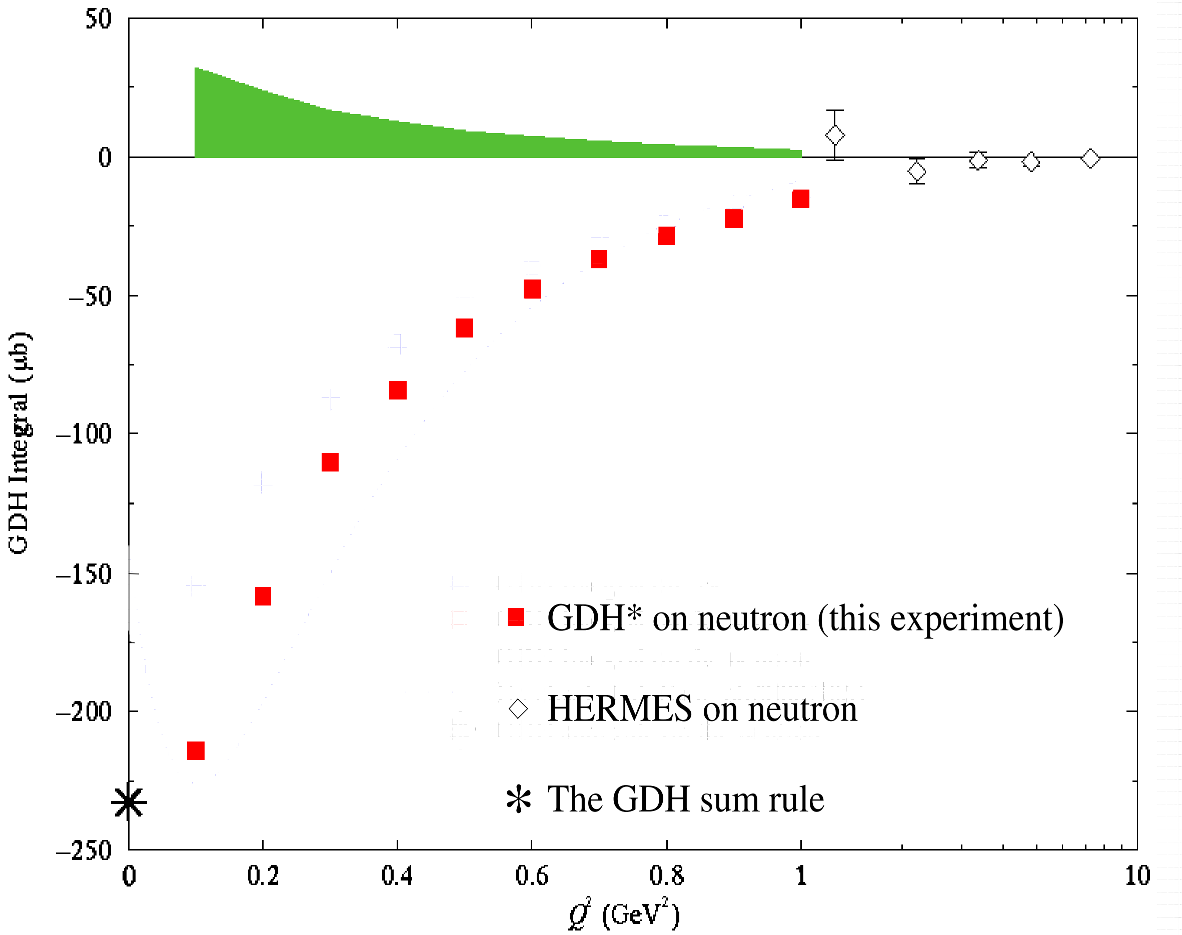

Figure 6.8: The GDH* integral on the neutron. Our estimated systematic uncertainty is 15%. The additional 5% uncertainty in comparison of the ^{3}He data comes from the extraction method needed to obtain neutron information from ^{3}He data. The integration range over the energy loss is limited to our kinematical domain. For the lowest Q^2 points, the integration covers only the Δ region. The larger systematic error due to the radiative corrections on the 0.86 GeV data is not shown here. Let us notice that the horizontal scale is linear up to 1 GeV^2 (for our data) and then logarithmic (for the HERMES data).

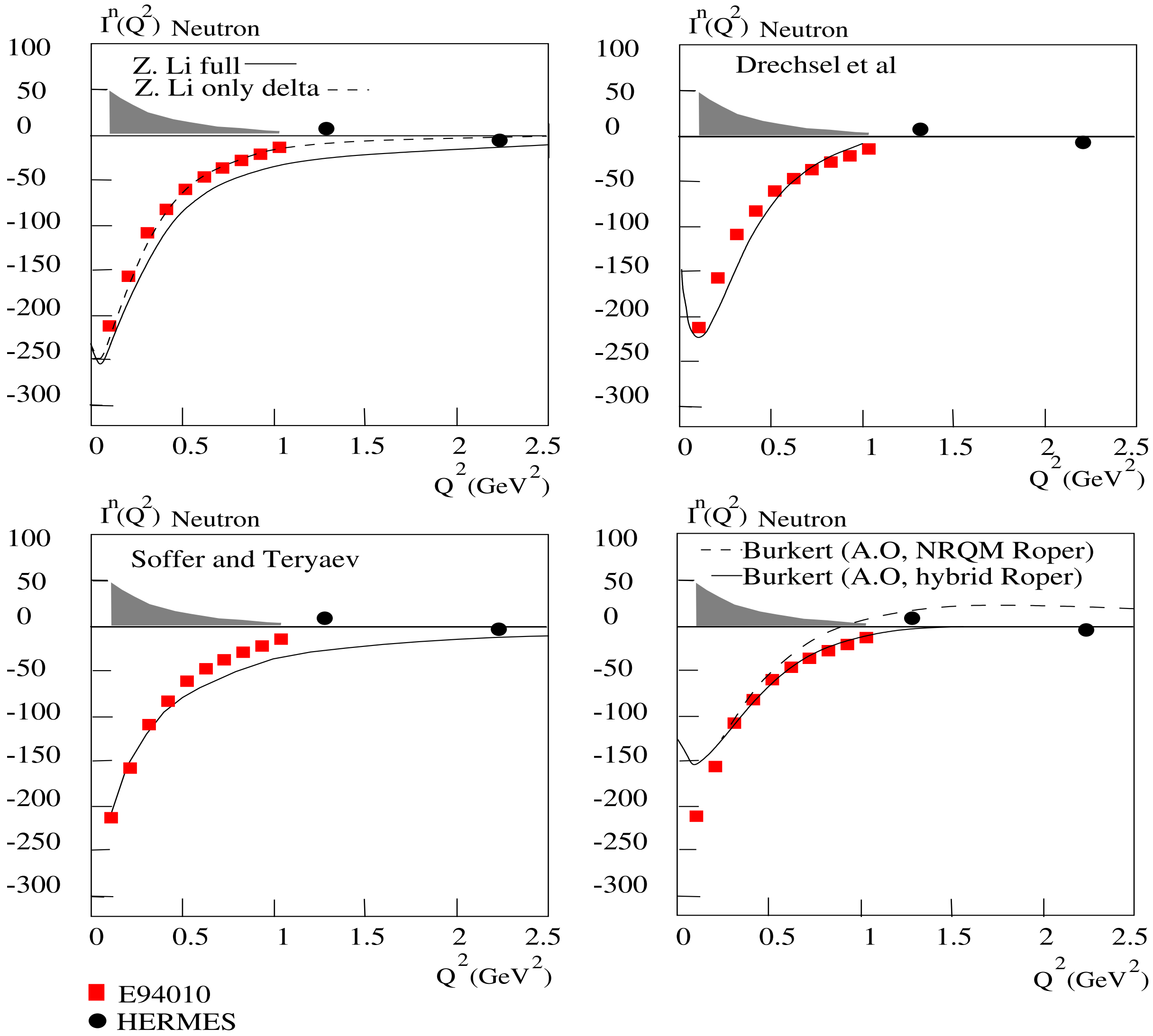

Figure 6.9: The GDH* integral on the neutron compared with different models. Our systematic uncertainty is 15%. The additional 5% uncertainty in comparison of the ^{3}He data comes from the extraction method needed to obtain neutron information from ^{3}He data. The integration range over the energy loss is limited to our kinematical domain. For the lowest Q^2 points, the integration covers only the Δ region. The larger systematic error due to the radiative corrections on the 0.86 GeV data is not shown here.

Chapter 7

Summary and Perspectives

We have presented the motivations in gathering doubly polarized data in the quasi-elastic, resonance and DIS domains. These data were used to calculate the extended GDH integral. The comparison of this quantity with the spin dependent forward Compton amplitude $\overline{S_1}$ (see section 3.3.2) is of particular importance for the unification of the two strong interaction descriptions (nucleonic/hadronic vs partonic) because $\overline{S_1}$ is the first quantity theoretically calculable in the full Q^2 domain of the strong interaction.

Such a data taking was make possible because of three major technical achievements:

- The beam of high duty cycle (100%), high current (up to 70 μA) and high polarization (70 %) (see section 4.2).
- The ^{3}He target of high density (above 10 atm) with a polarization of 35% and a length of 40 cm (see section 4.3.5).
- The large acceptance (6 msr) and high resolution ($\Delta P/P \simeq 10^{-4}$) spectrometers (see section 4.3.2).

These features, available at Jefferson lab, enabled us to achieve the highest luminosity in the world (about 10^{36} s^{-1}cm^{-2} with a current of 15 μA) as far as polarized ^{3}He targets are concerned. Consequently we were able to gather, in a rather short period of time (3 months), a large amount of data covering a large kinematical domain.

These data were utilised to calculate the GDH* integrals between Q^2=0.1 and Q^2=1.0 GeV^2. Both integrals on ^{3}He and the neutron have been presented (see fig. 6.7 and 6.8). The error achieved on the integrals is respectively of 10% and 15 %. We have analysed only part of our data and the analysis is continuing. Therefore we expect improvements on the statistical and the systematic uncertainties of these results.

The GDH* integrals qualitatively display the expected Q^2 evolution (see fig. 6.9). We expect that some strength is missing in our experimental measurement of GDH* (see the discussion in section 6.4.1) because of the limited integration range, the quasi-elastic contamination and a missing contribution of the Δ. Hence the difference between the models and the data can either be due to the missing strength and/or to a failure of the model.

We have no indication of a possible turn over at low Q^2. We will have to wait for an extension of this experiment to draw any conclusion on the existence and the position of the turn over.

Finally, there remains the delicate point of the extrapolation to the real photon limit. We have no definite conclusion on this question (see section 6.4.1). Here again, in order to clarify this issue, we have to wait for an experiment dedicated to the measurement of the GDH sum rule with a photon beam or for the extension of this experiment at lower Q^2 and larger integration range.

In addition to the GDH* integral, non-integrated quantities (on ^{3}He) are extracted from our data:

- The integrand of the GDH* integral, σ^{TT} (see fig. 6.5).
- The two spin structure functions $g_1^{^3He}$ and $g_2^{^3He}$ (see fig. 6.3).

The data on $g_1^{^3He}$ seem to indicate that the Bloom-Gilman duality holds for g_1 (see section 2.2.7, section 6.2.1 and fig. 6.4) although this is questionable for the Δ region. This will be the first time that an experiment demonstrates clearly this feature of the strong interaction for a polarized structure function.

In addition, our measurements show that in a large part of our kinematic domain (in the resonance domain, especially in the Δ region) $g_1^{^3He}$ exhibits similar behavior to $g_2^{^3He}$ but with the opposite sign. This is expected because the nucleon to Δ transition is mainly a spin flip transition. Beyond the Δ this may indicate that the higher twists are small.

Some important information remains to be extracted from our measurements:

- The longitudinal-transverse interference cross section, σ^{LT}.
- The results on the Burkhardt-Cottingham sum rule (see section A.8) should be available soon.
- A_1 and A_2. To this end we need the factor $R \equiv \sigma^L/\sigma^T$. R is well known in the DIS region [175]. However, it is not known in the resonance domain.

As soon as a reliable extraction method, accounting for the full nuclear effects is available, all our measurements on non integrated quantities will be used to extract the same quantities on the neutron. This difficult subject is a challenge for the theorists.

We have pointed out the interest to repeat the measurements at lower Q^2 and a larger integration range. This will be done by the experiment E97110 [112], which will take advantage of the new Hall A septum magnets to perform the measurement at smaller angles (6^o and 9^o). It will overlap part of our kinematics domain and will measure the GDH integral with a more complete mapping up to Q^2=0.02 GeV^2. This experiment will solve most of the issues that are currently limiting our results. Along with this experiment, other experiments at Jefferson Lab Hall B, Brookhaven (LEGS-spin), Bonn (ELSA), Duke University (TUNL), Grenoble (GRALL), Hamburg (HERMES) and Mainz (MAMI) will provide a full mapping of the GDH and extended GDH sum rule for the two nucleons. This experiment was a first step of a large "GDH effort" that will enhance our understanding of the strong interaction.

Appendix A

More on Sum Rules

We review different extensions of the GDH integral, how these extensions explain the Q^2 behavior of the integral and their interest for our understanding of the strong interaction. Useful theories and models are also reviewed in the context of the extension. Sections A.1 and A.2 present the first motivation to extend the GDH sum rule. However, as said in chapter 3, the interest is mostly historical since this method of extracting the higher twists was controversial, and the post-EMC data have shown that this estimate was wrong. The major interest to extend GDH is now to have an observable standing in all the domains of the strong interaction. This will help us to understand the transition between the partonic and hadronic degrees of freedom of the strong interaction and to check the theoretical calculations. Nevertheless, since Anselmino et al.'s work triggered the interest to extend the sum rule and since many papers refer to this work, I summarize the extraction method and its refinement.

A.1 Anselmino et al. Extraction of the Higher Twist Terms.

We have seen in section 3.3.1 why Anselmino et al. extended for the first time the GDH integral, in particular their interest to compute QCD power corrections. I detail here their method to extract these higher twist terms.

Anselmino parametrised $I_p(Q^2)$ to fit the EMC data. The most simple parametrisation is:

$$I_p(Q^2) = 2m_p^2 \Gamma_p^{as} \left[\frac{1}{Q^2+\mu^2} - \frac{c\mu^2}{(Q^2+\mu^2)^2} \right] \tag{A.1}$$

where μ^2 is a mass parameter giving the Q^2 variation rapidity of $I_p(Q^2)$. c is a parameter constrained by the sum rule at $Q^2=0$. Γ_p^{as} is the asymptotic value of the first moment as $Q^2 \to \infty$. This parametrisation allowed to estimate Γ^{as} and to deduce the higher twist corrections.

Higher twists are usually extracted differently with the sum rule approach. Balitsky et al. ([11]) states that higher twist corrections are negligible above $Q^2 = 1$ GeV^2. The higher twist factor of eq. 3.2 is $b_{p-n} = -0.015$ GeV^2 at Q^2=10.7 GeV^2 in the QCD sum rule calculation method while it is $b_{p-n} = -0.15$ GeV^2 using Anselmino method. Assuming the last result to be the right one, this shows that higher twist effects are important to interpret the DIS results and can be extracted using GDH*.

A.2 Corrected Anselmino et al. Extension

Burkert [27] argued that Anselmino extension is incorrect because the resonances have to be taken into account. To this end Eq. A.1 is modified as:

$$I_p(Q^2) = I_p^{res}(Q^2) + 2m_p^2\Gamma_p^{as}\left[\frac{1}{Q^2+\mu^2} - \frac{c\mu^2}{(Q^2+\mu^2)^2}\right] \tag{A.2}$$

where $I_p^{res}(Q^2)$ takes into account the resonance contribution and is estimated using a phenomenological fit to the experimental data. The higher twist correction found is of the same order as Anselmino et al.'s first method: $b_{p-n}/Q^2 \sim -0.1$ GeV^2.

A.3 Burkert and Li Model.

A.3.1 The A.O. Model.

Burkert and Li [29] estimate the GDH* integral by parametrising the pion photo and electroproduction and the non resonant background in the resonance region. Some experimental data are available in the $0 \leq Q^2 \leq 3$ GeV^2 range. The parametrisation is constrained by a fit to the experimental data if they are available. In this model, called A.O, the Δ transition form factor of eq. 2.14 is written as:

$$G_m^{\Delta}(Q^2) = G_m^{\Delta}(0)G_D(Q^2)e^{0.2Q^2}$$

where $G_D(Q^2)$ is the usual dipole form factor fit. The other transition amplitudes are given in [29]. The authors checked the influence of the different resonances on the GDH* evolution. They conclude that the low and intermediate lying resonances, up to D_{33}, are important in the GDH* saturation. This was qualitatively expected because of the $1/\nu$ factor in the integral.

The model shows the significant contribution of the Δ which is dominant in the $0 \leq Q^2 \leq 1$ GeV^2 region. It causes the sign flip of GDH* (on the proton) around 0.5 GeV^2. At $Q^2 > 1$ GeV^2 the contribution of the other resonances becomes more important and reaches 50 % of the extrapolated EMC results.

In [27] the major role of the Δ in the GDH* sign flip is explained in term of chiral symmetry restoration (section A.7): At small Q^2 the Δ dominates and it is mainly a M_{1+} transition (see section 2.2.3). Hence $\sigma_{3/2}$ dominates and GDH $^* < 0$. At higher Q^2 the chiral symmetry is restored so the hadron helicity is conserved , $\sigma_{1/2}$ dominates and GDH$^* > 0$.

In GDH$^*_{p-n}$ the Δ contribution cancels [26] hence other resonance effects are more visible. A.O can be used to determine the nature of the Roper ($P_{11}(1440)$) resonance. The Non Relativistic Quark Model (NRQM), see section A.6.1, predicts the $P_{11}(1440)$ resonance but the sign and the magnitude of its measured photo-coupling amplitude disagree with the NRQM predictions. It is suggested that $P_{11}(1440)$ is an hybrid of three quarks and a gluon. We can see in Fig. 3.2 two A.O predictions of GDH*, the first one taking the Roper resonance as three excited quarks (NRQM) and the second as a hybrid.

A.4 Scholten and Korchin GDH Integral Extension.

The role of the low and intermediate lying resonances is supported by O. Scholten and A. Korchin calculation [160]. The authors extend the integral such that it obeys the Lorentz invariance, gauge invariance, crossing symmetry and the unitarity, which are the assumptions of the GDH sum rule derivation. Their computation is based on an effective Lagrangian, formulated in terms of mesonic and nucleonic degrees of freedom. They used the generalization of the photoproduction cross section to the electroproduction cross section to extend the integral. Notice that they share the same definition as Ciofi degli Atti and Scoppeta [34], the first extension of Pantförder [143] or Bernard et al. (see section A.8): From eq. 2.18 and 2.17 we write the difference of the electroproduction cross sections as (the Hand convention is used here):

$$\sigma_{1/2} - \sigma_{3/2} = \frac{4\pi^2}{M_N(\nu - Q^2/(2M_N))}(g_1 - (Q^2/\nu^2)g_2) \tag{A.3}$$

Then a natural extension of the GDH integral will be:

$$I(Q^2) \equiv \frac{2M_N^2}{Q^2}\int_0^{x_0}(g_1(x,Q^2) - \frac{4x^2M_N^2}{Q^2}g_2(x,Q^2))dx = \frac{M_N^2}{4\pi^2\alpha}\int_{\nu_{thr}}^{\infty}\frac{\sigma^{TT}d\nu}{\nu} \tag{A.4}$$

(Let us note that the last quantity depends upon the virtual photon flux convention. As pointed out by Drechsel [62] it is better to define GDH* in term of scaling spin structure functions because they are uniquely defined) This extension agrees with the GDH sum rule at Q^2=0 and the Anselmino et al. extension at $Q^2 \to \infty$ since $g_2 \to 0$ when $Q^2 \to \infty$ (see the parton model prediction on g_2). The Scholten and Korchin model cannot predict the GDH* behaviour at large Q^2 where the nucleonic and mesonic degrees of freedom are not relevant anymore to the strong interaction.

A.5 The Unitary Isobar Model.

As already pointed out there are several definitions of GDH* that are all consistent with the GDH sum rule at the photon point and equivalent in the DIS domain. Following Pantförder [144], Drechsel et al. give three possible definitions of the generalized GDH integral [62]:

$$I_A(Q^2) \equiv \frac{M_N^2}{4\pi^2\alpha}\int_{\nu_{thr}}^{\infty}(1-x)\sigma^{TT}\frac{d\nu}{\nu}$$

$$I_B(Q^2) \equiv \frac{M_N^2}{4\pi^2\alpha}\int_{\nu_{thr}}^{\infty}\frac{1-x}{\sqrt{1+\gamma^2}}\sigma^{TT}\frac{d\nu}{\nu}$$

$$I_C(Q^2) \equiv \frac{M_N^2}{4\pi^2\alpha}\int_{\nu_{thr}}^{\infty}\sigma^{TT}\frac{d\nu}{\nu}$$

These three definitions lead to different Q^2 behaviors, in particular for the position of the turn over, see fig. 3.2. Our results have to be compared with I_c. The integrals are evaluated using the Unitary Isobar Model [59] that calculates the relevant multipoles for single pion electroproduction. At large W, where two pion production becomes important, experimental data are used to estimate this contribution [60]. The Unitary Isobar Model range is limited to W=2 GeV, which is the upper limit taken in the integration of $I(Q^2)$. The predictions on $I(Q^2)$ for the neutron can be found in [170] and [62]. As already said the model does not verify the neutron GDH sum rule at the photon point although it validates the proton one and reproduces well the photoproduction data from the GDH experiment at Mainz.

A.6 The GDH Sum Rule and Integral in a Constituent Quark Model Framework.

After a resumé of the Constituent Quark Model features I summarize Z. Li's work on the GDH sum rule in this framework.

A.6.1 Constituent Quarks Models.

Some estimates of the GDH integral and its extension at $Q^2 \neq 0$ used Constituent Quark Models (CQM). They are important prediction tools for the strong interaction in particular because they make predictions in the non perturbative QCD domain. For example, they predict the nature and the magnitude of the transition amplitudes in the resonance region. I will focus on Isgur and Karl CQM [94].

CQM gives a phenomenological approach of QCD. It supposes at first order that the nucleon is built of three "constituent quarks" in a non-relativistic harmonic oscillator potential. This picture explains well the baryon and meson mass spectroscopy. The constituent quarks are not the real quarks of QCD. They can be seen as the three valence quarks dressed with sea quarks. Consequently their characteristics differ from the QCD quarks ($m_{q_{QCD}} \neq m_{q_{CQM}}$, $\kappa_{q_{QCD}} \neq \kappa_{q_{CQM}}$,... See for example the discussion of Cardarelli [31]). The CQM quark spin is 1/2.

The Isgur and Karl CQM originally displays the SU(6)⊗O(3) mass symmetry. It is broken by the perturbative color magnetic hyperfine coupling with the sea quarks (one gluon exchange). The gluonic degree of freedom is formalized at short distance by the one gluon exchange. At long distance it is expressed via the "flux tube gluodynamic": Since QCD is a non-Abelian gauge theory, (the gluons interact with each other) the flux lines condense in tubes and the interquark forces can be described by colored string theory (the Veneziano empirical formula and seed of the superstring theory). The string vibration modes are the gluonic degree of freedom.

Nucleon Spin Prediction.

CQM predicts the following contributions of the quark spins to the nucleon spin structure [96], [97]:

- $\Delta q_{valence} \simeq 0.75$ (in a relativistic approach. The non relativistic one gives $\Delta q_{valence} = 1$).
- $\Delta q_{strange} \simeq -0.15$, $\Delta q^u_{sea} \simeq -0.15$ and $\Delta q^d_{sea} \simeq -0.15$

So $\Delta q \simeq 0.3$ as seen by experiments.

Resonances and CQM.

As stated, CQM relies on an approximate SU(6) symmetry. Consequently the hadrons, built of three constituent quarks, will obey a SU(6)⊗SU(6)⊗SU(6) symmetry. Young tableaus allow to classify the resonances in 4 multiplets (see for example Z. Li lectures [179] or Feynman lectures [75]: $6 \otimes 6 \otimes 6 = 56 \oplus 70 \oplus 70 \oplus 20$ (this group is larger than in Fig. 2.8 which does not include the strange quark) where the 56 multiplet is symmetric under quark permutations, the 20 multiplet is antisymmetric under quark permutations, one of the 70 multiplet is symmetric under two quark exchange (λ-type symmetry) and the other antisymmetric under two quark exchange (ρ-type symmetry).

Anomalous Magnetic Moment in CQM.

The anomalous moment κ is one of the two sides of the GDH sum rule, see eq. 3.3. It is the deviation from a pointlike magnetic moment due to the composite nature of the object. In the CQM:

$\kappa_N = \sum_q e_q \sigma_q \frac{M_N}{m_{q_{CQM}}}$ where σ_q is the nucleon spin fraction carried by the quarks or the antiquarks.

A.6.2 Z. Li GDH Sum Rule Derivation and Extension in a CQM framework.

Z. Li in [180] re-derives the sum rule and extends the integral in a CQM basis. This work gives useful insight into the nature of the sum rule, the behaviour of its extension and the tests it provides to the $SU(6)$ flavour symmetry. The extension is based on the generalisation to the virtual photon of the electromagnetic Hamiltonian developed in [37] to describe a many quark system. It can be written as:

$$\frac{1}{\sqrt{\pi\nu}}\mathcal{H}=h^c + h^p + \frac{Q^2}{\nu+\left|\overrightarrow{k}\right|}h'$$

where h^c represents the spin flip transition and the center of mass motion of the quark system, h^p the orbital momentum flip transition and $\overrightarrow{k}$ is the virtual photon momentum. The third term is the extension to virtual photons. Taking this Hamiltonian at the photon point and the magnetic moment as defined in (section A.6.1) one can derive the GDH sum rule.

The generalized GDH integral derivation follows the same computation as previously but taking into account the term $\frac{Q^2}{\nu+\left|\overrightarrow{k}\right|}h'$ in the Hamiltonian.

By constructing the nucleon wave function we can compute GDH* at intermediate Q^2. Write $I(Q^2) \equiv I_a(Q^2=0) + I_b(Q^2)$. For the neutron and in the $SU(6) \times O(3)$ framework used to construct the wave function, we find that $I_b^n(Q^2) \rightarrow_{Q^2\rightarrow\infty} 0$.

These results stand for the neutron and in a $SU(6) \times O(3)$ CQM, i.e. without hyperfine structure. Hence a deviation from this prediction tells how $SU(6) \times O(3)$ is valid for QCD.

Another study of the GDH sum rule in the CQM framework is done by Cardarelli et al. [31]. Assuming the GDH sum rule to be valid Cardarelli constrains the anomalous moment of the constituent quarks. One of the results of Cardarelli et al. study is the critical role of the Δ in the sum rule saturation.

A.7 GDH and the Chiral Perturbation Theory.

A.7.1 Chiral Perturbation Theory.

The chiral perturbation theory (Ch.P.T) is an approximation where the quark masses, the pion masses or the momenta of the incoming or outgoing particles are negligible in respect to the nucleon mass. The interest of the Ch.P.T for our experiment is that it provides exact calculations at small Q^2. Hence it allows to extend the GDH integral (Q^2=0) beyond the photon point. This was first worked by V. Bernard et al. [16] and was followed by the several papers from Ji et al. [107], [108].

Chiral Symmetry.

Take the Dirac Lagrangian $\mathcal{L}_\delta= \overline{\psi}(i\gamma_\mu\partial^\mu - m)\psi$. We define the left handed Dirac spinor ψ_l as $P_l\psi = \psi_l$ with $P_l = (1-\gamma_5)/2$ the left helicity projector. In the same way we define ψ_r with $P_r = (1+\gamma_5)/2$. If $m = 0$ then $\mathcal{L}_\delta$=$\mathcal{L}_l$+$\mathcal{L}_r$ with ψ_l (ψ_r) eigenstate of $\mathcal{L}_l$ ($\mathcal{L}_r$): The Dirac Lagrangian is decomposed into two non coupled Lagrangians. Hence, there is two symmetric classes of particle with left or right helicity. This is the Chiral symmetry.

QCD and Ch.P.T.

If the quarks have no masses then $\mathcal{L}_{QCD}$=$\mathcal{L}^l{}_{QCD}$+$\mathcal{L}^r{}_{QCD}$. Massless Goldstone bosons are generated by the spontaneous symmetry breaking due to the Ward identities and the quarks confinement (see the lectures of M. Knecht [116]). The small pion mass, with respect to the other hadrons masses and its spin parity identify it to the Goldstone bosons. The finite quark mass makes the pion mass to be non zero as a Goldstone boson mass should be. The calculations are carried out by adding a chiral symmetry breaking perturbative term to $\mathcal{L}_{QCD}$. The perturbative development is in $\frac{m_\pi}{m_N}$, in the quark masses or in the momenta of the incoming and outgoing (i.e. on shell) particles. All these quantities have to be small in the application domain of Ch.P.T.

Ch.P.T is valid for $Q^2 \ll m_\pi$ reactions and breaks down at larger Q^2. Ioffé in [92] suggests that the baryon chirality is restored for electromagnetic and weak process at large Q^2.

A.7.2 GDH Extension Using the Heavy Baryon Ch.P.T

V. Bernard et al. were the first to use non relativistic and relativistic Heavy Baryon Ch.P.T (Heavy Baryon means the nucleon mass is taken to be infinite) to compute the slope of GDH* at small Q^2 (i.e. $\sqrt{Q^2} < M_\pi$) [16] in a model independent way. They extend the integral the same way as previous authors, by taking the electroproduction cross sections. Their photon flux differs by a factor $e^2/(4\pi M_N^3)$ from the equation 2.18. The relativistic calculation including the Δ yields: $dI^n(k^2=0)/dk^2 = -1.7\ GeV^{-4}$ and $dI^p(k^2=0)/dk^2 = -2.2\ GeV^{-4}$ with $k^2 = -Q^2$. That is the GDH* slope for the neutron is:

$$dI^n(Q^2=0)/dQ^2 = 659\ \mu b/GeV^2 \tag{A.5}$$

and for the proton:

$$dI^p(Q^2=0)/dQ^2 = 853\ \mu b/GeV^2 \tag{A.6}$$

The predicted slope sign differs from the Burkert one (see Fig. 3.2).

Our experimental data may be at too high Q^2 to give insight on the region covered by the Ch.P.T and select the right evolution calculation.

Ji et al. used also the Heavy Baryon Ch.P.T to extend the GDH sum rule [107], [108], see section 3.3.2.

A.8 The GDH integral and the Burkhardt-Cottingham Sum Rule.

A.8.1 The Burkhardt-Cottingham (BC) Sum Rule.

The BC sum rule was derived by Burkhardt and Cottingham in 1970 [15] using dispersion relations for the forward Compton scattering. The sum rule states that the first moment of g_2 vanishes:

$$\int_0^1 g_2(x)dx = 0 \tag{A.7}$$

If the elastic contribution is removed from the integral we have:

$$I_2(Q^2) \equiv \frac{2M_N^2}{Q^2}\int_0^{x_0} g_2(x)dx = \frac{1}{4}\mu G_m(Q^2)(\mu G_m(Q^2) - G_e(Q^2)) \tag{A.8}$$

where x_0 exclude the elastic reaction. At the photon point:

$$I_2(Q^2) \rightarrow_{Q^2\rightarrow 0} \frac{\mu^4 - \mu^2}{4}$$

since $G_m(0) = \mu$ and $G_e(0) = 1$.

A.8.2 Evolution of the extended GDH integral using the BC Sum Rule.

Soffer and Teryaev explain the GDH* behaviour by the contribution of the g_2 structure function that appears as soon as the integral is extended. The BC integral has also a strong Q^2 dependence but not the addition of the two integrals. Consequently the authors suggest an extension of the GDH integral taking into account the BC sum rule [164].

The addition of the two integrals, $I_t = I_1 + I_2$, behaves smoothly so it is easily interpolated between the well known (for both sum rules) $Q^2 = 0$ point and the DIS elastic data (EMC for the proton [164] and E143 for the neutron [165]). The interpolation is:

$$I_t^n(Q^2) = \frac{2M_N^2}{Q^2}\Gamma_1^n\left[\frac{Q^2}{Q_0^2}\theta(Q^2-Q_0^2)\left(6-8\frac{Q^2}{Q_0^2}+3\left(\frac{Q^2}{Q_0^2}\right)^2\right)+\theta(Q^2-Q_0^2)\frac{Q_0^2}{Q^2}\right]$$

where $Q_0^2 \sim 1$ GeV^2 in order to assure the continuity of I_t in the case of the proton. θ is the Heaviside function. The elastic contribution is subtracted from I_2 using a rather old Sachs form factor parametrization but it is not critical since all the data and parametrization agree for $Q^2 \leq 1$ [114] which is our range of interest (at higher Q^2 the elastic contribution disappears). The GDH* interpolation is deduced by subtracting I_2 from I_t.

The principle of this extension differs from the previous ones but the Q^2 dependence of GDH* is also due to the Δ that causes the strong Q^2 behaviour of I_2 and thus of I_1. Let us note that the recent calculation of I_1 and I_2 from Drechsel et al. [62] does not agree with the assumption that I_t behaves smoothly with Q^2.

A.9 Ji Higher Twist Extraction Method.

Ji [101] proposes a new method to extract higher twists. They do not use the GDH extension anymore but parton-hadron duality in the resonance region. Hence our experiment provides also, according to this method, experimental data to extract higher twists.

A.9.1 Extraction Method for the twist four matrix elements.

The method is to use the OPE to extend in higher twists the n-th moment of a structure function:

$$M_n(Q^2) \equiv \int_0^\infty x^{n-2} F(x, Q^2) dx = \sum_{k=0}^{\infty} E_{n_k}(\frac{Q^2}{\mu^2}) M_{n_k}(\mu^2)(\frac{1}{Q^2})^k \tag{A.9}$$

where M_{n_k} is the nucleon matrix element of higher twist operator, μ a renormalisation mass scale and E_{n_k} a dimensionless coefficient expanded as a power serie of α_s. In the DIS region, twist 2 dominates. One uses a fit of a nucleon structure function to the DIS data to estimate and to subtract the twist two contribution in the resonance region where duality stands. Then one uses eq. A.9 and resonance region data to extract M_{n_4}.

Ji and Unrau worked first on an unpolarised structure function [105] then Ji and Melnitchouk [106] use this method and E143 experimental data on the first polarized structure function. They find twist four corrections with a magnitude being in accordance with the sum rule method but with opposite sign. These estimates are smaller by an order of magnitude than with the method initiated by Anselmino et al.

Appendix B

Etude expérimentale de la structure en spin du neutron et de l'Helium 3 à petit Q^2.

B.1 Introduction.

L'interaction forte est une des quatre forces à l'oeuvre dans la nature. Elle gère entre autre la structure du nucléon. La théorie de la Chromodynamique Quantique (QCD) modélise les hadrons comme un ensemble de quarks interagissant par échange de gluons. Une originalité de la force forte est que son intensité croît avec la distance. Il en découle la "liberté asymptotique" qui traduit que les quarks sont quasi-libres quand ils sont sondés avec des photons très virtuels et très énergétiques (i.e. quand on sonde à très courtes distances). Ce domaine cinématique est nommé "domaine de Bjorken" [20]). Dans cette limite l'interaction entre quarks est calculable par la méthode des perturbations (QCD perturbative: ou pQCD). C'est le modèle des partons [75]. Cependant dès que la distance entre quarks augmente l'intensité de la force forte croît et l'interaction devient non perturbative (npQCD). Nous ne connaissons pas à l'heure actuelle de méthode capable de calculer QCD dans le domaine non perturbatif. A encore plus basse énergie les quarks réagissent comme un tout cohérent, le hadron, qui devient le degré de liberté pertinent à ces énergies.

Le nucléon compose la grande majorité de la matière hadronique connue dans l'univers. Sa structure, hors du domaine de Bjorken, est mal connue à cause de la difficulté théorique inhérente à une interaction non perturbative. Il est donc primordial pour notre connaissance fondamentale de la nature, d'explorer plus en avant la structure du nucléon et l'interaction qui la régit.

Comme nous l'avons vu la transition entre le régime perturbatif et le régime non perturbatif s'accompagne d'un changement de description de la force forte: pour QCD les degrés de liberté sont les quarks (fermions) et gluons (bosons vecteurs) alors qu'en physique nucléaire, les degrés de liberté sont les nucléons (fermions) et les pions (bosons vecteurs). L'unification de ces deux descriptions est importante. L'expérience que nous résumons ici étudie de la structure en spin du nucléon dans le domaine de transition entre les deux descriptions. Grâce à des règles de somme portant sur des quantités caractérisant la structure en spin du nucléon, nous pourrons obtenir des résultats expérimentaux permettant d'étudier la transition entre le domaine assez bien compris de pQCD et celui mal compris de npQCD. L'étude de cette transition permettra de mieux comprendre npQCD. La grande qualité de nos données permet également de tester différents modèles décrivant l'interaction forte.

Notre expérience (expérience E94010) est le fruit d'une collaboration internationale. Elle s'est déroulée entre septembre et décembre 1997 auprès de l'accélérateur d'électrons Thomas Jefferson National Accelerator Facility (ou Jefferson Lab). Il délivre un faisceau continu d'électrons accélérés à des énergies de l'ordre de quelques GeV. Nous mesurons la diffusion inclusive d'électrons polarisés sur une cible polarisée d'^{3}He tenant lieu de cible effective de neutrons polarisée. Les données recueillies permettent l'étude de la structure en spin du neutron, en particulier des fonctions de structure en spin $g_1(Q^2,\nu)$ et $g_2(Q^2,\nu)$ ainsi que les sections efficaces $\sigma^{TT}(Q^2,\nu)$ et $\sigma^{TL}(Q^2,\nu)$ [134].

Dans la section B.2 nous définissons les variables cinématiques d'intérêt. Puis dans la section B.3 nous présentons des règles de somme et expliquons comment elles vont nous aider à mieux comprendre l'interaction forte et la structure du neutron. Dans la partie B.4 nous présentons l'appareillage de l'expérience et les résultats de l'analyse des données. La dernière partie, section B.5, présentera les résultats de l'expérience.

B.2 Définitions.

Dans notre expérience nous étudions la réaction inclusive doublement polarisée $\overrightarrow{^3He}(\overrightarrow{e},e')X$. Nous définissons dans la figure B.1 les variables cinématiques utiles:

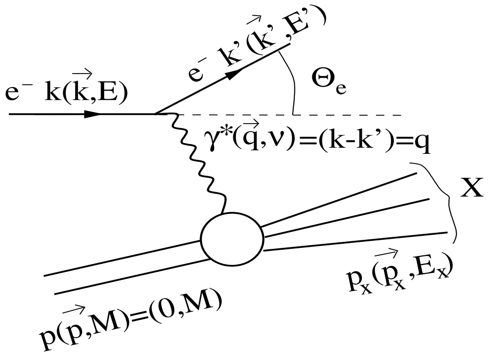

Figure B.1: Diagramme au premier ordre de diffusion d'un électron par un noyau.

ν=E-E' est l'énergie du photon virtuel. On définit également:

- $Q^2 \equiv -(k-k')^2 = -q^2$. $Q^2 \simeq 4EE'sin^2\frac{\theta_e}{2}$ pour les électrons ultrarelativistes.
- $W^2 \equiv (p+q)^2 = M_t^2 + 2pq - Q^2$ où M_t est la masse du centre de diffusion.
- $x \equiv \frac{Q^2}{2p.q} = \frac{Q^2}{2M\nu}$, la variable d'échelle (ou variable de Bjorken).

B.3 Règles de somme.

Nous présentons ici les règles de somme de Bjorken [19] et de Gerasimov-Drell-Hearn (GDH) [80], [63], [87]. La première est valable dans le domaine de Bjorken et la seconde à $Q^2 = 0$. La vérification expérimentale de ces relations constitue un test de la théorie [75]. Ainsi la vérification de la règle de somme de Bjorken a conforté la conviction que QCD était une théorie valide de l'interaction forte. Nous verrons qu'une généralisation de la règle de somme de GDH à $Q^2 > 0$ nous donne accès à un outil d'étude privilégié de l'interaction forte.

B.3.1 La règle de somme de Bjorken

La règle de somme de Bjorken s'écrit:

$$\int_0^1 (g_1^p(x) - g_1^n(x))dx = \frac{1}{6} g_a \tag{B.1}$$

où g_a est la constante de couplage axial mesurée dans la désintégration β du neutron. $g_1^p(x)$ et $g_1^n(x)$ sont les première fonctions de structure en spin du proton et du neutron. Cette règle de somme peut être généralisée à Q^2 fini par la technique du développement en produit d'opérateurs [134]:

$$\int_0^1 (g_1^p(x,Q^2) - g_1^n(x,Q^2))dx = \frac{1}{6} g_a f(Q^2) + HT(Q^2) \tag{B.2}$$

où $f(Q^2)$ vient des corrections radiatives de QCD (équations d'Altarelli-Parisi ou DGLAP, [147]) et $HT(Q^2)$ est le twist d'ordre quatre. Aux premiers ordres on a [93],[102]:

- $f(Q^2) = 1 - \frac{\alpha_s(Q^2)}{\pi} - 3.58 \left(\frac{\alpha_s(Q^2)}{\pi}\right)^2 - 20.2 \left(\frac{\alpha_s(Q^2)}{\pi}\right)^3 + ...$
- $HT(Q^2) = \frac{b_{p-n}}{Q^2}$ (twist 4).

La règle de somme de Bjorken a été vérifiée avec une précision de 10% [67].

B.3.2 La règle de somme de GDH.

La règle de somme de GDH, établie pour la photoproduction, s'écrit:

$$\int_{\nu_{seuil}}^{\infty} \frac{\sigma^{1/2}(\nu) - \sigma^{3/2}(\nu)}{\nu} d\nu = -2\pi^2 \alpha \frac{\kappa^2}{m_t^2} \tag{B.3}$$

où:

- $\sigma(\nu)$ sont les sections efficaces inclusives de photoproduction dans le cas de photons d'hélicité alignée avec le spin de la cible (3/2) ou anti-alignée (1/2).
- α est la constante de structure fine.
- m_t et la masse de la particule cible.
- ν est l'énergie du photon. Le seuil de production du pion dans le repère du laboratoire est: $\nu_{seuil} = m_\pi + (m_\pi^2 + Q^2)/2m_t$ avec $Q^2 = 0$ et m_π la masse du pion.
- κ est le moment magnétique anomal de la cible en magnéton de Bohr.

La validité de la règle de somme a été très discutée [2], [12], [13], [14], [18], [29], [54], [61], [115], [144], [158], [173] et sa vérification est en cours [1], [6]. Ce n'est pas l'objet principal de notre expérience bien que nos données éclairent la question.

On peut penser que l'extension de la règle de somme à $Q^2 > 0$ se fait naturellement en utilisant les sections efficaces d'électroproduction ($Q^2 > 0$) plutôt que les sections efficaces de photoproduction ($Q^2 = 0$. Cependant il y a ambiguïté sur l'expression du flux de photons virtuels (choix arbitraire, les conventions les plus utilisés sont celles de Hand et de Gilman) et sur le rôle de g_2, se référer à la revue de Drechsel et al [62]. En conséquence il existe plusieurs généralisations cette règle de somme. [8], [16], [26], [27], [28], [29], [31], [60], [101], [102], [103], [107], [108], [140], [160], [164], [165], [179].

Dans le domaine de diffusion profondément inélastique la généralisation se fait sans ambiguïté (car la fonction $g_2(x, Q^2)$ tend vers zéro quand on approche le domaine de Bjorken). On définit le premier moment de $g_1(x, Q^2)$ comme:

$$\Gamma_N(Q^2) \equiv \int_0^1 g_1^N(x, Q^2)dx \tag{B.4}$$

On a l'intégrale de GDH:

$$I_N(Q^2) \equiv \int_{\nu_{seuil}}^{\infty} \frac{\sigma^{1/2}(Q^2, \nu) - \sigma^{3/2}(Q^2, \nu)}{\nu} d\nu = \frac{2M_N^2}{Q^2} \Gamma_N(Q^2) \tag{B.5}$$

où M_n est la masse du nucléon. Notons que:

- On a généralisé seulement la partie intégrale de la règle de somme. On ne parle plus de "règle de somme de GDH" mais simplement "d'intégrale de GDH".
- Si on soustrait l'intégrale de GDH sur le proton à celle sur le neutron, on retrouve l'intégrale de Bjorken. On voit ici la connexion intime entre ces deux intégrales.

Comme nous l'avons dit il existe plusieurs méthodes pour généraliser l'intégrale de GDH. Nous ne citons[1] que celle de X. Ji [107], [108] car elle possède plusieurs attraits:

- Elle généralise la règle de somme et non uniquement l'intégrale.
- Elle lie l'intégrale à l'amplitude de diffusion Compton vers l'avant. Nous allons voir l'intérêt important de cette relation.

Soit $S_1(Q^2, \nu)$ la partie polarisée de l'amplitude de diffusion Compton vers l'avant. On définit $\overline{S_1} \equiv S_1 - S_1^{el}$ comme $S_1(Q^2, \nu)$ où la contribution élastique a été soustraite. On a alors la règle de somme généralisée:

$$\overline{S_1}(Q^2, \nu = 0) = 4 \int_{Q^2/2M_n}^{\infty} \frac{d\nu'}{\nu'} G_1((Q^2, \nu')) \tag{B.6}$$

où $G_1(Q^2, \nu) = g_1(Q^2, \nu)/(M_n^2 \nu)$.

Dans le domaine de la diffusion profondément inélastique on calcule $\overline{S_1}(Q^2, \nu = 0)$ avec la technique du développement en produit d'opérateurs (ou en développement en

[1] se reporter à la version anglaise pour la présentation des autres généralisations, les différentes modélisations de l'intégrale de GDH généralisée sur le neutron sont représentées sur la figure B.2

twists supérieurs) [134]. On attend que le développement en twist soit valide du domaine de Bjorken jusqu'à $Q^2 = 0.5$ GeV^2 [101].

A bas Q^2 on utilise la théorie des perturbations chirales pour exprimer $\overline{S_1}(Q^2, \nu = 0)$. Elle doit être valide de $Q^2 = 0$ GeV^2 jusqu'à $Q^2 = 0.2$ GeV^2 [107]. Certains auteurs espèrent repousser cette limite à $Q^2 = 0.4$ GeV^2 [30], [135].

Ces domaines et le domaine à Q^2 intermédiaire sont couverts par notre expérience (de $Q^2 = 0.1$ GeV^2 à $Q^2 = 1$ GeV^2), voir figure B.3.

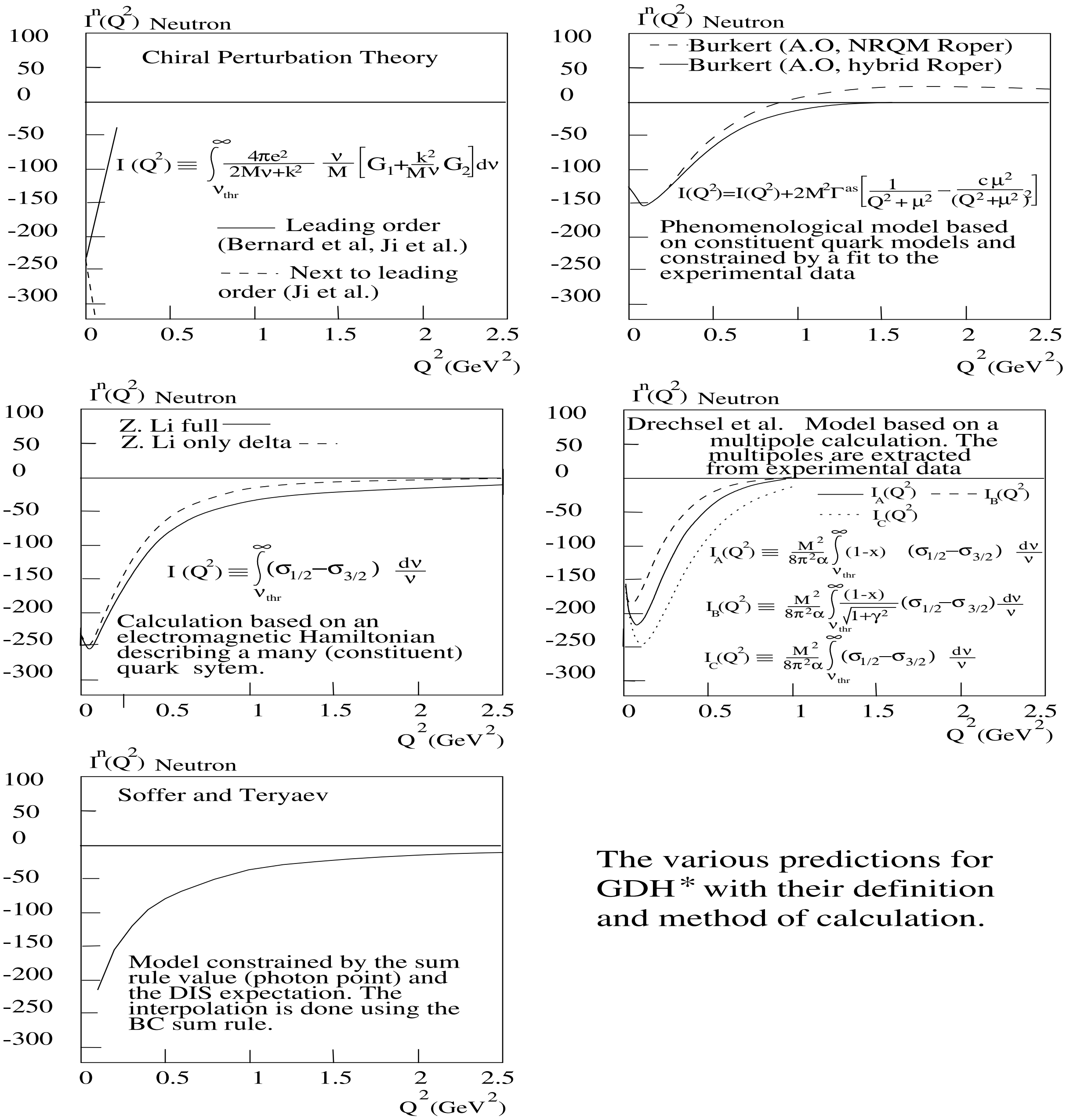

Figure B.2: Prédictions de différents modèles sur l'évolution en Q^2 de l'intégrale de GDH sur le neutron.

Nous avons donc une règle de somme valide sur tout le domaine de l'interaction forte, en particulier dans la zone de transition. Pour la première fois nous avons accès à une quantité calculable rigoureusement dans tout le domaine de l'interaction forte: l'amplitude de diffusion Compton vers l'avant. Cette quantité est ainsi un outil unique d'études de la force forte. Bien qu'expérimentalement cette quantité ne puisse être mesurée directement, elle peut cependant être comparée à des mesures expérimentales grâce à la règle de somme généralisée. Sur le plan théorique les calculs sont valables sur presque tout le domaine et peut être le domaine complet. La comparaison des calculs avec nos données expérimentales fixera le domaine de validité des développements. Au cas où les domaines se recouvriraient nous aurions alors à notre disposition un outil de calcul valable sur tout le domaine de l'interaction forte. Ce serait une avance significative pour notre compréhension.

B.4 L'expérience.

L'objet de notre expérience est l'étude de la structure en spin du neutron, en particulier la mesure de l'intégrale GDH généralisée et les fonctions de structure en spin dans la région de transition. Notre expérience se déroule dans la salle expérimentale A (ou Hall A) de Jefferson Lab. Nous décrivons brièvement ici la cinématique, l'appareillage nécessaire à l'expérience et l'analyse des données.

B.4.1 Couverture cinématique.

Le domaine cinématique (Q^2, W) couvert par notre expérience est présenté dans la figure B.3.

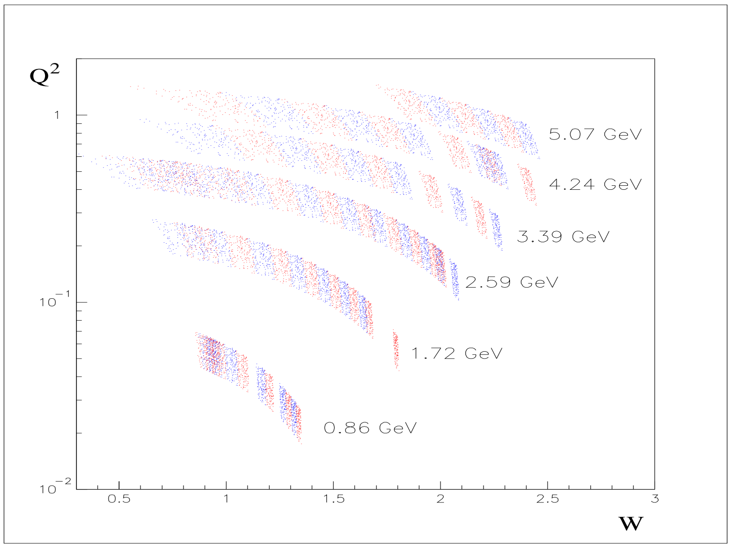

Figure B.3: Couverture cinématique de l'expérience. L'axe des ordonnées est Q^2 (en échelle log et en GeV^2). L'axe des abscisses est la masse invariante W (en GeV). Deux réglages consécutifs des spectromètres sont de différentes couleurs. Chaque bande correspond à une énergie du faisceau d'électrons.

Le spectre couvre la diffusion quasi-élastique, la région des résonances (la couverture n'est pas complète pour les plus basses énergies mais couvre au moins le Δ) et le début du domaine de diffusion profondément inélastique. La diffusion élastique est également mesurée pour les trois plus basses énergies. Idéalement les bandes devraient être horizontale, c'est à dire à Q^2 fixé au point où se fera l'intégration. Les contraintes de l'appareillage ne nous le permettent pas et nous avons choisi de couvrir le domaine de façon la plus uniforme possible. On intégrera à Q^2 fixé en interpolant entre les différentes bandes. Notons également qu'idéalement on devrait intégrer jusqu'à ν infini ce qui n'est pas réalisable. Cependant du fait de la pondération en $1/\nu$ de l'intégrale GDH les résonances de plus faible masse saturent l'intégrale GDH (en particulier le Δ, [27], [28], [164], [165], [179]). Notons que le rôle principale des données à 0.86 GeV est de servir de point de départ aux corrections radiatives (par la technique d' "unfolding" où les données de plus basses énergies incidentes sont utilisées pour corriger les données de plus hautes énergies de la "contamination" dues aux pertes d'énergies des électrons du faisceau. Les données doivent également être corrigées des pertes et "contamination" dues aux radiations par les électrons diffusés).

B.4.2 L'appareillage expérimental.

L'expérience consiste en la diffusion d'un faisceau d'électrons polarisés longitudinalement par une cible d'^{3}He polarisée transversalement ou longitudinalement par rapport à la direction du faisceau. Ces deux directions de polarisation permettent de séparer les deux fonctions de structure en spin $g_1(x,Q^2)$ et $g_2(x,Q^2)$. La réaction inclusive $\overrightarrow{^3He}\,(\overrightarrow{e},e')\,X$ est caractérisée par deux spectromètres à haute résolution quasiment identiques et situés à $\pm 15.5^o$ par rapport à la direction du faisceau. Il ne s'agit pas de détection en coïncidence. Nous utilisons simplement deux spectromètres pour doubler notre angle solide de détection. De plus la différence des résultats finaux entre les deux spectromètres permet une estimation de nos erreurs systématiques. La salle expérimentale est représenté dans la figure B.4.

B.4.3 Le faisceau d'électrons.

Le faisceau d'électrons est produit par une source d'arséniure de gallium contraint. La source est éclairée par un laser polarisé circulairement droit ou gauche. Sa polarisation détermine l'état d'hélicité du faisceau d'électrons. Cette hélicité est inversée à une fréquence de 1 Hz ou de 30 Hz pour éviter les erreurs systématiques dans nos mesures d'asymétrie.

Le faisceau est accéléré jusqu'à environ 45 MeV puis injecté dans un premier linac qui l'accélére d'environ 500 MeV. Un arc de recirculation reinjecte le faisceau dans un second linac identique et parallèle au premier. Un second arc peut reinjecter le faisceau dans le premier linac. Cette boucle est appelée une "passe" et on peut accélérer le faisceau jusqu'à 5 passes avant de le délivrer dans la salle expérimentale.

Energie.

La mesure absolue de l'énergie du faisceau est faite dans la salle expérimentale par deux appareils de mesure indépendants. Le premier, appelé "ARC" [51], mesure la déflexion du faisceau d'électrons dans un champ magnétique connu. Le second, appelé "eP" [150], mesure en coïncidence les angles des particules issues de la réaction élastique p(e,e'p). Cette mesure permet de remonter à l'énergie du faisceau. La précision de ces deux appareils est de quelques 10^{-4}. Ils étaient tout deux en période d'essai durant notre expérience et n'ont pas toujours pu fournir de mesure d'énergie. Notamment aucune mesure

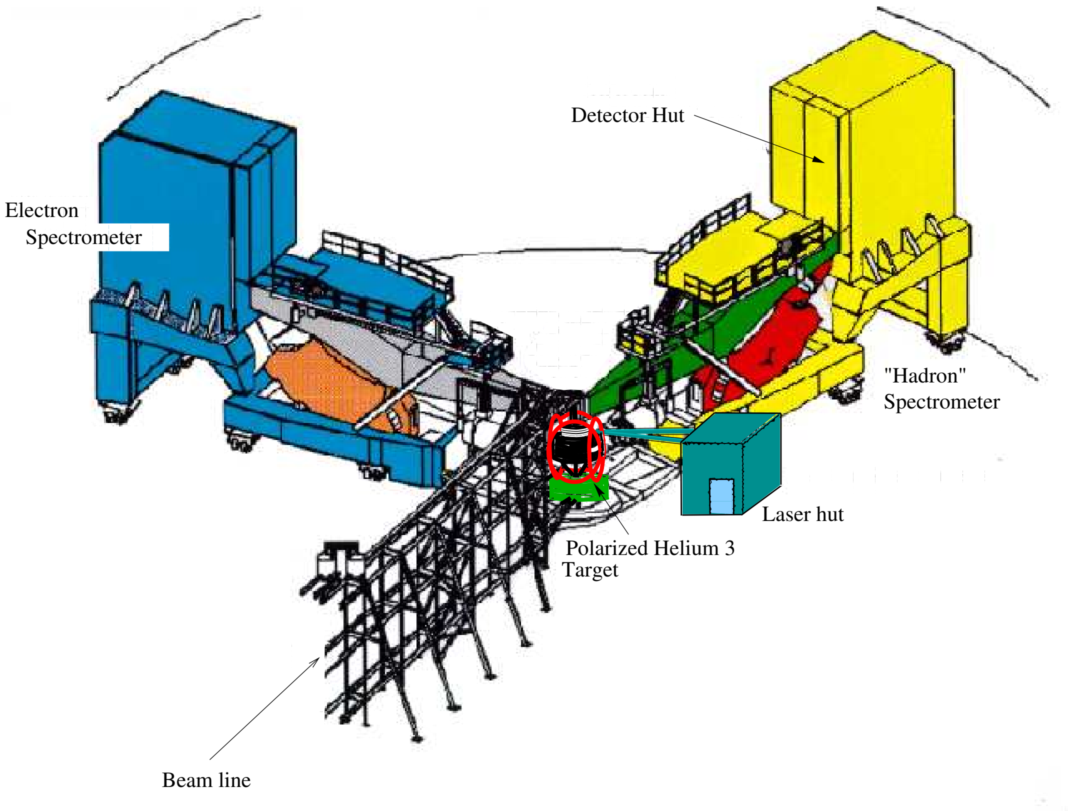

Figure B.4: La salle expérimentale A (Hall A).

d'énergie n'est disponible pour les deux plus basses énergies. Nous avons utilisé dans ce cas nos données élastiques pour mesurer l'énergie [40]. L'erreur sur ces mesures est de 10^{-3}. Ces précisions sont suffisantes pour notre expérience comme nous le verrons dans l'estimation de l'erreur systématique, section B.4.6. La table ci-dessous donne les résultats des mesures d'énergie [17], [50], [156]:

Nombre de Passes	ARC	Elastique	eP
1	-	862.0	-
2 (période 1)	-	1717.9	-
2 (période 2)	-	1716.9	1717.9±0.39 (stat)±0.2 (syst)
3	2581.1	-	-
4	-	-	3381.8±0.6 (syst)
5	4238.2	-	4238.6±0.36 (stat)±0.7 (syst)
5	5058.2	-	-

Polarisation.

La polarisation du faisceau est mesurée par un polarimètre Møller également situé dans la salle expérimentale [167]. Les polarisations moyennes pour chaque énergie de faisceau sont données dans le tableau ci-dessous [35]. L'erreur systématique est d'environ 3%, l'erreur statistique est négligeable.

Energie (GeV)	Polarisation moyenne
1.718 (période 1)	66.2 %
3.382	69.8 %
1.718 (période 2)	70.9%
4.239	70.5%
0.862	70.9%
2.581	68.9%
5.059	70.1%

Intensité

La mesure de l'intensité du faisceau est importante puisque le flux d'électrons incident est un des facteurs de normalisation de la section efficace. Elle est également importante pour les mesures d'asymétries: L'hélicité du faisceau est inversée à une fréquence de 1 ou 30 Hz. Si le nombre d'électrons contenus dans un paquet d'hélicité plus diffère de celui d'un paquet d'hélicité moins, on crée une fausse asymétrie ("asymétrie de charge") biaisant notre mesure. Le BCM (Beam Current Monitor) [124] est un ensemble de deux cavités haute fréquence encadrant un moniteur UNSER. Il mesure en ligne l'intensité du faisceau avec une précision de 1% [156] et son asymétrie de charge. En utilisant les mesures sur cibles non polarisées on montre que les corrections d'asymétrie de charge sont bien contrôlés: Les asymétries mesurées sont compatibles avec zéro [47].

Pendant l'expérience nous avons utilisé un courant variant de 3 à 15 μA. Bien que l'accélérateur eût pu délivrer jusqu'à 100 μA le meilleur compromis entre le taux de comptage, la dégradation de la cible par le faisceau et la dépolarisation de la cible était un courant de 10 μA.

Balayage et Position du faisceau

Le faisceau balaie la cible à une fréquence d'environ 20 kHz sur un rayon de quelque mm afin de répartir le dépôt de chaleur [38]. Quatre antennes (Beam Position Monitor) ainsi que les données des dipôles de balayage permettent de reconstruire la position dans un plan perpendiculaire au faisceau [48]. l'erreur de position est inférieure ùn mm.

B.4.4 La cible polarisée.

Nous avons construit une cible polarisée d'^{3}He que nous utilisons comme une cible effective de neutrons polarisée. En effet, à cause de la faible durée de vie du neutron libre, il n'existe pas de cible de neutron pure suffisamment dense. Le spin du noyau d'^{3}He vient de son neutron car le principe de Pauli oblige les deux protons du noyau à avoir leurs spins anti-alignés. Ainsi les protons, au premier ordre, ne contribuent pas au spin du noyau d'^{3}He et une telle cible peut être vue, du point de vue du spin, comme une cible de neutrons polarisés diluée par un ensemble de protons non polarisés. En fait les protons contribuent de l'ordre de 10% au spin de l'^{3}He à cause d'effets nucléaires [159].

La cible est un cylindre de verre de longueur 40 cm rempli d'^{3}He gazeux sous 12 Atm environs et 70 ^{o}c (en condition d'utilisation). La longueur et la haute densité de la cible permettent de conserver un taux de comptage raisonnable (de l'ordre du kHz) en dépit de la nature gazeuse de la cible. Le cylindre est connecté à une sphère de verre portée à environ 250 ^{o}c où l'^{3}He, mélangé à du Rubidium gazeux, est polarisé. La polarisation de la cible se fait en trois étapes:

- Les atomes du gaz de Rb de la chambre sphérique sont optiquement pompés avec un ensemble de lasers polarisés. C'est à dire que l'on dépeuple un des états de spin de l'unique électron de valence du Rb au profit de l'autre état de spin.
- La polarisation du Rb est transmise au noyau d'^{3}He par transfert de spin durant une collision entre les deux atomes.
- L'^{3}He polarisée se répand dans le cylindre cible par diffusion et convection. Le Rb reste, lui, dans la sphère grâce au gradient thermique entre la sphère et le cylindre.

La cible peut être pompée dans la direction transverse ou longitudinale par rapport à la direction du faisceau. Cela permet de mesurer avec une haute précision g_1 (quantité essentiellement longitudinale) et g_2 (quantité essentiellement transverse) ainsi que l'intégrant de la règle de somme GDH.

La polarisation de la cible est mesurée par Résonance Magnétique Nucléaire calibrée par deux techniques indépendantes [88], [89], [99], [122]:

1. La mesure de la polarisation thermique (connue) des protons d'une cible d'eau identique à la cible d'^{3}He.
2. La Résonance Paramagnétique Electronique.

Les deux calibrations sont en accord. La polarisation de la cible est connue à 4% près [99]. Sur la figure B.5 est donnée la polarisation de la cible durant l'expérience.

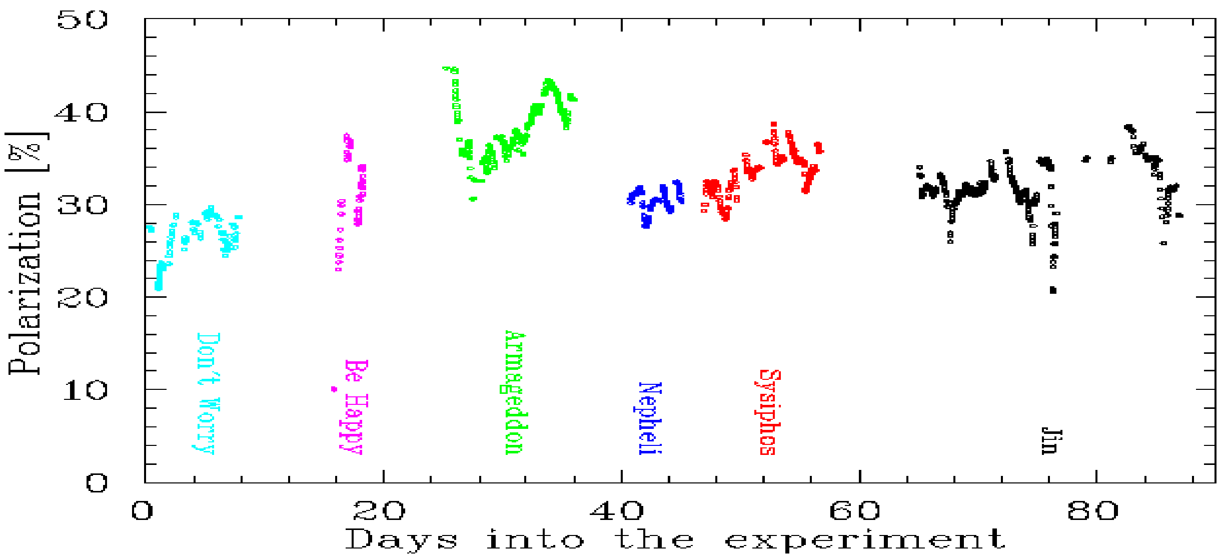

Figure B.5: La polarisation de la cible durant l'expérience.

B.4.5 Les spectromètres à haute résolution.

Les deux spectromètres à haute résolution de la salle expérimentale A sont indépendamment utilisés pour mesurer le moment des électrons diffusés. Leur angle solide de détection est d'environ 6 mSr. L'acceptance et le transport magnétique des spectromètres ont fait l'objet d'une prise de données ainsi que d'une analyse dédiée à l'expérience [111], [45], [131]. La résolution en moment est de l'ordre de $\Delta P/P \simeq 10^{-4}$.

Un ensemble de détecteurs est installé derrière les éléments magnétiques du spectromètres:

- Deux plans de scintillateurs déclenchent l'acquisition. L'efficacité de cet ensemble est typiquement de 90%.
- Deux paires de chambres à fils mesurent la trajectoire de la particule à la sortie du spectromètre (angles et positions) ce qui permet la détermination du vertex à la cible et mesure du moment. L'inéfficacité de détection est négligeable. L'inefficacité du programme de reconstruction des traces est de quelques pourcent [46].
- Deux détecteurs indépendants (un compteur Čerenkov et un calorimètre de verre au plomb) identifient les particules afin de rejeter les π^-. L'efficacité de rejet globale est de l'ordre de $\simeq 10^{-4}$ [120], [161], [162] ce qui est largement suffisant pour notre expérience: En effet, le rapport π^-/e^- n'a pas dépassé 5.

Comme nous l'avons mentionné, des données ont été prises à l'aide d'un ensemble de cibles minces de ^{12}C et d' une plaque percée de trous de positions connus ("sieve slit") afin d'étudier l'acceptance des spectromètres et leur transport magnétique. L'utilisation des cibles minces permet de contraindre la position du vertex pour l'étude du spectromètre. La "sieve slit" permet, elle, de contraindre les angles de diffusions.

B.4.6 Mesure de l'erreur systématique.

Les données sur le ^{12}C nous permettent d'estimer notre niveau de contrôle des facteurs suivants entrant dans le calcul de la section efficace:

- L'angle solide des spectromètres.
- Les efficacités des détecteurs.
- Le flux d'électrons incidents.
- La correction de temps mort de l'acquisition.

Une simulation reproduit notre expérience. Elle utilise les facteurs de forme du ^{12}C connus à 1% [32]. L'accord entre les sections efficaces simulées et mesurées est meilleur que 4% [111].

Nos données élastiques sur l'^{3}He polarisé comparées à une simulation [44] permettent une autre vérification, plus globale, du niveau de contrôle de nos systématiques. En plus des facteurs déjà cités nous vérifions:

- La densité de la cible en condition d'opération.

- Les polarisations de la cible et du faisceau.
- L'acceptance dans le cas d'une cible étendue.
- La dilution de l'asymétrie due aux matériaux non polarisés à l'intérieur de la cible.
- L'asymétrie de charge.
- Le contrôle des erreurs corrélées à l'hélicité, en particulier le temps mort de l'acquisition.

Nos données expérimentales sont en accord avec notre simulation [40], [50]. L'erreur systématique sur la section efficace élastique mesurée est typiquement de 6%. Elle est de 5% pour la simulation. L'erreur systématique sur l'asymétrie élastique est de 6%. Dans tout les cas l'erreur statistique est négligeable devant l'erreur systématique.

En conclusion l'écart entre la simulation et l'expérience est une estimation de l'erreur systématique entachant notre expérience. Elle est typiquement de 6%. L'erreur systématique des données inélastiques est donc de cet ordre. Néanmoins le calcul n'a pas encore été fait et nous l'estimons pour l'instant à 10%.

B.5 Résultats.

B.5.1 Résultats bruts.

Les asymétries longitudinale ($A_{\parallel}$) et transverse ($A_{\perp}$) sur l'^{3}He sont présentées dans la figure B.6. Les sections efficaces sont présentées dans la figure B.7. On note sur ces deux figures la transition du domaine hadronique au domaine partonique: Les structures disparaissent pour laisser place au comportement plus doux à grande énergie et grand ν caractérisant le domaine de la diffusion profondément inélastique. Notons également:

- la grande asymétrie au niveau du Δ. Elle est d'environ 2% et semble indépendante de Q^2.
- Le fait que $A_{\parallel}$ et $A_{\perp}$ sont semblables mais de signe opposé dans la région des résonances. Nous discuterons plus loin ce résultat.
- $A_{\parallel}$ domine largement $A_{\perp}$ dans le domaine de la diffusion inélastique profonde, en accord avec le modèle des partons et avec les expériences précédentes du SLAC ou du CERN étudiant la structure en spin du nucléon.
- Il est difficile de voir les résonances, à l'exception du Δ. Cela vient du fait que notre expérience est inclusive. Les effets nucléaires atténuent aussi significativement les résonances [34].

B.5.2 Les fonctions de structure en spin.

La figure B.8 présente les fonctions de structure en spin $g_1^{^3He}(Q^2,\nu))$ et $g_2^{^3He}(Q^2,\nu)$. Elles sont extraites en soustrayant les sections efficaces d'hélicité plus et moins (cf. document en anglais):

$$\frac{d^2\sigma^{\downarrow\Uparrow}}{dE'd\Omega}-\frac{d^2\sigma^{\uparrow\Uparrow}}{dE'd\Omega}=\frac{4\alpha^2}{M_N^3Q^2}\frac{E'}{E}[\frac{g_1(Q^2,\nu)}{\nu}M_N^2(E+E'cos\theta)-Q^2M_N^2\frac{g_2(Q^2,\nu)}{\nu^2}] \tag{B.7}$$

$$\frac{d^2\sigma^{\uparrow\Rightarrow}}{dE'd\Omega}-\frac{d^2\sigma^{\uparrow\Leftarrow}}{dE'd\Omega}=\frac{4\alpha^2}{M_N^3Q^2}\frac{E'^2}{E}sin\theta[M_N^2\frac{g_1(Q^2,\nu)}{\nu}+2EM_2^N\frac{g_2(Q^2,\nu)}{\nu^2}] \tag{B.8}$$

En inversant le système d'équations on obtient les fonctions de structures.

On note que, de même que $A_\parallel$ et $A_\perp$, $g_1^{^3He}(Q^2,\nu)$ et $g_2^{^3He}(Q^2,\nu)$ sont images miroirs. En effet $g_1(Q^2,\nu)$ est essentiellement une quantité longitudinale et $g_2(Q^2,\nu)$ une quantité transverse. On peut comprendre cette symétrie de deux points de vue:

- Dans la région du Δ, la transition Nucléon-Δ se fait essentiellement par basculement de spin (le rapport des multipôles E_{1+}/M_{1+} de l'ordre du pourcent): les sections efficaces sont essentiellement transverses et les sections efficaces longitudinales et d'intérférence longitudinale-transverse sont petites. Or la section efficace d'interférence longitudinale-transverse est proportionelle à g_1+g_2 (cf équation 2.20 dans la version anglaise de la thèse). On en déduit donc que $g_2 \simeq -g_1$ dans la région du Δ.

- Au delà du Δ la symétrie de g_1 et g_2 peut s'expliquer en écrivant la relation de Wilczeck-Wandzura [177]:

$$g_2^{ww}(Q^2,x)=\int_x^1 g_1(x',Q^2)\frac{dx'}{x'}-g_1(x,Q^2) \tag{B.9}$$

  où $g_2^{ww}(Q^2,x)$ est similaire à $g_2(Q^2,x)$ mais ne contient pas de twists supérieurs (twists plus grands 2). Dans le domaine des résonances, x est proche de 1 et donc le terme intégrale est petit. On s'attend donc à ce que $g_2^{ww}(Q^2,x) \simeq -g_1(Q^2,x)$. Notre expérience montre qu'en fait $g_2(Q^2,x) \simeq -g_1(Q^2,x)$. Cela implique que les twists d'ordre supérieur sont petits dans le domaine des résonances. Ce résultat peut paraître surprenant puisque les twists supérieurs sont des corrections en puissances de $1/Q$ [134] et qu'ils sont en partie responsables de la cohérence des diffusions dans le domaine des résonances.

B.5.3 La dualité.

Données expérimentales.

Sur la figure B.9 nous comparons nos résultat sur $g_1^{^3He}(Q^2,x)$ en fonction de x à 4.2 GeV (dans les résonances, avec en moyenne $Q^2=0.7\ GeV^2$) avec ceux de l'expérience E154 du SLAC (en diffusion profondément inélastique, les résultats sont évolués a $Q^2=5.0\ GeV^2$). Nous remarquons que si nous lissons nos données, c'est à dire que nous moyennons les effets des résonances, les deux courbes se superposent (sauf peut être dans la région du Δ).

La dualité de Bloom-Gilman (ou dualité hadron-parton).

On a observé que la fonction de structure non polarisée $F_2(x)$ mesurée dans le domaine de la diffusion profondément inélastique (description partonique de la force forte) se recouvre avec $F_2(x, Q^2)$ mesurée dans le domaine des résonances (description hadronique) si on lisse $F_2(x, Q^2)$ (i.e. si on moyenne sur les résonances). C'est la dualité de Bloom-Gilman. Cela signifie que les propriétés d'échelle des fonctions de structure (i.e. l'independance en Q^2), corrigées des effets radiatifs de QCD grâce aux équations DGLAP, sont encore valides dans la zone des résonance si l'on moyenne sur les réactions cohérentes (i.e. sur les résonances). Cela implique que les twists supérieurs doivent être petits dans la région des résonances malgré leur dépendance en $1/Q^{t-2}$ (t est l'ordre du twist). La dualité de Bloom-Gilman avait été constatée pour les fonctions de structure non polarisées et notre expérience montre clairement que la dualité est également vérifiée dans le cas polarisée. Ce résultat est en accord avec le fait que g_1 et g_2 soient images miroirs dans la zone de résonance (figure B.8) puisque la dualité implique que les twists supérieurs sont petits dans la région de transition entre pQCD et npQCD.

Note Ces considérations sont qualitatives puisqu'elles portent sur l'^{3}He pour nos données et sur le neutron pour l'expérience E154.

B.5.4 L'intégrale GDH généralisée.

Définissons l'intégrale GDH généralisée de la façon suivante (voir la section A.4 dans l'appendice A):

$$I(Q^2) = \frac{M_N^2}{4\pi^2\alpha} \int_{seuil}^{\infty} \frac{\sigma^{TT}(Q^2, \nu) d\nu}{\nu}$$

L'intégrant $\sigma^{TT}(Q^2, \nu)$ pour des énergies de faisceau constantes est présenté dans la figure B.10. L'intégration commence au seuil du pion pour le neutron afin d'extraire de ces données l'intégrale sur le neutron . L'intégrale est calculée à Q^2 constant par interpolation entre les données à énergies constantes (figure B.11).

L'intégrale généralisée sur l'^{3}He.

La figure B.12 présente l'intégrale de GDH généralisée portant sur l'^{3}He.

Avant d'interpréter ces données, remarquons que:

- L'intégration ne porte que sur notre domaine cinématique (voir fig. B.3). En particulier l'intégration ne va pas au delà du Δ pour les points de plus bas Q^2 (cf section B.4.1). Néanmoins les études théoriques s'accordent sur le rôle crucial du Δ dans la saturation de l'intégrale, en particulier à bas Q^2, du fait de la pondération de $\sigma^{TT}(Q^2, \nu)$ par $1/\nu$.

- La contribution du quasi-élastique est absente afin d'extraire l'intégrale sur le neutron. Cependant les domaines du Δ et du quasi-élastique se recouvrent et leurs contributions se mélangent. Une bonne séparation nécessite des modèles. Ici nous avons simplement commencé l'intégration à $\sigma^{TT}(Q^2, \nu)$=0. Notons que la contamination et la perte d'une partie de la contribution du Δ ont un effet décroissant sur l'intégrale. En effet $\sigma^{TT}(Q^2,\nu)$ dans le domaine de la réaction quasi-élastique est de signe opposé à $\sigma^{TT}(Q^2,\nu)$ dans les domaines des résonances et de la diffusion inélastique profonde. Un modèle du pic quasi-élastique est nécessaire pour extraire complètement la contamination du quasi-élastique.

- Nous utilisons les données de plus basse énergie comme point de départ des corrections radiatives. Pour les corriger nous devons ou bien utiliser un modèle, soit extrapoler nos données à plus basse énergie. Conséquemment les erreurs systématiques des points à plus bas Q^2 sont plus grandes.

L'intégrale sur le neutron.

L'intégrale de GDH généralisée est le seul résultat sur le neutron que nous présentons. L'extraction du neutron à partir de l'^{3}He [33], [34] dans la zone des résonances pour des quantités non intégrés comme les fonctions de structure ou les sections efficaces se heurte à des difficultés d'ordre théorique. L'intégrale sur le neutron est présentée sur la figure B.13. Sur cette figure nous avons porté les erreurs systématiques de l'expérience hormis celles liées aux corrections radiatives. Notre règle de somme sur le neutron dépend du modèle utilisé pour l'extraction. Nous avons ajouté une erreur systématique de 5% qui tient compte des incertitudes liées à l'extraction.

Tout comme pour l'intégrale sur l'^{3}He il convient de se rappeler:

- Les limites de notre intervalle d'intégration.
- Le fait que l'intégrale est diminuée par l'absence d'une partie du Δ et la contamination du quasi-élastique.
- Les incertitudes systématiques plus importantes liées aux corrections radiatives pour les points de plus bas Q^2.

Ces incertitudes systématiques ne sont pas représentées sur la figure.

Evolution en Q^2 de l'intégrale sur le neutron.

L'évolution en Q^2 de l'intégrale sur le neutron suit la forme prédite par les modèles (voir figure B.14). A cause de notre domaine d'intégration limité et de la contamination du quasi-élastique, nous ne pouvons pas conclure sur la qualité des modèles à reproduire les données. Il est probable que le modèle de Burkert et al, après avoir tenu compte des limitations de nos données expérimentales, simulera une évolution en Q^2 de l'intégrale avec une trop petite amplitude il faut attendre des simulations de GDH$*$ correspondant à notre interval d'intégration.

Nous notons qu'à grand Q^2 nos données sont cohérentes avec celles d'HERMES.

Nous n'avons pas d'indication d'un minimum à bas Q^2, cependant les limitations de nos données dans ce domaine empêche toute conclusion solide. L'existence du minimum est prédit par la plupart des modèles.

Une extrapolation de nos données à Q^2=0 utilisant le modèle le plus récent (Drechsel et al) indiquerait une violation de la règle de somme de GDH. Cependant cette conclusion dépend du modèle choisi: Nos données sont raisonnablement proches du modèle de Z. Li (contraint à Q^2=0 par la règle de somme) et une extrapolation par ce modèle valide la règle de somme. Nous discutons cependant d'une éventuelle violation de la règle de somme sur le neutron dans la version anglaise de cette thèse (voir section 6.4.1).

B.6 Conclusion.

Nous avons vu l'intérêt des règles de somme dans le cadre de la compréhension de la QCD non perturbative. Les travaux de Ji et al fournissent une règle de somme de GDH étendue sur tout le domaine de QCD. Celle-ci permettra pour la première fois de comparer des données expérimentales (l'intégrale de GDH étendue) à une quantité rigoureusement calculable (l'amplitude $\overline{S_1}$).

Notre mesure de la dépendance en Q^2 de l'intégrale étendue de GDH reproduit la forme prédite par les modèles mais non leur amplitude. Cela peut s'expliquer par les limitations de nos données ou par un échec des modèles. Après réductions des intervalles d'intégration des modèles et estimations de la contamination du quasi-élastique, nos données seront suffisamment précises pour pouvoir infirmer ou valider les modèles.

La dualité de Bloom-Gilman a été observée pour la première fois sur une fonction de structure polarisée (peut être à l'exception du domaine du Δ).

Un résultat remarquable est la symétrie de $g_1(Q^2,\nu)$ et $g_2(Q^2,\nu)$. Dans la région du Δ elle s'explique par le fait que la transition Nucléon-Δ se fait principalement par basculement de spin. Au delà de la région du Δ, la symétrie implique, via la relation de Wilczeck-Wandzura, que les twists d'ordre supérieur restent petits dans notre domaine cinématique. Ce fait est en accord avec l'observation de la dualité de Bloom-Gilman.

Les limitations de nos données à bas Q^2 ne nous permettent pas de conclure sur l'existence du minimum prédit par la plupart des modèles ni sur une éventuelle violation de la règle de somme de GDH sur le neutron. Du fait de ces limitations et de l'importance de tels résultats, il est nécessaire de reproduire nos mesures à plus bas Q^2. C'est le rôle de l'expérience E97-110 [112] qui se déroulera en 2001.

Pour conclure nous remarquerons que cette expérience est une première étape dans un vaste effort expérimental international de mesure de l'intégrale de GDH sur tout le domaine de l'interaction forte, y compris au point du photon, et ce sur les deux nucléons (Jefferson Lab Hall A, Hall B, Brookhaven, Bonn, Grenoble, Mayence et Hambourg). Associées á l'intérêt des théoriciens pour ce sujet, ces données devront permettre des avancées importantes dans notre compréhension de la QCD non perturbative.

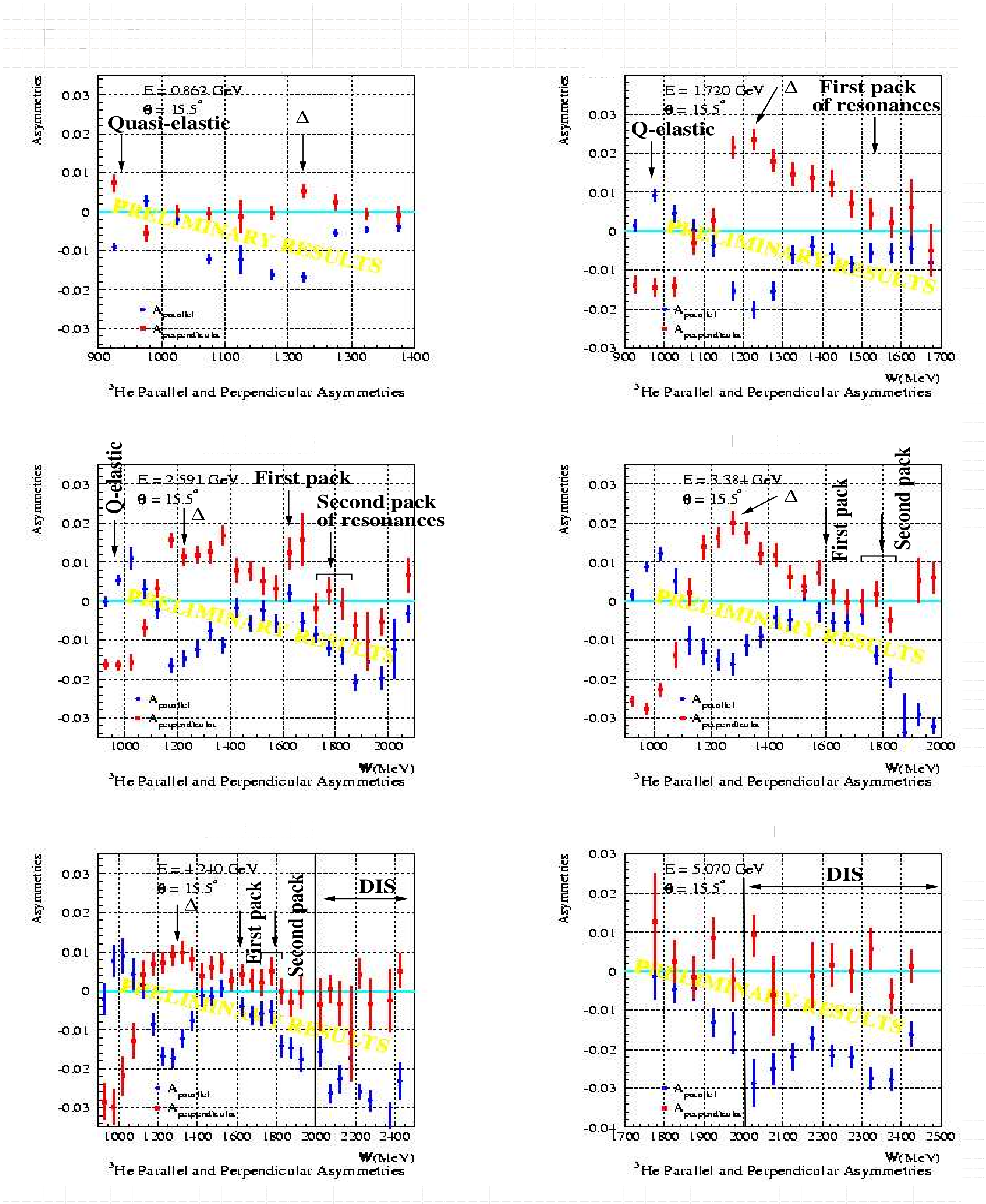

Figure B.6: Asymétries brutes. Le premier ensemble de résonances contient P'_{11}, D_{13} et S_{11}. Le second contient P_{15}, D_{15}, D_{33}, P_{13} $D_{13'}$ et $S_{11'}$. Seules les erreurs statistiques sont présentes.

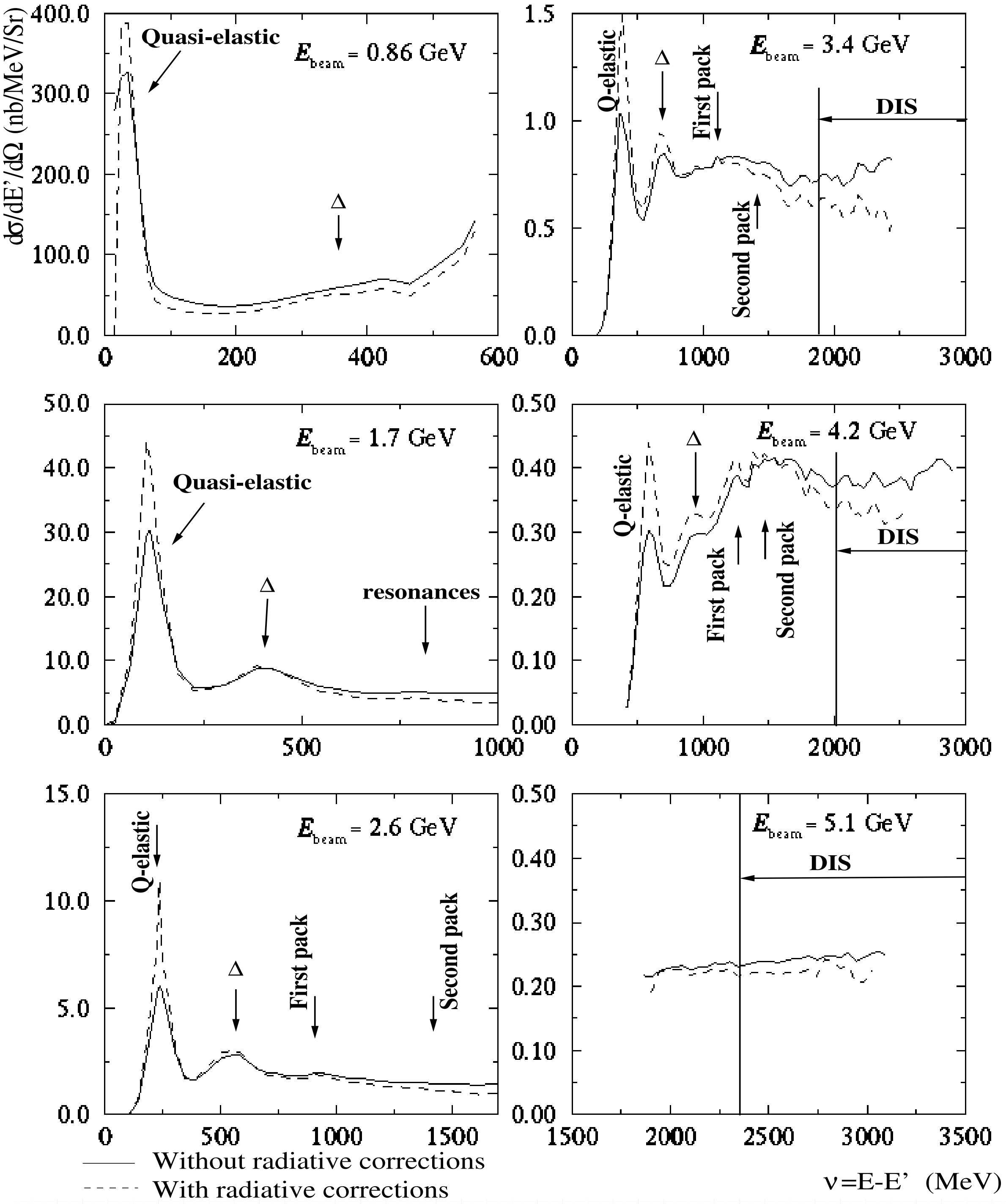

Figure B.7: Sections efficaces sur l'^{3}He. Le premier ensemble de résonances contient P'_{11}, D_{13} et S_{11}. Le second contient P_{15}, D_{15}, D_{33}, P_{13} $D_{13'}$ et $S_{11'}$. Seules les erreurs statistiques sont présentes.

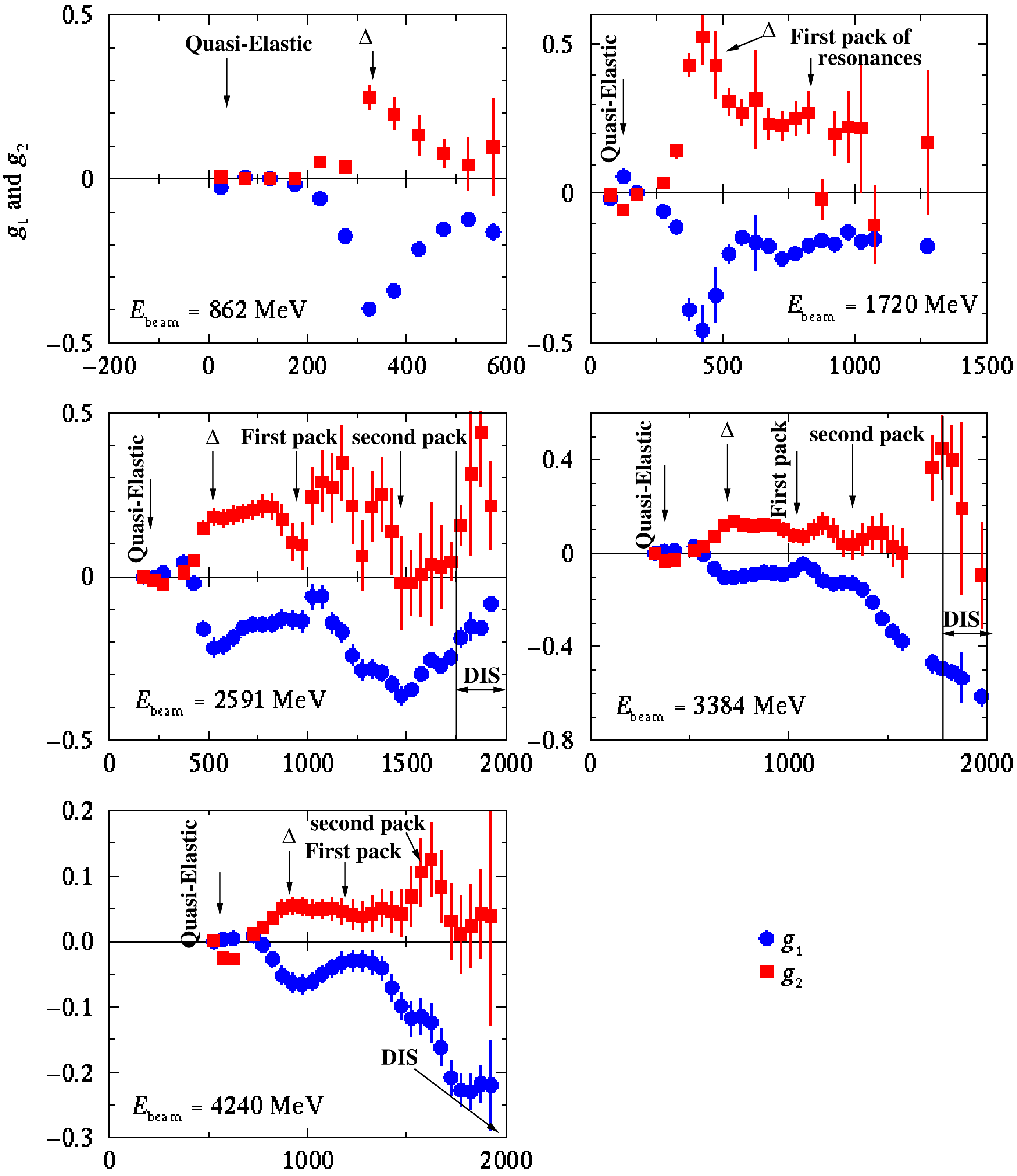

Figure B.8: Les fonctions de structure en spin $g_1^{^3He}(Q^2,\nu)$ et $g_2^{^3He}(Q^2,\nu)$. Le premier ensemble de résonances contient P_{11}', D_{13} et S_{11}. Le second contient P_{15}, D_{15}, D_{33}, P_{13} $D_{13'}$ et $S_{11'}$. Seules les erreurs statistiques sont présentes.

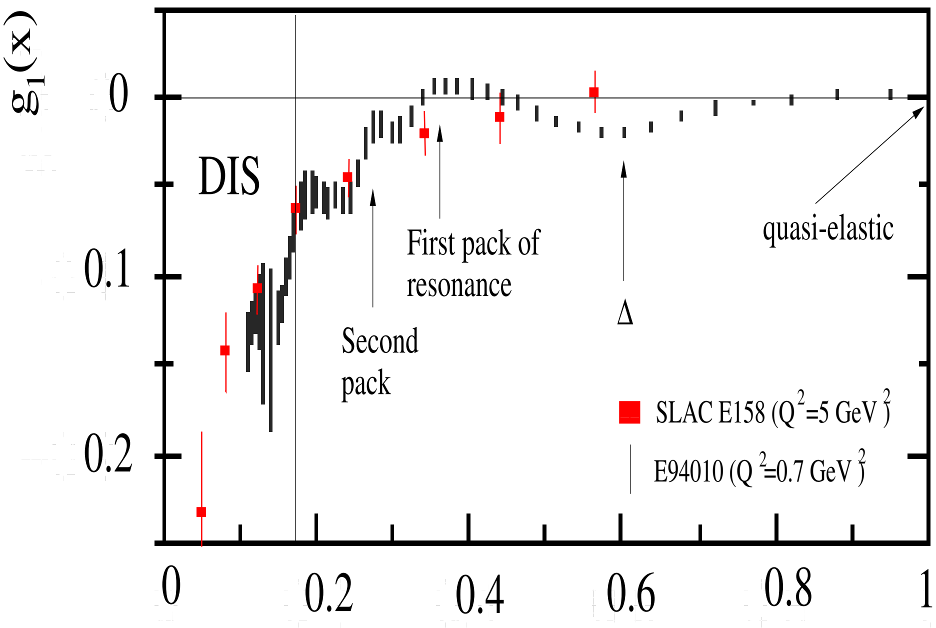

Figure B.9: Comparaison de g_1^{3He} issu de notre expérience avec g_1^n de l'expérience E154. Les positions des résonances sont valables uniquement pour nos données, les données du SLAC sont toutes dans le domaine de la diffusion inélastique profonde. Dans notre cas seules les erreurs statistiques sont présentes.

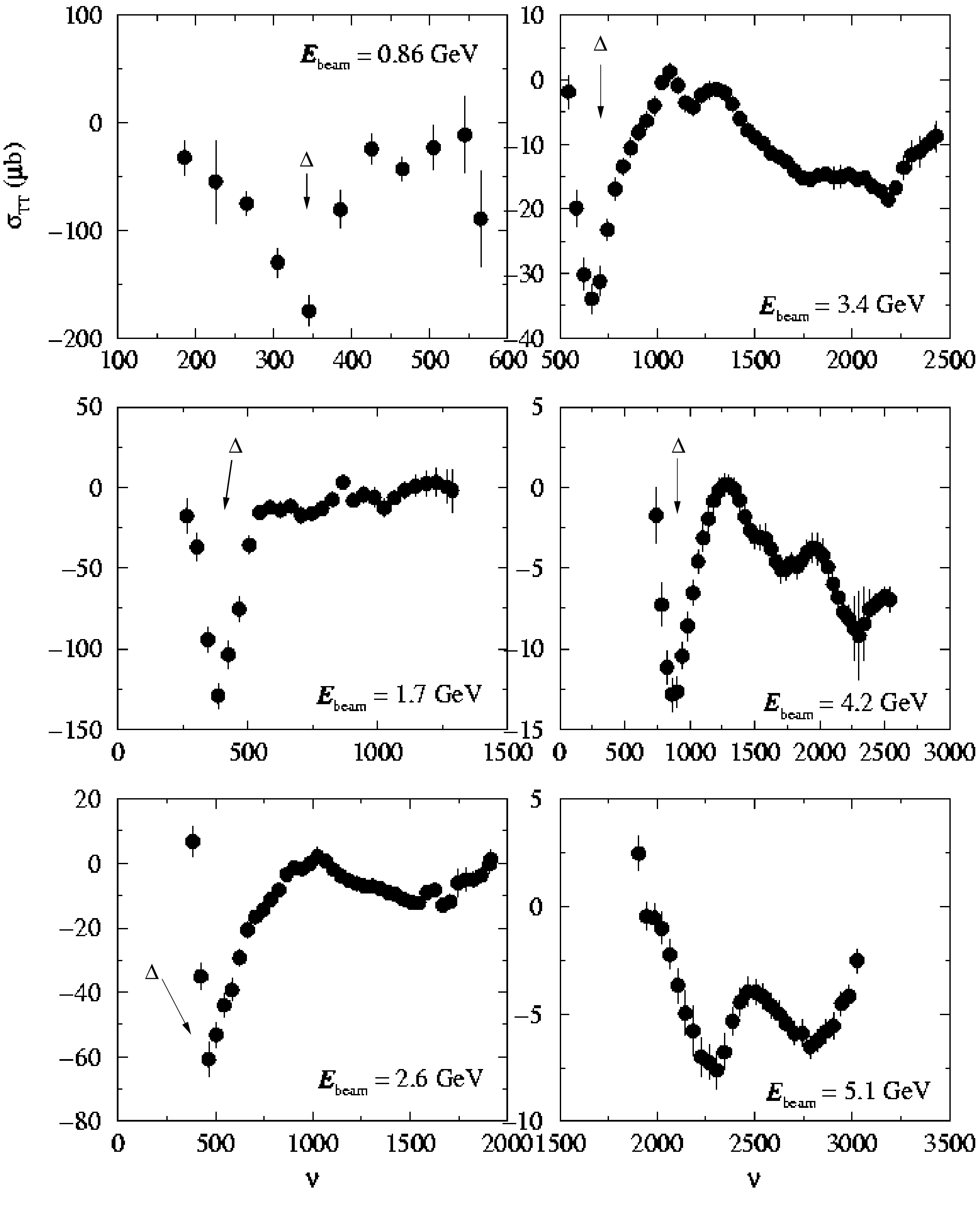

Figure B.10: $\sigma^{TT}(Q^2,\nu)$, l'intégrant de GDH*, sur l'^{3}He à énergies de faisceau constantes. Pour le flux de photons virtuels la convention de Gilman est utilisée. Seules les erreurs statistiques sont présentes.

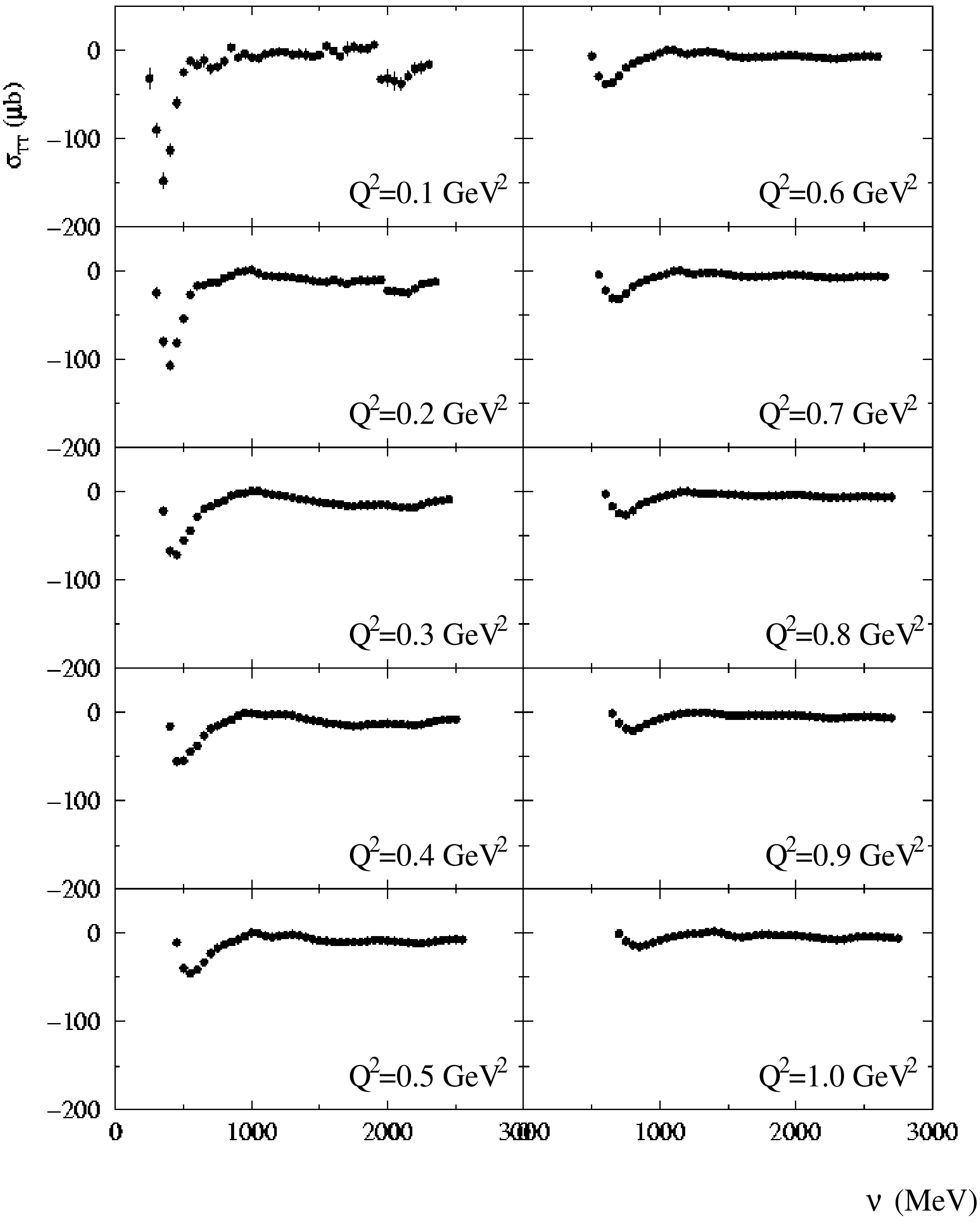

Figure B.11: $\sigma^{TT}(Q^2, \nu)$, l'intégrant de GDH*, sur l'^{3}He à Q^2 constant (après interpolation). Pour le flux de photons virtuels la convention de Gilman est utilisée. Seules les erreurs statistiques sont présentes.

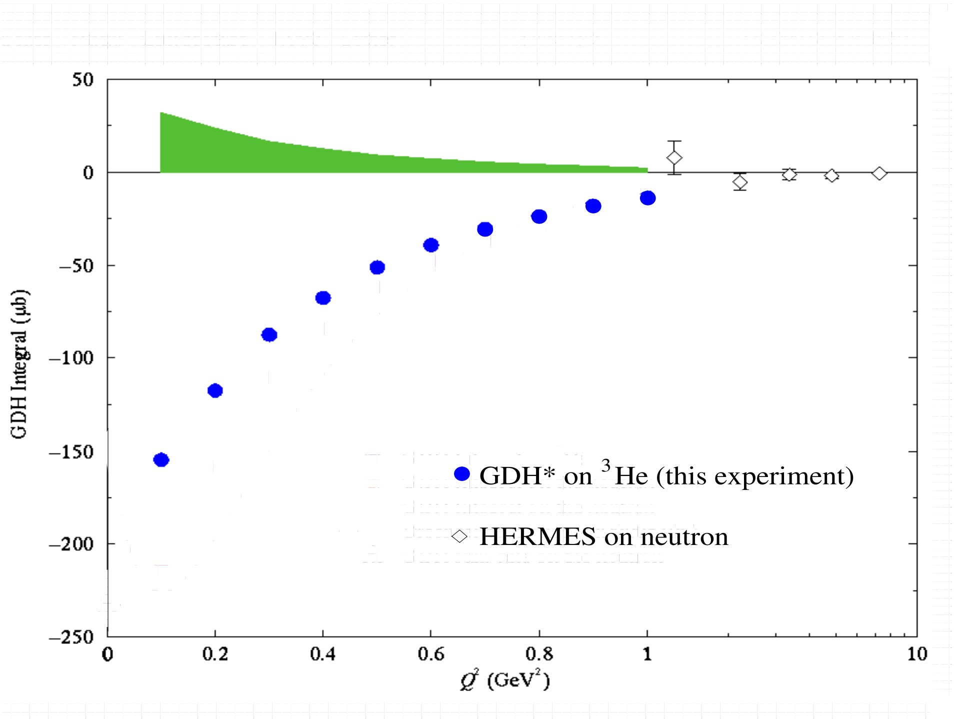

Figure B.12: l'intégrale GDH généralisée sur l'^{3}He pour notre expérience et l'expérience HERMES (neutron) [84]. La contribution quasi-élastique n'est pas incluse. Notre erreur systématique est estimée à 10%. L'intégration n'est faite que sur notre domaine cinématique accessible. Cela est important en particulier pour les points de plus bas Q^2 où l'intégration ne va pas au delà du Δ. Les erreurs systématiques dues aux corrections radiatives à bas Q^2 ne sont pas présentes. Notons que pour les données en dessous de 1 GeV^2 l'échelle est linéaire et qu'elle est logarithmique au dessus.

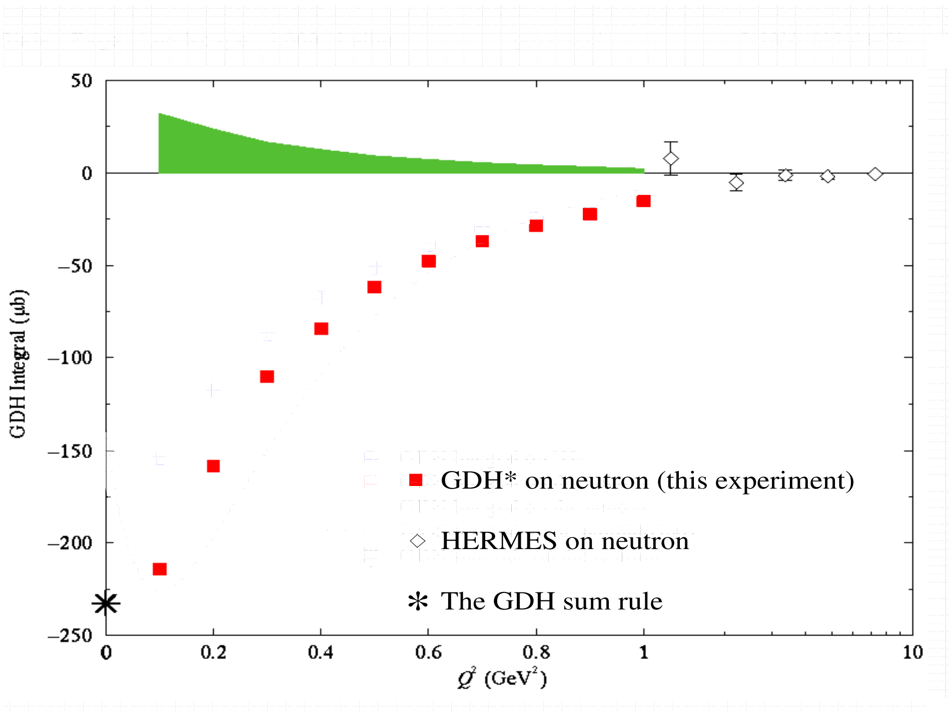

Figure B.13: L'intégrale GDH généralisée sur le neutron pour notre expérience et l'expérience HERMES [84]. Notre erreur systématique est estimée à 15%. Les 5% supplémentaire par rapport á la figure B.12 viennent de l'extraction des informations sur le neutron à partir de l'Helium. L'intégration n'est faite que sur notre domaine cinématique accessible. En particulier pour les points de plus bas Q^2 l'intégration ne va pas au delà du Δ. Les erreurs systématiques dues aux corrections radiatives à bas Q^2 ne sont pas présentes. Notons que pour les données en dessous de 1 GeV^2 l'échelle est linéaire et qu'elle est logarithmique au dessus. Seules les erreurs statistiques sont présentes.

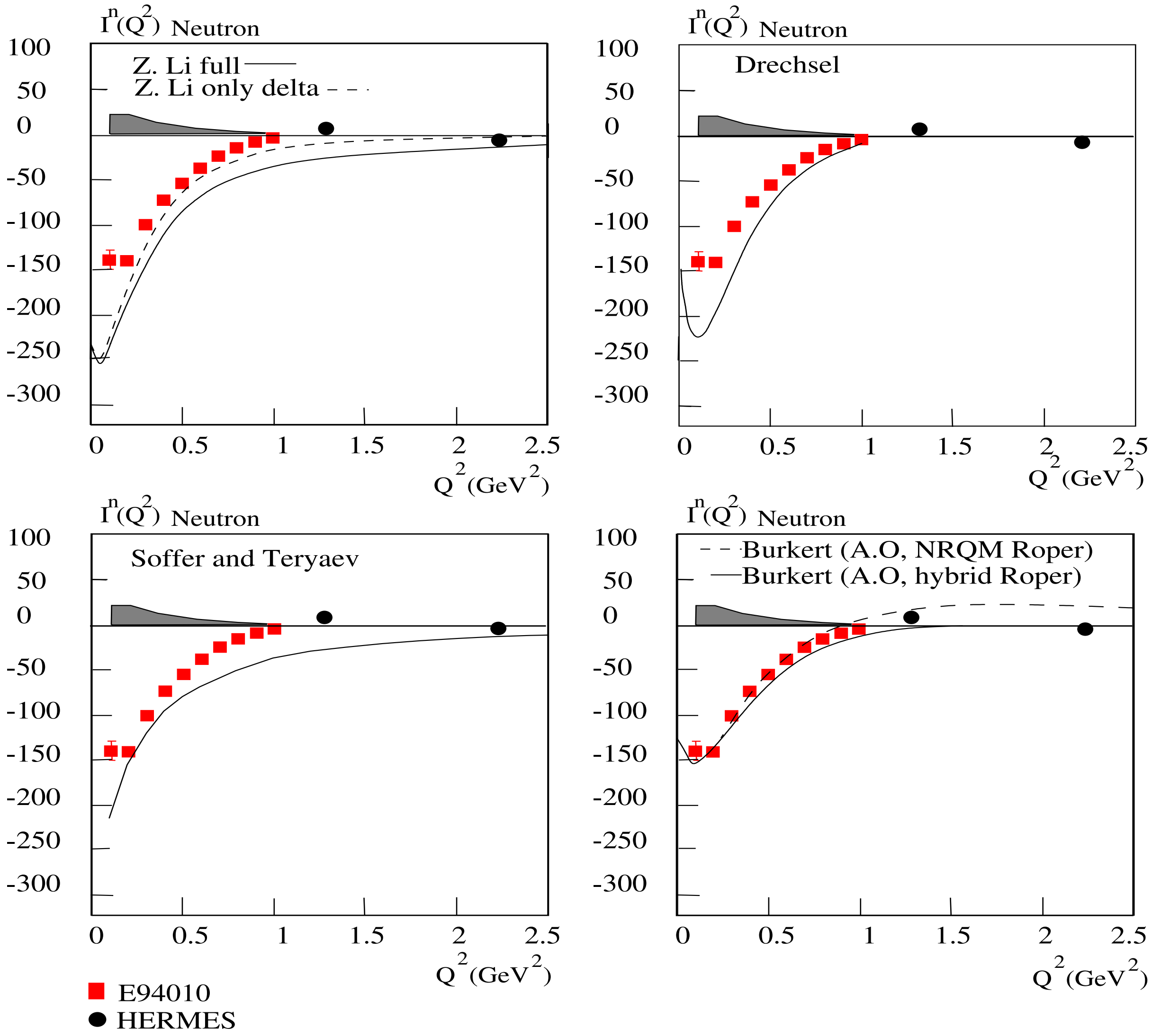

Figure B.14: L'intégrale GDH* sur le neutron comparée à différents modèles. Notre erreur systématique est estimée à 15%. L'intégration n'est faite que sur notre domaine cinématique accessible. En particulier pour les points de plus bas Q^2 où l'intégration ne va pas au delà du Δ. Les erreurs systématiques dues aux corrections radiatives à bas Q^2 ne sont pas présentes. Le modèle de Z. Li [180] est basé sur un Hamiltonien décrivant l'interaction d'un système de quarks. Les fonctions d'état du système sont construites dans le cadre du modèle des quarks constituants. Le modèle phénoménologique de D. Drechsel et al [59], [62] calcule l'intégrale de GDH* en terme de multipôles. J. Soffer et O. Teryaev modélisent la dépendance en Q^2 de l'intégrale de GDH* en utilisant la règle de somme de Burkhardt-Cottingham [164], [165]. Le modèle phénoménologique de V. Burkert et al [29] est une paramétrisation des données mondiales reposant sur le modèle des quarks constituant.

Appendix C

Kinematics.

The spectrometer settings are given in this appendix as well as the kinematic variables relevant to our experiment.

We recall that:

- E is the incoming electron energy;
- E' is the spectrometer central momentum setting;
- w is the invariant mass;
- ν is the energy loss for electrons having a momentum equal to the spectrometer central momentum setting;
- x is the scaling variable;
- Q^2 is the quadri-momentum transfer;

E (GeV)	E' (GeV)	w (GeV)	ν (GeV)	x	Q^2 (GeV^2)
0.86	0.86	0.91	0.00	-	0.054
0.86	0.85	0.92	0.01	2.83	0.053
0.86	0.84	0.93	0.02	1.40	0.053
0.86	0.83	0.94	0.03	0.92	0.052
0.86	0.81	0.96	0.05	0.54	0.051
0.86	0.75	1.02	0.11	0.22	0.047
0.86	0.69	1.07	0.17	0.13	0.043
0.86	0.59	1.16	0.27	0.07	0.037
0.86	0.54	1.20	0.32	0.06	0.034
0.86	0.46	1.27	0.40	0.04	0.029
0.86	0.43	1.29	0.43	0.03	0.027
0.86	0.39	1.31	0.47	0.03	0.024
0.86	0.36	1.34	0.50	0.02	0.023
0.86	0.31	1.38	0.55	0.02	0.019

E (GeV)	E' (GeV)	w (GeV)	ν (GeV)	x	Q^2 (GeV^2)
1.72	1.74	0.79	-	-	0.217
1.72	1.67	0.87	0.05	2.22	0.208
1.72	1.61	0.94	0.11	0.97	0.201
1.72	1.48	1.07	0.24	0.41	0.185
1.72	1.37	1.17	0.35	0.26	0.171
1.72	1.26	1.26	0.46	0.18	0.158
1.72	1.17	1.33	0.55	0.14	0.146
1.72	1.08	1.40	0.64	0.11	0.135
1.72	1.00	1.45	0.72	0.09	0.125
1.72	0.92	1.51	0.80	0.08	0.115
1.72	0.85	1.55	0.87	0.07	0.106
1.72	0.78	1.60	0.94	0.06	0.098
1.72	0.71	1.64	1.01	0.05	0.089
1.72	0.67	1.66	1.05	0.04	0.084
1.72	0.45	1.79	1.27	0.02	0.56

E (GeV)	E' (GeV)	w (GeV)	ν (GeV)	x	Q^2 (GeV^2)
2.59	2.58	0.64	0.01	-	0.486
2.59	2.53	0.72	0.06	-	0.477
2.59	2.50	0.76	0.09	2.78	0.470
2.59	2.48	0.79	0.11	2.26	0.467
2.59	2.38	0.91	0.21	1.14	0.448
2.59	2.27	1.03	0.32	0.71	0.428
2.59	2.18	1.11	0.41	0.53	0.410
2.59	2.01	1.26	0.58	0.35	0.379
2.59	1.85	1.39	0.74	0.25	0.349
2.59	1.71	1.49	0.88	0.20	0.322
2.59	1.58	1.57	1.01	0.16	0.298
2.59	1.46	1.65	1.13	0.13	0.275
2.59	1.35	1.72	1.24	0.11	0.254
2.59	1.24	1.78	1.35	0.09	0.234
2.59	1.15	1.83	1.44	0.08	0.217
2.59	1.06	1.88	1.53	0.07	0.200
2.59	0.98	1.93	1.61	0.06	0.185
2.59	0.90	1.97	1.69	0.05	0.170
2.59	0.85	2.00	1.74	0.05	0.160
2.59	0.83	2.01	1.76	0.05	0.156
2.59	0.71	2.07	1.88	0.04	0.134

E (GeV)	E' (GeV)	w (GeV)	ν (GeV)	x	Q^2 (GeV^2)
3.38	3.03	0.89	0.35	1.13	0.745
3.38	2.80	1.13	0.58	0.63	0.688
3.38	2.58	1.32	0.80	0.42	0.634
3.38	2.38	1.47	1.00	0.31	0.585
3.38	2.20	1.60	1.18	0.24	0.541
3.38	2.03	1.71	1.35	0.20	0.499
3.38	1.87	1.80	1.51	0.16	0.460
3.38	1.60	1.96	1.78	0.12	0.393
3.38	1.36	2.08	2.02	0.09	0.335
3.38	1.16	2.18	2.22	0.07	0.285
3.38	1.00	2.26	2.38	0.06	0.246

E (GeV)	E' (GeV)	w (GeV)	ν (GeV)	x	Q^2 (GeV^2)
4.24	3.63	0.95	0.61	0.98	1.120
4.24	3.35	1.23	0.89	0.62	1.033
4.24	3.09	1.44	1.15	0.44	0.953
4.24	2.86	1.61	1.38	0.34	0.882
4.24	2.64	1.75	1.60	0.27	0.814
4.24	2.43	1.88	1.81	0.22	0.749
4.24	2.08	2.07	2.16	0.16	0.642
4.24	1.84	2.20	2.40	0.13	0.567
4.24	1.77	2.23	2.47	0.12	0.546
4.24	1.70	2.26	2.54	0.11	0.524
4.24	1.39	2.41	2.85	0.08	0.429

E (GeV)	E' (GeV)	w (GeV)	ν (GeV)	x	Q^2 (GeV^2)
5.06	3.09	1.86	1.97	0.31	1.137
5.06	2.85	1.99	2.21	0.25	1.049
5.06	2.63	2.11	2.43	0.21	0.968
5.06	2.42	2.22	2.64	0.18	0.89
5.06	2.23	2.32	2.83	0.15	0.82
5.06	2.06	2.40	3.00	0.13	0.758

Appendix D

Integration Limits.

This appendix gives the integration limits on σ^{TT} when calculating GDH*(Q^2). The threshold is the pion threshold on the free neutron.

Q^2 (GeV^2)	ν (GeV)
0.1	2.300
0.2	2.350
0.3	2.450
0.4	2.500
0.5	2.550
0.6	2.600
0.7	2.650
0.8	2.700
0.9	2.700
1.0	2.750

Bibliography

[1] A. Thomas for the A2 -and GDH- collaboration. The GDH experiment at MAMI. Nucl. Phys. **79** 591 Proc sup. (1999)

[2] H.D.I Abarbanel and M.L. Goldberger. Phys. Rev. **165**, 1594. (1968)

[3] A. Abragam, Principle of nuclear magnetism, Oxford University Press, Oxford, 1961.

[4] A. Afanasev, C. Carlson and C. Wahlquist. Measuring polarized gluon and quark distribution with meson photoproduction. Phys. Rev. D. **58**. 054007. (1998)

[5] J. Ahrens. Talk given at Jefferson Lab. 1999.

[6] J. Ahrens et al. The GDH and A2 collaboration. Helicity Dependence of the γp$\rightarrow$Nπ below 450 MeV and Contribution to the Gerasimov-Drell-Hearn Sum Rule. Phys. Rev. Let. **84**. 5950. (2000)

[7] Amroun et al. ^{3}H and^{3}He electromagnetic form factors. Nuc. Phys. A **579** 596, (1994)

[8] M. Anselmino, B.L. Ioffe and E. Leader, On possible resolution of the spin crisis in the parton model. Sov. J. Nucl. Phys. **49**, 136, (1989)

[9] H. Arenhövel, D. Drechsel, H. J. Weber. Electronuclear sum rules. Nuc. Phys A **305** 485. (1978)

[10] H. Arenhövel The GDH sum rule for the deuteron. nucl-th/0006083 2000.

[11] I.I. Balitsky, V.M. Braun and A.V. Kolesnichenko. Phys. Lett. **B242** 245, (1990)

[12] S. Bass. Sea Polarization and the GDH Sum Rule(s) Z. Phys. A **355** 77, (1996)

[13] S. Bass The Drell-Hearn-Gerasimov Sum-Rule in QCD. Mod. Phys. Lett. A **12** 1051, (1997)

[14] S. Bass. M. Brisudová. The Spin and Flavour Dependence of the High Energy Photoabsorption. Eur. Phys. J. A **4** 251, (1999)

[15] H. Burkhardt and W. Cottingham. Ann. Phys. **16**, 543 (1970)

[16] V. Bernard, N. Kaiser and U. Meissner, Small Momentum Evolution of the Extended Drell Hearn Gerasimov sum rule. Phys Rev D **48** 3062. (1993)

[17] J. Berthot. Private communication. (berthot@clermont.in2p3.fr)

[18] N. Bianchi and E. Thomas. Parametrization of $\sigma^{1/2} - \sigma^{3/2}$ for $Q^2 \geq 0$ and non resonance contribution. Phys. Lett. B **450** 439. (1999)

[19] J.D. Bjorken. Applications of the chiral $U(6) \otimes U(6)$ algebra of current densities. Phys. Rev. **148**. 1467 (1966)

[20] J.D. Bjorken, Phys. Rev. **179** 1547. 1969.

[21] V. Burkert. Nucleon Resonance and Nuclei. CEBAF PR87-025. 1987

[22] V. Burkert. CEBAF and the Baryon Physics Program. CEBAF PR 96-001. 1996

[23] V. Burkert. Nucleon Structure and Nucleon resonances. Lectures given at the HUGS 1988 Graduate School. 1988.

[24] V. Burkert. Leptonic Production of Baryon Resonances. CEBAF PR 93-035. 1993.

[25] V. Burkert. Spin Degree of Freedom in Electron-Nucleon Scattering in the Resonance Region. CEBAF PR 87-006 . 1987.

[26] V. Burkert. Spin Structure Function of the Nucleon at Low Q^2 and υ. CEBAF PR 93-031. 1993.

[27] V. Burkert and B. Ioffé. On the Q^2 Variation of the Spin Dependant Electron-Proton Scattering. CEBAF PR 92-018. 1992.

[28] V. Burkert and B. Ioffé. Polarized Structure Function of the Proton and Neutron and the GDH and Bjorken Sum Rules. CEBAF PR93-034. 1993

[29] V. Burkert and Z. Li. What Do We Know About the Q^2 Evolution of the GDH Sum Rule. CEBAF PR 92-017. 1992.

[30] V. Burkert. Comment on the Generalized Gerasimov-Drell-Hearn Sum Rule in Chiral Perturbation Theory. nucl-th/0004001. 2000.

[31] F. Cardarelli. The Nucleon Drell Hearn Gerasimov Sum Rule within a relativistic quark model. Phys.Lett. B **418** 237. (1998)

[32] L. S. Cardman et al. The Charge Distribution of ^{12}C. Physics Letters. Vol. **91B** 2. 203 (1980)

[33] C. Ciofi degli Atti and S. Scopetta, E Pace, G. Salmè. Nuclear Effects in Deep Inelastic Scattering of Polarized Electrons off polarized ^3He and the Neutron Spin Structure Functions. Phys.Rev. C **48** 968. (1993)

[34] C. Ciofi degli Atti and S. Scopetta. On the extraction of the neutron spin structure function and the Gerasimov-Drell-Hearn integral from the process $^3\overrightarrow{He}(\overrightarrow{e}, e')X$ in the resonance region. Phys. Let. B**404** 223, (1997)

[35] E. Chudakov. E94010 collaboration meeting, July 1999. (gen@jlab.org)

[36] CODA. Cebaf Online Data Analyzer. http.//www.jlab.org/coda

[37] F. Close and Z. Li. Photo- and electroproduction of N* in a quark model. Phys. Rev. D **42** 2194. (1990)

[38] A. Deur. La Cible cryogénique de Hall A du Thomas Jefferson National Accelerator Facility. Rapport de stage de DEA, université Blaise Pascal, September 1997.

[39] A. Deur. Knock-on of δ-electron in Hall A electron arm. Effect of the aerogel Cerenkov. Jefferson Lab Technical note TN98-028. 1998.

[40] A. Deur, S. Jensen. Elastic Asymmetries Analysis for E94010. Jefferson Lab Technical Note E94010TN34. 2000

[41] A. Deur. and J.P. Chen. Magnetic Field Cartography of the Hall A ^{3}He Polarized Target. E94010 Technical Note E94010TN21. 1998.

[42] A. Deur. E94010 simulation and run plan optimization. LPC technical note PCCF RI 9913. 1999.

[43] A. Deur, Z.-E. Meziani. Experiment E94010 run plan. LPC technical note PCCF RI 9914. 1999.

[44] A. Deur. Single Arm Monte Carlo for Polarized experiment in Hall A. E94010 Technical Note E94010TN33. 2000.

[45] A. Deur. Acceptance simulation studies for the Hall A High Resolution Spectrometers. E94010 Technical Note E94010TN36. 2000.

[46] A. Deur. Vertical Drift chambers analysis for E94010. E94010 technical note E94010TN29. 1999.

[47] A. Deur. E94010 collaboration meeting. Sept 1999. (deurpam@jlab.org)

[48] A. Deur. Beam Position and Elliptical Raster Analysis. Jefferson Lab Technical Note JLab-TN-00-042. 2000.

[49] A. Deur. About the NMR relaxation times T1 and T2. Procedure to fill the reference cell. E94010 Technical Note E94010TN12. 1998.

[50] A. Deur. Elastic cross section analysis. E94010 Technical Note E94010TN35. 2000.

[51] D. Marchand. Mesure absolue de l'énergie du faisceau d'électron de Jefferson Lab. (Hall A) par une méthode magnétique: Projet arc. These, DAPNIA/SPHN-98-04T. 1998.

[52] T.W. Donnelly and A.S. Raskin. Consideration of Polarization in Inclusive Electron Scattering from Nuclei. Annals of Physics **169**, 247, (1986)

[53] D. Drechsel. The GDH Integral and the Spin Structure of the Nucleon. MKPH -T - 98-19. 1998.

[54] D.Drechsel and G. Krein. The GDH Sum Rule and the Single pion photoproduction multipole E_{0+} Close to Threshold. Phys. Rev. D **58** 116009. (1998)

[55] D. Drechsel. Form Factors and Exclusive Processes. Introduction and Overview. nucl-th 9811035. 1998.

[56] D. Drechsel. Nucl. Phy. **34** 181. (1995)

[57] D. Drechsel. Electromagnetic Investigations of Nucleon Resonances and Sum Rules. Proc. of International School on Nuclear Physics. Erice. Sept. 1999. MKPH-T-99-28.

[58] D. Drechsel. The Drell-Hearn-Gerasimov Sum Rule. Prog. Part. Nucl. Phys. **34** 181 (1995)

[59] D. Drechsel, O. Hanstein, S.S. Kamalov and L. Tiator. A unitary isobar model for pion photo- and electroproduction on the proton up to 1 GeV. Nucl. Phys. A **645** 145. (1999)

[60] D. Drechsel, S.S. Kamalov G. Krein and L. Tiator. The Generalized Gerasimov - Drell-Hearn Integral and the Spin Structure of the Nucleon. Phys.Rev. **59** 094021. (1999)

[61] D. Drechsel. The structure of the Nucleon. nucl-th/0003061. 2000.

[62] D. Drechsel, S.S. Kamalov and L. Tiator, The GDH Sum Rule and Related Integrals. hep-ph/0008306. 2000.

[63] S.D. Drell and A.C. Hearn. Phys. Rev. Lett. **16** 908. (1966)

[64] The E80 collaboration: M. Alguard et al. Deep inelastic scattering of polarized electrons by polarized protons. Phys. Rev. Lett. **37**. 1261. (1976)

[65] The E130 collaboration: G. Baum et al. Phys. Rev. Lett. **45**, 2000. (1980)

[66] The E143 collaboration: K. Abe et al. Measurement of the Proton and Deuteron Spin Structure Function g_1 in the Resonance Region. Phys.Rev.Lett. **78** 815. (1997)

[67] The E155 collaboration: P. Anthony et al, the E155 collaboration. Measurements of the Q^2-Dependence of the Proton and Neutron Spin Structure Functions g_1^p and g_1^n . hep-ph/0007248. 2000.

[68] The E155 collaboration: P. Anthony et al, the E155 collaboration. Inclusive Hadron Photoproduction from Longitudinally Polarized Protons and Deuterons. Phys.Lett. B **458** 536 (1999)

[69] P. Bosted, for the E155x collaboration. Very Preliminary Results for the Spin Structure Function g_2 from SLAC E155x. In proceeding of PANIC 1999. Nucl. Phys. A **663&664** 297c. (2000)

[70] J. Ahrens et al. www.pit.physik.uni-tuebingen.de/grabmayr/GDH/gdh_text.html.

[71] The EMC collaboration: J. Ashman et al. A measurement of the spin asymmetry and determination of the structure function g_1 in deep inelastic muon-proton scattering. Phys. Lett. B **206**. 2. 364. (1988)

[72] EPICS. http://www.jlab.org/accel/documents/epics_doc.html

[73] ESPACE Manual. E.A.J.M Offermann and M. Kuss. hallaweb.jlab.org/espace

[74] R.P. Feynman. Phys. Rev. Lett. **23**, 1415. (1969)

[75] R.P. Feynman. Photon-Hadron Interaction. Addison-Wesley 1989.

[76] K. Fissum. Private communication. (fissum@jlab.org)

[77] H. Fonvieille. La nature de la sonde électromagnétique. Lectures given at the Ecole Joliot-Curie. Maubuisson 1992.

[78] J. Friar et al. Neutron polarization in polarized ^{3}He targets Phys. Rev. **C42**. 2310. (1990)

[79] M. Gell-Mann. Phys. Lett. 8, 214. (1964)

[80] S. Gerasimov, Yad. Fiz.**2** 598 (1965), Sov J. Nucl. Phys. **2** 930. (1966)

[81] Gerasimov and Moulin. Nucl. Phys. **898**, 349 (1975)

[82] F. Gross. Electromagnetic Studies in Nuclei. CEBAF PR85-003. 1985.

[83] O. Hansen and Y. Roblin. Control System Design for the Hall A Polarized 3He Target. E94010 Technical Note E94010TN01. 1998.

[84] K. Ackerstaff et al. Determination of the Deep Inelastic Contribution to the Generalised Gerasimov-Drell-Hearn Integral for the Proton and Neutron. Phys.Lett. B **444** 531. (1998)

[85] P.D.B Collin and A.D. Martin. Hadron Interaction. Adams Hilger Ltd. 1984.

[86] R.A. Hofstadter. The structure of the nucleon. A. Benjamin, Reading, (MA), 1963.

[87] M. Hosoda and K. Yamamoto. Prog. Theor. Phys. **35**, 425. (1966)

[88] S. Incerti. The NMR System of the Hall A Polarized ^{3}He Target. Jefferson Lab Technical Note Lab-TN-98-049. 1998.

[89] S. Incerti and S. Jensen. Calculation of the water calibration constant for E94-010. E94010 Technical Note E94010TN28. 1999.

[90] S. Incerti, E. Lakuriqi and F. Xiong. The Effect of the Transverse Component of the Electron Beam Polarization on Experimental Asymmetries. E94010 Technical Note E94010TN06. 1998.

[91] S. Incerti. Private communication. (incerti@jlab.org)

[92] B. L. Ioffé. On Conservation of the Baryon Chirality in the Processes With Large Momentum transfer. Phys. Letters vol. **63B**, number 4. (1976)

[93] B. Ioffé. Sum Rules for Nucleon Spin Structure Function. hep-ph/9511264.

[94] N. Isgur and G. Karl, Phys. Lett **72B** 109 (1977).

[95] N. Isgur. Baryon and QCD. JLAB THY 97 11. 1997.

[96] N. Isgur. The Spin of the Proton. JLAB THY 97 14. 1997.

[97] N. Isgur. Valence Quark Spin Distribution Functions. Phys.Rev. D **59** 034013. (1999)

[98] S. Jaminion. Diffusion Compton virtuelle à Jefferson Laboratory et mesure des polarisabilités généralisées du proton. Thèse de l'Université Blaise Pascal. Decembre 2000.

[99] S. Jensen. Measurement of the neutron (^{3}He) spin structure functions at low Q^2; A connection between the Bjorken and the Drell-Hearn-Gerasimov sum rules. Ph.D. thesis, California Institute of Technology. July 2000.

[100] S. Jensen. Cell Wall Thickness measurement for E94-010. unpublished.

[101] X. Ji. Interpolating the Nucleon's Spin Dependant Sum Rules at High and Low Energies. Phys.Lett. B **309** 187. (1993)

[102] X. Ji and P. Unrau. Q^2-Dependence of the proton's G_1 Function Sum Rule. Phys.Lett. B333 228-232. 1994.

[103] X. Ji. Physics of Q^2-Dependence in the Nucleon's $G_1(x,Q^2)$ Structure Function Sum Rule hep-ph 9502288. 1995.

[104] X. Ji. Physics of Q^2-Dependence of Deep Inelastic Sum Rules. hep-ph 9403260. 1994.

[105] X. Ji and P. Unrau. Parton Hadron Duality: Resonances and Higher Twists. Phys. Rev. D Vol **52** 1 (1995)

[106] X. Ji and W. Melnitchouk. Spin Dependent Twist Four Matrix Element from g_1 Data in the Resonance Region. Phys. Rev. D Vol **56** 1 (1997)

[107] X. Ji and J. Osborn. Generalized Sum Rules for Spin Dependent Functions of the Nucleon. hep-ph 9905410. 1999.

[108] X. Ji, C-W. Kao and J. Osborn. Generalized Sum Rules at Order $\sigma(p^4)$ in Chiral Perturbation Theory. Phys. Rev. D **61** 074003. (2000)

[109] X. Ji. Q^2-Dependence of Deep Inelastic Sum Rules. hep-ph 9403260. 1994.

[110] X. Jiang, Ph.D. Thesis. Measurement of the Interference Structure Functions in Quasielastic Proton Knock Out from ^{12}C. University of Massachusetts Amherst. 1999.

[111] X. Jiang. Private communication. Jiang@jlab.org

[112] V. D. Burkert, D. Crabb, E Minehart et al., Jefferson lab experiment E91023;
S. Khun et al. , Jefferson Lab experiment E93009;
Z.-E. Meziani, G. Cates, J.-P. Chen et al., Jefferson lab experiment E94010;
J.-P. Chen, S. Gilad, C.Whisnant et al., Jefferson lab experiment E94117;
J.-P. Chen, G. Cates, F. Garibaldi et al., Jefferson lab experiment E97110;

[113] M. Jones. Private communication. (jones@jlab.org)

[114] M. Jones et al. Gep/Gem ratio by polarized transfer in $\overrightarrow{e}p \rightarrow e\overrightarrow{p}$. Phys.Rev.Lett. **84** 1398 (2000)

[115] I. Karliner. Saturation of the Drell-Hearn-Gerasimov Sum Rule. Phys Rev D. vol **7**, num 9. (1973)

[116] M. Knecht. Une Introduction a la Symétrie Chirale. Lectures given at the Ecole Joliot-Curie. Maubuisson 1998.

[117] T. Killian, Thermionic Phenomena by Vapors of Rubidium and Potassium. Phys. Rev. **27**, 578, (1926)

[118] I. Kominis. Target Cell Specification. E94010 Technical Note E94010TN25. 2000.

[119] I. Kominis. Private communication. kominis@jlab.org

[120] I. Kominis. Electron-Pion separation technical note. Unpublished. 1999.

[121] I. Kominis. Technical note. Unpublished

[122] I. Kominis. Ph. D Thesis. Princeton. To come.

[123] W. Korsch T. Averett. Experiment E97103. Search for Higher Twist Effects in the Neutron Spin Structure Function $g_2^n(Q^2)$. 1997.

[124] G. Laveissiere. Mesure de l'intensité d'un faisceau continu d'électrons. Rapport de stage de DEA, université Blaise Pascal, August 1996.

[125] J. J. LeRose. Jefferson Lab Hall A Collaboration Meeting, May 2000.

[126] J. J. LeRose. http://hallaweb.jlab.org/news/minutes/acc.html and Private communication. (lerose@jlab.org)

[127] D. Lhuillier. Diffusion Compton Virtuelle A Basse Energies. Thése d'université. Caen. DAPNIA/SPhN-97-01T. 1997.

[128] D. Lhuillier. Private communication. dlhuillier@cea.fr

[129] Lightbody, O'connel. Modeling Single Arm Electron Scattering and Nucleon Production by GeV Electrons. Computers in Physics. 57-64 May-June 1988.

[130] N. Liyanage, Ph.D. Thesis. A study of $^{16}O(e,e'p)$ Reaction at Deep Missing Energies. Massachusetts Institute of Technology. Feb 1999.

[131] N. Liyanage. E94010 Collaboration meeting. July 17 1999.

[132] N. Liyanage. Private communication and Spectrometer constant determination. Hall A internal note. October 1999. Unpublished.

[133] N. Liyanage. E94010 collaboration meeting, May 2000. (nilanga@jlab.org)

[134] A. V. Manohar. Introduction to Spin Dependent Deep Inelastic Scattering. UCSD/PTH 92-10. 1992.

[135] U. Meissner. Talk given at the GDH 2000 symposium. Mainz, June 2000. Proceedings to come.

[136] R. Michaels. Private communication. (rom@jlab.org)

[137] H.L. Middleton, The Spin Structure of the Neutron Determined Using a Polarized ^{3}He Target. Ph.D. Thesis, Princeton, 1994.

[138] R.G. Milner. Spin Structure of ^{3}He. In the proceeding of the 10th NIKHEF miniconference. Ed H. P. Blok. E. Jans and G. Van der Steenhoven. 1999.

[139] Mo and Tsai.. Radiative Corrections to Elastic and Inelastic ep and μP Scattering. Rev. Mod. Phys. **41**. 1 205. (1969)

[140] I. Musatov, O. Teryaev and A. Schäfer. The Elastic contribution to the Burkhardt-Cottingham and Generalized Gerasimov-Drell-Hearn Sum Rules. Phys.Rev. D **57** 7041. (1998)

[141] N. Newbury, A. Barton, G. Cates, W. Happer and H. Middleton.Gaseous ^{3}He-^{3}He magnetic dipolar spin relaxation Phys. Rev. A **48**, 4411. (1993)

[142] Ngo and Ngo. Physique Quantique, Introduction. Masson. 1991.

[143] V. Pandaripande. Aspect of Nuclear Structure Seen by Electron Scattering. Proc 10th NIKHEF miniconference. Ed H. Blok, E. Jans and J. Van der Steenhoven. 1999.

[144] R. Pantförder. Investigation on the Foundation and Possible Modification of the GDH Sum Rule. hep-ph 9805434. Ph. D. Thesis 1998.

[145] PAW (Physics Analysis Workstation) manual R. Brun et al. wwwinfo.cern.ch/asd/paw/

[146] Particle Physics Booklet. AIP. 1996.

[147] F. Halzen and A. Martin. Quark and Lepton. John Wiley & Sons. 1984.

[148] G. Quéméner. Private communication. quemener@jlab.org

[149] G. Quéméner. Cartographie magnétique des quadripôles des spectromètresa haute résolution du Thomas Jefferson National Accelerator Laboratory, Hall A, thèse de l'université Blaise Pascal, 1997.

[150] O. Ravel. Mesure absolue de l'énergie du faisceau d'électron de TJNAF. Thèse de l'université Blaise Pascal, 1997.

[151] Y. Roblin and A. Deur. Technical note on the laser control. Unpublished

[152] Y. Roblin and A. Deur. Technical note on the temperature control. Unpublished

[153] R. G. Roberts, The structure of the proton. Cambridge Univ. Press. 1990.

[154] M. Romalis. Laser Polarized ^{3}He Target Used for a Precision Measurement of the Neutron Spin Structure. Princeton, 1997

[155] A. Saha. Current, Charge and Energy Precision Measurements in Hall A. Internal note unpublished. saha@jlab.org

[156] A. Saha. E94010 Collaboration Meeting. March 1999.

[157] F. Sauli. Principle of operation of multiwire proportional and drift chambers. CERN 77-09. 1977.

[158] A.M. Sandorfi, C.S. Whisnant and M. Khandaker, Phys. Rev. D **50**. R6681. (1994)

[159] Schulze & Sauer. Inelastic electron scattering from three nucleon bound states with polarization. Phy. Rev. C **48** 38 (1993)

[160] O. Scholten and A. Korchin. Q^2 dependence of the Drell-Hearn-Gerasimov integral. Eur.Phys.J. A **6** 211. (1999)

[161] K. Slifer. E94010 collaboration meeting. Feb 2000.

[162] K. Slifer. Analysis of the Hall A Cerenkov for E94010. E94010 Technical note E94010TN32. 2000.

[163] K. Slifer. Shower Detector Calibration and Cut Optimization for E94010. E94010 Technical note E94010TN31. 2000.

[164] J. Soffer and O. Teryaev. Role of g_2 in Relating the Schwinger and Drell-Hearn-Gerasimov Sum Rules. Phys. Rev Let. **70**. vol 22. 3373. (1993.)

[165] J. Soffer and O. Teryaev. Comment on the Burkhardt-Cottingham and Generalised GDH Sum Rules for the Neutron. Phys.Rev. D **56** 7458. (1997)

[166] T. B. Smith. A Precision Measurement of the Neutron Spin Structure Functions Using a Polarized ^{3}He Target. Ph.D. Thesis, The University of Michigan, 1998.

[167] Satus Report on Activities in Hall A-1999. Ed E.J Brash, R.D. Ransom, C.W. De Jager.

[168] R.E. Taylor. Proc. of 4th Int. Symp. on Electron and Photon interactions at High Energies. Daresburg, Eng., 251. 1969.

[169] A.K. Thompson. Measurement of Asymmetries in Inclusive Quasi-Elastic Scattering of Polarized Electrons from Polarized 3He. Ph. D. Thesis. Massachusetts Institute of Technology. 1991.

[170] L. Tiator, D. Drechsel and S.S. Kamalov. Pion Electroproduction on the Nucleon and the Generalized GDH Sum Rule. MKPH-T-99-22. 1999.

[171] P. Ulmer. MCEEP, Monte Carlo for (e,e'p) Experiments. www.physics.odu.edu/~ulmer/mceep/mceep.html

[172] W. Van Orden. Introduction to Electron Scattering Theory. Lectures given at the HUGS 1988 Graduate School. 1988.

[173] Workman and Arndt. Saturation of the Drell-Hearn-Gerasimov Sum Rule Reexaminated. Phys Rev D **45** 1789, (1992)

[174] M.E. Washgull, Polarization of ^{3}He by Spin Exchange with High Density Laser Optically Pumped Rb Vapor. Ph.D. Thesis, Harvard University, 1991.

[175] L. W. Whitlow. A Precise Extraction of R=σ_L/σ_T from a global analysis of the SLAC deep inelastic E P and E D scattering cross-sections. Phys. Lett. B **250**. 193. (1990)

[176] P. de Witt-Huberts. Quasi-Elastic Scattering of Electrons with Nucleus. Lectures given at the HUGS 1988 Graduate School. 1988.

[177] S. Wandzura and F. Wilczek, Phys. Lett. **B72** 195. (1983)

[178] S. Ying. Gerasimov-Drell-Hearn sum rule and the nucleon structure. J.Phys. G **22** 293 (1996)

[179] Z. Li. Photo and Electroproduction of Baryon Resonances in Potential Quark model. Lectures given at the HUGS 1990 Graduate School. 1990.

[180] Z. Li. Polarized Structure Function of the Nucleon in the Resonance Region. Phys. Rev. D vol. **47** - 5 1854 (1993)

[181] G. Zweig. CERN report TH-401, 412. 1964.